**BROOKHAVEN**
NATIONAL LABORATORY

*Conceptual Design Report for a Fast Muon Trigger*

**PHENIX Experiment et, al.**

August 2007

**Physics Department/PO/2-182**

**Brookhaven National Laboratory**
P.O. Box 5000
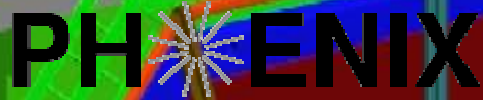Upton, NY 11973-5000
www.bnl.gov

# DISCLAIMER

This report was prepared as an account of work sponsored by an agency of the United States Government. Neither the United States Government nor any agency thereof, nor any of their employees, nor any of their contractors, subcontractors, or their employees, makes any warranty, express or implied, or assumes any legal liability or responsibility for the accuracy, completeness, or any third party's use or the results of such use of any information, apparatus, product, or process disclosed, or represents that its use would not infringe privately owned rights. Reference herein to any specific commercial product, process, or service by trade name, trademark, manufacturer, or otherwise, does not necessarily constitute or imply its endorsement, recommendation, or favoring by the United States Government or any agency thereof or its contractors or subcontractors. The views and opinions of authors expressed herein do not necessarily state or reflect those of the United States Government or any agency thereof.
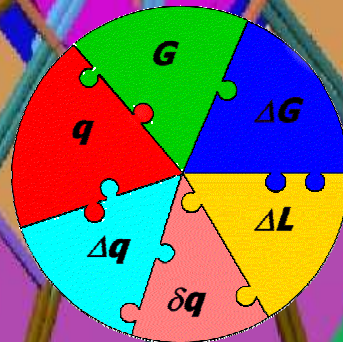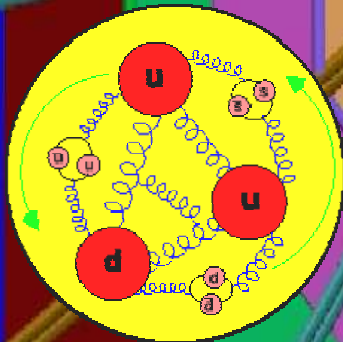
# PH✴ENIX

# Conceptual Design Report
# for a Fast Muon Trigger

# Conceptual Design Report

# for a Fast Muon Trigger

submitted to
**Brookhaven National Laboratory**
**July, 2007**

**PH ENIX**

| | |
|---|---|
| Spokesperson: | Barbara Jacak |
| | *Stony Brook University* |
| Deputy Spokesperson: | Yasuyuki Akiba |
| | *RIKEN* |
| Deputy Spokesperson: | Matthias Grosse-Perdekamp |
| | *University of Illinois, Urbana-Champaign* |
| Deputy Spokesperson: | Richard Seto |
| | *University of California, Riverside* |
| Operations Manager: | Edward O'Brien |
| | *Brookhaven National Laboratory* |
| Upgrades Manager: | Axel Drees |
| | *Stony Brook University* |

# Conceptual Design Report for a Fast Muon Trigger at PHENIX

A. Basye, D. Isenhower, D. Jumper, N. Sparks, R. Towell,
C. Watts, J. Wood, R. Wright
Abilene Christian University, Abilene, TX 19973, USA

J. Haggerty, D. Lynch
Brookhaven National Laboratory, Upton, NY 19973, USA

K. Barish, K. Oleg Eyser, R. Seto
University of California, Riverside, Riverside, CA 92521, USA

S. Hu, X. Li, S. Zhou
CIAE, Beijing, China

A. Glenn, E. Kinney, K. Kiriluk, J. Nagle
University of Colorado, Boulder, CO 80309, USA

C.Y. Chi, W. Sippach, W. Zajc
Columbia University and Nevis Laboratory, Irvington, NY 10533, USA

C. Butler, X. He, C. Oakley, J. Ying
Georgia State University, Atlanta, GA 30303, USA

J. Blackburn, M. Chiu, M. Grosse Perdekamp, Y. J. Kim, J. Koster,
D. Layton,N. Makins, B. Meredith, D. Northacker, J.-C. Peng,
R. Seidl, E. Thorsland, S. Wadhams, S. Williamson, R. Yang
University of Illinois, Urbana, IL 61801, USA

J. Hill, T. Kempel, J. Lajoie, G. Sleege, C. Vale, F. Wei
Iowa State University, Ames, IA 50011, USA

N. Saito
KEK, Tsukuba, Ibaraki,305-0801, Japan

B. Hong, B. Kim, K. Lee, K. S. Lee, S. Park, K.-S. Sim
Korea University, Seoul, 136-701, Korea

K. Aoki, S. Dairaku, K. Imai, K. Karatsu, T. Murakami,
A. Sato, K. Senzaka, K. Shoji, K. Tanida
Kyoto University, Kitashirakawa-Oiwakecho,
Kyoto, 606-8502, Japan

M. Brooks, M. Leitch
Los Alamos National Laboratory, Los Alamos, NM 87545, USA

J. Adams, A. Caringi, B. Fadem, J. Ide, P. Lichtenwalner
Muhlenberg College, Allentown, PA 18104, USA

D. Fields
University of New Mexico, Albuquerque, NM 87131, USA

Y. Mao, R. Han
Peking University, Beijing, 100871, China

G. Bunce, W. Xie
RIKEN Brookhaven Research Center (RBRC),
Brookhaven National Laboratory, Upton, NY 11973, USA

Y. Fukao, A. Taketani
RIKEN Institute, Hirosawa, Wako, 351-0198, Saitama, Japan

K. Kurita, J. Murata
Rikkyo University, Rikkyo, 3-34-1, Nishikebukuro,
Tokyo, 171-8501, Japan

August 3, 2007

# Contents

# List of Figures

vi

# List of Tables

xiii

# Chapter 1

# Executive Summary

This document is a Conceptual Design Report for a fast muon trigger for the PHENIX experiment that will enable the study of flavor separated quark and anti-quark spin polarizations in the proton. A powerful way of measuring these polarizations is via single spin asymmetries for $W$ boson production in polarized proton-proton reactions. The measurement is done by tagging $W^+$ and $W^-$ via their decay into high transverse momentum leptons in the forward directions. The PHENIX experiment is capable of measuring high momentum muons at forward rapidity, but the current online trigger does not have sufficient rejection to sample the rare leptons from $W$ decay at the highest luminosities at the Relativistic Heavy Ion Collider (RHIC). This Report details the goals, design, R&D, and schedule for building new detectors and trigger electronics to use the full RHIC luminosity to make this critical measurement.

The idea for $W$ boson measurements in polarized proton-proton collisions at RHIC was first suggested by Jacques Soffer and Claude Bourrely in 1995. This prompted the RIKEN institute in Japan to supply funds to build a second muon arm for PHENIX (south muon arm). The existence of both a north and south muon arm makes it possible to utilize a $Z^0$ sample to study and control systematic uncertainties which arise in the reconstruction of high momentum muons.

This document has its origins in recommendations made by a NSAC Subcommittee that reviewed the U.S. Heavy Ion Physics Program in June 2004. Part of their Recommendation 1 was to "Invest in near-term detector upgrades of the two large experiments, PHENIX and STAR". In Recommendation 2 the subcommittee stated "– detector improvements proceed at a rate that allows a timely determination of the flavor dependence of the quark-antiquark sea polarization through $W$-asymmetry measurements" as we are proposing here.

On September 13, 2004 DOE requested from BNL a report articulating a research plan for the RHIC spin physics program. The document was submitted to DOE on January 31, 2005. It pointed out that one of three top priorities for the program lies in the clean and elegant measurement of the quark and anti-quark

polarizations sorted by quark flavor through the parity-violating production of $W$ bosons.

The history of this proposal is as follows. A group of scientists from U.S. universities at Illinois at Urbana-Champaign, Colorado, California at Riverside, Iowa State and also from RBRC developed a letter-of-intent that was reviewed and approved by PHENIX Management in July 2004. Subsequently, Illinois, Riverside, Iowa State and Abilene Christian submitted a Major Research Instrumentation (MRI) proposal to the National Science Foundation (NSF). This proposal was approved by NSF for a period of 5 years starting September 1, 2005 at a total cost to NSF of $ 2,000,000. In addition, institutional contributions from Illinois, Riverside and Iowa State totaled $ 250,000. We anticipate that the above resources will provide funding for Resistive Plate Chambers (RPC) detectors in both the north and south PHENIX Forward Spectrometers and development of the fast muon level-1 trigger.

In the fall of 2005 a group of Japanese institutions under the leadership of Professor Naohito Saito of KEK submitted a proposal to take signals from the front-end electronics (FEE) of the stations of the PHENIX muon trackers to use as additional inputs for the muon triggering process. The additional information will make it possible to further increase the selectivity of the trigger for collisions which form $W$ bosons and thus fully utilize planned future upgrades of the collision rates at RHIC. Professor Saito of KEK is in charge of this program. His group along with other Japanese scientists have begun the development of the necessary electronics with funding from the Japanese Society for the Promotion of Science (JSPS). Starting in the Japanese Fiscal Year 2006 (JFY06) Professor Saito was granted a total of $ 2,600,000 over a period of 5 years for this project. $ 600,000 covers overhead expenses.

On February 20, 2007, a draft version of this CDR was used as the basis for a PHENIX internal management review of the complete fast muon trigger proposal including both the RPC program funded by the NSF-MRI and the muon tracker FEE upgrades funded by JSPS. The review committee was chaired by Dr. Mike Leitch of LANL with members Dr. Vincent Cianciolo of ORNL and Dr. Yousef Makdisi of BNL. The review report is available and will be used by the collaboration in planning for the next stages of the project [1].

On April 13, 2007 at our quarterly PHENIX muon trigger meeting at BNL we toured the AGS experimental area that subsequently was selected to serve as the staging and assembly area for the RPC chambers. On May 18, 2007 there was a safety review of plans for this staging area chaired by Dr. Makdisi. John Hill and Ralf Seidl of our collaboration and Don Lynch, PHENIX engineer, made formal presentations.

A fundamental goal of nuclear physics and the RHIC spin program is to understand the quark-gluon structure of the nucleon, the fundamental bound state of QCD. Study of $W$ spin physics using parity violating weak interactions has sev-

eral advantages, namely a large $Q^2$, independence of quark fragmentation function information and the elimination of u-quark dominance resulting in more accurate studies of the roles of d quark.

A collaboration of 75 members from 19 institutions has been formed to carry out this project. These members bring expertise in all phases of the design, and construction of RPC detectors, design and commissioning of fast readout electronics for both the RPC and muon tracker FEE, design of level-1 trigger systems, mechanical and integration issues and a detailed knowledge of all aspects of the PHENIX experiment.

In order to complete this project successfully, we clarify in this proposal the responsibilities for the groups building the RPCs and the level-1 trigger using NSF funds and also for the group building FEE electronics for the muon tracker stations using JSPS funds. In addition we present a management plan that discusses the roles and responsibilities of the participating institutions. We propose to construct the fast muon trigger over a period of three years with prototyping of the RPCs and electronics in FY07, installation of the trigger in the south muon spectrometer arm in FY08 and the north muon spectrometer arm in FY09.

The structure of the proposal is as follows. The physics motivation for the Trigger project and measurements proposed are discussed in section 2. In section 3 is a detailed description of the RPCs, electronics for both the RPCs and muon tracker FEE, the level-1 trigger, mechanical structure and quality assurance of the various systems and installation of all systems and integration into the present PHENIX detector. Section 4 describes the Monte Carlo studies of the performance of the muon trigger. Section 5 outlines the management structure for the project and responsibilities of the participating institutions. The budget for the project is discussed in Section 6 along with an R&D schedule.

The project has been proceeding with rapid progress over the last year in converging towards a full design of the RPC chambers, MuTr FEE modifications, and Level-1 electronics. Expertise in the workings of RPC chambers is being gained by members of the collaboration, in addition to taking advantage of significant existing expertise (in particular the Korean groups having worked on the CMS RPC assembly).

In terms of the $W$ physics program overall, we have identified outstanding background issues that are important to understand in order to carry out the program. The current plan is to install additional two interaction lengths of absorber before the muon spectrometer to reduce this background to what we believe will enable the measurement. This implies the installation of only RPC layers 2 and 3 (as described later) and the MuTr FEE trigger modifications for MuTr stations 1 and 2. We expect this staged installation over FY09 and FY10. After taking initial data, a determination of whether the physics necessitates leaving the absorber in place or additional detector information will have to be made. Studies are underway to understand the full implications of this additional absorber material on

all aspects of the spin and heavy ion program.

# Chapter 2

# Physics Measurements with the Fast Muon Trigger

## 2.1 Overview

### 2.1.1 Physics Motivation

The nucleon is the only stable state of quarks and gluons known, the constituent which gives the atomic nucleus its mass, and thus the mass of the visible matter which surrounds us. A central goal of high-energy nuclear physics is to determine and understand the structure of the nucleon and in turn contribute to the understanding the theory of the strong interaction itself.

Spin is one of the most fundamental concepts in physics, deeply rooted in Poincare invariance and therefore in the structure of space-time itself. All elementary particles we know today carry spin, including the spin-1/2 quarks and the spin-1 gluons that make up nucleons. Spin, therefore, plays a central role also in our theory of the strong interactions, Quantum Chromodynamics (QCD), and to understand spin phenomena in QCD will help to understand QCD itself.

While we understand that quarks and gluons make up nucleons, they have not been seen in isolation. This odd property that they are only found bound to singlet states of the strong "color" charge they carry, is known as confinement. Understanding the inner structure of strongly interacting systems that are composed of quarks and gluons, namely the nucleon, is at the heart of investigation of confinement in QCD. The fact that the proton and neutron also carry spin (1/2 h-bar each) gives spin a central role in understanding nucleon structure.

The PHENIX Muon Trigger upgrade will make it possible to determine the spin contributions of the sea and valence quarks to the spin of the proton through measurements of single spin asymmetries $A_L$ in $W$ boson production in polarized proton collisions.

### 2.1.2   Nucleon Structure: Present Understanding

Despite decades of study, a detailed understanding of the nucleon has eluded us. Our theory of the strong interaction, Quantum Chromodynamics (QCD), born whole as a lagrangian, describes a force which is too strong and complicated for the calculational techniques we have developed so far. Only in high-energy collisions has one been able to apply a quite sophisticated perturbation theory, due to the small value of the strong coupling $\alpha_s$ at the high-energy scale, that is, asymptotic freedom. Recent theoretical advances in lattice techniques and significant increases in available computation power imply that we are close to the beginning of a new era of non-perturbative QCD calculations which can be realistically compared to data.

Unpolarized deep inelastic lepton scattering and Drell-Yan experiments have provided most of the data from which we have formed our present understanding of nucleon structure at high energy, an understanding which is still primitive. The 1-dimensional momentum fraction of the quarks on the light cone has been mapped out from relatively low values up to roughly 85%, over a broad but unfortunately correlated range of resolution scales, i.e., $Q^2$. Already this has revealed a rich phenomenology of structure which can be understood, over many orders of magnitude in $Q^2$, as the rapid fluctuation of color field energy in matter. Given the empirical partonic structure at one resolution scale, we now can reliably calculate the structure at some other scale, even if we cannot predict the structure *ab initio*.

Nonetheless, we still have little understanding of the physics or even the empirical distributions at large momentum fraction. At very low momentum fraction, we are hampered by the experimental correlation with low $Q^2$ (large distance scale) resolution in order to test our understanding of the quark-gluon fluctuations which are observed. New, precise electron scattering experiments, using both the electromagnetic and weak force, give us the spatial charge and magnetization distributions of quarks in the nucleon, but are difficult to connect to the 1-dimensional light-cone momentum distributions. The newly recognized use of exclusive reactions to determine generalized parton distributions will allow us to empirically connect these two regimes.

At high energy, there remain two fundamental aspects of the nucleon partonic structure which are mostly poorly determined by experiment. One is the nature of the quark and gluon motion transverse to the light-cone momentum direction, in other words, the true 3-dimensional momentum distribution. The other is the nature of the nucleon spin.

At present, we have a limited set of high-energy data which tell us the alignment of the quark spins along the light-cone momentum direction, as a function of the momentum fraction. These distributions are unknown at both high and very low momentum fraction, and the resolution range in $Q^2$ explored is much narrower than in the unpolarized case. In fact, even these data are limited to the

case where the nucleon spin is along the light-cone momentum direction. Until the advent of the RHIC polarized proton collider data, there was no precise and clearly interpretable data on the polarization of the gluons along the nucleon spin direction. The polarized lepton scattering experiments have made it clear that the quark spins only contribute about 30% to the nucleon spin. The gluons, which make up roughly 50% of the total (unpolarized) partonic momentum distribution, may be expected to carry a significant fraction of the nucleon spin, but this distribution is almost completely unknown at present.

The RHIC spin program using longitudinally polarized protons promises to answer the question of the gluon spin contribution definitively. First measurements using the existing PHENIX spectrometer have already constrained the polarized gluon distribution.

Given a measurement of the gluon spin contribution, a fundamental question will be how the quark and gluon contributions mutually arise in the nucleon bound state. In particular, how is the polarization of the sea quarks, which are formed from the gluon field, affected by the polarization of this field? The muon trigger upgrade will be instrumental in this investigation by facilitating a measurement of the polarized quark and anti-quark distributions using $W$ boson production.

When one explores the polarization of quarks with the nucleon spin perpendicular to the light cone, our understanding of both transverse momentum and spin are strongly tested, and at least in experiment, intrinsically linked to each other. Ever since the observation of a large asymmetry in high-energy proton scattering, it has been clear that transverse effects would play an important role. These effects have been shown to persist even at RHIC energies, almost undiminished in size. Recent progress has been spurred by the observations of transverse asymmetries in lepton scattering from transversely polarized protons. First glimpses from these experiments have prompted intense theoretical activity, with new insight gained into the role of gauge links in calculating partonic field operators. We now have firm predictions relating the fragmentation process in lepton scattering to that in Drell-Yan. The possibility of a distribution arising from the correlation of spin and longitudinal momentum fraction is now widely accepted, and again there are early first glimpses from lepton scattering. A natural explanation for this correlation is the existence of significant quark orbital angular momentum. In fact, orbital angular momentum is essentially unexplored experimentally at the partonic level. Exclusive reaction experiments, if able to determine the generalized parton distributions sufficiently well, can give us information only about the total angular momentum. Theoretically, there is now a much more thoroughly developed formalism to describe transverse measurements. The distributions are functions not only of momentum fraction and $Q^2$, but now transverse parton momentum $k_T$ as well. While the dependence can be modeled, there is evidence that one can develop the transverse momentum distribution directly from perturbative QCD (pQCD). Thus, using transversely polarized protons at RHIC, one should

be able to explore these new distributions in a regime where pQCD can be safely applied, for example using spin-dependent two-hadron correlation functions [30]. If the longitudinal program finds that the gluon contribution to the nucleon spin is small, the transverse physics will be the only effective avenue at RHIC to study the partonic nature of orbital angular momentum.

Below we give a more detailed description of what we hope to learn from this program.

### 2.1.3 Nucleon Structure: Gluon Polarization

Our present knowledge of the partonic structure of the nucleon is encoded in the so-called parton distribution functions (PDF) which depend on Bjorken $x$, the light-cone momentum fraction, and the momentum scale $Q^2$. Since the quarks are spin-1/2 particles, we can actually define two quark distributions, so-called helicity distributions, which describe the partons with the same or opposite helicity of that of a proton with helicity along the light cone direction. We will denote the polarized PDFs by $q_f^{\rightarrow}(x, Q^2)$ and $q_f^{\leftarrow}(x, Q^2)$, where $f$ is the flavor of the quark or a gluon, however we will typically denote the unpolarized gluon distribution as $g(x, Q^2)$. In general, the unpolarized PDFs are then the sum of the helicity distributions: $q_f(x, Q^2) = q_f^{\rightarrow}(x, Q^2) + q_f^{\leftarrow}(x, Q^2)$. It is common to also define $\Delta q_f(x, Q^2) = q_f^{\rightarrow}(x, Q^2) - q_f^{\leftarrow}(x, Q^2)$.

The distributions for charged partons can be extracted directly from inclusive deep inelastic lepton scattering (DIS) experiments (in which only the scattered lepton is detected) if the $Q^2$ and energy $\nu$ of the photon are sufficiently high. Deep inelastic neutrino scattering allows one to separate quark and anti-quark distributions, which the charged lepton scattering cannot distinguish. One can attempt to isolate the charged partons by flavor using so-called flavor tagging, where the known valence quark content of hadrons is correlated with the flavor of the quark which absorbed the virtual photon. The simultaneous detection of the final state lepton and a final state hadron, known as semi-inclusive DIS (SIDIS), necessarily depends on modeling of the fragmentation process. Lepton scattering from the gluon distribution is complicated, as the gluon has no electromagnetic or weak charge, thus extraction is more model dependent. To date the most successful DIS program has been the analysis of di-jets [11], which primarily (but not exclusively) derive from the photon-gluon fusion diagram. If there is insufficient energy to produce jets, one may attempt to substitute leading hadrons, but again, one is now more model dependent. In fact, global fits are regularly made by a number of groups around the world, using not only the DIS data, but also data from hadron colliders and theoretical constraints derived from QCD sum rules [12, 13, 14].

The dependence on these functions on $Q^2$ can be directly related to the fluctuation of the gluons into quark-antiquark pairs and the radiation of gluons by quarks through the DGLAP equations, and this provides an means in principle to

determine the polarized gluon distribution from the $Q^2$ evolution of the polarized quark distributions measured in DIS. The results of a recent analysis [9] of the available polarized DIS data (from SLAC, CERN, and DESY) are displayed in Figure 2.1 and show that the present uncertainties on $\Delta G$ are so large that even the sign of the gluon polarization is barely constrained; much more precise polarized DIS data, over a broader range in $x$ and $Q^2$, would be necessary to provide better limits. The fact that the photon-quark asymmetry $A_1$ itself has only very small $Q^2$ dependence gives this type of analysis only a small "lever arm."
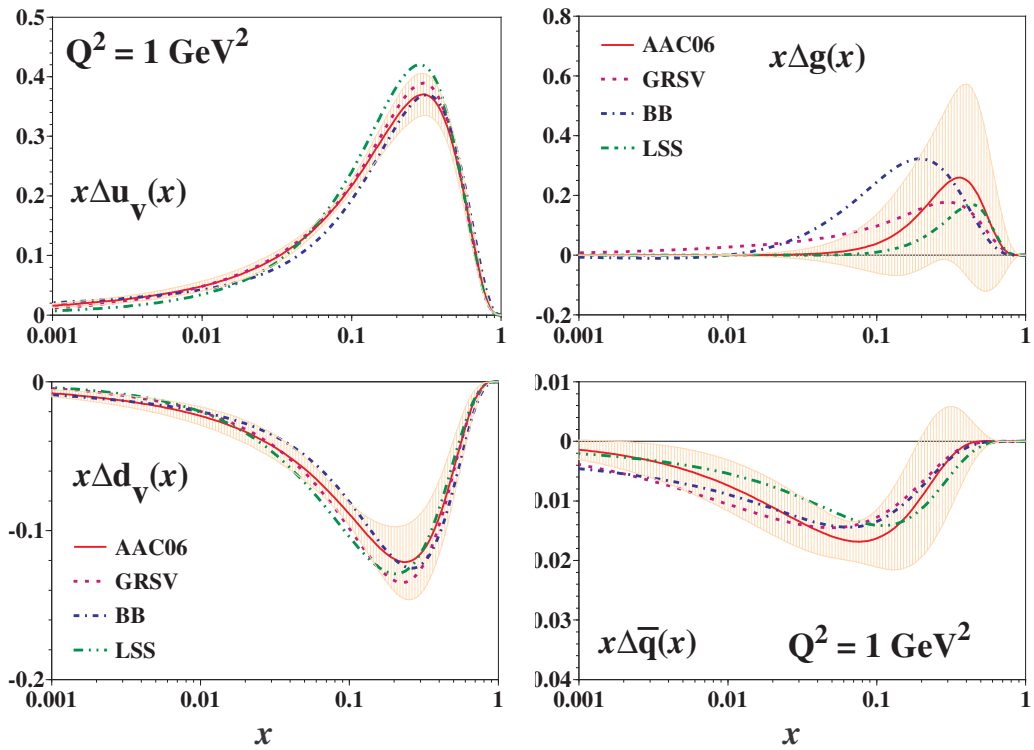


Figure 2.1: Comparison of polarized PDFs at $Q^2 = 1$ GeV$^2$. The solid curves and bands are the uncertainties on the AAC PDFs. The others are the GRSV, BB, and LSS parameterizations.

The RHIC spin program will provide the first precise measurement of the $x$-dependence of the polarized gluon distribution $\Delta G(x)$. The PHENIX experiment, which has excellent particle identification and high rate capabilities, is well suited to this measurement as we are sensitive to $\Delta G$ through multiple channels and each of these channels has independent experimental and theoretical uncertainties. Our main sensitivity is through inclusive hadron production, direct photon production, and heavy quark production.

In unpolarized $p + p$ experiments the gluon distribution function has been measured using single- and di-jet events as well as from direct photon events. In

9

both cases, jets or high $p_t$ photons carry information directly from the underlying hard scattering process which can be calculated using pQCD. As the cross sections factorize into a hard scattering and a proton structure part a measurement determines the parton distribution functions connected to the processes, schematically

$$\sigma \sim q\left(x_A\right) \otimes G\left(x_B\right) \otimes \left|\mathcal{M}_{\mathrm{pQCD}}\right|^2$$

where $x_A$ and $x_B$ are the fraction of proton momentum carried by the partons entering the hard scattering process. The theoretical problems present in the interpretation of fixed-target data have been largely resolved for the collider environment [16, 17]. PHENIX's first direct $\gamma$ cross-section measurement indicates that these calculations are valid at RHIC.



**Gluon Compton Scattering**      **Quark Anti-Quark Annihilation**
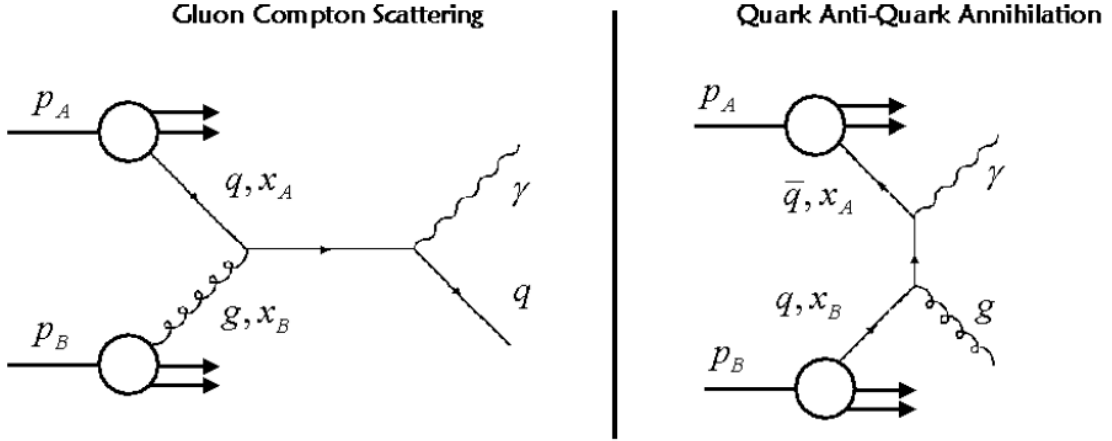
Figure 2.2: Direct photon production in the gluon compton and quark anti-quark annihilation processes. The ratio of the two processes has been studied using PYTHIA and was found to be about 9:1.

At RHIC, direct photon production is dominated by quark-gluon Compton scattering (see Figure 2.2), which ensures that the double spin asymmetries from direct photon production provide the cleanest theoretical access to the gluon polarization $\Delta g/g$.

Helicity conservation at the quark-gluon vertex gives rise to a double spin asymmetry

$$A_{LL} \sim \frac{\Delta q_f\left(x_A\right)}{q_f\left(x_A\right)} \otimes \frac{\Delta g\left(x_B\right)}{g\left(x_B\right)} \otimes a_{LL}^{qg \to q\gamma}$$

from which $\Delta G/G$ can be extracted. The hard scattering asymmetry is denoted by $a_{LL}^{qg \to q\gamma}$ and is calculated for the underlying quark-gluon Compton diagram with perturbative QCD. Background from the quark anti-quark annihilation process has been studied using the event generator PYTHIA and was found to be small.

The left panel of Figure 2.3 displays the impact of PHENIX direct photon (inclusive) data on the range of allowed polarized gluon distributions.
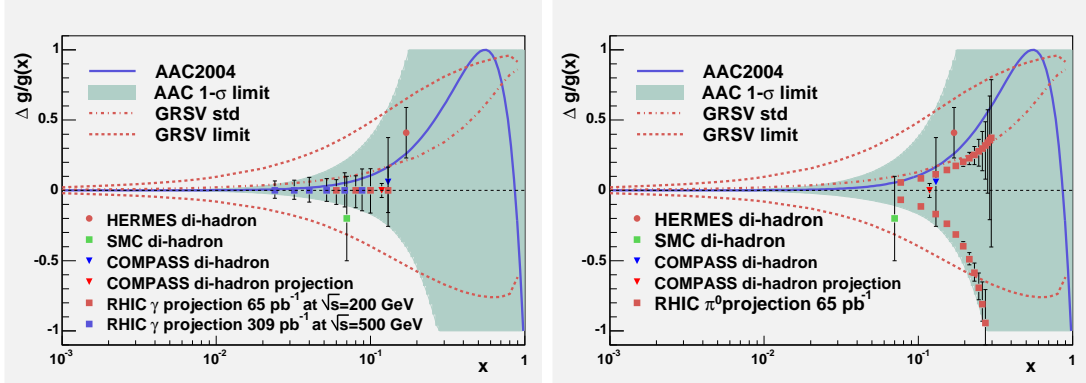


Figure 2.3: Expected sensitivities for PHENIX's direct photon (left) and neutral pion measurements (right).

PHENIX is sensitive to $\Delta G$ through multiple channels, which will result in a robust measurement over an extended $x$-range. The right panel of Figure 2.3 displays the expected impact after an NLO global analysis of the PHENIX neutral pion measurement data on the range of allowed polarized gluon distributions. The kinematic coverage for these various channels within PHENIX are shown in Figure 2.4. The complementary measurements cover slightly different kinematic ranges, and most importantly provide alternative ways to the gluon polarization with different systematic and theoretical uncertainties. Figure 2.5 compares the $x$-$Q^2$ footprint of these channels to that of the DIS experiments.

## 2.1.4 Nucleon Structure: Quark Polarization

While $\Delta q$ has been fairly well measured, the anti-quark's contribution to $\Delta q$ is not well-known. As mentioned above, given a measurement of the gluon spin contribution, a fundamental question will be how the quark and gluon contributions mutually arise in the nucleon bound state. In particular, how is the polarization of the sea quarks, which are formed from the gluon field, affected by the polarization of this field? Addressing this question is central to the field and is the main motivation for the muon trigger upgrade.

In order to answer this more detailed question, experiments at CERN [2, 3] and DESY [29] have and are attempting to determine the spin contributions of the different quark flavors separately, especially the more difficult-to-measure contributions from the sea quarks. The technique used by the CERN and DESY experiments is the so-called "hadron tagging" and is based on the measurement
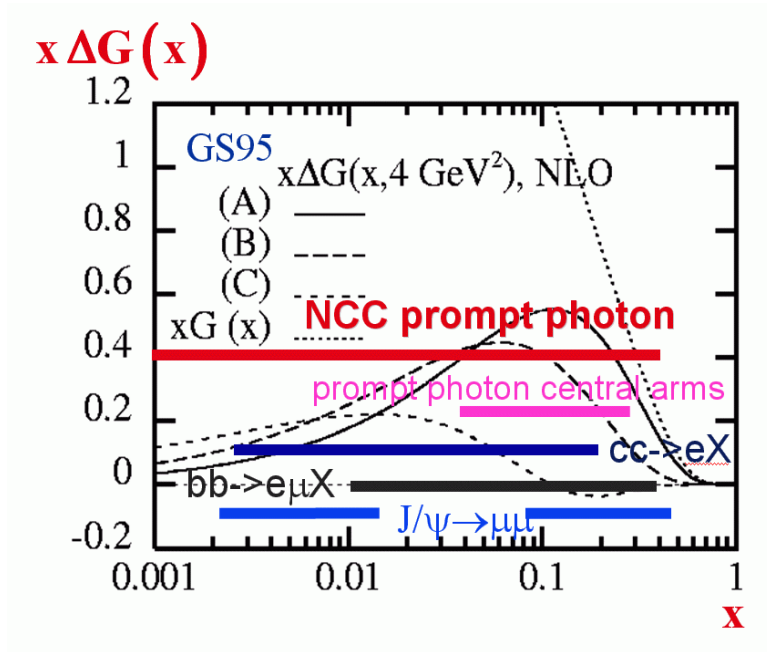
Figure 2.4: Kinematic coverage for PHENIX measurements that are sensitive to $\Delta G$. For example, future measurements with the electromagnetic NoseCone Calorimeter (NCC) in the forward direction will extend the accessible $x$-range in PHENIX to $x \longrightarrow 0.001$. The range in $x_{Bj}$ covered for different processes is indicated and compared to different models for $\Delta G(x)$.
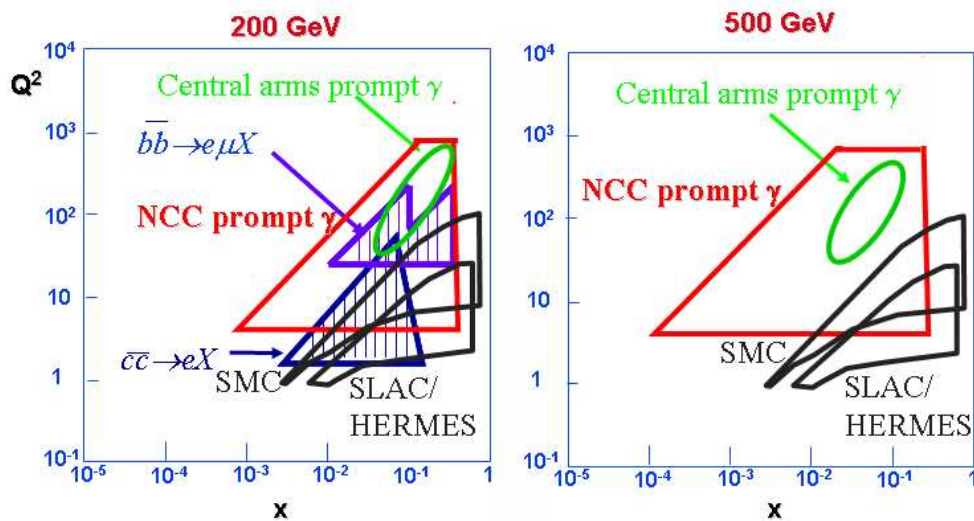


Figure 2.5: Range of $x$ and $Q^2$ accessible by various DIS experiments compared to those accessible at PHENIX.

12

of semi-inclusive asymmetries, in which a final state hadron (i.e., a hadron containing a large fraction of the energy transferred to the nucleon) is detected in coincidence with a deep-inelastically scattered lepton. Using a statistical analysis and empirical fragmentation models, one can exploit the greater than random probability that the final state hadron contains the struck quark (calculated in a fragmentation model), and use the hadron species to limit the possible flavor of the struck quark. Measuring concurrently a sufficient number of semi-inclusive asymmetries using identified leading pions and kaons allows an extraction of the spin contributions from the different quark and anti-quark (sea) flavors. The results of the analysis of the HERMES data [29] are shown in Figure 2.6.

To date, this extraction has been performed only within a leading order (LO) QCD "framework", that is, with the effects of the $Q^2$ evolution only minimally included and no attempt at inclusion of higher twist effects. The limited statistical accuracy of the data allows no strong conclusions about the polarization of the sea quarks. Several theoretical programs to extend the semi-inclusive analysis procedure to next-to-leading order (NLO) are underway [4, 5, 6], but progress has been slow.

A chief concern with the HERMES analysis is the relatively low $Q^2$ of the data ($< Q >^2 \approx 2.5 GeV^2$), which may result in large NLO corrections. The forthcoming analysis from COMPASS will certainly use a data sample with somewhat higher $Q^2$ which will likely have smaller NLO corrections. Furthermore, it will extend the determination to almost an order of magnitude smaller $x$ value than HERMES. Nonetheless, the HERA collider experiments have shown just how strongly coupled the resolution of the sea distributions are to the $Q^2$ of the probe, so it remains important to measure the spin-flavor composition of the nucleon up to the highest $Q^2$ possible.

Despite these efforts with lepton scattering, a common systematic uncertainty to both experiments' analysis is the hadron-tagging technique itself, which relies on the use of fragmentation function models that in some cases (e.g., s quark fragmentation to kaons) are not well known due to a general lack of data, especially at lower energies. While there is hope that new (and voluminous) data from the Belle experiment [7] will significantly improve this situation, there will remain issues related to possible differences in how the fragmentation process occurs starting from the initial quark-antiquark pair of e+e- colliders and the process starting from a quark struck from a nucleon.

Furthermore, both COMPASS and HERMES suffer from the "u-quark dominance" caused by the weighting of the fundamental photon-quark interaction by the square of the quark charge as well as the intrinsic inability of electromagnetic probes to distinguish quarks and anti-quarks. Hence it will remain difficult to extract precise information about the up, down and strange sea quark (and anti-quark) polarized distributions. Since the weak interaction lacks this bias, intense high energy neutrino beams are ideal for this type of semi-inclusive analysis.
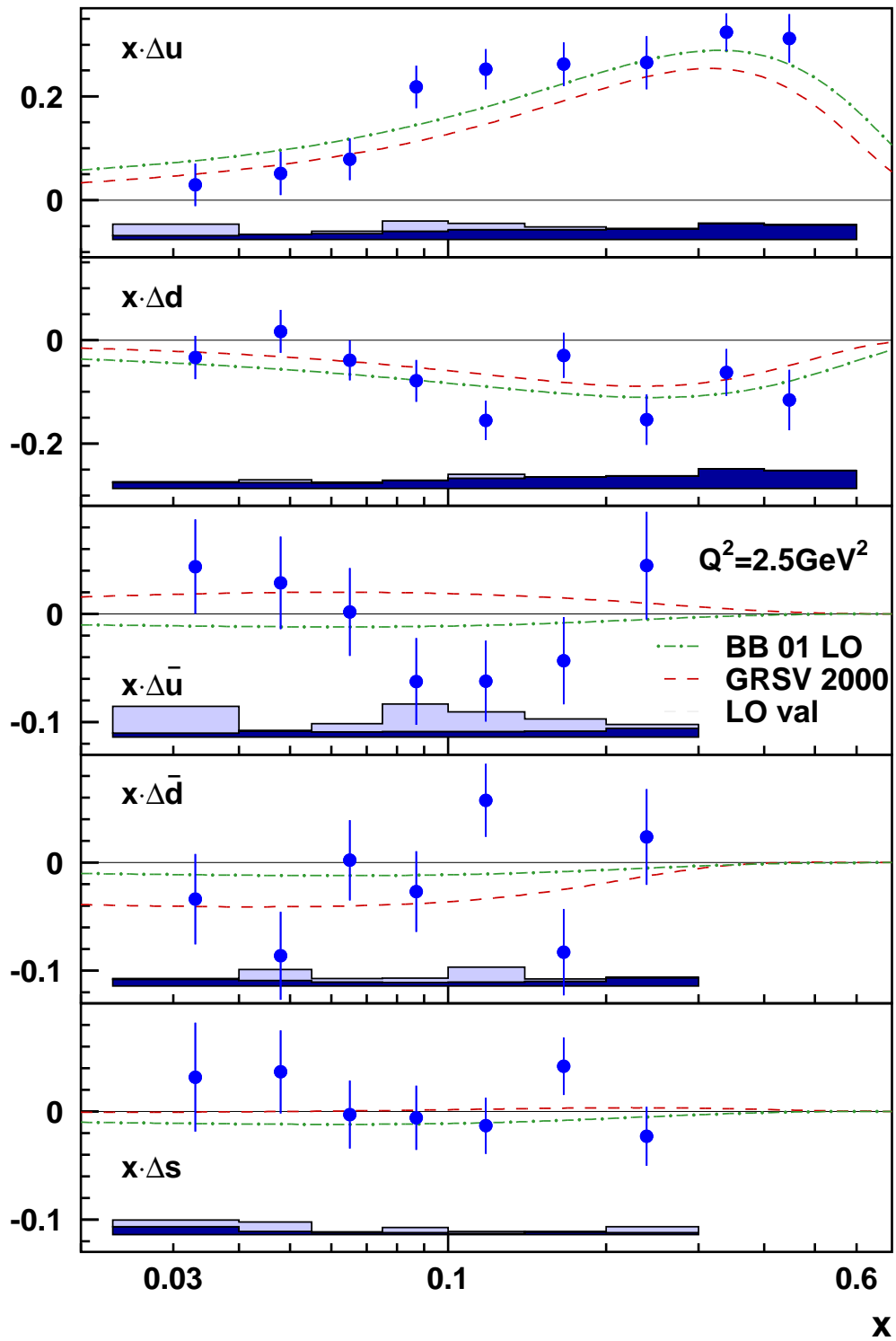
Figure 2.6: Results of HERMES spin-flavor decomposition using a leading order analysis of semi-inclusive deep-inelastic electron scattering.

## 2.1.5 Transverse Spin Physics

It is fair to say the much of the interest in high-energy spin physics can be traced to two surprising results: the observations of large lambda hyperon polarizations [20] and large single spin asymmetries in pion production from polarized nucleon-nucleon collisions [21]. The general expectation from pQCD at leading twist was that these asymmetries would be vanishingly small, due to the chiral dynamics of QCD. It was therefore startling when E704 discovered very large asymmetries in pion production from polarized $p+p$ collisions at $\sqrt{(s)} = 20$ GeV. The expectation that yet higher energy would cause these asymmetries to vanish, was again invalidated by the STAR discovery that these effects persisted to the much higher $\sqrt{(s)}$ of 200 GeV [22], since it was thought that any power corrections should be suppressed at higher energies, despite the fact that the predictions of unpolarized cross-sections agree very well with the data. The single spin asymmetries for $\pi^0$ mesons detected at STAR, as a function of Feynman $x$, are shown in Figure 2.7. Given that the magnitude of asymmetries at high energies are typically only a few percent, these forward asymmetries are quite large. One might question whether the forward reactions are too soft to apply perturbative QCD, but the cross sections are well described by NLO pQCD [23] as well as by PYTHIA [10]. The existence of large single spin asymmetries at RHIC, along with the good theoretical understanding of the unpolarized cross-sections gives hope that transverse spin effects can be used as a tool to probe the transverse structure of protons.
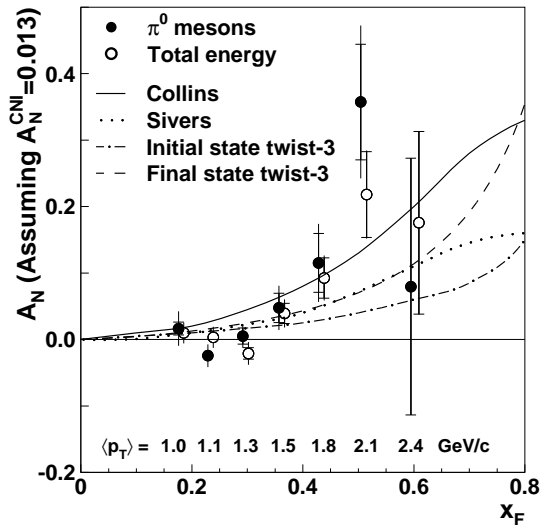


Figure 2.7: Single spin asymmetry from $\pi^0$ mesons at forward rapidity ($\langle \eta \rangle = 3.8$) as a function of Feynman $x$, measured at the STAR experiment from transversely polarized $p+p$ collisions at $\sqrt{s} = 200$ GeV [22].

There are three basic sources for the single spin asymmetries observed so far:

1. the existence of the Sivers function [24] which describes the correlation between the spin direction of the proton and the transverse momentum of the parton. Partons from the Sivers distribution fragment with the normal unpolarized fragmentation functions.

2. the existence of Collins fragmentation functions [25] which provide a correlation between the momentum of the final state particles with the direction of the initial parton spin. The initially transversely polarized quarks are described by the transversity distribution [26].

3. Higher twist mechanisms in the initial and/or final state [27].

The recent observation of azimuthal asymmetries in semi-inclusive pion electroproduction at HERMES, from both longitudinally [28] and transversely polarized nucleon targets [29] along with the STAR results has sparked renewed and intense theoretical study of this physics. Using the transversely polarized target data, HERMES has made a extraction of the separate asymmetries arising from the Sivers mechanism and the Collins mechanism. Additional efforts at BELLE have made the first extraction [31] of a Collins fragmentation function for $e^+e^-$ annihilation. Spin dependent fragmentation functions for two pion states, so called interference fragmentation functions, also have been proposed [33], and there is a preliminary observation once again at HERMES [32].

The existence of sizeable Collins fragmentation functions will allow the extraction of the transversity distribution of the nucleon $\delta q_f(x)$. Just as in the case of $\Delta q_f$, the transversity is a measure of the alignment of quarks along or opposite the nucleon spin; the critical difference is that in the longitudinal case, the nucleon spin is along the light-cone direction, while in the transverse case, it is perpendicular to this direction. Non-relativistically, this is a trivially different distribution, but once on the light-cone these are "independent" distributions, of the same leading order. A common (correct) model of the of the quark-gluon structure could predict both distributions, but you cannot determine one distribution from the other. The transversity is interesting for a number of reasons. Besides completing our knowledge of the nucleon at leading order, it is notable for being mainly sensitive to the valence quark spin structure, and furthermore, its $Q^2$ evolution is quite different due to the lack of coupling between gluon transversity functions and quark transversity functions. These attributes provide an important test of our understanding of the longitudinal antiquark and gluon spin structure functions, especially with regard to relativistic effects.

The existence of Sivers distributions also provides an interesting window into the structure of the nucleon. This function accounts for the possibility that a parton's transverse momentum depends on the orientation of the nucleon spin. Orbital angular momentum of the quarks about the spin axis would naturally

provide just such a correlation. At present, this connection is still not understood theoretically at the partonic level, but the distribution function itself is now generally accepted and well defined.

Effects in forward hadron production from transversely polarized $p+p$ collisions are somewhat more complicated than in polarized SIDIS, but as usual, the effects are typically larger and easier to study. Formally, there has been considerable progress in working out a formalism of possible distributions and fragmentation functions, for example as given in Refs. [34, 35, 36]. Predictions based on models of the nucleon are now being constrained by the data, but there is still much more data needed. As an example, the calculation of the asymmetry in pion production for the E704 experiment is shown in Figure 2.8, taken from Ref. [36]. These models explore maximal bounds for the various distributions, but the point here is that the distributions in $x_F$ are quite different, and they do not change much as a function of energy.
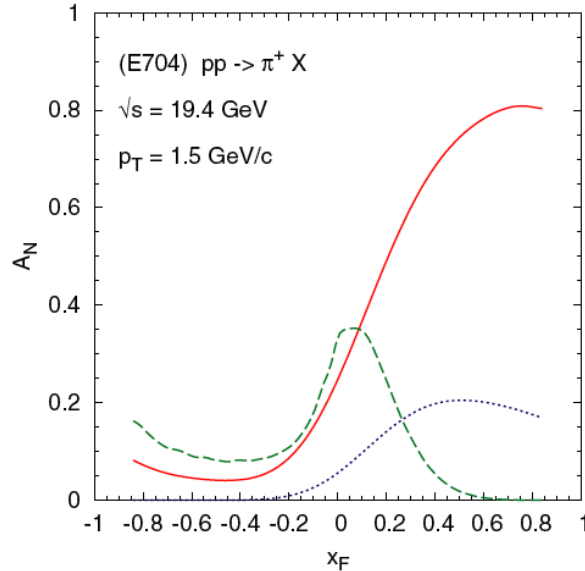


Figure 2.8: Different contributions to $A_N$, plotted as a function of $x_F$, for $p^\uparrow p \to \pi^+ X$ processes and E704 kinematics. The different lines correspond to solid line: quark Sivers mechanism alone; dashed line: gluon Sivers mechanism alone; dotted line: transversity $\otimes$ Collins. All other contributions are much smaller. Taken from Ref. [36].

A future forward electromagnetic calorimeter, the NoseCone Calorimeter (NCC), along with the recently installed Muon Piston Calorimeter (MPC) and the standard PHENIX central detectors will allow an important series of transverse spin measurements to be carried out at PHENIX. These experiments should permit us to separate out the mechanisms contributing to the forward inclusive asymmetry.

Specifically, the Sivers distribution can be measured in the azimuthal asymmetry of back-to-back di-hadrons or di-jets, where one of the hadrons is the forward $\pi^0$ or jet. The Collins fragmentation function can be measured in the hadron distribution around a jet axis. The two hadron Collins function can be measured by di-hadron correlations in the near side of a jet. Whatever is left can be use to test calculations of higher twist effects.

In general the exploration of transverse spin asymmetries in SIDIS and $p + p$ collisions requires one to investigate the dependence of the asymmetries on the $p_T$ of the hadrons. This raises serious questions about the universality of the distribution and fragmentation functions which can be investigated in both experiment and theory. It has as well forced modelers to include the intrinsic $k_T$ of the partons in some fashion. These issues are being addressed aggressively by the theoretical community.

## 2.2 Determination of Sea and Valence Polarized Quark Distributions Using $W$ Boson Production

The collisions of high-energy polarized protons at RHIC provide a completely new means to use the weak interaction as a probe of the polarized parton distributions, namely $W^{\pm}$ production, leading to a very high energy muon or electron, of the same charge as the $W$ and with an energy of roughly half the $W$ mass, as shown in Figure 2.9.

This reaction mechanism offers a number of advantages over deep-inelastic scattering: there are no systematic uncertainties from fragmentation models, there is no u-quark dominance arising from the intrinsic vertex coupling strength, the parity violating nature of the weak interaction provides a natural polarization measurement so that only a single spin asymmetry is required, and the $Q^2$ of the measurement is very high, essentially at the mass squared of the $W$ boson. Because the neutrino is not detected, one actually measures the single spin asymmetry in the production of the charged lepton as a function of rapidity and $p_T$, and then relates these asymmetries to those of the parent $W$ bosons.

The (parity violating) single spin asymmetry $A_L^+(y_W)$ for $W^+$ from a polarized proton as a function of the $W$ rapidity $y_w$ can be written in leading order QCD (ignoring heavy quark contributions) as

$$A_L^+(y_W) \equiv \frac{\sigma_+ - \sigma_-}{\sigma_+ + \sigma_-} = \frac{-\Delta u(x_a)\bar{d}(x_b) + \Delta\bar{d}(x_a)u(x_b)}{u(x_a)\bar{d}(x_b) + \bar{d}(x_a)u(x_b)}, \qquad (2.1)$$

where $\sigma_{\pm}$ refers to $\bar{p}p \to W \to l\nu$ cross sections for positive and negative helicities of the polarized proton $a$ impinging on the unpolarized proton $b$. The light cone
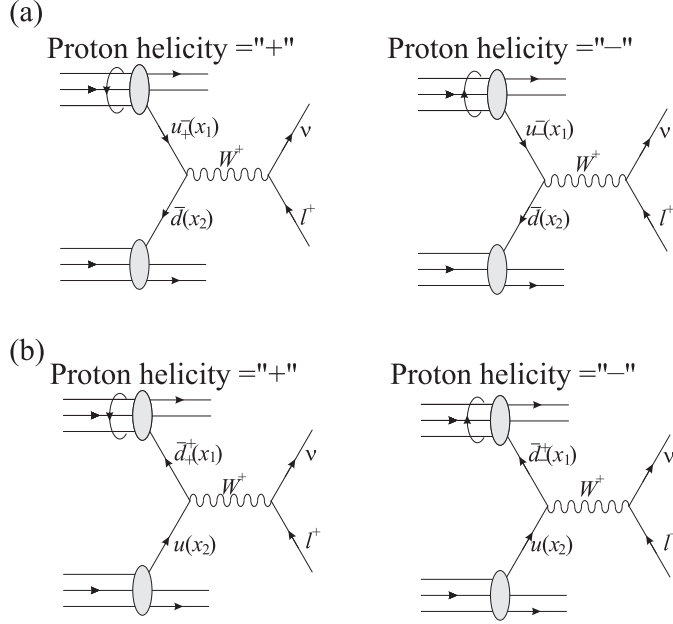
Figure 2.9: $W^{\pm}$ production in polarized pp scattering.

fractions $x_{a,b}$ are defined as $(Q/\sqrt{s})e^{\pm y_w}$. The expression for $W^-$ production can be found by the substitutions $\bar{d} \to \bar{u}$ and $u \to d$. In the case that we look at very asymmetric collisions, these expressions simplify further, since one of the light cone fractions is much larger than the other, and the sea distribution falls rapidly with increasing $x$:

$$A_L^+(x_a \gg x_b) \approx \frac{-\Delta u}{u} \; A_L^+(x_b \gg x_a) \approx \frac{-\Delta \bar{d}}{d}$$

$$A_L^-(x_a \gg x_b) \approx \frac{-\Delta d}{d} \; A_L^-(x_b \gg x_a) \approx \frac{-\Delta \bar{u}}{\bar{u}} \tag{2.2}$$

In fact, the rapidity of the $W$ cannot be determined precisely from the rapidity of the decay lepton, but at large absolute lepton rapidities, the resulting smearing is manageable.

Precise calculations of these asymmetries, including the effects of the lepton decay distribution as well as the resummation of soft gluon radiation, have been performed. Figure 2.10 shows, for example, the $W^+$ asymmetry as a function of lepton $p_T$, integrated over four lepton rapidity ranges. The most forward (graph d) and backward (graph a) rapidities correspond to the acceptance of the muon arms of the PHENIX spectrometer. The three curves show predictions based on different sets of polarized PDFs, and show that there is significant sensitivity to the sea quark polarization in particular ranges of $p_T$. Results for the asymmetry show even stronger sensitivity.
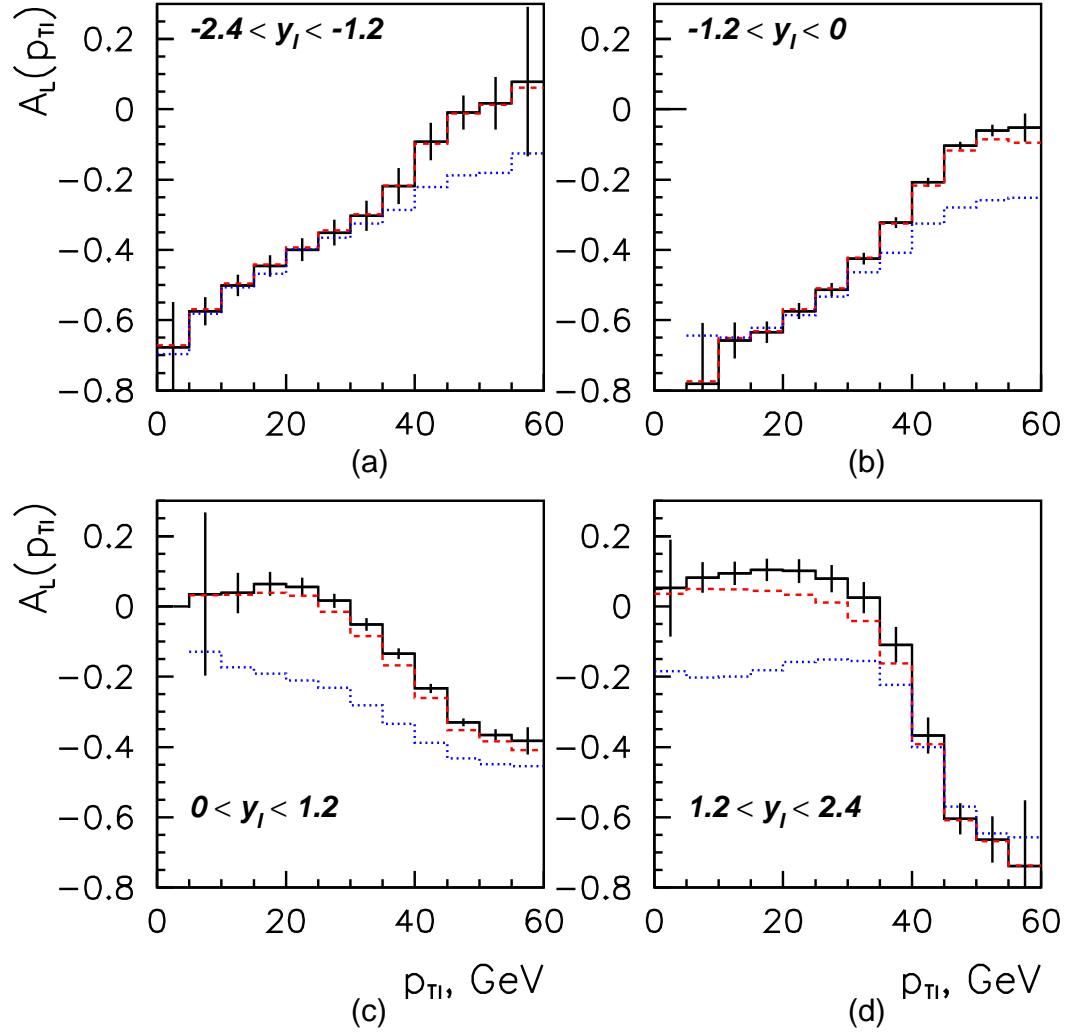
Figure 2.10: Expected single spin asymmetries for leptons from $W^+$ production as a function of $p_T$ for different regions in rapidity (taken from Ref. [40]). The error bars are statistical projections. The solid and dashed curves are predictions using the Gehrmann-Stirling PDF sets A and B, respectively; the dotted curve is the GRSV valence-like PDF set.

We note here, that even a measurement of $W$ production without polarization provides important information about the unpolarized light quark sea distributions. The ratio of unpolarized $W^+$ to $W^-$ production in $pp$ scattering at RHIC will directly probe the $\bar{d}/\bar{u}$ ratio.

Since the instantaneous rate of observed $W$ decay leptons is not high, it is critical that the muon trigger have both high efficiency and discrimination. Specifically, it should be sensitive to the higher average momenta of the $W$ decay muons and insensitive to muons resulting from hadron decay, especially from hard jets.

## 2.3 Measurement of Flavor Asymmetry of Light Sea Quarks in Nucleons

A quark and antiquark sea in the nucleon has been known to exist for a long time [52]. Given their non-perturbative nature, sea quarks are difficult to calculate from first principles. Therefore, various models have been proposed to describe sea quarks in the nucleon. The earliest models have assumed flavor symmetry of sea quarks in the nucleon. Since this assumption was not based on any known symmetries, it remained to be tested by experiments.

It has already been shown by neutrino-induced charm production experiments [53, 54] that the strange quark content in the nucleon is not as large as up and down sea quarks. This asymmetry can be attributed to the large mass difference between the strange quark and up and down quarks. For the light up and down quarks, it was still possible that their distributions in the nucleon sea are symmetric. To test the flavor symmetry of up and down quarks in the nucleon sea, Gottfried in 1967 proposed the measurement of the Gottfried sum [55]:

$$S_G = \int_0^1 [F_2^{\mu p}(x) - F_2^{\mu n}(x)]/x dx = \frac{1}{3} + \frac{2}{3}\int_0^1 [\bar{u}(x) - \bar{d}(x)]dx. \qquad (2.3)$$

In Eq. (2.3), $S_G$ equals 1/3 if $\bar{u}(x)$ and $\bar{d}(x)$ are identical. Early experiments [56, 57, 58] suffered from large systematic errors and could not reach a definite conclusion, although they consistently showed a value below 1/3.

More recently, the NMC collaboration reported measurement on Gottfried sum with muon DIS data in the 1990s. Their measurement covered the smaller $x$ region (down to 0.004), allowing an accurate determination of $S_G = 0.235 \pm 0.026$ [59]. This result provided the first strong evidence that $\bar{u}(x) \neq \bar{d}(x)$.

Following the NMC measurement, the $\bar{d}/\bar{u}$ ratios as a function of $x$ were measured using other experimental techniques. These new measurements include the NA51 [60] and E866 [61] experiments with Drell-Yan process and the HERMES experiment [62] with semi-inclusive deep inelastic scattering. Results from E866 experiment and NA51 experiment are shown in Figure 2.11. The $\bar{d}/\bar{u}$ asymmetry is clearly established from these experiments.
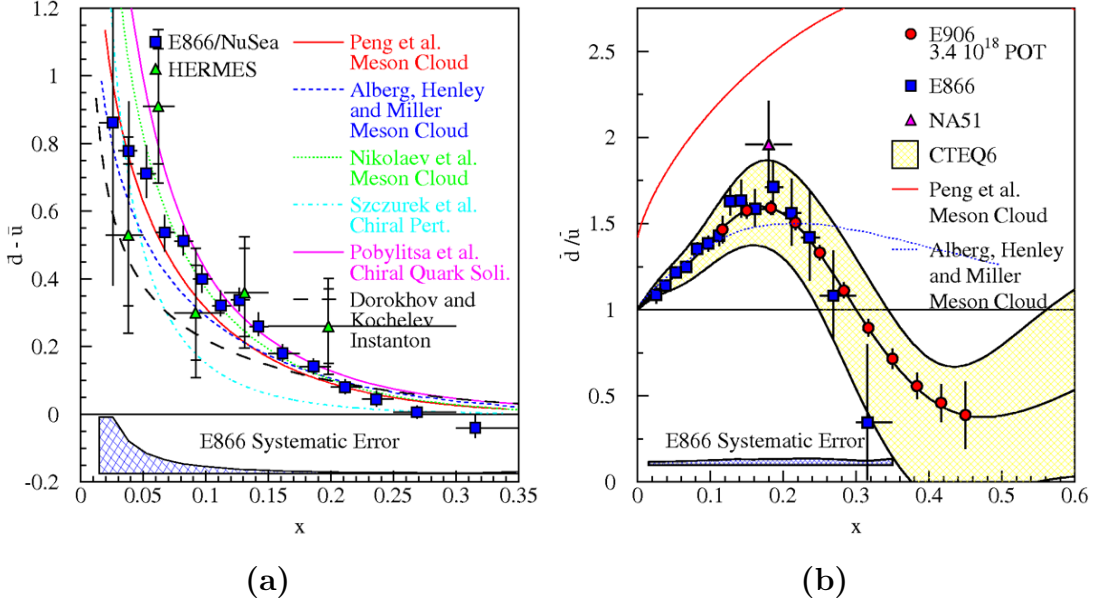
Figure 2.11: Measurement from E866 experiment on (a)$\bar{d} - \bar{u}$ (b)$\bar{d}/\bar{u}$ compared with prediction by different theoretical models.

Various theoretical models have been proposed to explain the $\bar{d}/\bar{u}$ asymmetry. Review articles [63, 64, 65] have detailed descriptions on these models. Many models, e.g. meson-cloud model, chiral quark model, and soliton model, attribute the flavor asymmetry to the presence of isovector mesons (especially the pions). Other models such as instanton models, lattice gauge approach and Pauli-blocking model, consider the effects of the valence quarks on the quark-antiquark sea. While these models are capable of describing the $\bar{d} - \bar{u}$ data, significant difficulties are encountered to reproduce the $\bar{d}/\bar{u}$ data at $x > 0.2$, where the E866 data suggest a rapid fall-off of this ratio.

To better determine mechanisms which generate the flavor asymmetric nucleon sea, it is necessary to extend the $x$ range of existing $\bar{d}/\bar{u}$ ratio measurements. At the high $x$ region, Drell-Yan experiments at the new 120 GeV Fermilab Main Injector (E906) and at the 50 GeV J-PARC have been proposed. At the other end of the $x$ range, Drell-Yan measurements at RHIC could extend the present knowledge on the $\bar{d}/\bar{u}$ ratio down to around $x = 10^{-3}$, which is an order of magnitude lower than the E866 experiment.

At RHIC, $W$ boson production in $p+p$ collisions could provide an independent measurement of the *udbar* ratio. The differential cross section for $W^+$ production in $p + p$ collisions can be written as [66]

$$\frac{d\sigma}{dx_F}(pp \to W^+ + X) = K\frac{\sqrt{2}\pi}{3}G_F\left(\frac{x_1 x_2}{x_1 + x_2}\right)\left\{\cos^2\theta_c[u(x_1)\bar{d}(x_2) + \bar{d}(x_1)u(x_2)] + \right.$$
$$\left. \sin^2\theta_c[u(x_1)\bar{s}(x_2) + \bar{s}(x_1)u(x_2)]\right\}. \tag{2.4}$$

where $u(x)$, $d(x)$, $s(x)$ are the distribution functions for up, down and strange quarks in the proton. $x_1$ and $x_2$ are the momentum fraction of the partons in the colliding protons and $x_F = x_1 - x_2$. $G_F$ is the Fermi coupling constant, $\theta_c$ is the Cabbibo angle, and $K$ is a factor from first-order QCD correction ($K = 1 + \frac{8\pi}{9}\alpha_s(Q^2)$). By interchanging $u$ with $\bar{u}$, $d$ with $\bar{d}$, one obtains the expression for $W^-$ production

$$\frac{d\sigma}{dx_F}(pp \rightarrow W^- + X) = K\frac{\sqrt{2}\pi}{3}G_F\left(\frac{x_1 x_2}{x_1 + x_2}\right)\left\{\cos^2\theta_c[\bar{u}(x_1)d(x_2) + d(x_1)\bar{u}(x_2)] + \right.$$
$$\left. \sin^2\theta_c[\bar{u}(x_1)s(x_2) + s(x_1)\bar{u}(x_2)]\right\}. \tag{2.5}$$

The calculation of $W$ production at RHIC using Eqs. (2.4) (2.5) is shown in Figure 2.12.
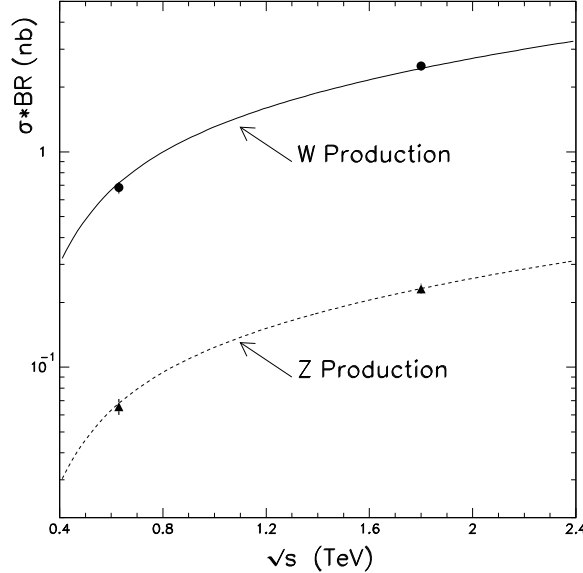


Figure 2.12: Two curves correspond to prediction of the product of cross section for the $W$ and $Z$ boson production and electron decay branching ratio using Eqs. (2.4) (2.5). The data points correspond to UA2 [67] and CDF [68] $W$ and $Z$ boson measurements.

An observable directly related to the $\bar{d}/\bar{u}$ ratio is the ratio of differential cross sections for $W^+$ and $W^-$ production. Given the fact that the contribution from the strange quark is small, this ratio can be derived from Eqs. (2.4) (2.5)

$$R(x_F) \equiv \frac{\frac{d\sigma}{dx_F}(pp \rightarrow W^+ + X)}{\frac{d\sigma}{dx_F}(pp \rightarrow W^- + X)} \approx \frac{u(x_1)\bar{d}(x_2) + \bar{d}(x_1)u(x_2)}{\bar{u}(x_1)d(x_2) + d(x_1)\bar{u}(x_2)}. \tag{2.6}$$

23
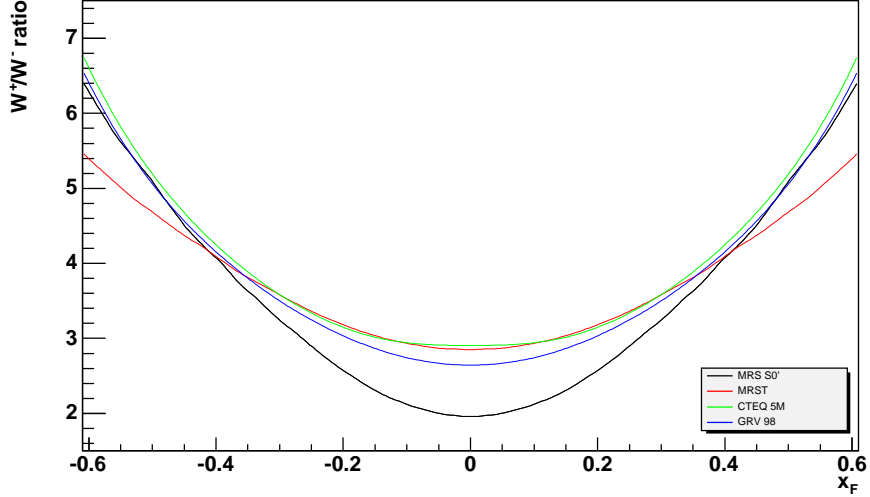
Figure 2.13: Prediction of the ratio $R(x_F)$ of $W$ production in $p + p$ collisions at RHIC ($\sqrt{s} = 500$ GeV) using the MRS S0', MRST, CTEQ5, and GRV98 PDFs.

$R(x_F)$ is clearly symmetric with respect to $x_F = 0$. At the kinematic region $x_F \gg 0$, where $x_1 \gg x_2$, the ratio can be approximated as

$$R(x_F \gg 0) \approx \frac{u(x_1)}{d(x_1)} \frac{\bar{d}(x_2)}{\bar{u}(x_2)}. \tag{2.7}$$

while at $x_F = 0$, the ratio is

$$R(x_F = 0) \approx \frac{u(x)}{d(x)} \frac{\bar{d}(x)}{\bar{u}(x)}. \tag{2.8}$$

Eqs. (2.7) and (2.8) show that a measurement of $W^+$ relative to $W^-$ production in $p+p$ collisions allows a direct determination of $\bar{d}/\bar{u}$, provided that the value of $u/d$ is known. For the PHENIX detector, the $x_F$ coverage for $W$ production is very broad, thanks to the forward muon detector system and the barrel detectors (for $e^\pm$ detection). To illustrate the sensitivity of $R(x_F)$ to the $\bar{d}/\bar{u}$ ratio, Figure 2.13 shows the calculations for $p + p$ collisions at $\sqrt{s} = 500$ GeV using the MRS S0', MRST, CTEQ5, and GRV98 PDFs.

At $x_F = 0$, which corresponds to $x_1 = x_2 = 0.16$ (see Table 2.1), the $\bar{d}/\bar{u}$ ratio is well determined to be $\simeq 2.0$. Eq. (2.8) shows that $R(x_F = 0) \simeq 2\bar{d}/\bar{u}(x = 0.16)$. Figure 2.13 shows that, $R(x_F = 0)$ for the $\bar{d}/\bar{u}$ asymmetry MRST, CTEQ5, and GRV98, all have very similar predictions. In contrast, the calculation using MRS S0', which has symmetric $\bar{d}$, $\bar{u}$ distributions, gives a significantly lower value for $R(x_F = 0)$: $R(x_F = 0) \simeq 2$.

A distinct advantage of extracting the $\bar{d}/\bar{u}$ ratio from $W$ boson production in $p + p$ collisions is that no correction for the nuclear effect in deuteron and no

Table 2.1: Values for $x_1$ and $x_2$ at different $x_F$ for $W$ production in $p+p$ collisions at $\sqrt{s} = 500$ GeV.

| $x_F$ | $x_1$ | $x_2$ |
|---|---|---|
| 0.0 | 0.161 | 0.161 |
| 0.1 | 0.218 | 0.118 |
| 0.2 | 0.289 | 0.089 |
| 0.3 | 0.370 | 0.070 |
| 0.4 | 0.475 | 0.057 |
| 0.5 | 0.547 | 0.047 |
| 0.6 | 0.640 | 0.040 |
| 0.7 | 0.735 | 0.035 |
| 0.8 | 0.831 | 0.031 |

assumption on the validity of charge symmetry (i.e. $u_p = d_n$, $u_n = d_p$, $\bar{u}_p = \bar{d}_n$, etc) are required. This is in contrast to the Drell-Yan experiments and the Gottfried-sum measurement, which require nuclear binding corrections on the effect in the deuteron and the assumption of charge symmetry to relate the neutron with the proton parton distributions. It is also worth noting that the $\bar{d}/\bar{u}$ ratio extracted from $W$ boson production explores the symmetry of nucleon sea at a very large value of $Q^2$ ($Q^2 = m_W^2 \simeq 6500$ GeV$^2$). A comparison with $\bar{d}/\bar{u}$ obtained from E866 Drell-Yan would reveal how the sea quark asymmetry evolves with the $Q^2$ scale.

At large $x_F$, $x_2$ becomes small, and $x_F \simeq x_1$, as shown in Table 2.1. Therefore, $R(x_F \gg 0)$ probes $u/d$ at large $x$ as well as $\bar{d}/\bar{u}$ at small $x$ (see Eq. (2.7)). The value of $\bar{d}/\bar{u}$ at small $x$ is quite well determined from the E866 Drell-Yan measurement. In fact, one expects $\bar{d}/\bar{u} \to 1$ as $x \to 0$ from the consideration from perturbative QCD. Therefore, the main interest for measuring the $W^+/W^-$ ratio at large $x_F$ in PHENIX is to determine the $u/d$ ratios at large $x$. As discussed in a later section, the $u/d$ ratio at large $x$ is still poorly determined experimentally and remains a very interesting topic to study at RHIC.

A detailed simulation code has been written to calculate the $W$ production cross sections using Eqs. (2.4) (2.5) and the expected statistical accuracy for measuring the $W^+/W^-$ ratio in PHENIX. Figure 2.12 shows that this code can reproduce the $W$ and $Z$ boson production cross sections measured at UA2 and CDF. The differential cross section for $W$ production at RHIC energy is shown in Figure 2.14. This code also takes into account the $W^\pm \to l^\pm \mu$ decay. The experimental observable in PHENIX is the $l^+/l^-$ ratio as a function of the rapidity $y$ of the charged leptons. The expected $l^+/l^-$ and the statistical uncertainties for an integrated $p+p$ luminosity of 950 pb$^{-1}$ are also shown for several different PDFs.

The acceptance of the muon arms has been included in the calculation. Figure 2.15 clearly demonstrates that the $W$ production data anticipated at PHENIX has a sufficient accuracy to test the $\bar{d}/\bar{u}$ asymmetry in the nucleon sea.
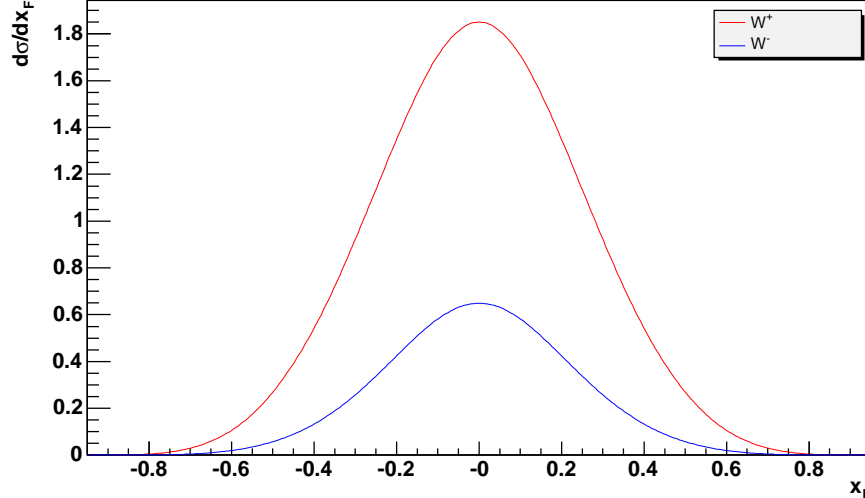


Figure 2.14: Differential cross section for $W$ production at RHIC ($\sqrt{s} = 500$ GeV) as function of $x_F$ calculated with MRST PDF.

In conclusion, the forward muon trigger upgrade for the PHENIX detector at RHIC will enable measurements on $W^+$ and $W^-$ production in $p + p$ collisions. These measurements will provide a unique opportunity to probe $\bar{d}/\bar{u}$ asymmetry at high $Q^2$ without complications of nuclear effects. These data will provide a sensitive test of existing theoretical models and should help us to obtain a more complete picture of the origin for the sea quark asymmetry in the nucleon.

## 2.4  The $d/u$ Ratio Measurement at Large $x$

Compared with sea quark distributions in the nucleon, the valence quark distributions are usually considered to be well-known. While extensive measurements on the parton distributions have been made in deep-inelastic scattering (DIS) experiments at medium ($\sim 0.3$) and small $x$ regions, there exist only very few experimental data in the region where the valence quarks dominate the nucleon ($x > 0.5$) [72].

Measurement of the $d/u$ ratio in the high $x$ region addresses the following physics issues: As the sea quark distribution drops much faster as $x \to 1$ than the valence quark distribution, partons at large $x$ are dominated by the valence quarks. In addition, experimental data on the $d/u$ ratio at large $x$ will help distinguish
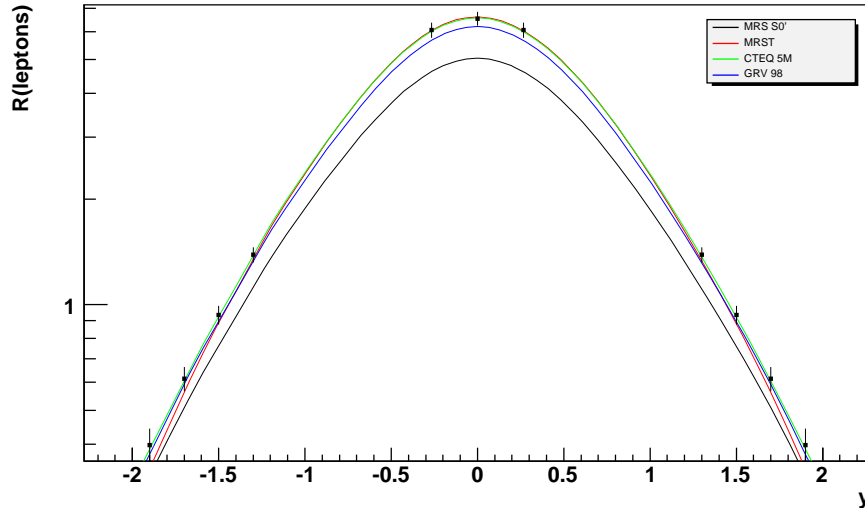
Figure 2.15: The data points correspond to the expected $l^+/l^-$ ratio and its statistical uncertainty with PHENIX detector as a function of charged lepton rapidity $y$. The four curves correspond to $l^+/l^-$ ratio predicted by MRS S0', MRST, CTEQ5, and GRV98 PDFs.

different theoretical models which predict different asymptotic behavior of the $d/u$ ratio at $x \to 1$.

In the SU(6) symmetric model, the $d/u$ ratio is simply equal to $1/2$. However, Close and Carlitz [73, 74] pointed out that the dominance of the $S = 0$ diquark configuration would lead to $d/u = 0$ at $x \to 1$. On the other hand Farrar and Jackson [75] considered one-gluon exchange and predicted that $d/u = 1/5$ at $x \to 1$ as a result of $S_z = 0$ diquark dominance. Moreover, the valence quark distribution at high $x$ will be important input for calculating hard processes leading to the production of new massive particles at the LHC energy [72].

Traditionally, the $d/u$ ratio at large $x$ was determined from experimental data of the $F_2^n/F_2^p$ ratio in which $F_2^n$ can be extracted from the deuteron structure function $F_2^D$ and $F_2^p$. However, the $d/u$ ratio extracted from experimental data largely depends on the chosen model to account for the nuclear effects at large $x$ such as nucleon Fermi motion, nuclear binding, EMC effect etc. For instance, Figure 2.16 shows how the extracted value of the $d/u$ ratio is influenced by considering nuclear binding alone or nuclear binding and Fermi motion together. It is interesting that the $d/u$ appears to approach either $0$, $1/2$ or $1/5$, corresponding to the three values predicted by three different theoretical models, depending on the method of the nuclear correction. Measurement with $F_2^n/F_2^p$ also involves comparison between different targets which might contribute to the systematic error. Furthermore, deep inelastic data is conducted in the low $Q^2$ region where higher-twist effects should be considered [77]. Therefore, it is necessary to seek

measurements in other processes. In addition, as shown in Figure 2.17, the $d/u$ ratio depends on $Q^2$, so it also helps to measure the $d/u$ ratio at higher $Q^2$, e.g. $Q^2 = M_W^2$, to study the evolution of valence quark asymmetry.
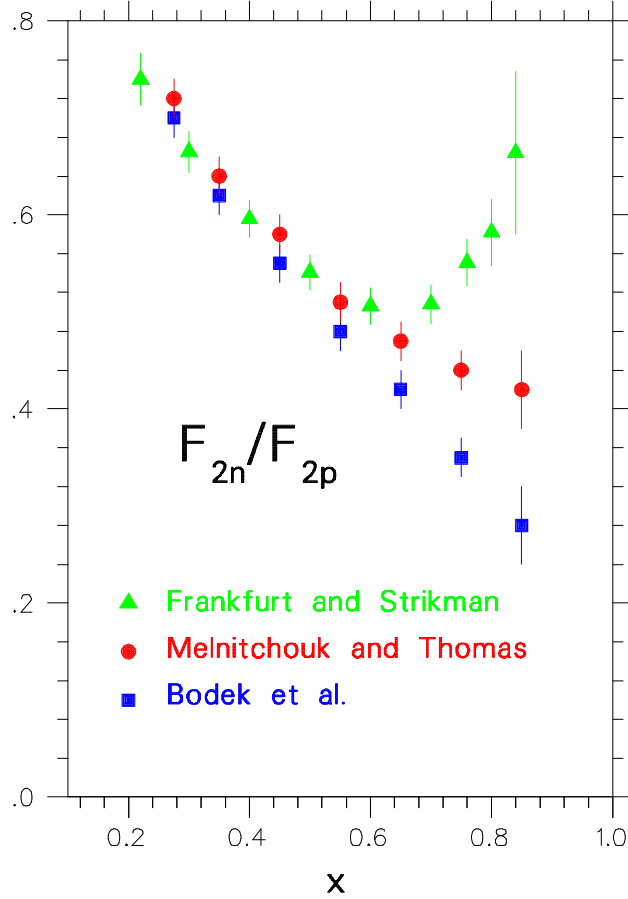


Figure 2.16: This figure that shows different $d/u$ ratios can be extracted from $F_2^n/F_2^p$ using different models for nuclear effects.

Among the model-independent measurements of the $d/u$ ratio, one possibility is $W$ production in $p+p$ or $p+\bar{p}$ collisions. The advantages of using $W$ production in $p + p$ collisions to probe $d/u$ at large $x$ are the following: First, this method does not rely on the theoretical models for nuclear effects in the deuteron. Second, no assumption on charge symmetry is needed in this measurement [76].

The experimental variable one can use to extract the $d/u$ ratio from $W$ production data in $p + p$ collisions is $R_{pp}$ was introduced in a previous section:

$$R_{pp} \equiv \frac{\frac{d\sigma}{dx_F}(pp \to W^+ + X)}{\frac{d\sigma}{dx_F}(pp \to W^- + X)}. \tag{2.9}$$

28
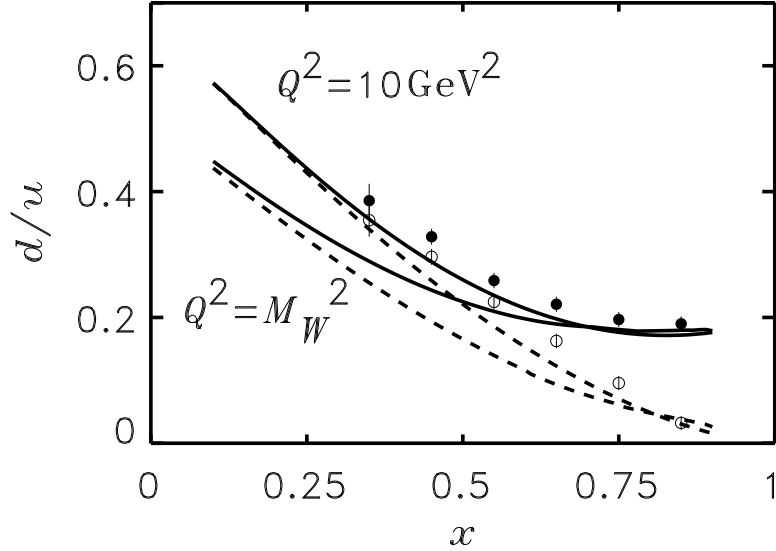
Figure 2.17: Open (closed) circles represent the $d/u$ ratio from SLAC data [77] analyzed assuming binding effects and Fermi motion. The dashed curves are the $d/u$ ratio at $Q^2 = 10$ GeV$^2$ and $Q^2 = m_W^2$ calculated with CTEQ parameterization [78] while the solid curves are calculated with a modified $d$ quark distribution as in Ref. [76].

As shown in a previous section, at large $x_F$ $(x_1 \gg x_2)$,

$$R_{pp}(x_F) \approx \frac{u(x_1)}{d(x_1)} \frac{\bar{d}(x_2)}{\bar{u}(x_2)}; \qquad (2.10)$$

at $x_F = 0$ $(x_1 = x_2 = x)$,

$$R_{pp}(x_F) \approx \frac{u(x)}{d(x)} \frac{\bar{d}(x)}{\bar{u}(x)}. \qquad (2.11)$$

At the RHIC center of mass energy of $\sqrt{s} = 500$ GeV, if $x_2 \lesssim 0.04$, then $x_1 \gtrsim 0.6$. Therefore, the ratio $R_{pp}$ measured at large $x_F$ will be sensitive to the valence quark distribution at large $x$. In Figure 2.18, the ratio $R_{pp}$ has been shown to be large at large $x$. Figure 2.19 shows the $l^+/l^-$ ratio with expected statistical uncertainty at the PHENIX detector. Therefore, measurement of $l^+/l^-$ at large rapidity will be able to distinguish between two different parameterizations.

In summary, measurement of $W$ boson production in $p+p$ collisions will provide an opportunity to constrain the behavior of the valence quark distribution at high $x$. This measurement will not require modelling of nuclear effects in contrast to previous deuteron target measurements. This measurement would distinguish theoretical models which describe different asymptotic behaviors of the $d/u$ ratio at $x \to 1$. Therefore, the future RHIC run at $\sqrt{s} = 500$ GeV will help to reveal the mechanism behind flavor symmetry breaking in the nucleon.
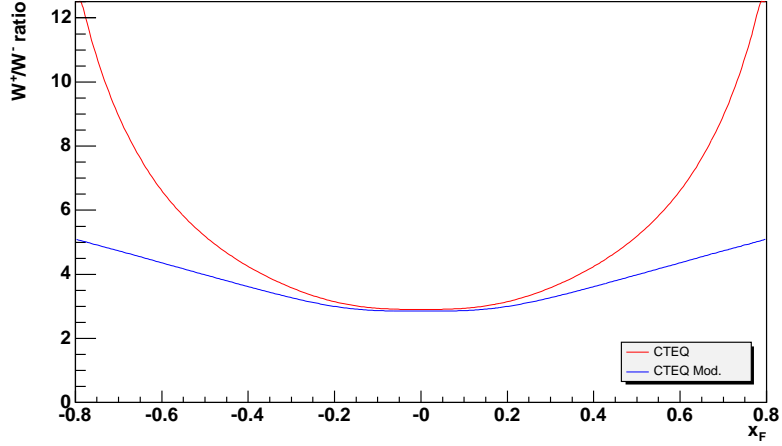
Figure 2.18: Prediction of the $R(x_F)$ ratio for $p+p$ collisions at $\sqrt{s} = 500$ GeV at RHIC. The dotted curve is calculated with CTEQ parameterization [78] while the solid curve is calculated with modified $d$ quark distribution as Eq.(6) in Ref. [76].
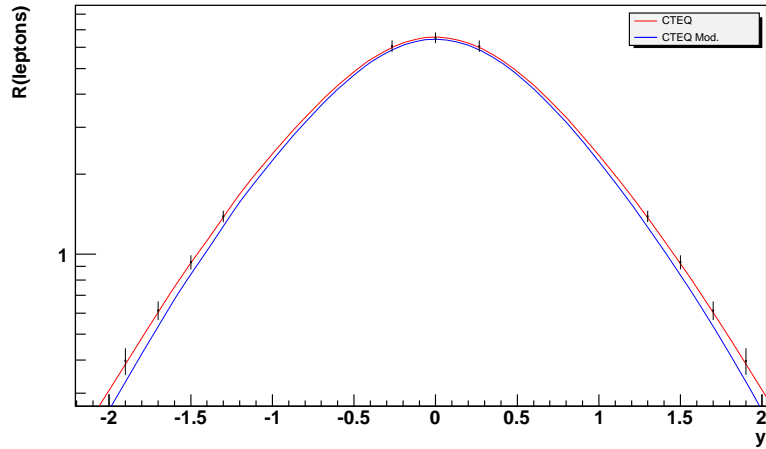


Figure 2.19: Prediction of the $l^+/l^-$ ratio as a function of rapidity $y$ for $p+p$ collisions at $\sqrt{s} = 500$ GeV at RHIC. The data points correspond to expected value at PHENIX and the error bars correspond to statistical uncertainty. The two curves are calculated with CTEQ parameterization [78] and CTEQ parameterization with modified $d$ quark distribution as Eq.(6) in Ref. [76].

## 2.5 Dimuon Measurements in Heavy Ion Collisions

Heavy quarkonia production is considered to be one of the most important probes of the hot and dense state created in relativistic heavy ion collisions. At RHIC energies $J/\psi$ yields, especially the contributions from $\chi_c$ and $\psi'$ states, are expected to be suppressed in a quark gluon plasma due to color screening and gluon rescattering [41, 42]. Intriguing measurements of $J/\psi$ suppression at lower energies have been reported from CERN-SPS experiments [43, 44], At $\sqrt{s_{NN}} = 200$ GeV competing processes such as charm recombination may also play an important role. PHENIX measures $J/\psi \to \mu^+\mu-$ at forward $(1.2 < |y| < 2.2)$ and $J/\psi \to e^+e-$ at mid $(|y| < 0.35)$ rapidities.

PHENIX recently observed that the $J/\psi$ suppression, relative to binary scaling of $p+p$, is larger at forward rapidity than mid rapidity [45]. The effect is particularly evident when looking at the ratio of $R_{AA}^{\mathrm{forward}}$ (i.e. integrated over $1.2 < |y| < 2.2$ and $p_T$) to $R_{AA}^{\mathrm{mid}}$ (i.e. integrated over $|y| < 0.35$ and all $p_T$) as shown vs. centrality in Figure 2.20. The double ratio shows that the suppression
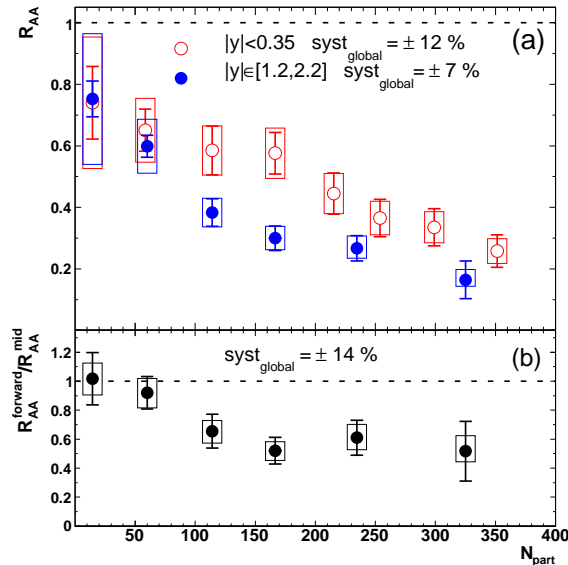


Figure 2.20: (a) $J/\psi$ $R_{\mathrm{AA}}$ vs. $N_{\mathrm{part}}$ for $Au + Au$ collisions. Mid (forward) rapidity data are shown with open (filled) circles. (b) Ratio of forward/mid rapidity $J/\psi$ $R_{\mathrm{AA}}$ vs. $N_{\mathrm{part}}$.

becomes greater at forward rapidity for $N_{\mathrm{part}} > 100$, but pinpointing the onset will require a large increase in statistics. Such a narrowing of the rapidity distribution is expected if a significant fraction of $J/\psi$'s are formed from recombination of unrelated $c\bar{c}$ pairs [46].

Recombination is expected to have manifestations in the $J/\psi$ $p_T$ distribution. Calculations for $\langle p_T^2 \rangle$ centrality dependence [47, 48] conclude that recombination causes a significant reduction in $\langle p_T^2 \rangle$ which brings the models into better agreement with the data [49], but the magnitude of the effect and even the expectation without recombination varies significantly between the models. According to [48], differentiating between recombination of thermally distributed or pQCD $c\bar{c}$ pairs may be possible with sufficient statistics.

The $J/\psi$ $R_{AA}$ as a function of $p_T$ appears to be fairly flat within statistics up to 5 GeV as shown in Figure 2.21. The large high $p_T$ heavy flavor electron
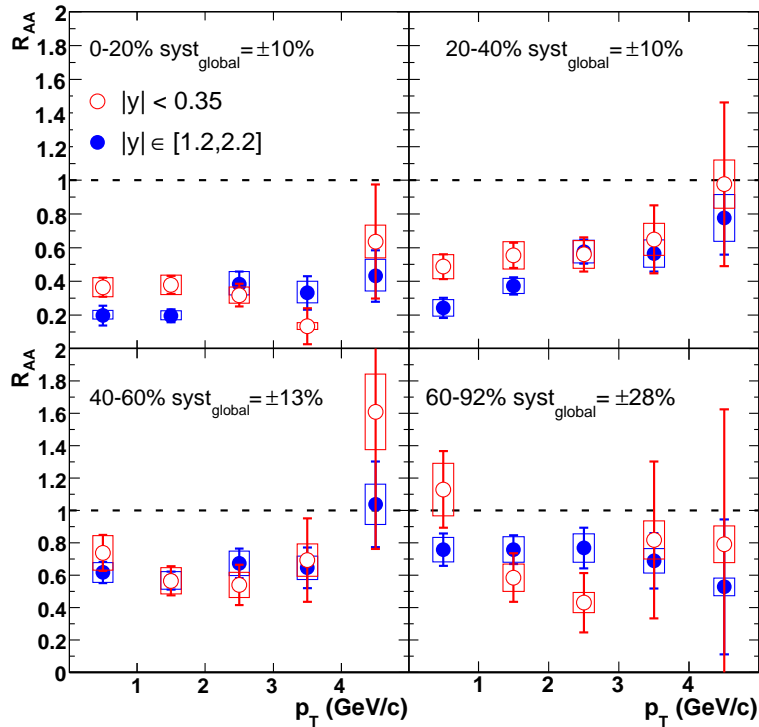


Figure 2.21: $J/\psi$ $R_{\mathrm{AA}}$ vs. $p_T$ for several centrality bins in $Au+Au$ collisions. Mid (forward) rapidity data are shown with open (filled) circles.

suppression observed by PHENIX [50] if combined with a large recombination component could cause $R_{AA}$ to drop at high enough $p_T$. An AdS/CFT correspondence calculation [51] also expects more suppression at high $p_T$. Disentangling the recombination contribution should also be aided by future PHENIX measurements of $J/\psi$ elliptic flow. Increased statistics provided by RHIC II luminosities will be essential to sufficiently address these measurements.

RHIC II luminosities will also allow PHENIX to begin quantitative study of $\Upsilon$ production in heavy ion collisions. PHENIX expects to measure $\sim$ 1000 $\Upsilon \rightarrow$

$\mu^+\mu^-$ from an integrated luminosity of 18 nb$^{-1}$, corresponding to $\sim 12$ weeks of RHIC II $Au + Au$ running.

# Chapter 3

# The Fast Muon Trigger System

## 3.1 Overview

In this chapter we describe the hardware configuration of the proposed first level muon trigger, its design parameters, results from R&D work and plans for future R&D. The trigger is based on fast tracking through the muon spectrometer magnets and will use information from new resistive plate chamber (RPC) tracking stations and the existing muon tracker stations in the PHENIX muon arms. The trigger project includes the construction and installation of fast RPC tracking stations in each muon spectrometer arm and additional front end electronics for the muon tracker that will transfer muon tracker information to the first level trigger processors.

The existing PHENIX spectrometer includes two muon spectrometers at forward and backward rapidity (pseudorapidity 1.2-2.2) referred to as the north and south muon arms. The arms consist of significant absorber material close to the collision region (in order to absorb hadrons). There are then three stations of cathode strip chambers for measuring the trajectory of particles in a magnetic field (with an integrated B-dl of approximately 0.75 Tesla-meters). This is sufficient for determining the charge sign of the particles - a critical component for the $W$ physics measurement. Following that is a muon identifier - interleaved layers of absorber and active detector. Currently a Level-1 trigger is based on the muon identifier information only. A muon or punch through (only dE/dx) hadron that reaches the back of the muon identifier stack must have a minimum momentum of $\sim 2.2$ GeV. The Level-1 trigger rejection for muons is dominated by the lower range muons and hadrons, whereas the muons from $W$ decay have typical total momentum $> 40$ GeV. It is this difference we will exploit in building the new fast muon trigger system.

Data taking for $W$-physics will take place with a luminosity of $L = 1.6 \times 10^{32}$ cm$^{-2}$s$^{-1}$ with a total cross section of $\sigma_{tot} \approx 60$ mb at $\sqrt{s} = 500$ GeV. This corresponds to a collision rate of 9.6 MHz. We assume that the muon trigger for

$W$-physics will be assigned 2 kHz of the PHENIX data acquisition bandwidth. This leads to a required rejection factor of $R = 5000$. Experience with the Monte Carlo simulation of the present first level muon trigger and the electron and photon triggers shows that a safety factor of 2 is needed between the rejection observed in the simulation and the actual measured rejection. We therefore aim at a target rejection factor of $R = 10000$. The present muon triggers in the two spectrometers presently each have a rejection of $250 \lesssim R \lesssim 500$ depending on beam background levels. With stable and low beam background its counting rate is dominated by muons from hadron decays. Trigger performance simulations are summarized in section (3.5.2).

The trigger will be installed in two stages. The configuration for the first stage consists of the new trigger front-end electronics for MuTr stations 1 and 2 and RPC stations 2 and 3. In addition we will introduce 30 cm of Cu-absorber upstream of muon tracker station 1. The absorber will be mounted to the backend of the central magnet yoke and will reduce the low momentum hadron punch through by almost a factor 10. The reduction of low momentum hadrons penetrating into the muon tracker volume reduces the false high $p_T$ muon background in the offline analysis (as described in detail in Section 4.2 and 4.3). The second installation stage assumes that new detectors, such as the FVTX, the NCC or if necessary an additional MuTr station, will solve the false high $p_T$ background problem. We then can remove the absorber and introduce in this space instead the double RPC station 1A and 1B with the goal to reach the maximum possible rejection power for the trigger in light of the increased RHIC luminosity. RHIC luminosity for proton-proton collisions will increase by a factor of 3 from electron cooling starting in 2012. At this time, based on actual data, we also will evaluate the rejection power which can be gained by instrumenting muon tracker station three with trigger front end electronics.

In the following we briefly discuss some of the main challenges which need to be solved in the course of the muon trigger project.

- The new muon tracker electronics will take input signals from the backplane of the existing muon tracker front end electronics with signal dividing ratio of 1:9. There is considerable concern how the presence of the new boards will impact the stability and performance of the present muon tracking electronics and in particular how it will impact the position resolution. In order to address this concern and to study the impact of the new electronics a detailed R&D program has been put in place. First tests took place with one full muon tracker octant at Kyoto University. The tests demonstrated stable operation of the octant with the new electronics in place and at the same time retained the position resolution measured for cosmic rays. A second round of tests then was carried out at Tokkhu University using a 600 MeV electron beam. For the future it is planned to carefully introduce the new electronics in small steps in the PHENIX muon arms and closely

monitor possible impacts of the new electronics on stability and position resolution. It is planned to introduce new MuTr electronics for two octants in the north muon spectrometer for run 8. This evaluation process will be carried out in close collaboration with our colleagues working on the muon tracking chambers. We plan that each new installation step will only be carried out after a formal review of the performance of detectors with the new electronics installed in the previous step. A detailed discussion of the muon tracker trigger electronics, including the stepwise evaluation process can be found in section (3.4).

- Present PHENIX first level triggers rely on the BBC collision trigger to reject beam related backgrounds. At the luminosities expected for the $W$-physics program the collision rate will approach 1 collision per bunch crossing and the BBC collision trigger will be ineffective in removing beam related backgrounds. It is therefore necessary to introduce timing resolution in the trigger which will make it possible to reject beam related backgrounds. The intrinsic timing resolution for the RPCs is about 1-1.5 ns. The actual timing resolution will be determined by the front end electronics. The RPC front-end electronics is discussed in section (3.3).

  Offline, the timing resolution is also essential to remove the background from high momentum cosmic ray muons to the very low cross section $W$-signal.

  Despite the new timing resolution there will be irreducible beam background, namely the background which travels with the outgoing beams. We have carried out analysis of the present muon triggers as well as test measurements with scintillators and RPCs in order to investigate this outgoing beam background problem. Our results suggest that outgoing beam background is strongly suppressed.

- The integration of the RPC stations into existing spaces in the muon spectrometer is difficult. In section (3.6.1) we provide a conceptual 3-D design model which explains the proposed installation procedures.

## 3.2 Resistive Plate Counters (RPCs)

### 3.2.1 RPC Detector Design

**Introduction**

Resistive plate chambers are proposed as a suitable solution to build a first level high $p_T$ muon trigger because of their fast response and good time resolution, flexibility in signal readout, robustness and the relatively low cost of production [79].

This technology has been widely adopted in many experiments, Belle, Barbar, and all experiments at LHC [80].

The PHENIX Forward Muon Trigger RPC will be similar to the CMS design and the production scheme used will be similar to that of CMS. The RPC gas cells will be constructed by the group from Korea University. A complex, expensive and automated RPC construction facility exists at Korea University, which has been used for making CMS End-Cap RPC's. The chamber frame components will be produced in China by the CIAE and PKU groups. The chamber assembling and QA will be done at BNL. The RPC working principle and the R&D tests are documented in this section. The QA process will be discussed in the QA section.

### RPC Description

The RPCs are built with two parallel plates of high resistive material, like phenolic polymer (bakelite) or glass, as electrodes. The plates have a resistivity $\rho$ of the order of $1 - 10 \times 10^{10}$ $\Omega$ cm. The sensitive gas volume gap is typically 2 mm thick between the two plates. In order to keep the plates at a fixed distance over the entire plate area, spacer disks of polycarbonate are glued on the plates. The gas gap is closed at the edges with polycarbonate strips (with the same thickness as the spacers) to ensure gas tightness. Two small gas tubes are inserted into the gas gap on the opposite corners of the chamber for gas inlet and outlet.

The outside surfaces of the RPC plates are coated with graphite for distributing high voltage on one side and the ground on the other in order to establish a strong electric field in the gas gap. The graphite coat has a surface resistivity of about a couple of hundred $\Omega$s per squared cm. The graphite surface is then covered with high resistive thin film, for example PET or Mylar, in order to prevent potential damage to the graphite coat.

The signal readout, typically made of copper strips or pads, is located outside of the sensitive gas volume. This is one of the very attractive features of using RPCs. Ionizing particles create electron-ion clusters in the gas, where an intense constant electric field is present between the two parallel electrode plates. An avalanche is created by multiplication in the gas, so that the cluster charge, $q_0$, becomes $Q = q_0 e^{\alpha x}$ after a distance $x$, where $\alpha$ is the first Townsend coefficient and increases strongly with ratio of the electric field to the density. RPC's operate at high gain, $< e^{\alpha x} > \sim 10^7$, on average. The drift of the charge $Q$ towards the anode induces on the pick-up electrode the fast charge $q$, which is collected by the RPC readout electronics. The RPC gain factor depends exponentially on $x$, the signal charge has a very large dynamic range from 20 fC to 20 pC.

### RPC Design constraints for PHENIX

**Operating parameters**  The basic construction and operating parameters of the PHENIX Forward Trigger RPC are given in Table 3.1. The performance

requirements for the PHENIX Forward Trigger RPC are given in Table 3.2. These parameters are the same as the requirements for the CMS RPC with the exception of the higher rate capability CMS requires, $r > 1$ kHz.

Table 3.1: Construction and operating parameters for the PHENIX Forward Muon Trigger RPC.

| Bakelite thickness | 2 mm |
|---|---|
| Bakelite bulk resistivity | $2.0 - 5.0 \times 10^{10}$ $\Omega$ cm |
| Gap width | 2 mm |
| Gas mixtures | 95% $C_2H_2F_4$, 4.5% i-$C_4H_{10}$ and 0.5% $SF_6$ |
| Operating high voltage | 9 kV |
| Number of gaps | 2 |

Table 3.2: The performance requirements for the PHENIX Forward Muon Trigger RPC.

| Efficiency | $> 95\%$ |
|---|---|
| Time resolution | $\leq 3$ ns |
| Average cluster size | $\leq 2$ strips |
| Rate capability | 0.5 kHz/cm$^2$ |
| Operating plateau | $> 300$ V |
| # of streamers | $< 10\%$ |

**Geometry**   A fast muon trigger has to separate high energy muons from lower energy muons originating from hadron decays. The RPC stations should therefore be highly segmented in the angle $\phi$ defined around the $z-$axis and have a reasonable lever arm around the magnetic volume of the MuTrs. A $\phi$ segmentation of at least 360 segments or 1 degree angular intervals will thus be used, where applicable. One station, RPC1 will be situated upstream of the MuTr station and one station, RPC2 will be downstream of it. Furthermore a better spatial resolution of the MuID as well as added redundancy to the downstream bend information of a track require a third station RPC3 located downstream of MuID5. RPC2 and RPC3 consist of only one plane of a double gap RPC detector, while in RPC1 two detector planes RPC1A and RPC1B will be used for redundant upstream track information. While it is not necessary to have a high segmentation in the polar angle $\theta$ for $p + p$ collisions it is advisable to have several segments for the trigger logic if it becomes necessary to prescale the inner segments due to beam related

background. In RPC1A and RPC1B 4 segments in $\theta$, each covering an interval of 5.52 degrees starting at 12.36 degrees will be implemented. In RPC2 and RPC3 the angular interval will be 2.76 degrees starting at the same inner angle, resulting in 8 segments in RPC2 and 6 segments in RPC3 where the two outer segments are not possible due to space limitations.

Since the cluster size of the RPC readout pads is about 1-2 cm the minimal readout strip size is 0.81 cm. As the RPC information will be combined with the MuTr FEE information for the trigger the geometry of the readout of the MuTr will be matched in the RPC modules by having rectangular readout strips which are radial only in the center of the half octants. Close to the octant edges the strips will become trapezoidal due to the radial edges of the RPC. An example of the strip design can be seen in Figure 3.8 for a complete RPC2 octant.

The CMS front end electronics readout chips contain 32 channels each. Therefore strip counts in each octant (half-octants for RPC2/3) of multiples of 32 are aimed for. Additionally, in order to build a trigger based on the hit positions of RPCs 1, 2 and/or 3 angular projections of the strips from the collision point have to match. Therefore 32 and 64 strips have been used. The actual active strip counts will be slightly smaller due to inactive edges in the RPC detectors.

The dimensions of the different segments in $\theta$ (rings), the pickup strip sizes and their number can be found in the Tables 3.3 and 3.4 respectively. The dimensions and angles were calculated starting with the opening in $\theta$ at the $z$-position of RPC1B.

**Module constraints**  Further constraints will involve the actual construction of the detector gas gaps and the support structure around each gas gap.

The maximal size of the bakelite gaps, which can be processed by the production facility at Korea University is 2 m $\times$ 1.25 m. In order to reduce dark currents at the gap edges a stripe of 25 mm width along the gas gap edges will not be coated with graphite. As a consequence the stripe along the edges will be inactive. Along two edges of the bakelite gaps additional 19 mm will be needed inside the detector module box for HV and gas services. The gas inlets require 50 mm space at the corners of the gaps to avoid damage to the inlets during transport through contact with the support frame. The support frame is a quadratic aluminum profile of $16 \times 16$ mm$^2$ and adds additional 16 mm of inactive area along the outer edges of the detector modules. Therefore the total inactive space at the detector edges varies between 41 mm without services and 60 mm with room for HV and gas services. The height of the detector box consists of the 16 mm of the aluminum support frame and two 6 mm thick honeycomb plates as top and bottom covers for the box. The 16 mm of the support frame corresponds to the thickness of the double gas gap arrangement inside the detector box including the signal plane and various layers of insulating and shielding materials.

The readout strips will be fed through to the electronics in different ways

Table 3.3: RPC dimensions, all sizes in mm, all angles in degrees.

| Ring | $\theta/(\deg)$ | RPC1A | | RPC1B | | RPC2 | | RPC3 | |
|---|---|---|---|---|---|---|---|---|---|
| | | radius | width | radius | width | radius | width | radius | width |
| possible | | | | | | 5280.2 | | 5231.7 | |
| | 34.36 | 933.2 | 773.1 | 1016.8 | 842.3 | 4675.4 | 3873.2 | - | - |
| Ring 8 | | | | | | Strips: 477.55 × 60.5 (64) | | | - |
| | 31.60 | Strips: 185.15 × 12.1 (64) | | Strips: 201.72 × 13.2 (64) | | 4207.5 | 3495.6 | - | - |
| Ring 7 | | | | | | Strips: 450.04 × 60.5 (58) | | | - |
| | 28.84 | 751.8 | 6228 | 819.1 | 678.6 | 3766.5 | 3120.3 | 4991.4 | 4135.0 |
| Ring 6 | | | | | | | - | | - |
| | 26.09 | Strips: 166.15 × 9.7 (64) | | Strips: 181.03 × 10.6 (64) | | - | - | - | - |
| Ring 5 | | | | | | | - | | - |
| | 23.33 | 588.7 | 487.7 | 641.4 | 531.4 | 2949.4 | 2443.4 | 3908.6 | 3238.0 |
| Ring 4 | | | | | | Strips: 390.56 × 38.2 (64) | | Strips: 517.57 × 50.6 (64) | |
| | 20.57 | Strips: 153.15 × 15.2 (32) | | Strips: 166.86 × 16.6 (32) | | 2566.8 | 2126.4 | 3401.5 | 2827.9 |
| Ring 3 | | | | | | Strips: 376.88 × 38.2 (56) | | Strips: 499.18 × 50.6 (56) | |
| | 17.81 | 438.7 | 363.4 | 477.9 | 395.9 | 2197.7 | 1820.6 | 2912.3 | 2412.7 |
| Ring 2 | | | | | | | - | | - |
| | 15.06 | Strips: 143.67 × 11.4 (32) | | Strips: 156.53 × 12.4 (32) | | - | - | - | - |
| Ring 1 | | | | | | | - | | - |
| | 12.30 | 297.6 | 246.6 | 324.3 | 268.6 | 1491.1 | 1235.3 | 1976.1 | 1637.0 |
| possible | | | | | | 1468.4 | | 1926.4 | |
| Upstream side $z$-position | | 1365.1 | | 1487.3 | | 6839.0 | | 9063.0 | |

Table 3.4: RPC dimensions for each second layer of modules, shifted 28 mm downstream relative to the first layer; all sizes in mm, all angles in degrees.

| Ring | $\theta/$(deg) | RPC1A radius | RPC1A width | RPC1B radius | RPC1B width | RPC2 radius | RPC2 width | RPC3 radius | RPC3 width |
|---|---|---|---|---|---|---|---|---|---|
| possible | | | | | | 5280.2 | | 5231.7 | |
| | 34.36 | 952.4 | 789.0 | 1035.9 | 858.2 | 4694.5 | 3889.1 | - | - |
| Ring 8 | | | | | | - | | | - |
| | 31.60 | Strips: 188.95 × 12.3 (64) | | Strips: 205.52 × 13.4 (64) | | - | - | - | - |
| Ring 7 | | | | | | | - | | - |
| | 28.84 | 767.2 | 635.6 | 834.5 | 692.4 | 3781.9 | 3133.1 | 5006.8 | 4147.8 |
| Ring 6 | | | | | | Strips: 426.99 × 49.0 (64) | | Strips: 565.28 × 64.8 (64) | |
| | 26.09 | Strips: 169.56 × 9.9 (64) | | Strips: 184.43 × 10.8 (64) | | 3362.1 | 2785.2 | 4450.9 | 3684.3 |
| Ring 5 | | | | | | Strips: 408.82 × 49.0 (57) | | Strips: 541.22 × 64.8 (57) | |
| | 23.33 | 600.8 | 497.7 | 653.5 | 541.4 | 2961.5 | 2453.4 | 3920.6 | 3248.0 |
| Ring 4 | | | | | | - | | | - |
| | 20.57 | Strips: 156.29 × 15.6 (32) | | Strips: 170.00 × 16.9 (32) | | - | - | - | - |
| Ring 3 | | | | | | | - | | - |
| | 17.81 | 447.7 | 370.9 | 486.9 | 403.4 | 2206.7 | 1828.1 | 2921.3 | 2420.1 |
| Ring 2 | | | | | | Strips: 365.38 × 28.6 (64) | | Strips: 483.71 × 37.8 (64) | |
| | 15.06 | Strips: 146.61 × 11.4 (32) | | Strips: 159.48 × 12.4 (32) | | 1847.4 | 1530.4 | 2445.7 | 2026.1 |
| Ring 1 | | | | | | Strips: 357.33 × 28.6 (54) | | Strips: 473.06 × 37.8 (54) | |
| | 12.30 | 303.7 | 251.6 | 330.4 | 273.7 | 1497.2 | 1240.4 | 1982.2 | 1642.1 |
| possible | | | | | | 1468.4 | | 1926.4 | |
| Upstream side $z$-position | | 1393.1 | | 1515.3 | | 6867.0 | | 9091.0 | |
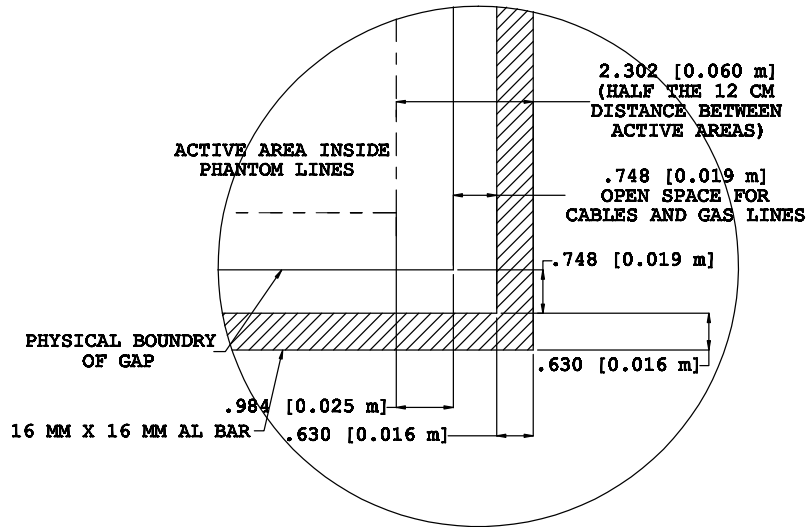
Figure 3.1: Inactive areas at the edges of the detector module.

depending on the specific configuration of the detector modules.

- If the 19 mm for services are present this space can be also used to feed the readout cables to a connector integrated in the support frame. In this case both gaps can be of identical dimension and the maximal two-gap detector efficiency will extend all the way to the edge of the active area of the detector module.

- Along detector edges without services, the space necessary for the signal cables will be created by reducing the dimension of one gas gap by 10 mm. This creates the space necessary to couple out the signal wires. However, along the edge of the active area the last 10 mm of the detector will operate with single gap efficiency at about $90 - 95\%$.

- The RPC1A and RPC1B octants are not broken down in smaller detector modules and therefore it is not possible to readout the inner rings of signal pads along the edges of the detector modules. Instead we split the top gap and read out the inner rings along the boundary between the "split gap". This leads to an strip of 20 cm width with only single gap efficiency.

**RPC1 octant design**

Special care has been taken to minimize the dead area in RPC1. The space in the region of RPC1 is limited in the transverse plane. However, one can accommodate two detector module layers each in RPC1A and RPC1B overlaying such, that we are left without inactive area in the azimuthal $\phi$-direction.
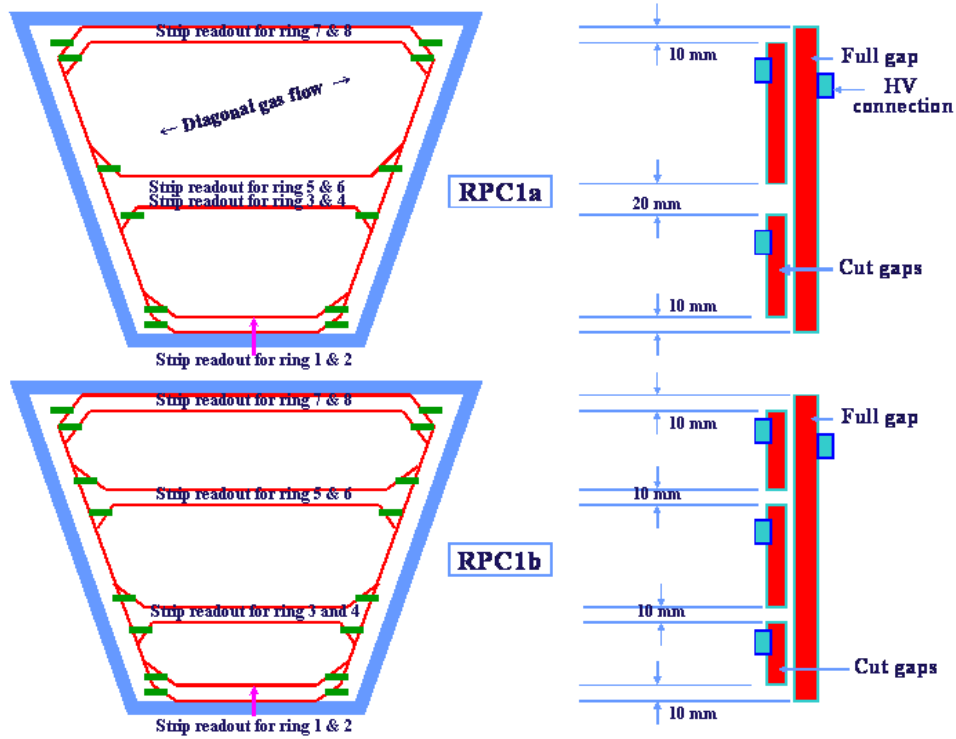
Figure 3.2: Split gap geometry for RPC1A/B.

The relatively small size of the octants in RPC1 makes it possible to cover the full octant with one detector module. This approach reduces the inactive area also in $\theta$. However, the inner rings of signal pads in this configuration have to be read out in between split gaps. As a consequence RPC1 stations have areas with the lower single gap efficiency. Having two stations RPC1A and RPC1B makes it possible to displace the location of the split gaps in stations 1A and 1B and thus guarantee that at least one station has full efficiency. RPC1A will have on split gap between the combined rings of signal pads 5+6 and 3+4. RPC1B will have two splits Gaps. One between rings 1+2 and 3+4 and the second between rings 5+6 and 7+8.

The split gaps, and therefore the front end electronics in RPC1, will be located on the downstream side of the detector. Figure 3.3 shows the actual detector including the support structure and the boxes for the FEE. The support structure itself and the detector installation will be described in section 3.6. In addition a schematic layout of the strips of RPC1 is shown in Figures 3.4 and 3.5.
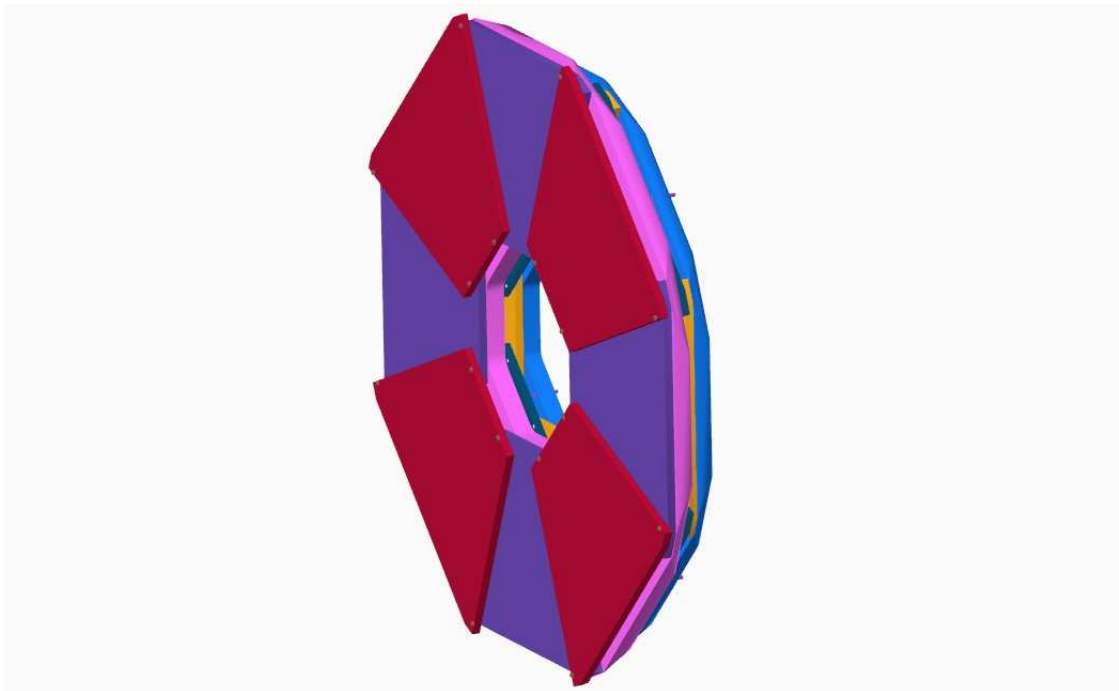
Figure 3.3: Detector view of the full station RPC1. The inner layer shows RPC1A with boxes for the frontend readout electronics (FEE) attached to them, the outer layer shows RPC1A with its FEE box attached to it.

**RPC 1A Downstream**
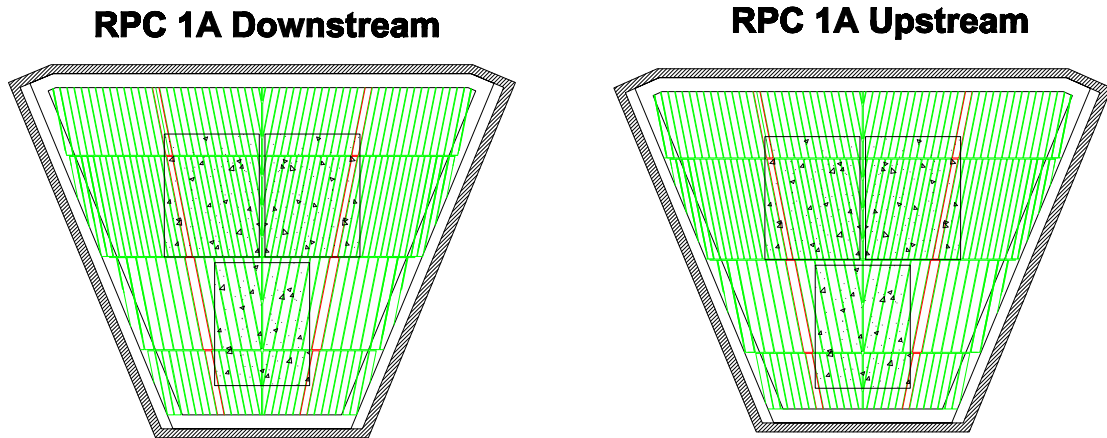
**RPC 1A Upstream**



Figure 3.4: Strip design, inactive areas and electronics boxes (assuming 220 mm × 177 mm) for RPC1A. The left plots displays the downstream modules, the right plot shows the upstream modules(at $z+28$ mm).

**RPC 1B Downstream**
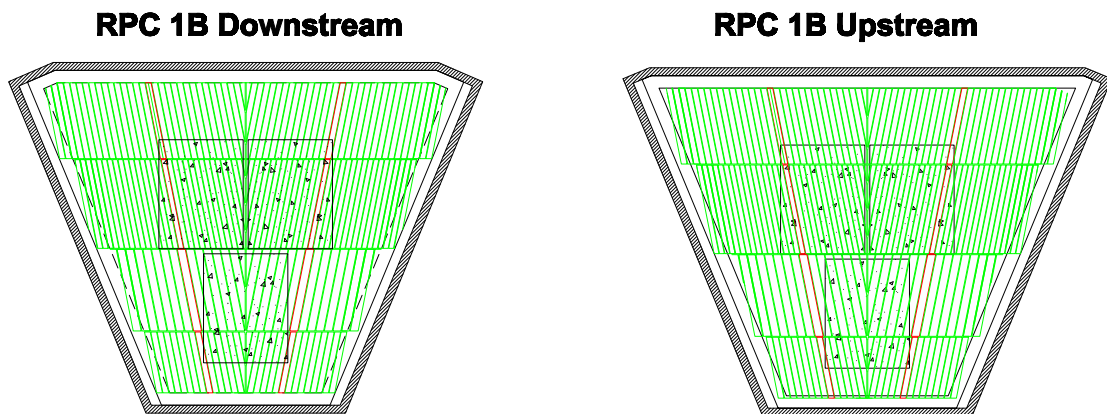
**RPC 1B Upstream**



Figure 3.5: Strip design, inactive areas and electronics boxes (assuming 220 mm × 177 mm) for RPC1B. The left plots displays the downstream modules, the right plot shows the upstream modules(at $z+28$ mm).

**Total Envelope Dimensions**

3951.8

3325.8

1444.4

1196.7

4770.2

**Acive Area Dimensions**

4710.2

3205.8

1504.4

Overlapped Representation

Convergence of Active Area in Theta.

Total Area = 8561324.7 mm^2
Active Area = 7491470.4 mm^2
Dead Area = 1109854.3 mm^2
Ratio of active area = 0.8703641B5

All dimensions in (mm).
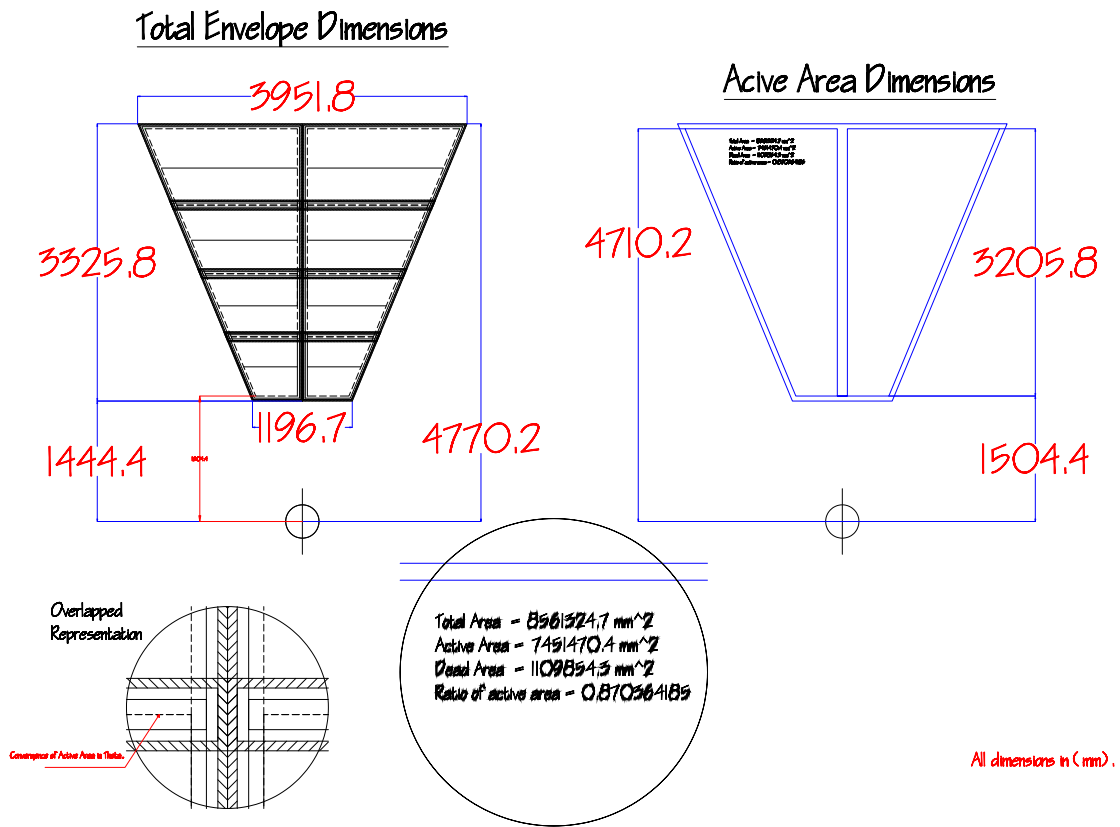
Figure 3.6: Layout of the RPC2 detector modules. (*note: dimensions not upto-date*)

## RPC2 octant design

Size and weight limitations relevant for the installation of the RPC detectors make it necessary to break down RPC2 and RPC3 in half octants as largest structural units. In RPC2/3 the size of the inactive areas along the edges of the detector modules are similar to the size of the existing inactive areas in the muon tracking chambers. Therefore it is not necessary to overlap octants in the azimuthal direction.

The size limitations in the gap production make it necessary to subdivide the half octants into 4 (RPC2) and 3 (RPC3) separate detector modules. In this geometry all signal pad rings can be read out along the detector edges and no split gaps are required. Furthermore it is possible to overlap the detector modules in the radial direction so that no inactive are exist in the $\theta$-direction.

A schematic view of the RPC detector modules for a RPC2 half octant are shown in Figures 3.6 and 3.7, the signal pickup strip geometry is displayed in Figure 3.8.
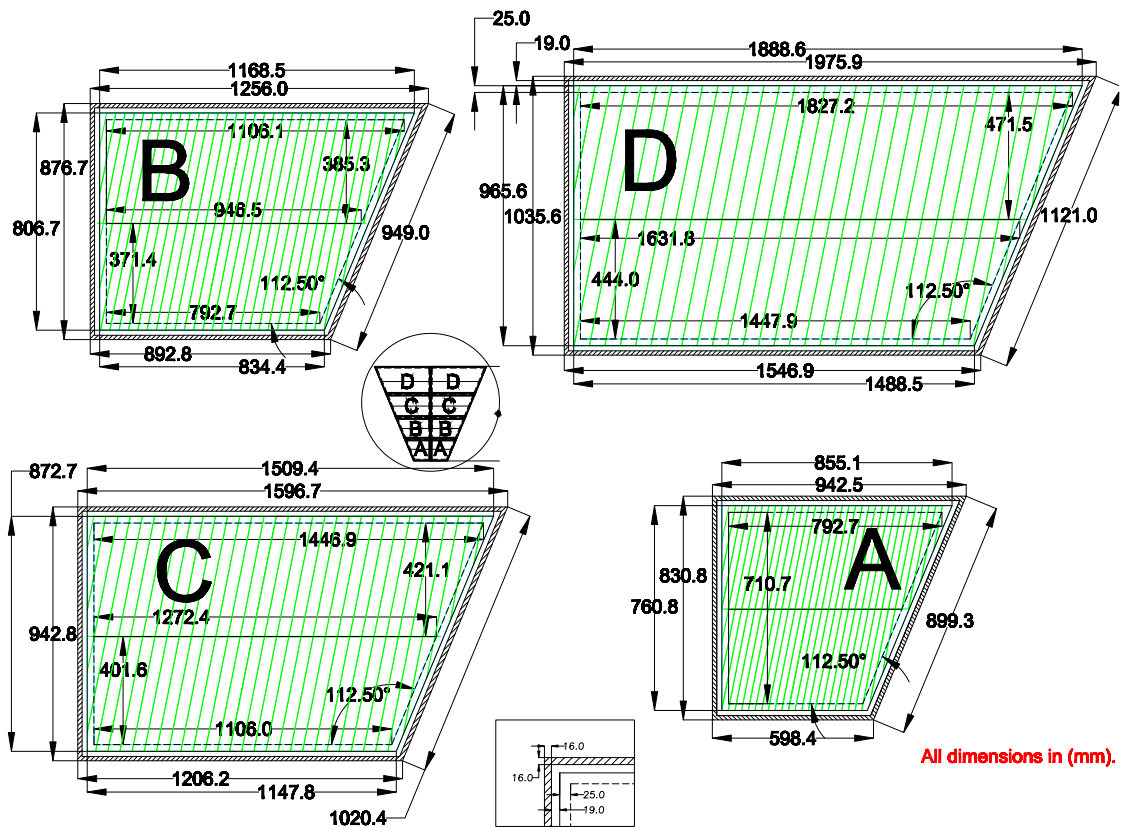
Figure 3.7: Dimensions of the RPC2 detector modules. (*note: dimensions not uptodate*)
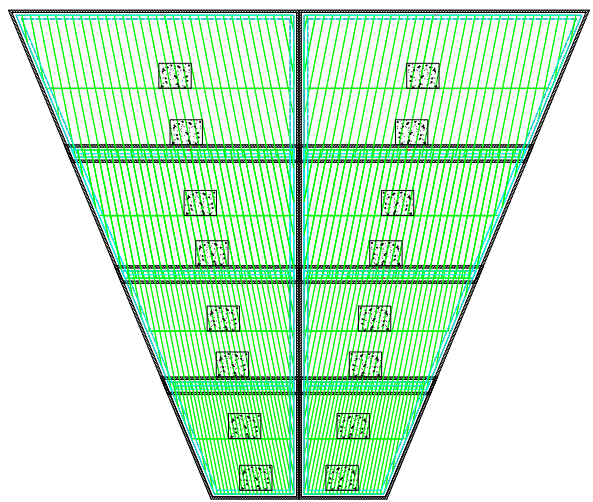


Figure 3.8: Readout strip layout in each of the 8 rings of RPC2 including the dead areas at the boarders and schematically the size of the readout electronics.
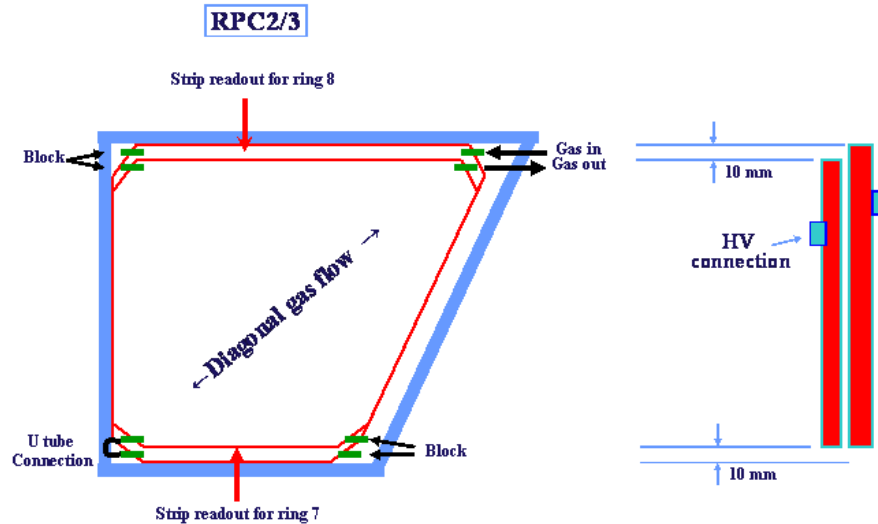
Figure 3.9: Gap and readout design of one detector module, gas and HV services of RPC2/3.

**RPC3 octant design**

RPC3 closely follows the design of RPC2 except that rings 7 and 8 are missing due to space limitations in the interaction region.

## 3.2.2 Construction of RPC Gaps

The PHENIX muon trigger RPC is a standard double gap structure, which has been developed for the Compact Muon Solenoid (CMS) collaboration at the Large Hadron Collider (LHC) at CERN. The cross-sectional view of a gas gap is shown in Figure 3.12, and the construction procedure is given below. More details can be found in Refs. [83, 84, 85].

Thin graphite layers both on the high voltage and on the ground sides of gas gaps are coated by a silk screen method. The surface resistivity of the carbon surfaces is controlled by a 20 $\mu$m thick silk screen mesh. The surface resistivity of the carbon layer ranges from 100 to 250 k$\Omega$/square($\square$) after being drying for 5 days. The silk screen method for the graphite coating is relatively fast for mass production, and is effective in controlling the uniformity of the surface resistivity. The operation table and the accessories for silk screening are shown in Figure 3.13.

The carbon layers of the gas gaps are electrically protected by a 190 $\mu$m thick polyester(PET) sheet. Adhesive based on ethylene vinyl acetate (EVA) is used to glue the PET film on the graphite coated bakelite sheet. The thin film of the 'hot' adhesive is extruded through a long 500 $\mu$m wide slit, and is immediately
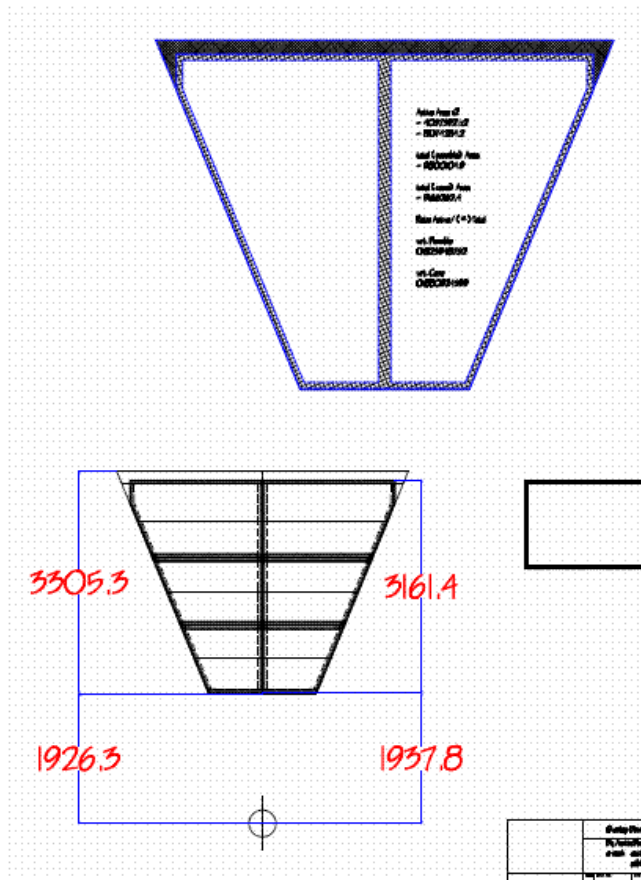
Figure 3.10: Layout of the RPC3 detector modules. (*note: dimensions not upto-date*)
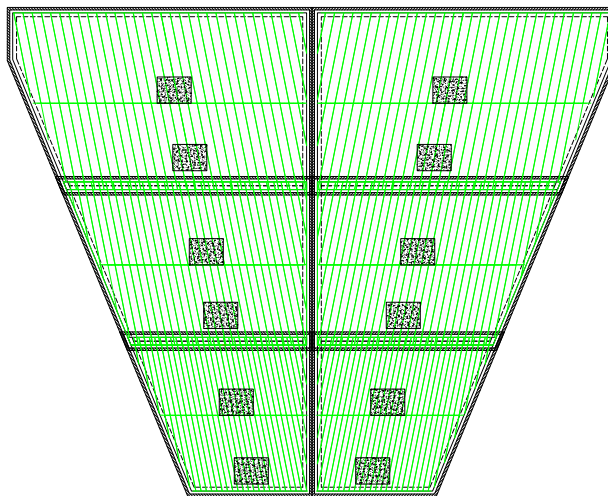


Figure 3.11: Readout strip layout in each of the 6 rings of RPC3 including the dead areas at the boarders and schematically the size of the readout electronics.
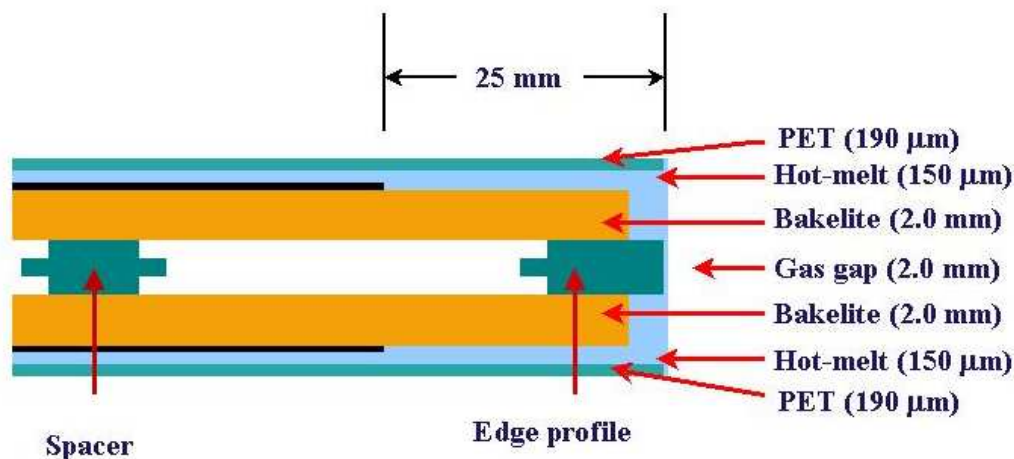
Figure 3.12: Cross-sectional view of a RPC gas gap.

dispensed over the carbon coated bakelite surface. The PET film is immediately placed on the hot glue surface, and then pressed by an air-pressure loaded roller. The thickness of the thin adhesive after hardening is $160 \pm 20$ $\mu$m. Figure 3.14 shows the extrusion machine and the control device of the PET film coating.

Three flat metric tables, rubber chambers for pressurization, specially machined jigs to fix the spacers and the peripheries are used to assemble the gas gaps. The facility shown in Figure 3.15 was designed and manufactured to enable three consecutive assemblies using 3 sets of flat metric tables and rubber chambers. Coin shaped spacers maintain the uniform thickness of the gas volume. They are made of polycarbonate for which the bonding strength with epoxy resin is excellent. Edge profiles along the periphery of the gas gap for gas sealing and block components of gas inlets and outlets are also made of polycarbonate for the same reason. The mechanical tolerances in thickness of the spacers and edge profiles are $\pm$ 10 and $\pm$ 30 $\mu$m, respectively. Positioning of the spacers is guided by special jigs made out of 5 mm thick plexiglass plates, where holes of 13 mm diameter are machined in the exact positions of the spacers. The edge profiles, running along the periphery for the gas sealing, are also fixed by jigs that were machined out of 6 mm thick aluminium plates. Each flat metric table, where a few sets of gas gaps can be assembled, slides into a chamber for epoxy curing. The maximum working time for the epoxy is 60 minutes, and the glue curing time to get the full hardening is approximately 24 hours at 25 °C. During the glue curing time, an air loaded rubber chamber uniformly applies a positive pressure of 20 hPa over the whole surface of the gas gaps and the metric table.

50

Figure 3.13: Silk screen table and the accessories for the graphite coating. The coating area and the thickness of the carbon layer are controlled by the silk mesh (upper right). The multi-layer shelves (lower left) allow for the drying of the carbon layers for many gaps in parallel. A few samples were made to monitor the variation of the surface resistivity as a function of time (lower right).

In CMS, the application of the linseed oil coating to the forward RPCs has been quite successful to reduce the spurious noise in the avalanche mode operation. The complete polymerization of the linseed oil layer, coated inside the gas gap, would ensure the reliability of the long term operation. The oil coating facility, shown in Figure 3.16, consists of two oil tanks, one lifting device, two air pumps, one air compressor, and a press device which vertically holds the gas gaps both during the oil coating and the air drying. The lifting device, holding a 200 liter oil tank, is moving-up vertically with a constant speed of 2 cm per minute. The lifting device hydrostatically injects the oil into the gas gaps which are mounted vertically in the pressing device. The air pump applies approximately - 100 hPa to the gas gaps from outside to keep the pressure below 1 atm even after the oil is fully loaded. As the lifting device is lowered, a thin linseed oil layer automatically remains over the inside surfaces of the gas gaps. The thickness of the oil layer is $3 \sim 5$ $\mu$m. Right after the drain and suction of the linseed oil from the gas gaps, air with relative humidity of 40% is applied to polymerize the oil layers. The flow rate applied per gas gap ranges from 70 to 100 $l/h$. The period of applying
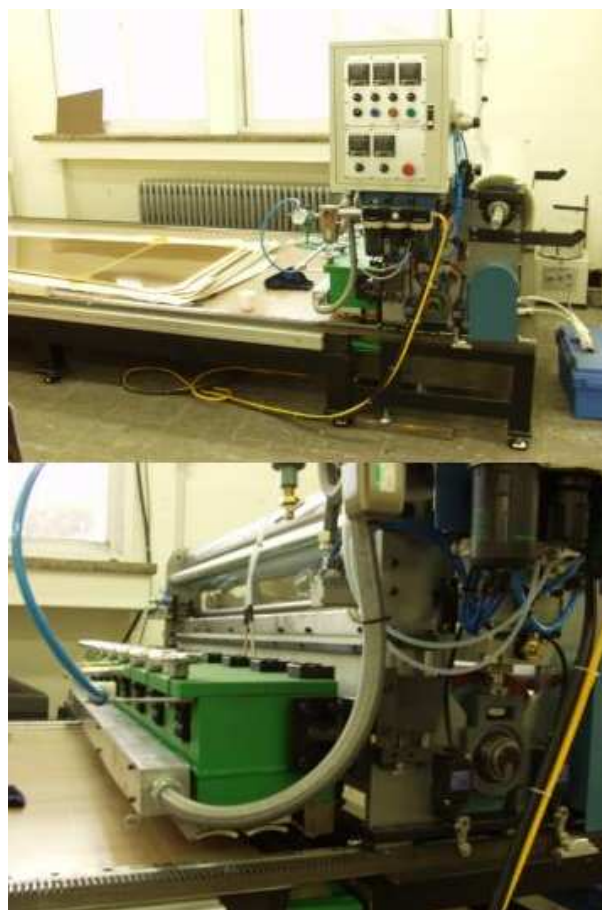
Figure 3.14: PET film coating machine for the protection of the graphite layers. The hot adhesive is extruded through a 500 $\mu$m wide slit of the extrusion tank shown in the lower panel.

the air flow ranges from 40 to 60 hours. The flow rate and its period depend on the size of the gap. The addition of humidity to the air is important to avoid any deformation of the gas gaps due to the drying process. The test results for samples, produced with this oil coating facility, to check the polymerization of the oil layer were satisfactory.

### 3.2.3 Detector Module Construction

The construction of the individual detector modules will be performed in three steps:

1. RPC gap production at Korea University: The production line at Korea University which has been developed and used for the construction of the

Figure 3.15: Facility for the gas gap assembly.

gas gaps for the CMS endcap RPCs will also manufacture the gas gaps for the PHENIX muon trigger PRCs. A detailed discussion of the production process can be found in the previous section.

2. RPC detector module box production at CIAE and PKU: The detector module boxes to support the gas gaps will be produced at CIAE and PKU with help of the CMS group at PKU which performed similar tasks for the CMS RPCs. In addition to the honeycomb and the aluminum profiles for the box itself also the signal strip plane of each module will be produced here. The gas and HV services internal to the gas box and the readout cables will also be provided by CIAE and PKU. Those include the HV and signal cables within the detector module box, gas lines, insulating Cu-foils and all HV and gas connectors. All parts will be shipped from CIAE to BNL for final assembly.

3. Module box and detector assembly at BNL: The RPC gaps from Korea University as well as the module box components from CIAE and PKU will be shipped to BNL. On arrival the components will go through receiving Q&A. After assembly of the detector modules and half octants a detailed performance survey of the detectors will be carried out to guarantee the integrity of all detector hardware prior to installation in PHENIX.

The construction of the RPC assembly and Q&A facility at BNL as well as the actual Q&A and detector and half octant assembly will be carried
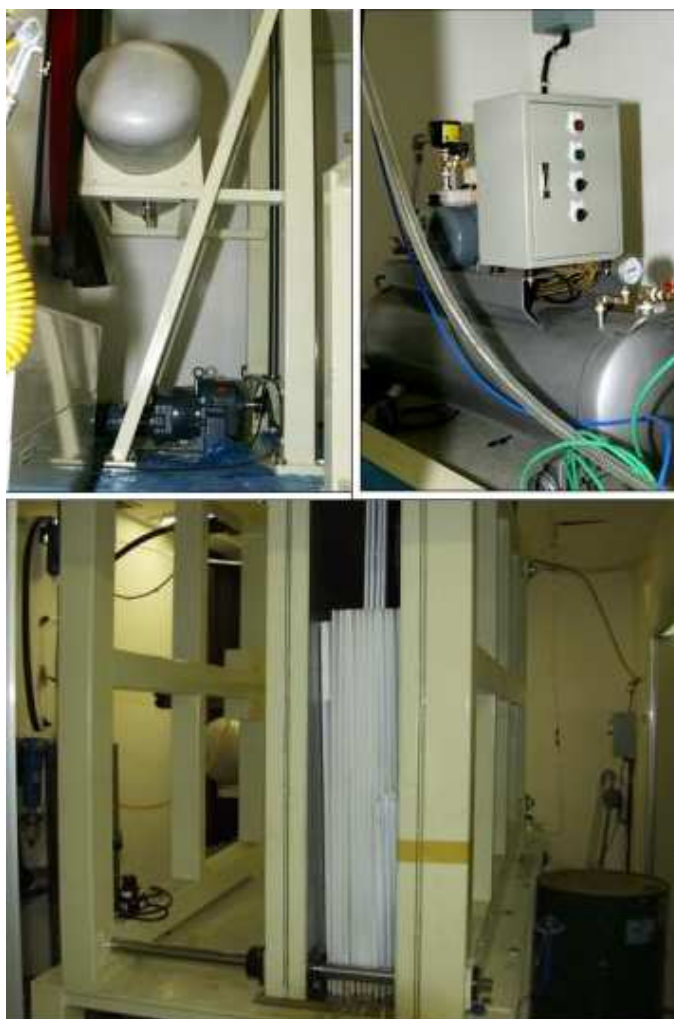
Figure 3.16: Facility for oil coating. The 200 $l$ oil tank and the lifting device are shown in the upper left panel. The pressure inside the gas gaps and the movement of the oil tank are controlled at the control panel shown in the upper right panel. Before oiling, the gas gaps are vertically mounted inside a pressing device, as shown in the lower picture.

out by physicists, students and technicians from CIAE, PKU, ACU, GSU, Muhlenberg and UIUC.

The shipping of RPC gaps from Korea and box components from China has to be in accordance with import and customs regulations which have to be addressed together with logistics experts from BNL. A first shipment of Korean gaps to GSU declared as education/research instruments with no commercial value was successful.

### 3.2.4  RPC R&D Studies at Georgia State and Colorado

RPC R&D tasks have been divided up into a set of focused studies on RPC performance, electronics readout and mechanical studies. There are five RPC R&D test systems currently available in five institutions within the PHENIX Forward Muon Trigger collaboration (see Table 3.5).

Table 3.5: RPC test systems in collaborating institutions and the associated focusing tasks.

| Institutions | Major tasks |
|---|---|
| Univ. of Colorado | RPC readout electronics; cluster size and efficiency |
| CIAE & PKU | Construct RPC chamber components and QA |
| Georgia State Univ. | Prototype construction, RPC performance test and QA |
| Nevis Laboratory | RPC readout electronics development |
| UIUC | pos. resolution, gas composition, rate capability |

Three double-gap prototype RPC's have been built at GSU. One was sent to University of Colorado and one to Nevis Laboratory for developing front end readout electronics suitable for RPC signal dynamics. The third one is kept at GSU for further RPC performance study. In the GSU chambers there are two independent gas cells with gas-gap width of 2 mm, each of which is enclosed by two 2 mm thick bakelite sheets of $30 \times 30$ cm$^2$ in size. The material for the spacers and the side strips is polycarbonate. The chamber enclosure framebox is made of aluminum, which is designed for the purpose of easy assembling and switching out the readout strip board, as shown in Figure 3.17. The high voltage and gas connectors are mounted on the aluminum side-bar. The readout board has four sets of strip configuration made by the Nevis group.

Extensive test results with cosmic rays have been reported both by CU, GSU and UIUC groups at the PHENIX Forward Muon Trigger meetings.

CU will play an important role in testing prototype detectors and readout electronics for the RPCs to be used in the PHENIX forward trigger upgrade. To facilitate the testing, the Colorado group completed a prototype test-stand which includes a large light tight box, a three component gas mixing system, high voltage supplies, trigger scintillators and a data acquisition system. Figure 3.18 shows a picture of the test stand and a RPC built at Georgia State University. A 2 cm $\times$ 1 cm $\times$ 10 cm plastic scintillator, called a "finger", is connected to a PMT several centimeters above the RPC and one 1 cm $\times$ 1 cm $\times$ 10 cm finger scintillator sits below the RPC. These scintillators are used in coincidence as a cosmic ray hardware trigger. Several feet above the RPC sits a paddle scintillator which allows for additional trigger flexibility. A large paddle scintillator, shown
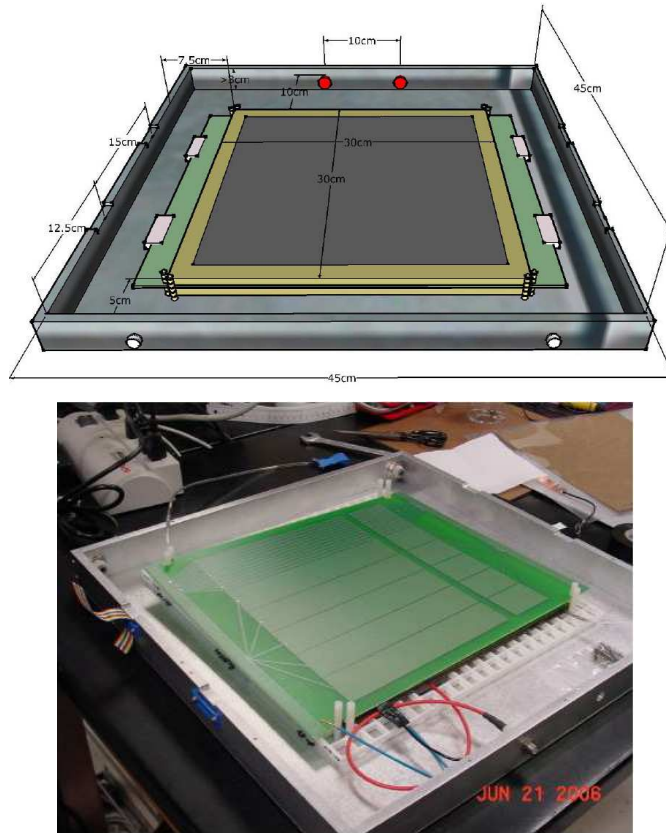
Figure 3.17: RPC framebox and the signal readout printed circuit board with variable strip configurations.

below the RPC in Figure 3.18, is used to reject a cosmic shower component.

Inside the RPC there are 4 cm and 0.5 cm wide copper readout strips on an easily replaceable printed circuit board sandwiched between the two gas gaps. For the tests presented here we read out eight 0.5 cm strips. The strip, over which the finger scintillators sit, is the center strip where the largest signals are most likely to occur. All tests were conducted with a gas mixture of 95% isobutane, 4.5% R134a, and 0.5% $SF_6$. The current data acquisition system at Colorado consists of two oscilloscopes connected to a PC which uses custom software to allow the oscilloscopes to work as a single 8 channel DAQ which records the complete waveform from each readout strip over a 500 ns window. Some example waveforms for an event are shown in Figure 3.19.

50 $\Omega$ resistors are used between the end of each strip and ground to terminate the strip. This matches the impedance of the oscilloscope and should significantly reduce any signal reflection. This does not perfectly match the impedance of the strip.
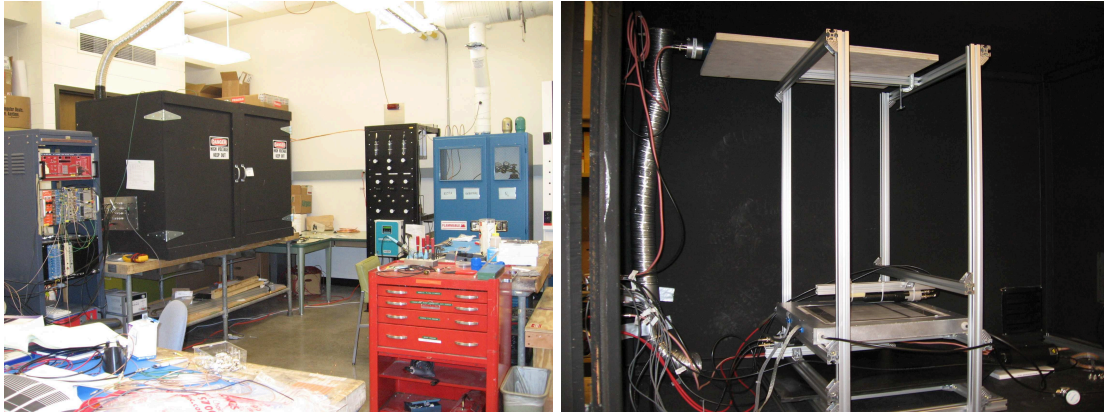
Figure 3.18: The figure on the left shows the entire set up of the test-stand. The figure on the right shows the inside of the high voltage box where the RPC is set up.

The paddle scintillator, positioned a few feet above the RPC, was used to test what effect particles coming in at horizontal angles had on the detector and to reduce any false coincidence rate. The hardware trigger was set up to include the paddle scintillator as well as the finger scintillators. Only events that triggered all three scintillators are now used. Placing the large paddle at the back of the box allowed us to veto a large contribution of the shower component which caused a high side tail on the cluster distribution.

Several tests were completed to understand the cluster width distribution of the detector and subsequently modify the setup to make the distribution as narrow as possible. The number of adjacent strips that fire each time a particle hits the detector is the cluster width. For example, if a particle hits the detector on the center strip and another adjacent strip shows a pulse below threshold (the RPC gives negative going pulses shown in Figure 3.19), then the cluster width is two. Quantifying the cluster width distribution is of critical importance for simulations and the final design of the strip layout forward trigger upgrade RPCs. An example cluster distribution with this configuration is shown Figure 3.20. As indicated by the small number of events with zero hit channels, the detector is $\sim 99\%$ efficient in this configuration. The efficiency scan shown in Figure 3.21 shows that we can reach a plateau at $\sim 9.3$ kV for a -4 mV threshold. This lower than expected for other facilities due to altitude of $\sim 5300$ ft in Boulder Colorado.

The Colorado group will continue to study the performance of the current chamber for various voltages, gas mixtures, strip widths, and other parameters. CU also plans to study a prototype using gas gaps from the group which will supply the production chambers.
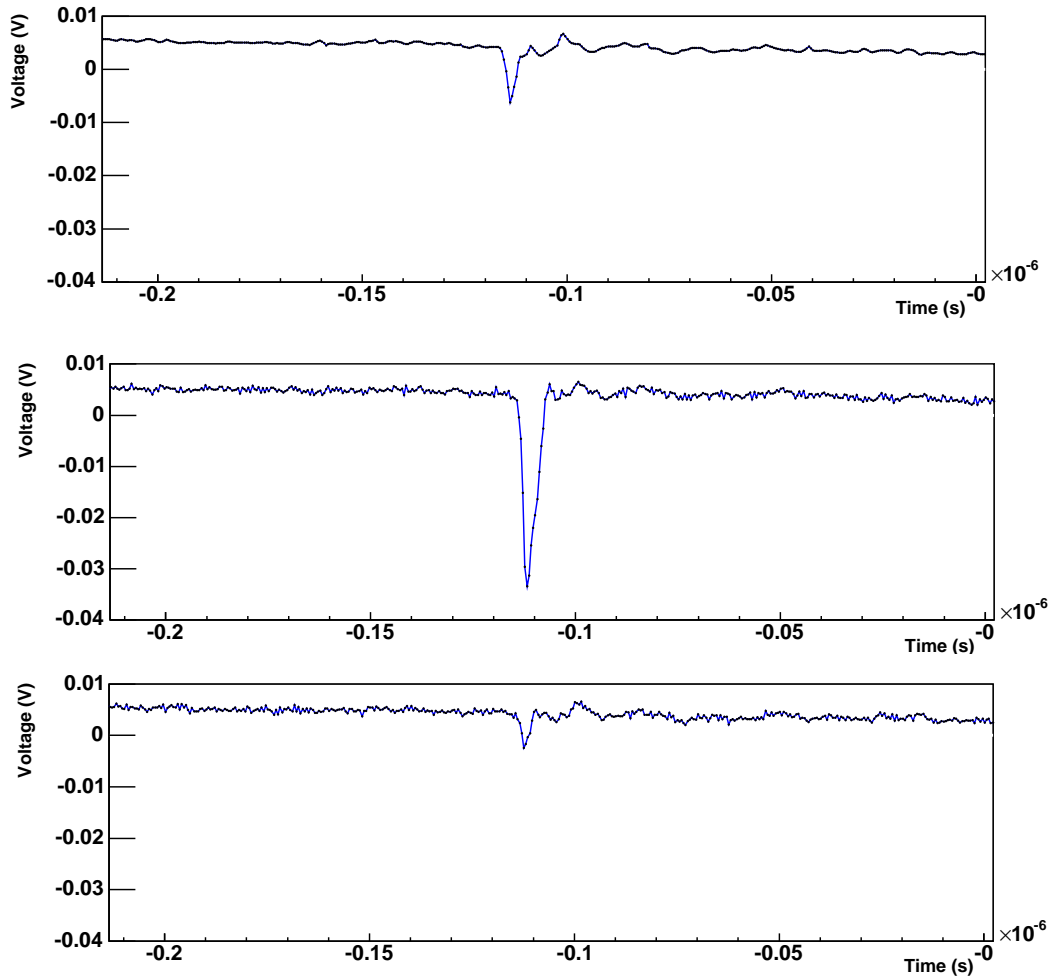
Figure 3.19: Example signals induced on the center and neighbor 0.5 cm terminated strips. Measurements with gas gaps manufactured at GSU. GSU gas gaps have been manufactured with the goal to acquire experience with RPC technology in general and are different from the CMS gas gaps received from Korea University.
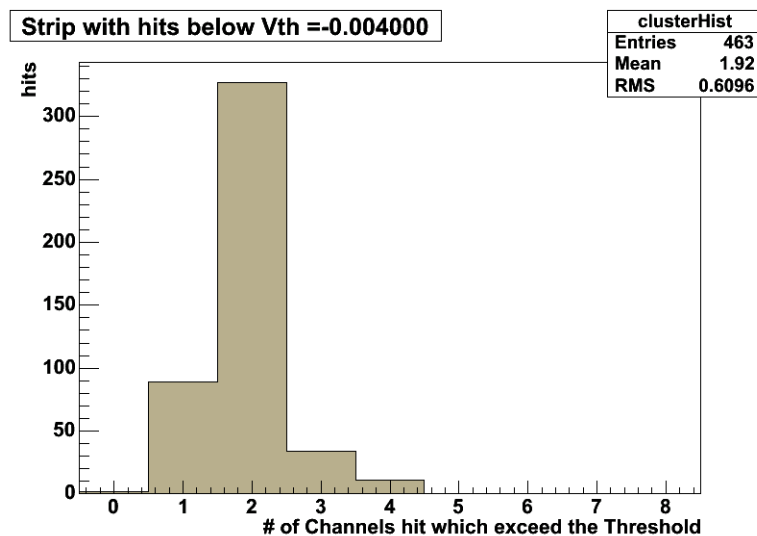
Figure 3.20: Cluster width distribution for 0.5 cm terminated strips from a three scintillator coincidence plus shower scintillator veto trigger. Measurements with gas gaps manufactured at GSU. GSU gas gaps have been manufactured with the goal to acquire experience with RPC technology in general and are different from the CMS gas gaps received from Korea University.
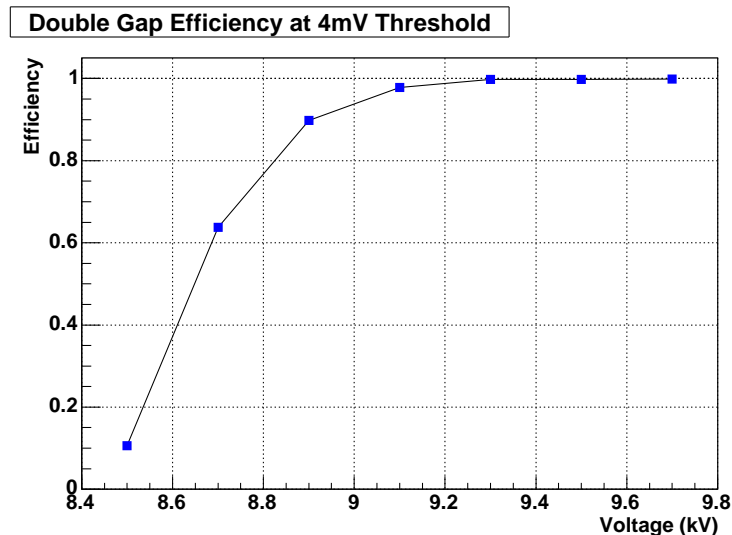


Figure 3.21: Efficiency scan for 0.5 cm terminated strips from a three scintillator coincidence plus shower scintillator veto trigger. Measurements with gas gaps manufactured at GSU. GSU gas gaps have been manufactured with the goal to acquire experience with RPC technology in general and are different from the CMS gas gaps received from Korea University.

### 3.2.5 RPC R&D Studies at UIUC

The goal of the RPC research and development is to characterize the efficiency, cluster size, timing resolution, position resolution, rate capability, and radiation hardness of the CMS RPCs. As this is done, we will gain experience with the operation and proper handling of the CMS RPCs. In order to gain more experience with the RPCs it was decided to first construct and test prototypes at UIUC and Georgia State University. In this section, we outline the UIUC setup and the results obtained thus far from the UIUC prototype.
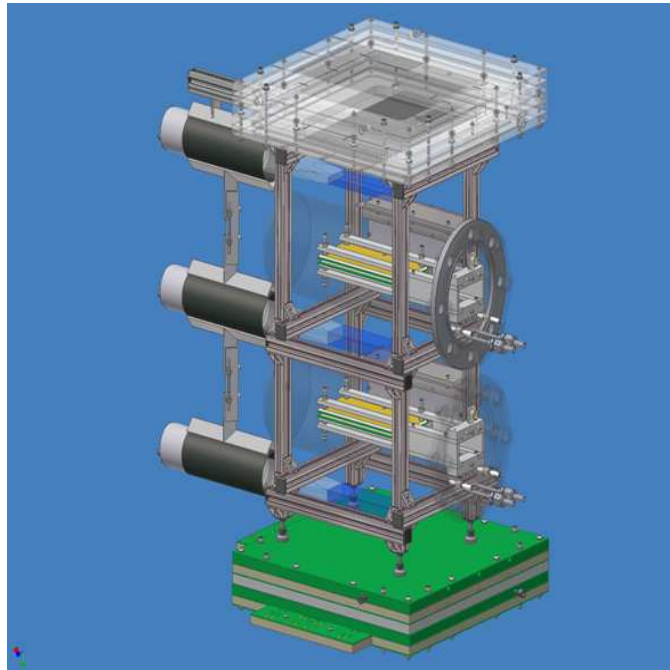


Figure 3.22: The UIUC RPC teststand.

The UIUC test-stand is shown in Figure 3.22. Sets of two $1 \times 4$ ft$^2$ scintillators, read on both ends with 4 inch photo multipliers, are placed above and below the test stand to create a trigger for muon events. As seen in the figure, the two UIUC RPCs are placed in gas cylinders near the middle of the teststand. Three $6 \times 18$ cm$^2$ scintillators located above and below each RPC cylinder are used for obtaining the timing resolution of the RPC. Above and below this RPCs and scintillators are sets of two single wire drift chambers which resolve the x and y coordinates and have a position resolution of approximately 0.1 cm. The square drift chambers have a sense wire in the middle of the chamber and a drift space of 20 cm. Because the sense wire is in the middle of the drift chambers, it is necessary to also have four $10 \times 20$ cm$^2$ scintillators (not shown in figure) to distinguish one half of the drift plane from the other half. The scintillators and

drift chamber signals are read out into NIMC discriminators and CAMAC TDCs.

The UIUC prototypes are double gap RPCs with a 2 mm gap spacing between the 2 mm bakelite plates. A PCB with 15 copper readout strips is sandwiched in between the bakelite plates and insulated from ground by a PET film. Each strips output signal is sent into an ADC channel. A second copy of the RPC signals is discriminated and sent to a TDC. The surfaces of the bakelite plates closest to the PCB are kept at ground while the surfaces farthest are set at a negative high voltage. The readout strips measure $6 \times 1$ cm$^2$ and are separated from one another by a spacing of 2 mm.The details of the RPC design are shown in Figure 3.23. A unique feature of the UIUC prototypes is that the RPC gas gaps are located in gas vessels. In this design it is not necessary to gas seal the gaps and changes to the gap configuration or read out plane can be made easily.
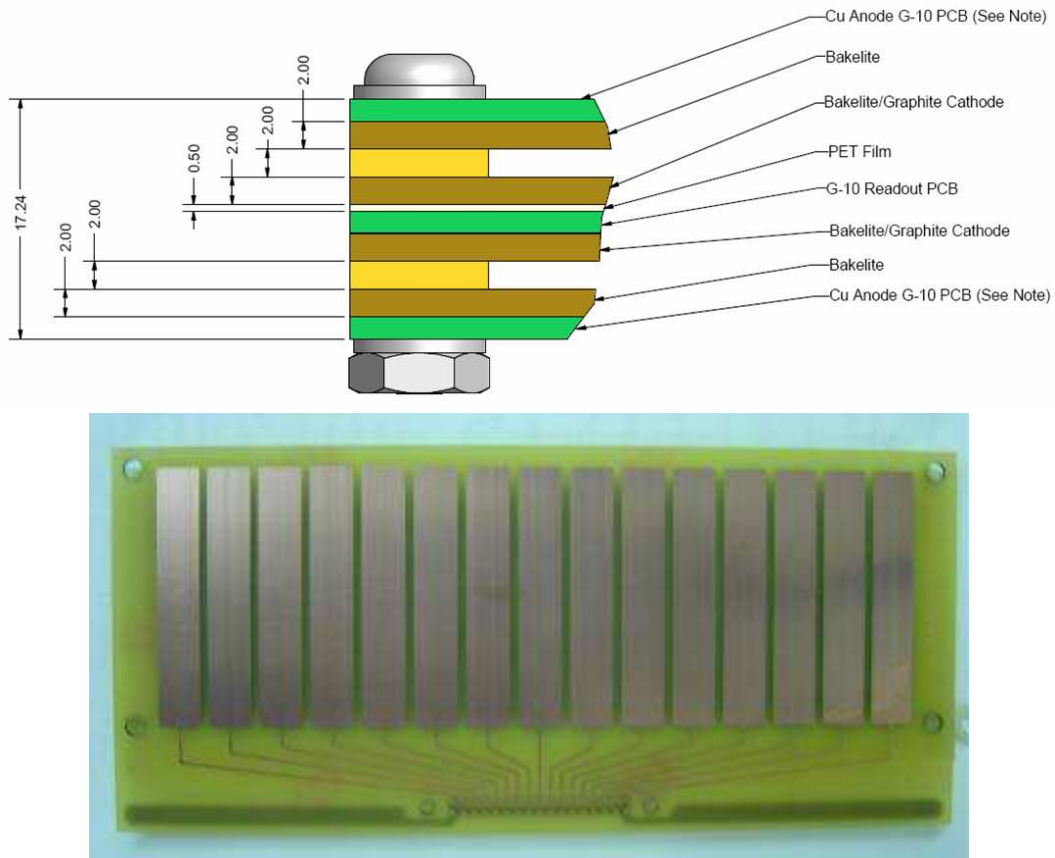


Figure 3.23: The UIUC RPC prototype design and the readout strip layout.

First results of cosmic ray tests of one UIUC prototype are shown in Figures 3.24 (a), (b) and 3.25 (a), (b). These are preliminary results as the test stand development is still in progress. The position resolution of the RPC was

found by subtracting an interpolated track from the drift chambers from the RPC position and fitting a Gaussian to the resulting distribution. There are three methods by which the RPC positions were calculated. In the TDC average method, the average position of all strips that have a pulse above the discriminator threshold is the calculated position of the muon. This method works well for small cluster sizes (avalanche mode), but if the cluster size is large (streamer mode), this method will fail. This failure can be seen in Figure 3.24 (a) at -13 kV. In the ADC Gaussian method, a Gaussian is fit to the ADC charge spectrum of the strips that were hit. The mean of this fit is the position. In the ADC maximum method, the maximum of the ADC charge spectrum is the position.



(a)                                                    (b)
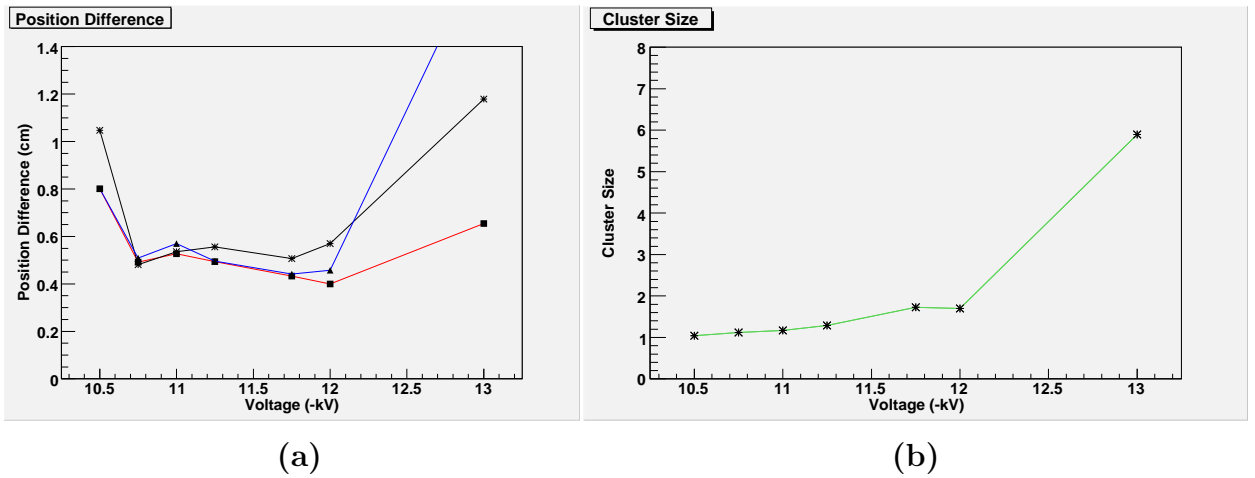
Figure 3.24: (a) RPC Position Resolution: The red line with squares is the ADC Gaussian Method, the blue line with triangles is the TDC average method, the black line with asterisks is the ADC maximum method. (b) RPC Cluster Size. Measurements with bakelite gaps manufactured at UIUC. UIUC bakelite gaps have been manufactured with the aim to acquire experience with RPC technology in general and are different from the CMS gas gaps received from Korea University.

One can see that the Gaussian and TDC methods both work well for small cluster sizes, as the position resolution is at or under 0.5 cm (except the first data point) when the cluster size is below 2. The Gaussian method continues to produce under 1 cm resolution even at a large cluster size, where the TDC method fails. This method is the best of the three at all high voltages. The ADC method is the least precise at small cluster sizes, but is better than the TDC method at large cluster sizes. All three methods yield resolutions well under 1 cm when the cluster size is small, which is the desired goal of the RPCs for PHENIX. Using the tracking of the test stand, we have developed an event display to show cosmic ray muon tracks as they pass through the teststand. This is a very powerful cross check that our tracking is functioning properly. Figure 3.26 shows thirty cosmic
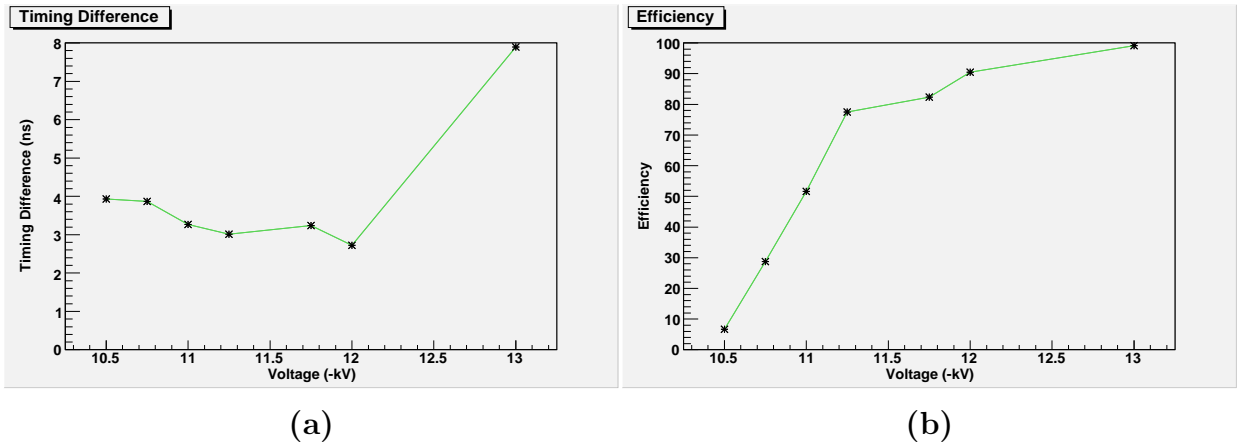
Figure 3.25: (a) RPC Timing Resolution. (b) RPC Efficiency. Measurements with bakelite gaps manufactured at UIUC. UIUC bakelite gaps have been manufactured with the aim to acquire experience with RPC technology in general and are different from the CMS gas gaps received from Korea University.

ray muon tracks passing through our drift chambers, scintillators, and the RPC.

Figure 3.24 (b) shows the average cluster size of the RPC as a function of high voltage. The cluster size is simply the number of strips that register a hit via the TDC in an event. The small average cluster sizes seen at -12 kV and below indicate
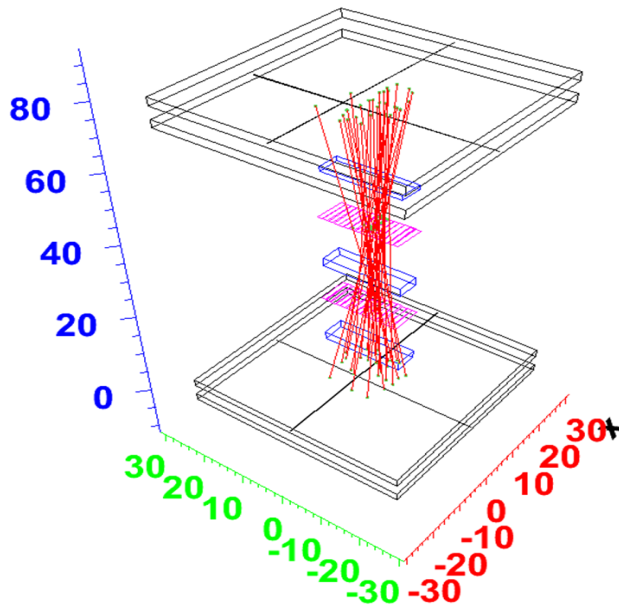


Figure 3.26: The Event Display.

63

that the RPC is running in avalanche mode. At -13 kV, the average cluster size is much larger and indicates that the RPC is operating in streamer mode. The data shown are only for the central eleven strips, as the two outermost strips one each side were very noisy. Figure 3.25 (a) shows that the timing resolution of the UIUC prototype stays between 2.7-4.0 ns for all high voltages. Finally, Figure 3.25 (b) shows the efficiency of the RPC as a function of high voltage. The efficiency of the RPC is a very early result, as the current maximum pre-amplifier gains are not sufficient and may cause a loss in efficiency. It seems that the plateau may be starting around -11.25 kV, but this remains uncertain until the pre-amplifier problem is rectified.

In conclusion, the UIUC RPC test stand has the capability to characterize the position resolution, timing resolution, cluster size, and efficiency of a RPC. The rate capability of the UIUC RPCs has not yet been measured. In order to do this, we plan to use $^{55}$Fe sources. Additionally, it is planned to use GIF at CERN to study radiation hardness and the MT6 test beam at FNAL to obtain rate capability measurements.

## 3.2.6   R&D Prototype Plans

This section provides a summary of the sequence of RPC prototypes for the muon trigger upgrade project in PHENIX. The prototype R&D which has been carried out so far is presented in sections 3.2.4 and 3.2.5 of this document.

High rate bakelite RPCs for trigger applications have been developed for the CMS and ATLAS experiments where a dedicated momentum sensitive trigger spectrometer is required for the fast identification of high momentum muons over very large areas. Bakelite RPCs are a very cost efficient detector solution but at the same time a highly delicate technology with significant challenges to master in the optimization of design parameters, the choice of materials and operation conditions. In order to minimize the technology risks we have chosen to adapt exactly the existing CMS RPC design as it is used for the CMS endcap muon trigger RPCs. We collaborate with the CMS and PHENIX groups at Korea University in Seoul which have agreed to manufacture the PHENIX RPC gaps using the identical CMS procedures and gap manufacturing facility at Korea University. In addition we work with our PHENIX colleagues at CIAE and PKU in Beijing. They have assumed responsibility for the RPC detector module construction and assembly and will collaborate closely with their CMS colleagues at PKU who carry out the identical task for the CMS trigger RPCs. As a consequence of this strategy the goal of the PHENIX muon trigger RPC R&D is not the development of new detector technology but aims to build a broad and solid knowledge base for the use of high rate bakelite RPCs in PHENIX. There has been no previous experience with fast trigger RPCs in PHENIX.

PHENIX bakelite RPC prototype tests have been carried out in the PHENIX

Table 3.6: List of bakelite RPC prototypes used in the preparation of the conceptual muon trigger design. All prototypes have been built by PHENIX groups with the aim to develop in-house expertise in CMS bakelite RPC technology. The prototype tests also have been used to determine the cluster size as critical input to the trigger performance calculations. Finally an important focus is to reach stability in the detector operation with low dark currents.

| Manuf. | # of Prtyps | Test Location | Important Results |
|---|---|---|---|
| PKU | 2 | BNL, Boulder, CIAE | beam background timing |
| GSU | 1 | GSU | $1^{st}$ gen., stability |
| GSU | 2 | GSU | $2^{nd}$ gen., signal shapes, stability |
| GSU | 5 | GSU, Boulder, UIUC | $3^{rd}$ gen, eff., cluster size, stab. |
| GSU | 3 | GSU, Boulder, UIUC | in preparation, stability |
| UIUC | 3 | UIUC | stability, pos. res., pos. dep. Eff. |

IR with RHIC beams and with cosmic rays at BNL, at CIAE, at GSU in Atlanta, at the University of Colorado in Boulder and at UIUC in Urbana. The beam studies at BNL have produced a survey of the timing structure of beam related backgrounds in PHENIX. The work at GSU has focused on the actual construction of RPC prototypes and the relation between the choice of design parameters, materials and construction procedures on one side and detector performance and operation on the other side. A $3^{rd}$ generation GSU RPC prototype is shown in Figure 3.27. In the future GSU will take leadership in setting up the Q&A test stand in the RPC assembly facility at BNL.

The Boulder group has carried out detailed measurements of prototype efficiencies and cluster sizes for an early RPC prototype and a $3^{rd}$ generation prototype from GSU. The Boulder results have been used as input in the muon trigger simulations. For the future the University of Colorado group plans a performance survey of prototypes based on gas gaps from Korea University and plans to evaluate front end electronic prototypes from Nevis.

The RPC test stand in Urbana includes position sensitive drift chambers and has been used to study the RPC position resolution and position dependent efficiencies. The group has studied three prototypes which have been built at Urbana as well as a $3^{rd}$ generation prototype obtained from GSU. In the future the group plans to investigate the rate capability of RPC prototypes with radioactive sources at UIUC and the test beam at FNAL. It is further planned to test the radiation hardness of PHENIX RPC prototypes at the Gamma Irradiation Facility (GIF) at CERN. The layout of the cosmic ray test stand and a cut view of the UIUC prototype are shown in Figure 3.28. An exploratory result on position sensitive
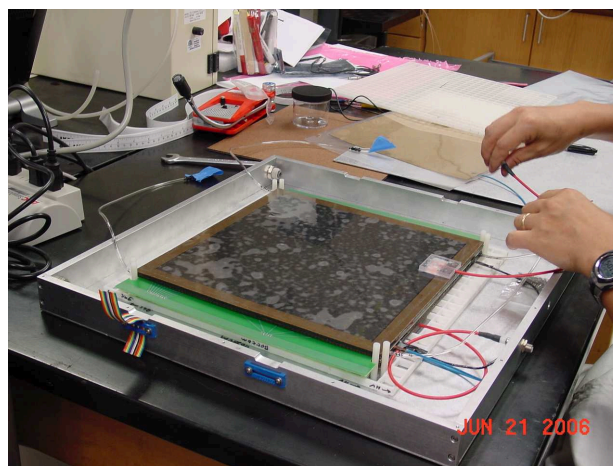
Figure 3.27: Assembly of a $3^{rd}$ generation prototype at GSU. The active area of the 2-gap bakelite RPC is $30 \times 30$ cm$^2$. The bakelite used in the chamber was acquired from PAN-PLA the Italian CMS bakelite vendor. GSU has provided these prototypes to Colorado, UIUC and Nevis.
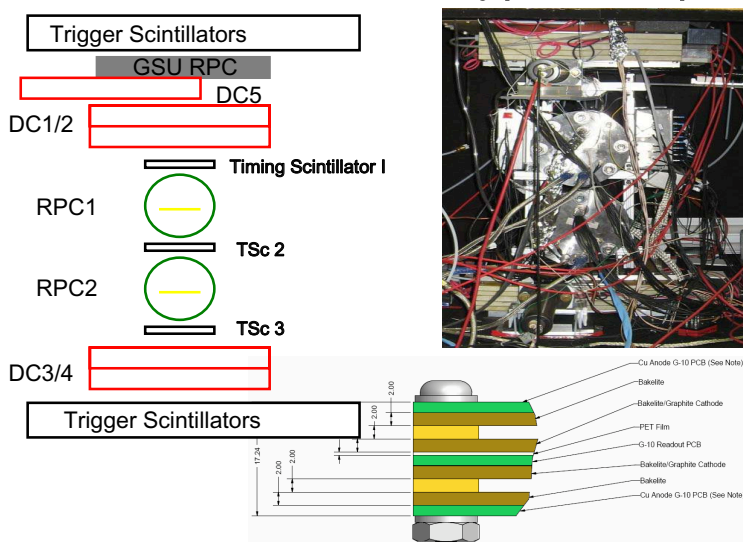


Figure 3.28: Shown is the layout of the cosmic ray test stand in Urbana together with a photograph of the setup and a cut view of a UIUC prototype. 5 drift chamber planes give position resolution, 11 scintillators provide trigger, timing and assistance with resolution of the left right ambiguity in the drift chamber tracking. The RPC prototype is designed to be easily modifiable with alternate signal strip planes or different choices for the resistive plate material.

efficiencies is shown in Figure 3.29. Detailed results of the R&D can be found in sections 3.2.4 and 3.2.5..
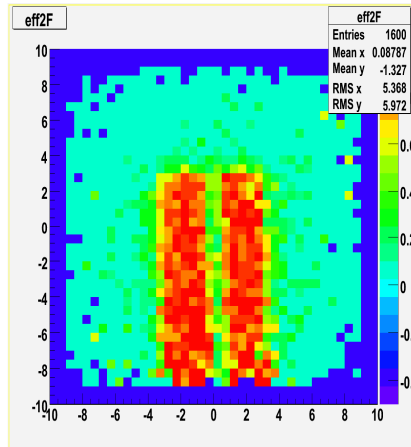


Figure 3.29: The figure shows position-dependent detection efficiencies for cosmic rays in one of the UIUC prototypes at a gap high voltage of 11 kV. The rectangular contours of the RPC are visible as the red area. The color code indicates high efficiencies with red. The apparent low efficiency in the center of the RPC is presently not understood. Possible solutions include an artifacts in the drift chamber tracking that are caused by high background noise levels in the laboratory. Measurements with bakelite gaps manufactured at UIUC. UIUC bakelite gaps have been manufactured with the aim to acquire experience with RPC technology in general and are different from the CMS gas gaps received from Korea University.

In the reminder of this section we will discuss the future prototype plans for the muon trigger upgrade:

- **Prototype generation A.**
  3 prototypes will be produced at GSU based on 8 RPC gas gaps manufactured at Korea University with the CMS gas gap production line. 2 prototypes will have oiled gas gaps and one prototype will be generated without oiled gas Gaps. The 8 gaps from Korea have arrived at GSU on January 24th 2007 and RPC prototypes have been manufactured based on the Korean gas gaps. We plan detailed studies of the detector performance with and without oil at GSU, Colorado and UIUC. The detectors will be also used for the front end electronics development at Nevis. Figure 3.30 shows the 8 gaps from Korea on arrival in Atlanta. Shipping and import procedures from Korea to the US were surprisingly smooth and efficient.

Figure 3.30: Shown are eight RPC gaps on arrival from Korea University at GSU in Atlanta. 5 gaps have been produced with the standard CMS oil coating; 3 gaps without and detailed comparisons of the performance of the different detector gaps will be carried out.

- **Prototype generation B.**
  We plan to acquire a full CMS detector module including the front end electronics and all artwork installed. The study of the chamber will further enhance our understanding of the CMS RPC technology and will provide important input to the RPC detector design and the detector integration in PHENIX. We plan to acquire a CMS detector module by July 1st 2007.

- **Prototype generation C.**
  One prototype C module will be built using the BNL assembly facility using all parts for the detector module box from the CIAE/PKU production. For the prototype construction we plan to use the new certified CMS bakelite vendor. We aim to complete the prototype C on September 1st 2007. The detector will be studied first at BNL, Colorado and UIUC and then at the MT6 test beam line at Fermi National Accelerator Laboratory starting from January 2008. It is planned to place prototype C parasitically into the halo of the MT6 test beam and exercise the longterm operation of the detector. In a last step we plan to bring prototype C to CERN for radiation hardness studies at the Gamma Irradiation Facility (GIF) there.

- **Prototype generation D.**
  Prototype D will be the first complete half octant build using the final choice of detector materials and detector assembly procedures and using the assembly facility at BNL. The detector will be used to fully develop

the half octant integration including all services to the chamber. We plan to complete prototype D by February 1st 2008. The half octant will be used to test the Q&A facility at BNL and to develop all jigs and holding structures needed for RPC2 and RPC3 half octant installation in PHENIX. Later single detector modules of the half octant may be taken to the MT6 test beam line at FNAL and the GIF facility at CERN.

## 3.3    RPC-Front End Electronics (FEEs)

The front-end electronics are designed to measure the arrival time of the RPC signal with respect to the RHIC crossing beam clock. Summary information is sent to the Level 1 (L1) trigger system to generate the L1 trigger. The front-end electronics (FEE) are split into two parts, on-chamber preamp/discriminators and front-end modules (FEM). The front-end modules will be mounted outside of the detector.

### 3.3.1    Amplifier Discriminator Board

The RPC chamber has 11 different strip sizes ranging from 11.4 mm by 141 mm to 64.6 mm by 554.2 mm. We have used a simulation to estimate the impedance and capacitance of the strips. We find that the smallest strip has an impedance of about 46 $\Omega$s and a capacitance of 16.0 pf. The largest strip has 9.7 $\Omega$s of impedance and 286 pf of capacitance. The strip width is always much smaller than length. The propagation time in the longest strip is around 5-6 ns and the rise time of the pulse is comparable to the strip's propagation. Therefore, the long strips should be viewed as a transmission line.
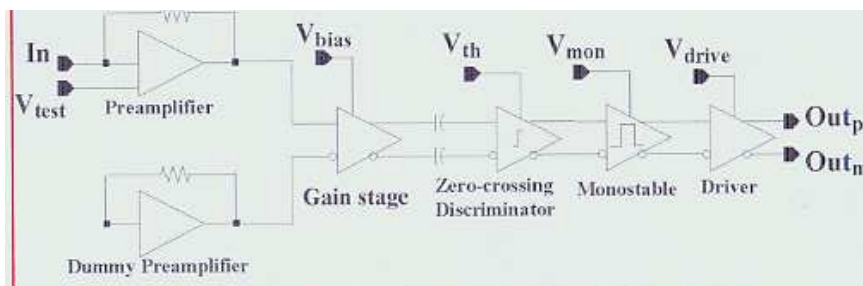


Figure 3.31: Block diagram of the Bari CMS chip.

The CMS RPC group in Bari, Italy has built a preamp/discriminator chip using the AMS 0.8 um BiCMOS process [82]. The chip consists of a preamplifier, additional gain stage, zero crossing discriminator, a monostable circuit and an output driver. The chip is powered with + 5 V and has a power consumption of

69

45 mW per channel. We have evaluated the chip including a meeting with the Bari group and have concluded that using this chip to readout our RPC detector is likely the best solution. However, we would like to implement a full simulation of the chip before making a final decision.
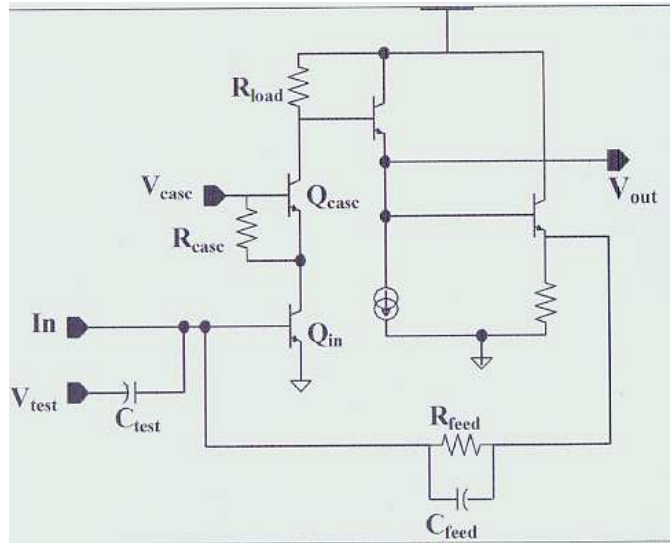


Figure 3.32: Preamplifier diagram of CMS chip.

The preamplifier diagram of the CMS chip is shown in Figure 3.32. The input impedance of the preamp is 15 $\Omega$s to match the 4 cm strip size of the CMS RPC detector. The calculated ENC is about 1.7 fC for the case of a 15 $\Omega$s impedance. The expected charge from the RPC ranges from 20 pC to 20 fC. The block diagram of zero crossing discriminator with a 4 ns time constant CR network is shown in Figure 3.33. The monostable circuit which follows gives the discriminator an output with a width of about 100 ns. The output of the chip is differential LVDS and the power consumption of the chip is 45 mw/per channel. The thresholds are brought out to the packaged pins. Based on the CMS RPC experience, a 100 fC threshold will suffer no efficiency loss. The chip timing resolution is less than 0.6 ns for a signal of less than 0.5 pC. For larger signals the timing resolution becomes a few ns. The chip has test pulse inputs and each chip contains 8 channels.

CMS has built two different readout boards, one with 16 channels and the other with 32 channels. The size of the boards are similar, with the 32 channel being $230 \times 105$ mm$^2$. Figure 3.34 shows a picture of the readout board. There is a cable adapter board interfacing the coaxial cables from the detector strips to the amplifier/discriminator boards. The output cable is envisioned to be standard twisted flat cable. The length will be between 10 and 20 meters depending on the location of the FEM crates. We are exploring the possibility of using the CMS 32 channel readout boards along with their cable adapters. Bari gave us a 16

channel board and we will receive four 32 channel boards as part of a joint order with CMS. We are working with Flavio Loddo from the CMS Bari group on the logistic issue of re-fabricating the CMS RPC readout chip. We have heard from Europractice that it is possible to fabricate the chip, but they will need to make new masks in the new 8 inch fab, as the old 4 inch fab is closed. The minimum order is 2 wafers, or about 5000 chips and the lead-time is about 3 months. The price is 50,000 Euro plus packaging cost.
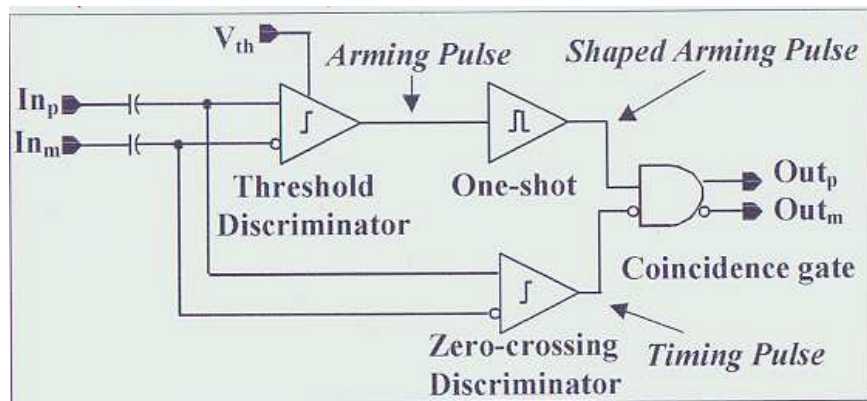


Figure 3.33: Block diagram of zero crossing discriminator with a 4 ns time constant CR network.
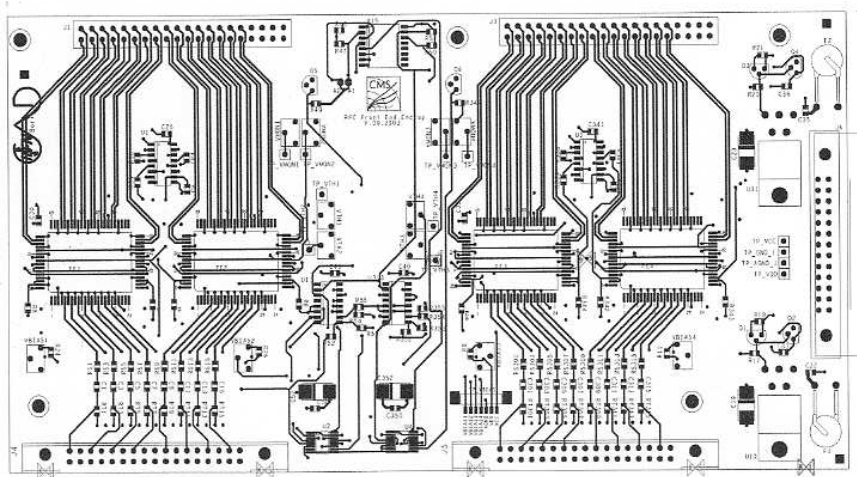


Figure 3.34: Picture of the readout board.

## 3.3.2  Digital Backend Electronics

The goal of the front-end module (FEM) is to determine the arrival time of the discriminated signal pulse relative to the beam clock. In order for the pulse to fall into a predetermined time window, the hit information is sent to the L1 system every beam clock. The resolution needed for the L1 trigger window is around 15ns. Once the L1 trigger decision is received, we will send the triggered event data to the Data Collection Modules (DCM). The block diagram of the FEM is shown in Figure 3.35.
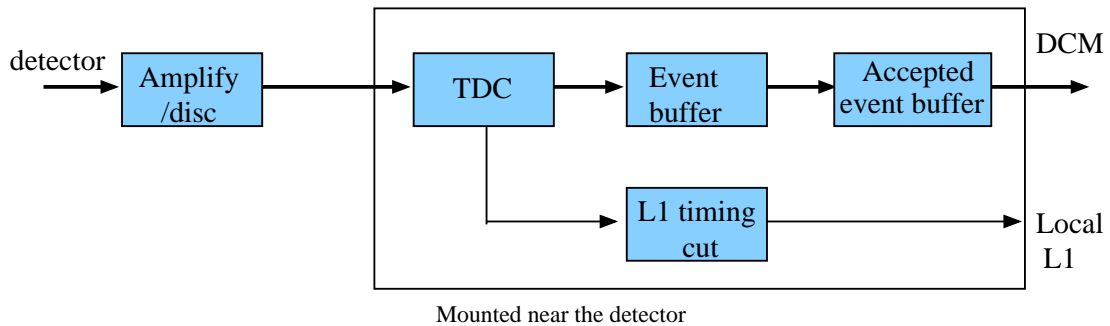


Figure 3.35: Block diagram of the FEM.

The project is in the early stage of the design. The idea is to receive 4 times the RHIC beam clock from the Granule Timing Module (GTM). A 32 times beam clock, 320 MHz, can be generated locally and serve as a timing digitizer clock. Based on this clock, the time digital converter (TDC) bin size will be 3.3 ns. A loadable constant table could be use to correct the TDC offset every beam clock.

A proof of principle FPGA code has been written. The code contains the necessary phase lock loop (PLL), 40 beam clock delay, five L1 triggered events buffer, time window cut for the L1 trigger data and data format for 48 input channels. The device we choose is the ALTERA Cyclone class FPGA. The FPGA can deal with the PLL frequency without any problem in the simulator. We are exploring the possibility of cutting the timing bin size in half inside the FPGA.

A preliminary design of the FEM has not been done yet. The packing density of the FEM will be determined by the cable. If we use the standard twisted flat cable between FEM and discriminator board, we can pack 64 channels into a 6U high VME style board. The strip data between station1a and 1b data are .OR.ed together for L1. The even and odd ring's data are .OR.ed together in stations 2 and 3 before sending to L1 as a trigger primitive. Each module will generate 32 bits of .Yes/No. data to L1 on every beam crossing. An interface module is needed to collect FEM generated L1 trigger information into the L1 system and to collect all L1 triggered data from FEMs to be sent to the DCM. Conceptually each interface module is needed for every 8 FEMs. Serializer/deserializer chip sets

Table 3.7: List of the number of RPC channels, FEMs, interface modules, and RPC FEM crates needed for the RPC systems.

| Station | 1a+1b | 2 | 3 | total |
|---|---|---|---|---|
| Channels | 3072 | 3848 | 2872 | 9792 |
| FEM | 48 | 64 | 48 | 190 |
| Interface | 6 | 8 | 6 | 20 |
| Crates | 3 | 4 | 3 | 10 |

can be used for sending data from FEM to the interface module. The L1 triggered event data from the FEM will be sent to the interface module by a token passing method. The data to the DCM and L1 system will be sent via optical cable with 8b/10 encoding. The DCM data will be running at 1.6 Gbits/sec and the L1 fiber will be running at 3.4 Gbits/sec. One or two separate slow control modules per RPC station are needed to interface with the GTM and PHENIX slow control system. Based on this summary, Table 3.7 give a list of the number of various components needed for the systems.

### 3.3.3 R&D Plans

The most important item on the electronics R&D is to determine how to connect the chamber signal to the preamp/discriminator board. Issues regarding the strip termination, grounding, signal cable type and the length between the strips and amplifiers need to simulated and understood. This not only effects the electronics design, but also mechanical issues. Once the simulation is understood, we will compare with measurements that we will make from the detector.

## 3.4 Muon Tracker FEE Upgrade

### 3.4.1 Overview Requirements and Specifications

The muon tracking front-end-electronics (FEE) upgrade is proposed to provide hit information as primitives for the Level-1 trigger. When the hit information from MuTr and RPCs are combined, it will provide sagitta information which is directly sensitive to the particle momentum. Since most of the charged tracks that satisfy the current LVL-1 trigger in the Muon Arm based on the MuID subsystem, are the low momentum particles, typically $\sim 2$ GeV/$c$, we can expect large improvements in the rejection factor.

Indeed, simulation studies have shown that a muon trigger utilizing the cathode information would provide a rejection factor of more than 20,000, which is

more than enough to fit into the current data acquisition band width.

To realize such a trigger, the cathode signal has to be split into two streams: one for the current FEE for slow and precise readout ot the charge induced on the cathode, the other for a fast, but rough readout. Such an additional readout stream should not affect the current slow and precise readout, especially with respect to the noise performance, because the position resolution is determined from the noise in the readout. While the design value of the chamber position resolution is 100 $\mu$m, current which can be achieved by the noise level as low as 1% of the most probable value (MPV) of the charge induced on the cathode strips. Therefore, the first requirement for the additional readout should be not to introduce significant noise into the existing FEE.
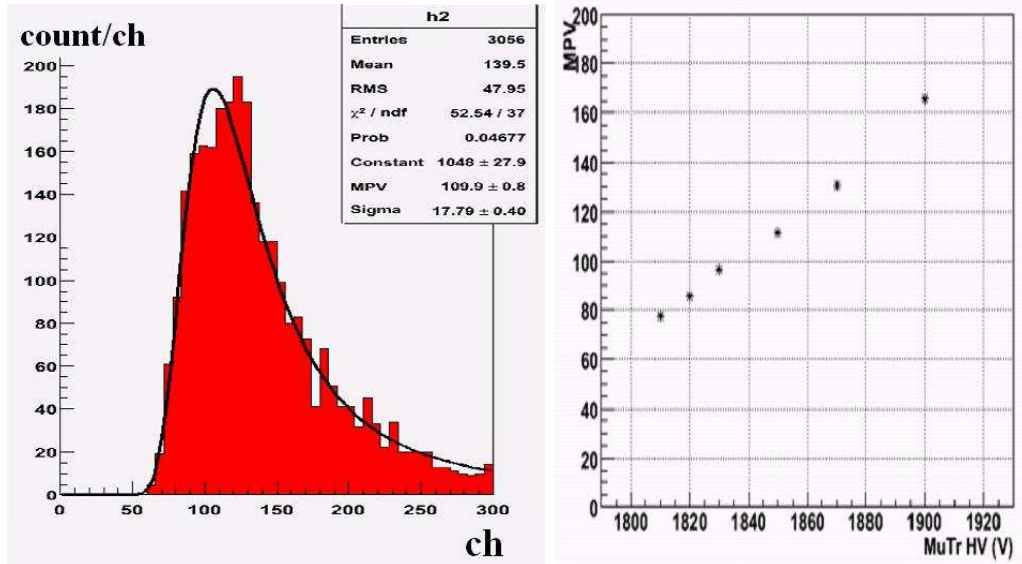


Figure 3.36: *left*: Charge distribution of the Muon Tracking Chamber.The distribution is fit to Landau distribution to extract the most probable value, MPV. *right*: The MPV of the charger distribution versus high voltage applied to the Muon Tracking Chamber.

A slight increase in the noise level can be compensated by the additional high voltage applied to the Muon Tracking chamber. As can be seen in Figure 3.36, the gain in the chamber would be increased with the high voltage applied to the chamber; with an additional voltage of 50 V, we can extract ~30% more charge, therefore the noise increase of ~30% can be fully compensated. Since this level of HV increase can be acceptable in the Muon Tracking chambers, we can set the goal of the noise performance to be ≤30% increase in the noise level.

Another requirement for the new trigger is its timing resolution. Ideally the timing resolution of the hit information should be better than the time interval

of the beam crossings, which is 106 nsec. As mentioned in the previous sections, we would use more than two stations of Muon Tracking chambers and the hit information will be combined to issue the trigger signal. Therefore the timing resolution from a single chamber can be somewhat worse *e.g.* 140 nsec.

Since the anode wire spacing is 1 cm, the drift time alone would contribute significantly to the timing resolution by $\sim$ 100 nsec. We cannot allow further degradation in the timing resolution in the cathode hit information. We have decided to employ a constant fraction discriminator (CFD) to determine the timing of the hit information. As shown in Figure 3.37, the CFD can provide stable timing information independently from the input pulse height.

To summarize the requirements for the additional readout electronics;

- not to introduce significant noise more than 30%.

- to provide a hit information with timing resolution of 150 nsec or better.
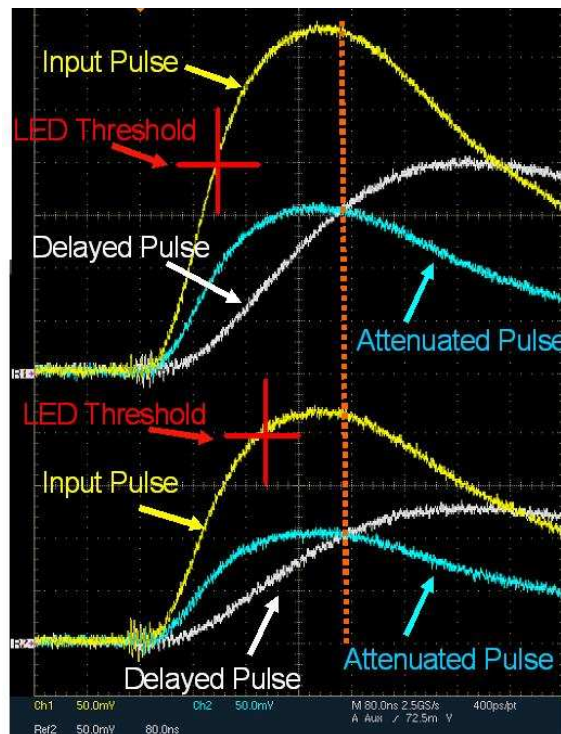


Figure 3.37: Sample of input, delayed and attenuated pulses. The crossing point of delayed and attenuated pulses does not depend on the input pulse height.

## 3.4.2 Amplifier Discriminator Board

The main function of the Amplifier Discriminator board (AD board) is to provide the strip hit information of the MuTr chamber. The outputs of AD board are sent to the transmitter board for further processing of the trigger decision.

Currently, the signal of the MuTr chamber is read out with Front End Electronics (FEE) which are designed to precisely measure the amount of charge induced on the strips. These data are used to measure the passage point of the particle by offline analysis. 100 $\mu$m position resolution is the design value. A 1% noise level for a typical charge is required to achieve this resolution..

To get the strip hit information at the online level, we propose to split the raw signal line from the chamber as shown in Figure 3.38. One goes to the Cathode PreAmplifier (CPA) on the current FEE as before and the other one connects to the AD board to provide the strip hit information.

The AD board manipulates 64 channels on a 6U size card and consists of op-amplifiers and comparators. Figure 3.39 shows the prototype of the AD board. The charge flows into AD board, is amplified with the gain of 10 mV/fC and shaped. Then the signal is discriminated to make one bit information. The 64 channel LVDS outputs are sent to a transmitter board which serializes strip hit information and transmits with optical cable.

The splitting ratio of the charge can be controlled by adding the capacitor $C_{split}$ shown in Figure 3.38. The ratio of the charge that flows into the FEE and the AD board equals the ratio of the CPA effective capacitance ($\sim$900 pF) and $C_{split}$. The typical amount of the induced charge is 100 fC. Therefore, if we choose 100 pF as $C_{split}$, the expected typical charge that flows into the AD board is 10 fC. Quite a low noise level should be achieved on the FEE to produce the required position resolution so using only a small fraction of the raw signal can be allowed. Moreover, adding the $C_{split}$ means increasing the load capacitance and results in a worse noise level. However, we need enough charge for the AD board to create an efficient trigger. In view of these factors, we should determine the $C_{split}$ value with extreme caution.

In the discriminator part, we use a cable-less Constant Fraction Discriminator (CFD), which is modeled after the MuID readout system, which we call pseudo CFD, to minimize the time jitter due to the pulse height variation. The fact that the pseudo CFD technique needs no delay cable helps us with respect to the space and channel density. We also use a Leading Edge Discriminator (LED) whose threshold voltage is programmable for every channel. By requiring the logical AND of LED and the pseudo CFD, the AD board is resistant to noise and the timing of the outputs is well defined.
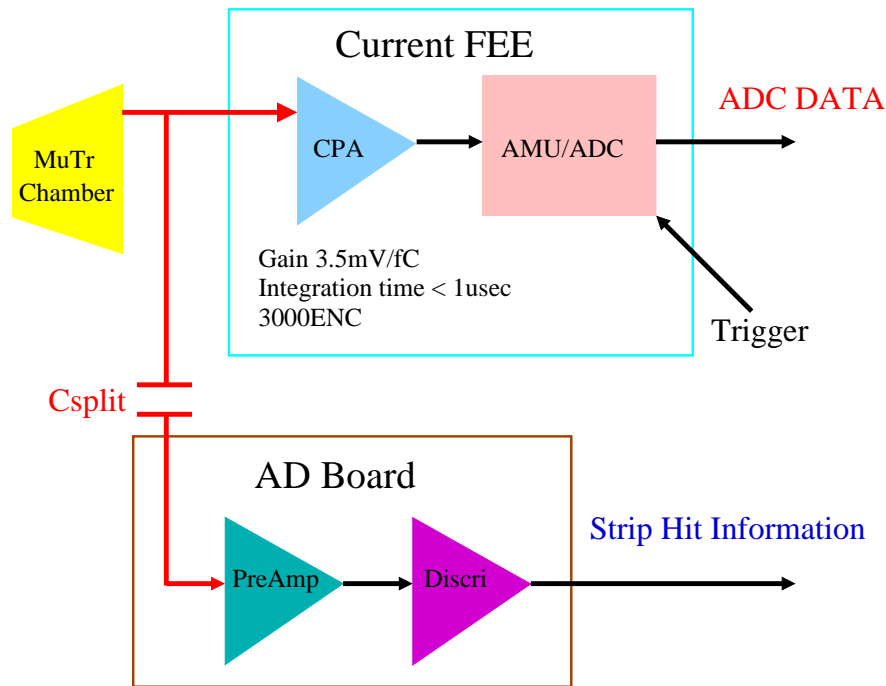
Figure 3.38: The new configuration of chamber readout.

### 3.4.3 Data-Transmitter Receiver

Figure 3.40 represents a brief diagram of a transmitter board. The board will be placed near the AD(Amplifier Discriminator) board. It receives parallel 64-bit outputs from the AD-board and serializes them. Then it transmits serialized data to the counting house.

Figure 3.41 shows the logic of a FPGA placed on a transmitter board. This data-format is necessary because TLK, which is a serialize&deserialize device, has only 16-pins to use as input. Moreover, an asynchronous FIFO is necessary because the beam clock has so much jitter that it can not be used for TLK. Since the beam clock counter (16 bits) and carrier extend(16 bits) are added to the original 64-bit data inside the FPGA, the data transmitting rate would be 960 Mbps.

In the counting house, the receiver&merger board will be placed to receive serialized data and merge them into octant information of the MuTr. Figure 3.42 is a block diagram of the receiver&merger board. As shown in Figure 3.42, it receives serialized data from some transmitter boards. Then it merges data and transmits them to the LL1 board.
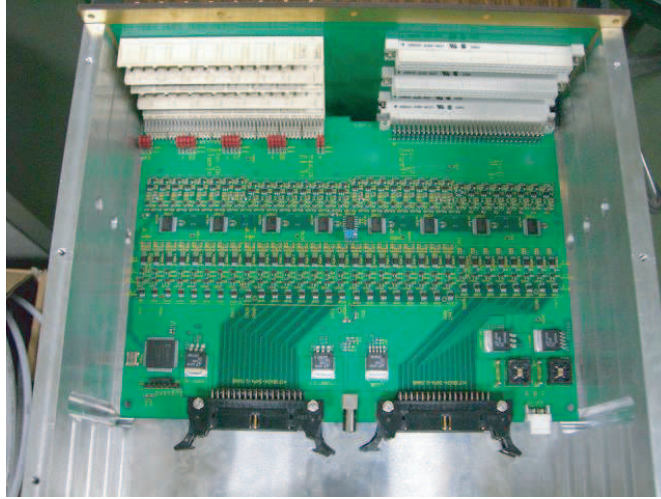
Figure 3.39: Prototype AD board.
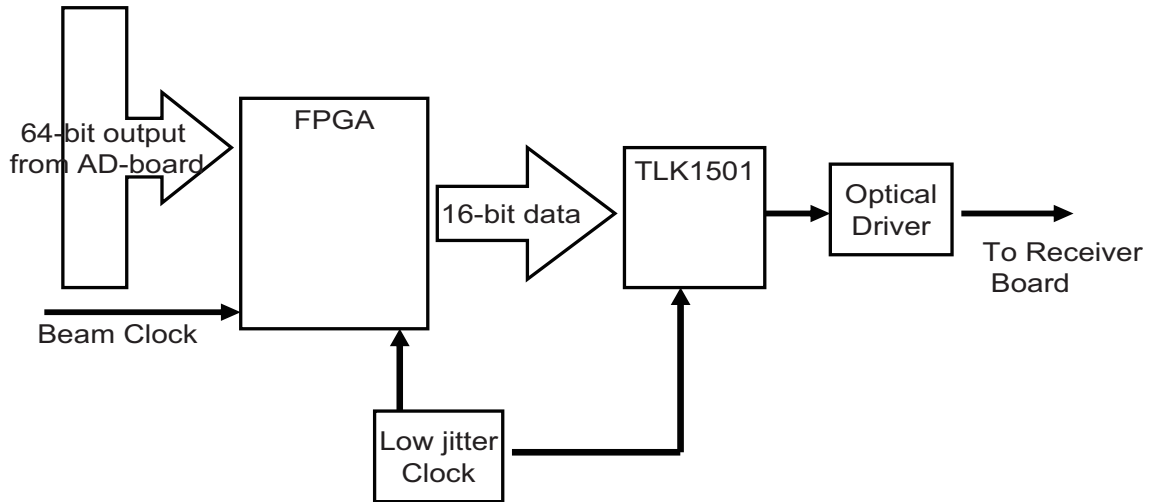


Figure 3.40: Block diagram of data transmitter board.

### 3.4.4 R&D Studies

**R&D Studies at Kyoto**

The existing FEE of the MuTr chamber is well commissioned so we proposed to split the raw signal from the chamber to FEE and AD board. We acquire the data for the charge induced on the strips using the FEE as before and extract the strip hit information by the AD board. This configuration prevents us from changing the whole readout system and helps us in terms of cost.
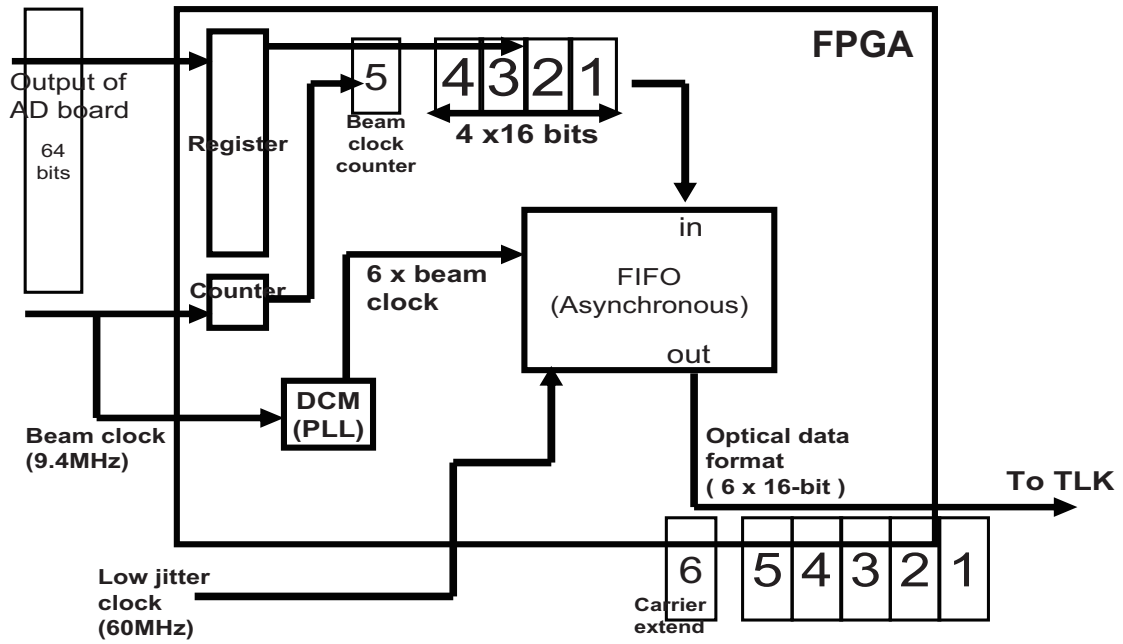
Figure 3.41: Brief FPGA logic of transmitter board.
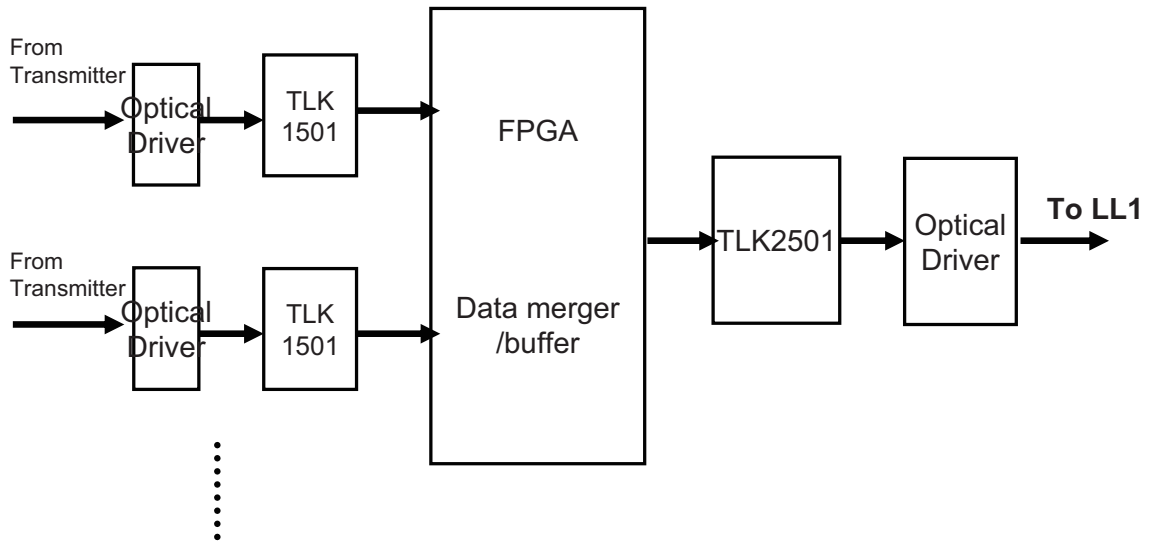


Figure 3.42: Block diagram of data receiver&merger board.

The one of the key points on the development of AD the board is how to split the raw signal with a constant fraction. We need to keep the linearity of the FEE output for the position resolution. It can be realized by putting the capacitor $C_{split}$ in front of the preamplifier on the AD board as shown in Figure 3.38. Seen from upstream, the charge sensitive amplifier seems to be a large capacitor in the high frequency region. So we can control the split ratio by the value of $C_{split}$. We confirmed it with a one channel test board, and measured the effective capacitance of the CPA on the FEE to be about 900 pF.

We produced a prototype AD board based on these results which has 64 channels on a 6U size card. We selected 100 pF as $C_{split}$ for this prototype and expect 10% of the raw signal for the AD board.

**Beam Tests with 600 MeV electrons**

To evaluate the prototype AD board, we conducted an experiment with a duplicate of a MuTr chamber exposed to a 600 MeV/$c$ electron beam at the Laboratory of Nuclear Science, Tohoku University.

Figure 3.43 shows the Most Probable Value (MPV) of ADC counts out from FEE as a function of high voltage applied to the MuTr chamber. In PHENIX, the current operating voltage is typically 1850-1900 V. The plot shows the MPV when the MuTr chamber is read out with FEE alone or both FEE and AD board whose $C_{split}$ is 100 pF. When the AD board is added to the readout system, we can get about 10% of signal from FEE. The RMS noise is also shown in Figure 3.44 with ADC value and it increases by a factor of 1.25 on average. This means that, if the $C_{split}$ is 100 pF, we need the signal gain of ~1.4 to recover the noise level before the split. The analysis of the position resolution is in progress.

With regard to the performance of the AD board, we can obtain good efficiency for the strip hit information if the time jitter is not considered. Figure 3.45 shows the turn on curve without applying the time gate. Because of the drift time of the electron in the MuTr chamber and not fully optimized pseudo CFD, the time jitter of the discriminated outputs has 200 nsec width. But we presume to be able to reduce this time jitter by optimizing the constant of the pseudo CFD circuit.

Based on the results of the experiment and improving the pseudo CFD performance, we will be able to finalize the AD board development.

# 3.5   Trigger Processors (LVL-1)

## 3.5.1   Design of LVL-1 Trigger Hardware

In this section we will describe the detailed design of the forward muon trigger Local Level 1 (LVL1) trigger hardware. The LVL1 hardware will be designed to fully integrate with the existing PHENIX Level-1 architecture, acting as a Local
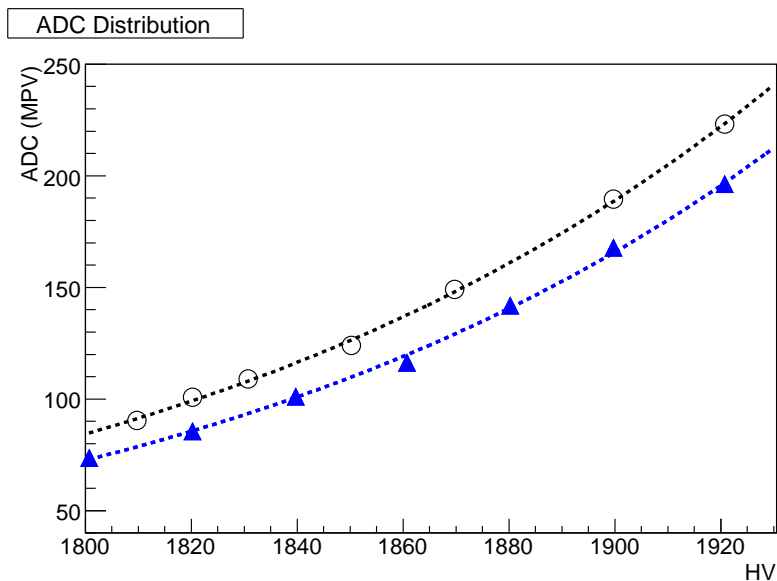
Figure 3.43: The Most Probable Value (MPV) of ADC counts vs High Voltage (HV) of MuTr chamber. Results from readout with FEE alone is shown as open circles. Triangles come from the readout with combined system of FEE and AD board. $C_{split}$ is 100 pF.

Level-1 system to feed reduced bit information into the Global Level-1 (GL1) trigger system. These reduced bits will then be available to the combinatorial logic in GL1 used to implement the actual triggers.

### RPC and MuTr Channel Counts

Before we describe the forward muon trigger LVL1 system in detail, it is important to set the scale of the problem by enumerating the channel counts and data bandwidth into the LVL1 system. Table 3.8 show the Level-1 channel counts for the RPC system. The Level-1 trigger will use four theta segments in each RPC, as opposed to the eight segments used for readout. To accomplish this, adjacent rings (with identical strip sizes) will be logically combined at the FEM level prior to being set to Level-1.

In addition to the RPC hit pads, the forward muon Level-1 trigger will also make use of the muon tracker hit information. The per octant muon tracker channel count information is shown in Table 3.9.

Data will be transmitted to the Level-1 system from the detector front end electronics via optical fibers operating at 2.5 Gb/s. The forward muon Level-1 system will reside in a 9U VME crate in the PHENIX rack room. Data will be collected at the octant level and each octant will be processed independently, with
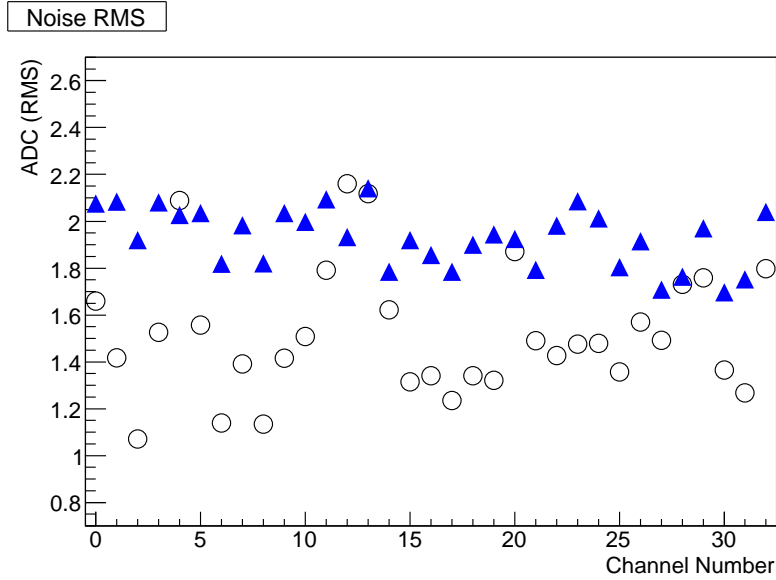
Figure 3.44: The RMS noise measurement for typical channels in units of ADC counts. Symbols are the same as Figure 3.43.

Table 3.8: Level-1 RPC channel counts per octant. Note that Level-1 RPC channels are combined into four theta segments, as opposed to the eight segments used for readout.

| Arm | RPC1A | RPC1B | RPC2 | RPC3 |
|-------|-------|-------|------|------|
| North | 192 | 192 | 256 | 192 |
| South | 192 | 192 | 256 | 192 |

Table 3.9: Muon Tracker channel counts by station and octant.

| Arm | Station 1 | Station 2 | Station 3 | Octant Total |
|-------|-------------|--------------|--------------|---------------|
| North | 96 ch/octant | 192 ch/octant | 320 ch/octant | 608 ch/octant |
| South | 96 ch/octant | 160 ch/octant | 256 ch/octant | 512 ch/octant |

the exception of candidate summary information for the invariant mass trigger as described below. The number of fibers per octant is shown in Table 3.10. The complete MuTr+RPC system will require 11 input fibers at 2.5 Gbit/s, yielding 1248 channels of LVL1 information per beam crossing.
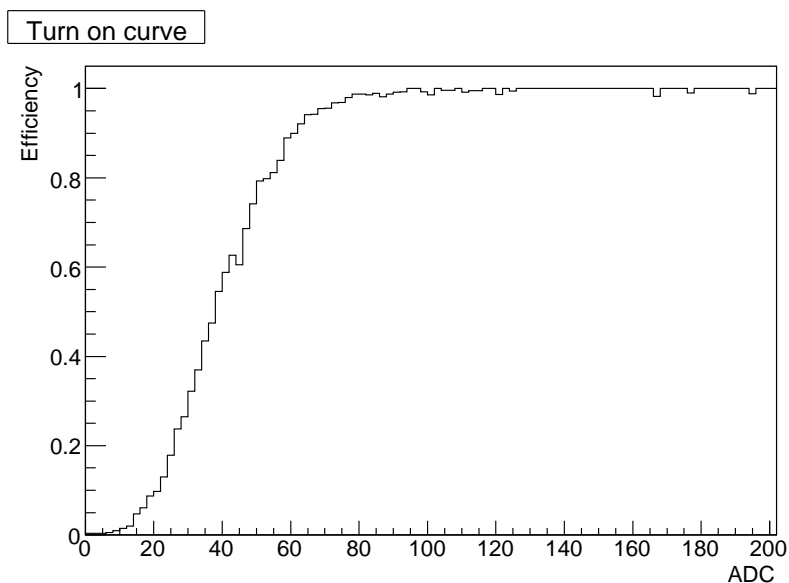
Figure 3.45: Turn on curve without applying the time gate. Horizontal axis is the ADC counts of FEE.

Table 3.10: Forward muon trigger Level-1 fiber counts by station and octant, assuming 2.5 Gbit/s fibers.

| Arm | Station 1 | Station 2 | Station 3 | Octant Total |
|---|---|---|---|---|
| RPC | 1/octant (1a —— 1b) | 2/octant | 1/octant | 5/octant |
| MuTr | 1/octant | 1/octant | 2/octant | 4/octant |

**Block Diagram of the LVL1 System**

A block diagram of a single forward muon trigger Level-1 board is shown in Figure 3.46. Each board will be 9U VME format board with four FPGA processing elements, each element handling a single octant from the ROC and MuTr detectors. A complete system for one arm will consist of two boards, a complete system for the entire detector will consist of two sets of two boards, or four boards in total.

The design of the forward muon Level-1 hardware is driven by the requirement that all the data for a single octant come to a single FPGA processing element. Unlike previous Level-1 designs (the MuID LL1, for example) the forward muon Level-1 boards will not make use of separate discrete elements to deserialize the incoming fiber data. Because of the large amount of data that must be fed to each processing element the only practical way to get data into the FPGA is route the
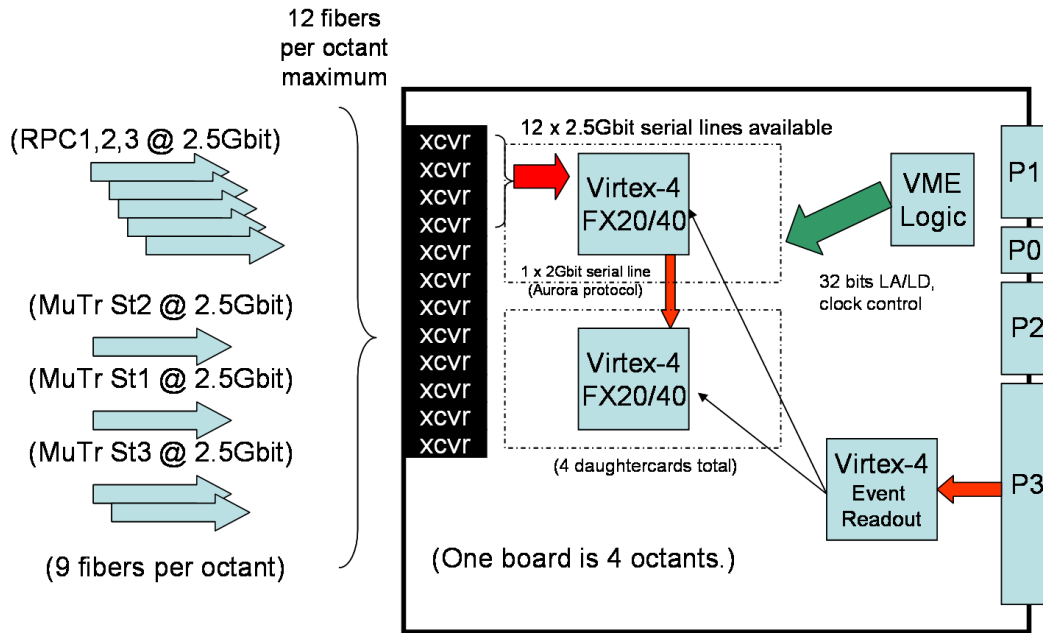
Figure 3.46: Block diagram on the forward muon trigger LVL1 system. The system for one arm will consist of two VME 9U hardware boards, each processing one half-octant. Within a given board, each octant will be processed in a single FPGA, which will accept data from nine input fibers at 2.5 Gbit/s.

serial streams directly into the FPGA's themselves, making use of modern FPGA's that incorporate SERDES (serializer/deserializer) hardware on the FPGA silicon. This is discussed in more detail in the section on FPGA selection (below).

In order to bring in up to 44 fiber connections to a single forward muon trigger board, we plan to utilize the Agilent AFBR-742B parallel fiber optic receiver modules (or equivalent) to bring in up to 12 fiber connections per module in a small form factor package. One of these modules will serve as the input for each of the four FPGA daughtercards.

The FPGA processing engines will be manufactured as daughter cards mounted on the main board using shielded connectors. We have investigated connectors available for use with differential serial streams and found a number of connectors that are rated at speeds up to 10 Gb/s. Thus, routing the serial stream from receivers on the front of the board to the FPGA daughter cards should not present a serious difficulty. However, it will still be necessary to conduct analog simulations on the full design to insure that signal integrity is properly maintained. At the present time we are designing the daughter cards to use 1.0 mm SMT high speed connectors from ERNI, rated at speeds up to 10 Gb/s. The reference receiver clock required for the FPGA SERDES modules (14x beam clock) will be

generated from the beam clock using a Synergy SY89429 clock synthesizer, as was used successfully in the MuID LL1 system. (It is important to realize that for the receiver end the phase relationship between the reference clock and beam clock is not important as it is for the transmitter, because the receiver will phase shift the reference clock to match the incoming data.)

The advantages of using FPGA daughter cards are numerous. Because FPGA technology is changing rapidly, the use of daughter cards will allow us to take advantage of advances in FPGA technology for future Level-1 development without a complete redesign of the forward muon Level-1 infrastructure. A similarly flexible approach was taken with the MuID LL1 trigger boards, and it has since proved quite valuable for PHENIX, at various times providing trigger logic for the MuID LL1, ERT LL1, ZDC, NTC and RxNP LL1 trigger systems. For maximum flexibility we plan that the FPGA core voltages will be generated locally on the daughter cards using voltage regulators (with appropriate filtering as necessary). The daughter cards themselves will be supplied with 3.3 V and 12 V power.

In addition to the FPGA daughter cards, the Level-1 board itself will include additional FPGA's. An inexpensive Virtex-E FPGA will be used for VME logic, addressing and communication. We have already licensed a set of software cores implementing the Cypress 960/964 chipsets originally used in the PHENIX Level-1 trigger boards. This core has been implemented and tested in a Level-1 trigger crate. The use of the software cores allows us to maintain compatibility with existing Level-1 software and trigger systems despite the fact that the original Cypress chipsets are no longer available. In addition, although we do not currently utilize more than A32/D32 transfers to configure the FPGA logic the VME interface is capable of 64-bit block transfers.

**FPGA Selection**

The forward muon trigger system requires 11 input fibers operating at 2.5 Gbit/s, delivering 1,248 bits per beam crossing. As a comparison, the MuID LL1 processed 1,920 bits per crossing in five Virtex-E XCV2000E FPGA chips. We want to do something equivalent to this in one chip. This would argue that we would need one chip with (1248/1920)*5 = 3.3 times the available logic. However, the peak utilization in the MuID LL1 chips is 21%, so there's a factor of two or so if we let ourselves go to higher utilization, meaning we need  1-2x the logic for the forward muon trigger.

In the Virtex-5 series, only the LX85T and LX110T have the available logic along with sufficient Multi-Gigabit Transceivers (MGTs). In the Virtex-4, the FX60 and FX100 series should have enough logic and have sufficient MGTs. There is a great deal of experience with the Xilinx Virtex-4 FPGA series, particularly with fully utilizing the available transceivers. The Virtex-5 series offers some advantages over the Virtex-4 series and a new FPGA fabric that promises a larger

equivalent number of gates in a smaller package. We are currently evaluating each of the Virtex-4 and Virtex-5 series to determine which offers the best combination of price and performance.

In order to gain experience with the Multi-Gigabit Transceivers in the Xilinx FPGA lineup, we have purchased a PCI Express development card containing a XC4FX60 FPGA with multiple transceiver connections (2xSFP and 2xHSDDC2) that we have been using to develop the necessary experience with the hardware and Xilinx software logic cores. This development platform will allow us to design, test and implement a large part of the necessary logic before the forward muon trigger hardware is available, thus accelerating the development cycle.

**Additional Design for Invariant Mass Trigger**

In order to implement the invariant mass trigger (for the $J/\Psi$ and upsilon in heavy-ion collisions) the processing of each octant is no longer independent. The final candidate lists from each octant must be combined in order to calculate the invariant mass of each unlike-sign candidate pair.

We are still trying to fully develop the additional design and logic elements that will be required to implement the invariant mass trigger. Our initial plan would be to implement the two boards that process a full arm as a slave/master pair. The slave board would send the candidate list from each daughter card to an FPGA on the master board via a backplane serial link. The same FPGA would also collect the candidate list information from the daughter cards on the master board and combine lists to generate the invariant mass trigger via a set of lookup tables. Provision would need to be made to flag events in which the candidate list from a given octant overflowed. Presumably these events could be flagged to generate a GL1 trigger. This would prevent trigger inefficiency and maintain the unusual events for further study.

## 3.5.2   Monte Carlo Determination of Trigger Performance

### Introduction

In order to develop and refine the design of the muon forward trigger a set of increasingly sophisticated Monte Carlo simulations were performed. These simulations relied on the full PHENIX detector simulation package PISA, and simulated events were generated using the full PHENIX detector geometry expected to be in place during the time period when the muon forward trigger is expected to be running (including the NCC and FVTX detectors). The goal of these simulations was to demonstrate sufficient rejection power and redundancy in the trigger design to achieve the stated physics goals of the polarized proton program. As an additional benefit, at the end of this section we will discuss the possible use of the

forward muon trigger as a dimuon trigger for heavy-ion running in the RHIC-II era.

**Simulation Events**

Approximately one million minimum-bias proton-proton events at $\sqrt{s} = 500$ GeV were simulated using the PYTHIA event generator [87]. These events were then passed through the PHENIX detector simulation, and a subsequent detector response package, which resulted in a standard PHENIX nano-DST (nDST) containing simulated "hits" information for all the detectors in the simulation.

In addition, approximately 500 HIJING [88] minimum-bias $Au + Au$ collision events at $\sqrt{s_{NN}} = 200$ GeV were also simulated and passed through the PHENIX detector response to generate nDST's. These events were used to study the dimuon trigger discussed at the end of this section.

## 3.5.3   Detector Response

Because the simulations were used to evolve the design of the forward muon trigger, and therefore needed to be rapidly capable of responding to changes in RPC design parameters, the RPC response was not integrated into PISA but was instead simulated within the trigger simulation itself. This allowed us to evolve the simulation response quickly as additional performance data became available from the RPC test benches without re-processing the GEANT hits data into nDST's. The detector response of the MuTr chambers and the MuID was done using the standard PHENIX simulation response packages, including hits clustering and response tuned to match the PHENIX detector.

For the RPC's, true Monte Carlo hit information at each plane was digitized according to the geometry information presented in Section 3.2.1. A hit in an RPC strip may fire one or more adjacent strips, so hit "clustering" was taken into account using measurements from the RPC test stand at the University of Colorado. The data from the test bench was fit to a Gaussian distribution with an average radius for multiple strips to fire, and this distribution was used to generate the probability that adjacent strips to the main strip would also fire. The addition of RPC clusters is an important feature of the simulations because the LVL1 trigger is based hit RPC strips, not RPC clusters, so the additional multiplicity represented by the cluster hits can adversely affect the trigger rejection.

In addition, the RPC noise rate is also included in the simulations. The RPC noise rate (in Hz/cm$^2$) is used as input to a Poisson distribution to determine how many noise hits there are in a given RPC chamber within a single event (106 ns crossing window). These noise hits are randomly distributed throughout each RPC chamber, and digitized into hit strips as described above. Noise hits are permitted to generate clusters in the same way as real hits.

### 3.5.4 Trigger Algorithm

The forward muon trigger algorithm is RPC-driven, and works by making combinations of RPC1-2 hits and then using projections of this combination to establish confirming hits in RPC3 and MuTr Station 2. The full detector granularity of the RPC stations is not used in the LVL1 trigger. Instead, rings of identical strip width will be combined at LVL1 to form four regions in theta over the full acceptance, as opposed to the nominal eight regions. Of the two stations at RPC1, it is assumed that only RPC1A is instrumented for the trigger. In the trigger simulations, hits matching is done within windows in theta angle at the RPC chambers. Practically, this will correspond to a hardware mapping between channels in the different RPC detectors (see Section 3.5.1).

The trigger algorithm proceeds as follows:

- A MuID LVL1 1-Deep muon LVL1 trigger is required. This is determined using a simulation of the existing MuID LVL1 trigger system. The 1-Deep requirement is set to require three of the five MuID gaps fire in a given trigger symset.

- Combinations of RPC1 and RPC2 hit strips are made. Each RPC1 and RPC2 hit strip must be in the same octant, and the strip centers must be within 14 degrees in theta of one another, and within three degrees in phi.

- Using the RPC1-2 hits, a straight line is projected into MuTr Station 2. The closest MuTr Station 2 hit strip to the projection is found, and the distance between the projection and the hit in terms of the number of MuTr strips is calculated. This distance must be less than or equal to three strips. The MuTr Station 2 hit must be in the same octant as the RPC1 and RPC2 hits.

- A matching RPC3 hit is searched for in the same octant as the RPC1 and RPC2 hits is searched for within a ten degree window in theta, if the theta angle of the track is less than 28.92 degrees. This requirement searches for a matching hit in RPC3 within the smaller acceptance window of RPC3. If the track theta angle is greater than 28.92 degrees, no RPC3 hit is required.

A track which satisfies all of the above conditions is called a candidate track, and one or more candidate tracks in an event satisfies the trigger condition and the event is accepted. A diagram of the trigger algorithm is shown in Figure 3.47.

Note that timing requirements on the RPC3 hits are not included in the simulation, as all of the hits in the simulation are collision related and not beam background related. The real trigger will include a timing window cut on the RPC3 hits passed up the LVL1 which will make the trigger rejection insensitive to beam related backgrounds.
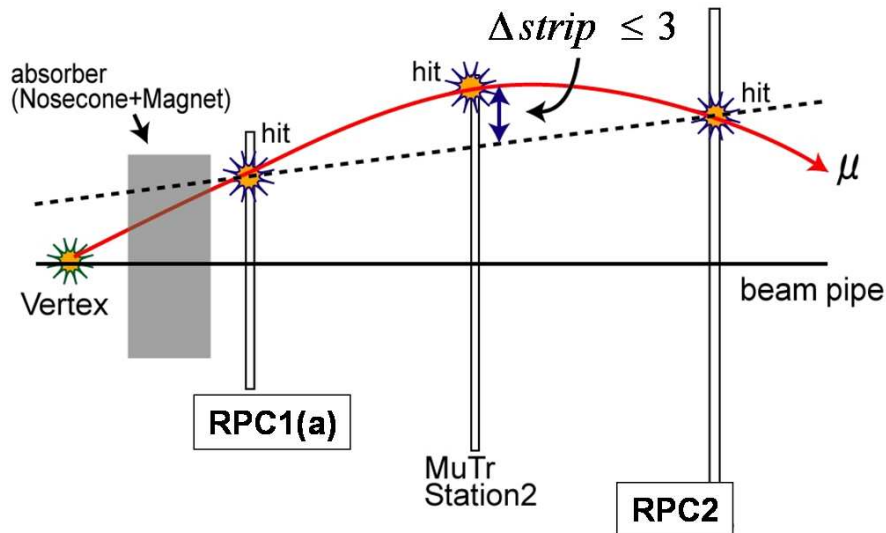
Figure 3.47: A diagrammatic view of the muon forward trigger algorithm. See text for details.

Table 3.11: Trigger efficiency for single muons at 25 GeV/$c$ as a function of phi angle between the RPC1 and RPC2 hit strips.

|  | North Arm | South Arm |
|---|---|---|
| $\Delta\phi \leq 2$ degrees | 95% | 92% |
| $\Delta\phi \leq 3$ degrees | 98% | 96% |

### 3.5.5 Trigger Performance in $p + p$ Collisions

The efficiency of the trigger algorithm was checked using 25 GeV/$c$ single muon tracks, again simulated using the full PHENIX Monte Carlo. These efficiencies for single muon tracks are listed in Table 3.11 as a function of the phi angle cut between the RPC1 and RPC2 hits. An angle cut of 3 degrees is chosen to maintain high efficiency for high-momentum single muon tracks. In the tables that follow we will quote rejection power for both the three degree and two degree RPC angle cuts, with the understanding that additional rejection power can be obtained by a small sacrifice of efficiency for high momentum muons.

The rejection of the muon forward trigger is characterized by processing the 1M PYTHIA events through the trigger simulation and counting the number of events passing the trigger requirements. The expected rejection of the muon forward trigger is listed in Table 3.12. A nominal RPC noise rate of 10 Hz/cm$^2$ was assumed in these simulations. The combined north and south arm rejections

89

Table 3.12: Trigger rejections for $p + p$ minimum bias events at $\sqrt{s} = 500$ GeV. A nominal RPC noise rate of 10 Hz/cm$^2$ was included in the simulations. The standard configuration of the trigger in the simulation consists of MuID*RPC1-3*MuTr-2.

|  | North Arm | South Arm | Both Arms |
|---|---|---|---|
| $\Delta\phi \leq 2$ degrees | 76,691 | 23,179 | 17,798 |
| $\Delta\phi \leq 3$ degrees | 47,463 | 15,573 | 11,726 |

are sufficient to achieve the physics goals of the $W$ physics program with polarized protons.

Finally, we examined the stability of the trigger rejection vs. the noise rate of the RPC chambers. The results are shown in Figure 3.48. The trigger rejection factor for the combined arms remain above 10,000 for RPC noise rates $<$50 Hz/cm$^2$.
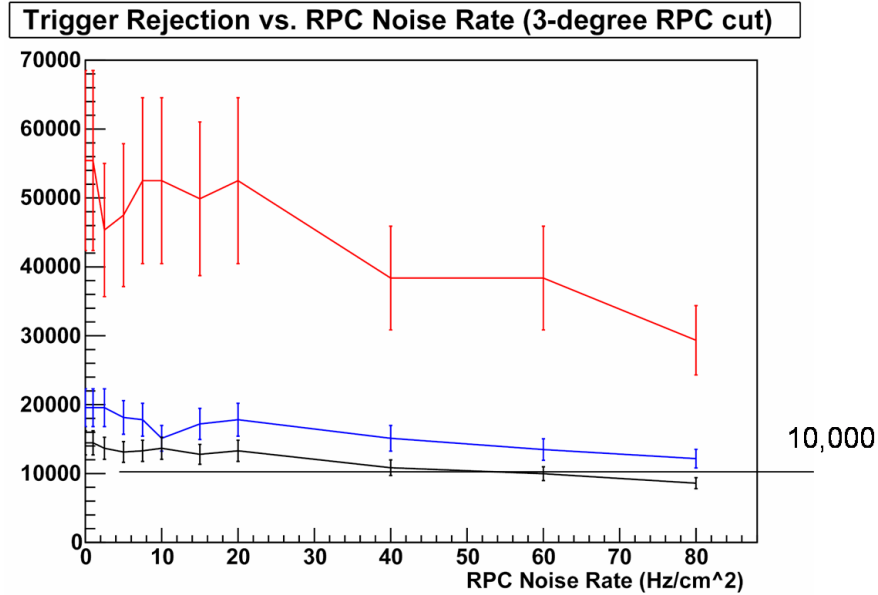


Figure 3.48: Forward muon trigger rejection versus RPC noise rate. The error bars shown are the statistical errors on the rejection factors.

### 3.5.6 Performance of a $J/\Psi$ Trigger for HI Collisions

With coming luminosity upgrades at RHIC and RHIC-II, it is possible that PHENIX will soon see event rates in the neighborhood of 40 kHz for $Au + Au$

collisions. Event rates this high will require an LVL1 trigger if the experiment is to be able to make use of all this luminosity for physics. Because of this coming need, we have also examined the possible us of the muon forward trigger as a dimuon $J/\Psi$ trigger in a heavy-ion collision environment.

Because the forward muon trigger in $p + p$ collisions is designed to select very high momentum tracks in the spectrometer, some modifications are required to the trigger algorithm. The general procedure of matching RPC and MuTr Station 2 hits is the same, with the caveat that there is no cut on phi angle between the RPC1 and RPC2 hits and the distance in strips between the RPC projection and the MuTr Station 2 hit widened to less than ten strips. Note, however, that all RPC and MuTr hits are still required to be in the same octant. This constraint is imposed by the design of the LVL1 electronics (see Section 3.5.1) and implies somewhat poor efficiency for very low momentum tracks.

Once single-muon candidate tracks are found, additional trigger steps proceed as follows:

- Candidate tracks are sorted by charge sign based on the sign of the difference between the MuTr Station 2 projection and the nearest MuTr Station 2 hit ($\Delta Strip$).

- Momentum is calculated for each candidate track using a lookup table that correlates $p_Z$ of the muon with the $\Delta Strip$ difference for the MuTr Station 2 hit (one LUT for each arm). The lookup table is somewhat crude, and only the mean of the $p_Z$ distribution for each value of $\Delta Strip$ is used for the LUT, although a different table is used for each theta segment in the trigger. The transverse momentum is calculated from the theta/phi angles of the hit at RPC2.

- After all combinations are complete, the positive and negative candidate lists are combined and an invariant mass calculated for each combination.

Any candidate track pair with opposite sign and an invariant mass between 2 GeV/$c^2$ and 5 GeV/$c^2$ is considered to have fired the trigger. An invariant mass distribution for $J/\Psi$s in the south arm is shown in Figure 3.49, demonstrating the invariant mass resolution of the trigger at LVL1.

The forward trigger rejection was examined in combination with a 1-Deep, 1-Deep, 1-Shallow and 2-Deep MuID LL1 triggers. A 1-Deep, 1-Shallow trigger is typically used as a dimuon trigger for $J/\Psi$. A 2-Deep trigger yields better rejection, but at the expense of efficiency for the $J/\Psi$. Rejection factors obtained from 500 HIJING $Au + Au$ minimum bias events are shown in Table 3.13.

It has been noted that in heavy-ion running, multiplicities in the muon tracker chambers are typically higher than predicted by HIJING events alone. Because of this, studies in the muon arms are often done using so-called double-HIJING

**Invariant Mass of Candidate Pairs (South)**

Invariant Mass (GeV/c$^2$)
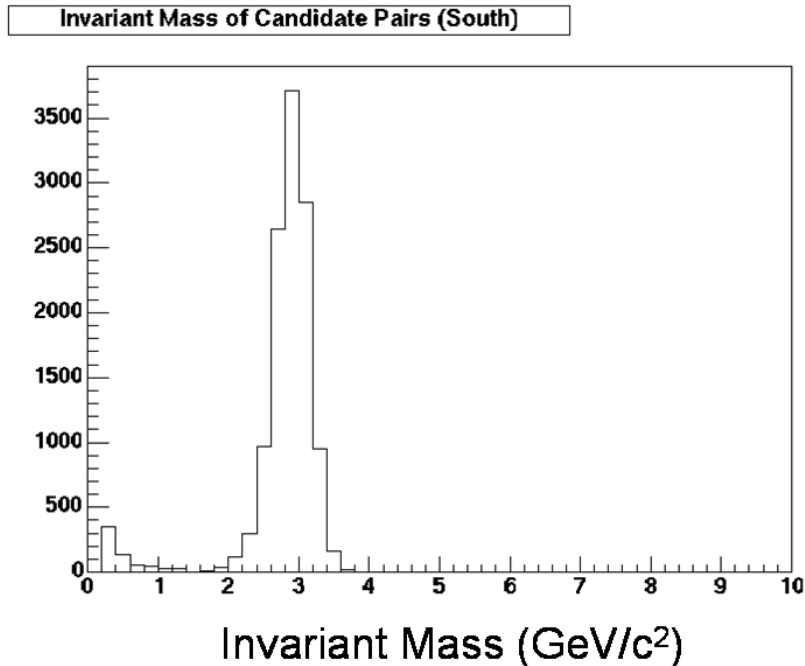
Figure 3.49: Invariant mass of dimuon pairs in the south arm for single $J/\Psi$ events in the PHENIX Monte Carlo. The mass resolution of the $J/\Psi$ peak is approximately 600 MeV.

Table 3.13: Trigger rejections for $Au + Au$ minimum bias (HIJING) events at $\sqrt{s} = 200$ GeV. A nominal RPC noise rate of 10 Hz/cm$^2$ was included in the simulations. Rejections listed are combined for the two muon arms.

|  | MuID LL1 Alone | MuID LL1 + Dimuon Trigger |
|---|---|---|
| 1-Deep MuID LL1 | 2.4 | 4 |
| 1-Deep, 1-Shallow MuID LL1 | 2.7 | 4 |
| 2-Deep MuID LL1 | 12.5 | 15 |
| 2-Deep MuID LL1 + match | 12.5 | 50 |

events. These events consist of constructing a single event from two HIJING events from the same centrality and vertex class. We have also studied the trigger rejection for these events, and the rejection factors are shown in Table 3.14. As expected, the obtained rejection factors are substantially reduced.

Based on an interaction rate of 40 kHz a rejection factor of ∼10 would be barely adequate, and only if we assume a factor of two improvement in PHENIX

Table 3.14: Trigger rejections for $Au+Au$ minimum bias (double-HIJING) events at $\sqrt{s} = 200$ GeV. A nominal RPC noise rate of 10 Hz/cm$^2$ was included in the simulations. Rejections listed are combined for the two muon arms.

|  | MuID LL1 Alone | MuID LL1 + Dimuon Trigger |
|---|---|---|
| 1-Deep MuID LL1 | 2.4 | 4 |
| 1-Deep, 1-Shallow MuID LL1 | 2.5 | 4 |
| 2-Deep MuID LL1 | 6.5 | 8 |
| 2-Deep MuID LL1 + match | 6.5 | 27 |

DAQ rate as well. Finally, we have studied the improvement in rejection power if an explicit match is made to trigger particles in the MuID LL1, instead of merely requiring the global presence of a MuID LL1 trigger. Such a matching would require a re-implementation of the existing MuID LL1 trigger to include the ability to cluster groups of hit MuID LL1 symsets and transmit this information to the forward muon trigger. The effect of including this explicit MuID LL1 hit symset match on the rejection for single- and double-HIJING events is shown in the last row of Tables 3.13 and 3.14.

While more study and design will be required to fully establish the feasibility of a dimuon trigger for heavy-ion collisions using the muon forward trigger hardware, we consider the current studies to be encouraging. Finally, we note that the invariant mass distribution from double-HIJING events, as shown in Figure 3.50, is relatively free from background above the $J/\Psi$ peak, meaning that this invariant mass trigger could be easily extended as an upsilon trigger with very high rejection power.

## 3.6   Assembly and Mechanical Integration

### 3.6.1   RPC

The full detector octants (RPC1A/B) and the detector half-octants (RPC2/3) consist of detector modules, the support and services for each detector module and the overall support structure. The actual detector assembly takes place in the RPC factory at BNL. The completed (half) octants are then moved by truck to the PHENIX experimental hall (building 1008) and are craned into the interaction region(IR) or the Tunnels (RPC3).
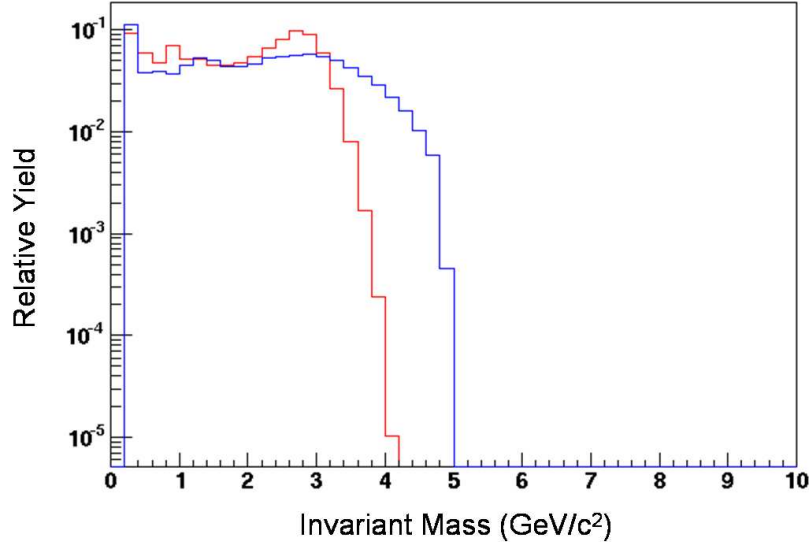
Figure 3.50: Normalized invariant mass trigger distributions from 500 $Au + Au$ double-HIJING events for the north (blue) and south (red) arms for unlike-sign candidate pairs. At this level the invariant mass distributions are free from candidates above 5 GeV/$c^2$ in both the north and south arms.

**RPC1 installation**

The complete detector octants for RPCs 1A and 1B, the support frame and the front end readout electronics will be prepared in the Brookhaven RPC factory. In the interaction region the first step in the installation is attaching the additional absorber material (Fe) to the return yoke of the central magnet (see Figure 3.51). Since the yoke is not completely accessible by crane one has to use a separate rigging mechanism to move the absorber parts into place. The weight of the absorber material has to be balanced by a counterweight during the installation. To the absorber the first layer of the support structure will be attached and every second RPC1A octant is put into place. The second half of the RPC1A octants is then placed onto the first half and the additional support rings (see Figure 3.54). The next layer of the support structure and again every second RPC1B octant is then installed (see Figure 3.58). As a last step the remaining RPC1B octants are placed and the full RPC1 detector is finished (Figure 3.59) . The HV, gas and readout channels are all connected through the patch panel of each module at the outer side of each octant. All are then led out of the return yoke region.
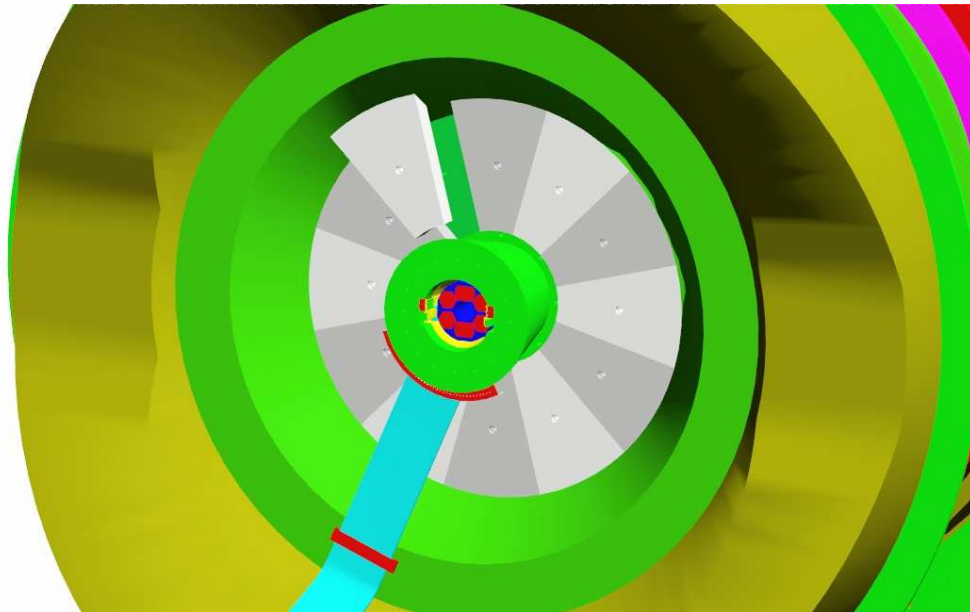
Figure 3.51: Installation of the absorber material (grey) onto the return yoke of the central magnet.
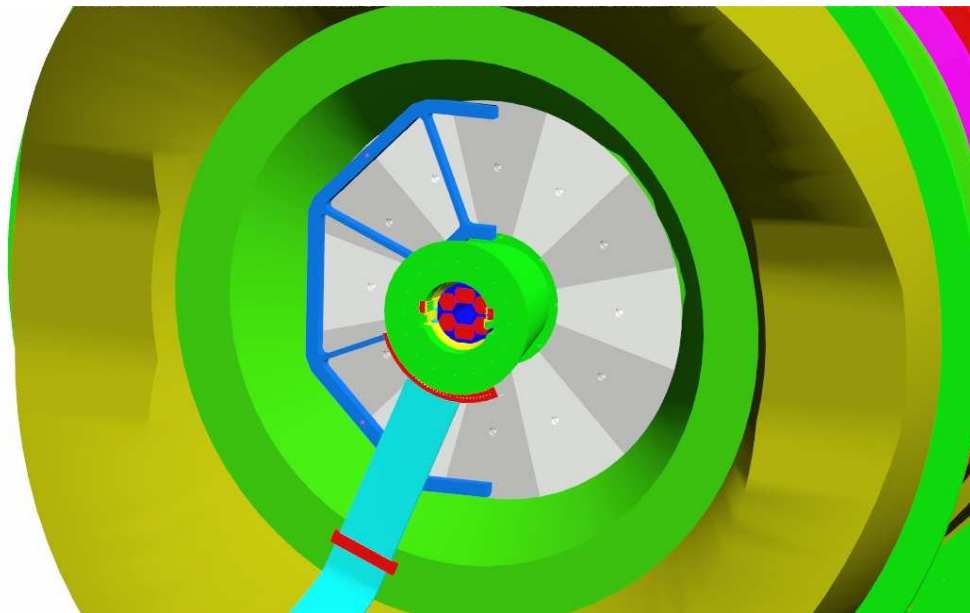


Figure 3.52: Half of the support ring (aqua) is installed onto the absorber.
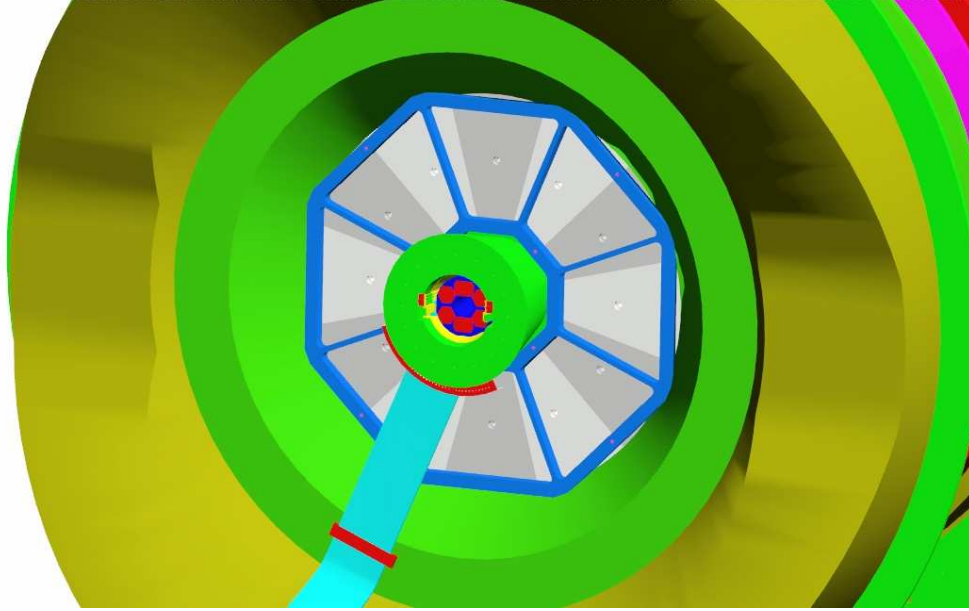
Figure 3.53: Second half of the support ring (aqua) is installed onto the absorber.
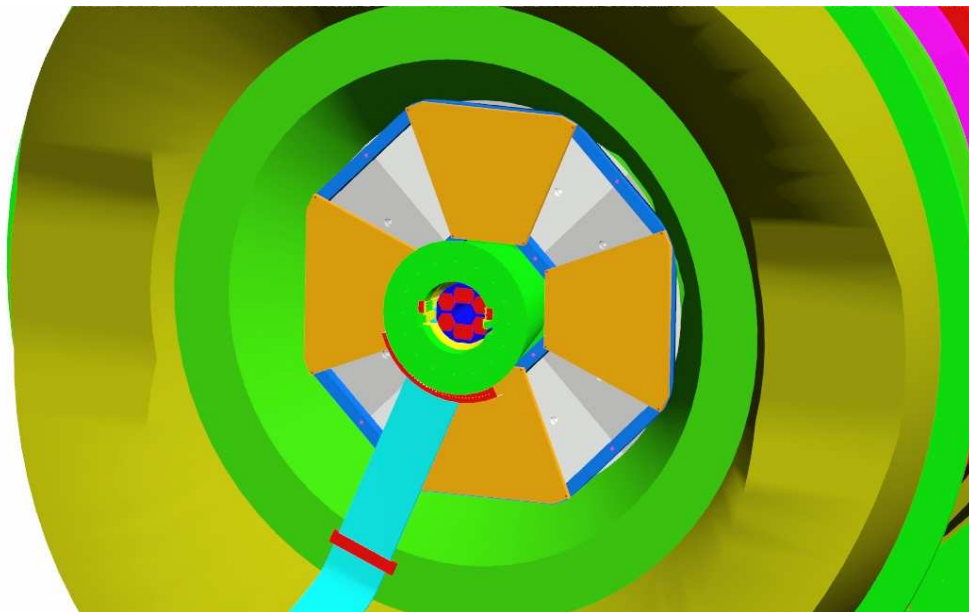


Figure 3.54: First half of RPC1A (yellow) is installed.
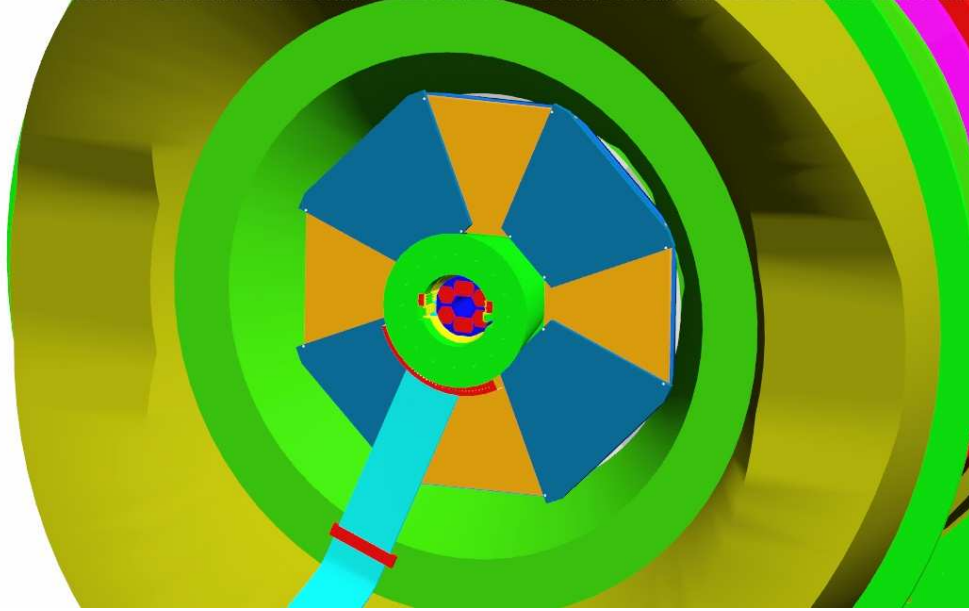
Figure 3.55: Full RPC1A (yellow/blue) is installed.
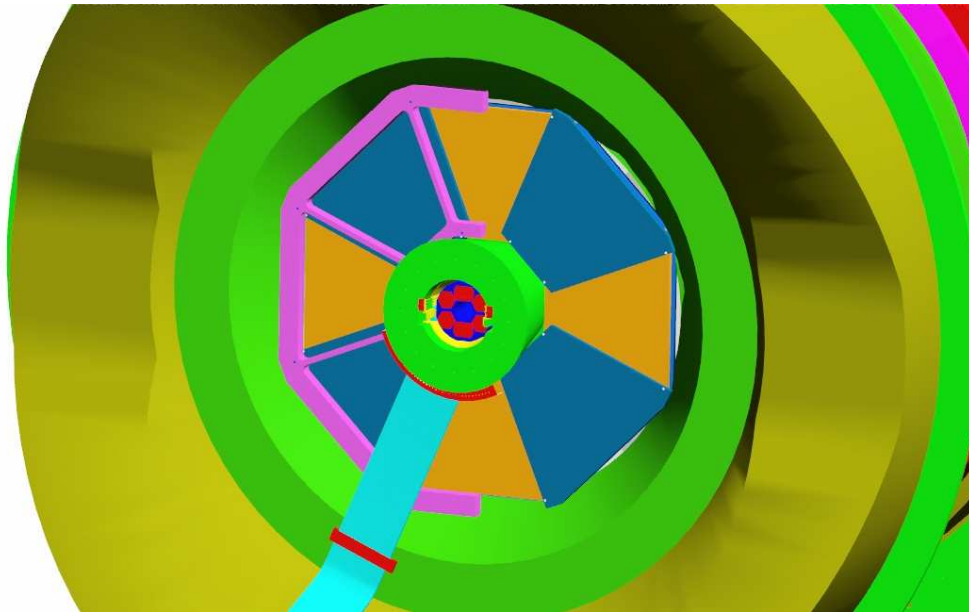


Figure 3.56: Half of the second support ring (pink) is installed onto the absorber.
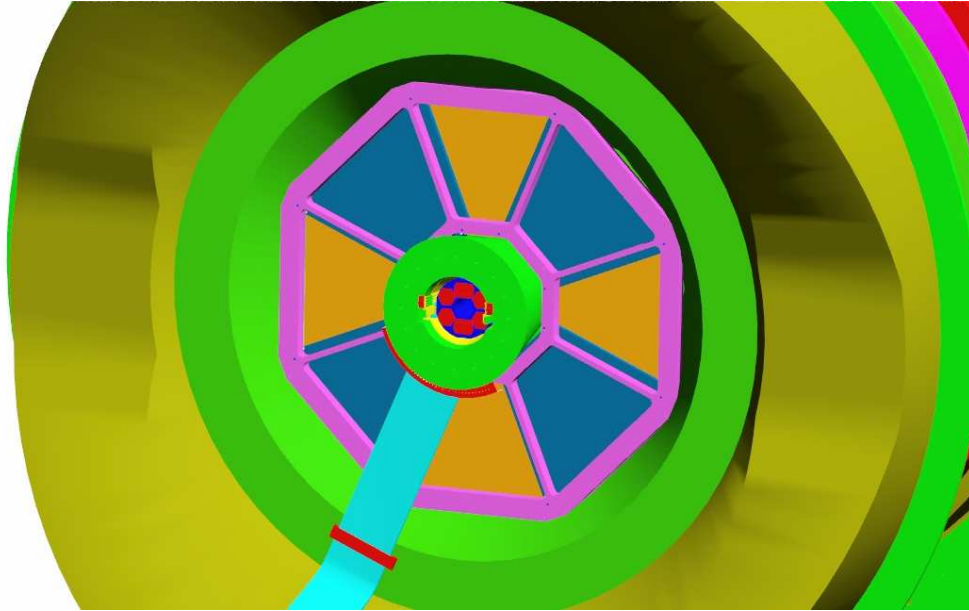
Figure 3.57: Second half of the second support ring (pink) is installed onto the absorber.
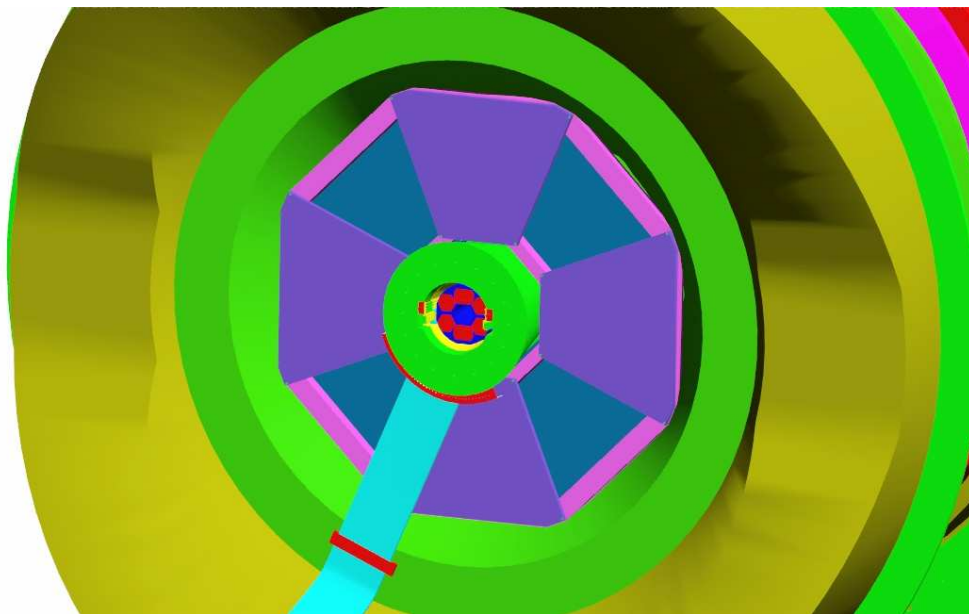


Figure 3.58: Half of RPC1B (purple) is installed.
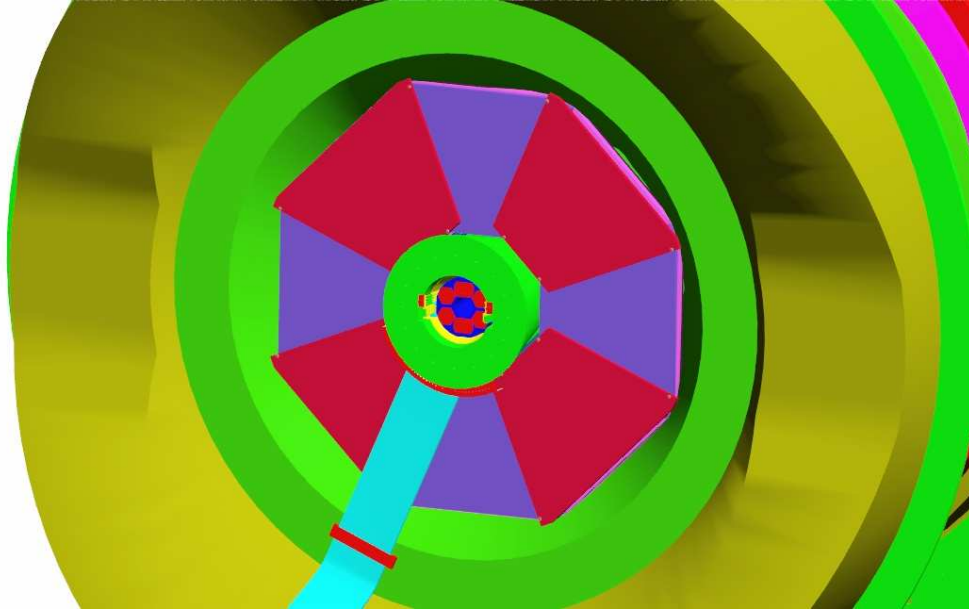
Figure 3.59: Complete RPC1 (purple/magenta) installed.
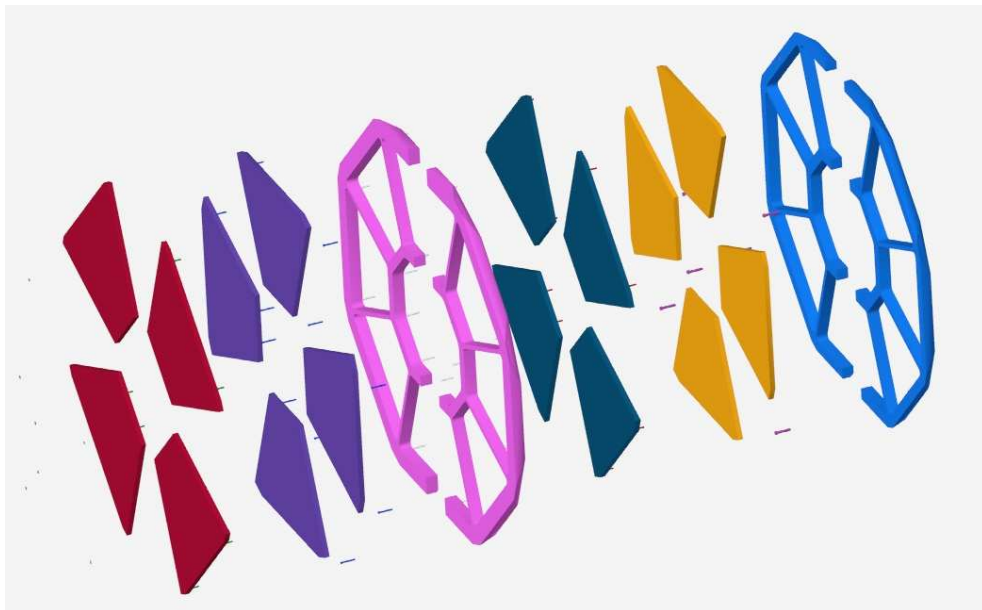


Figure 3.60: View of all separate detector parts of RPC1.
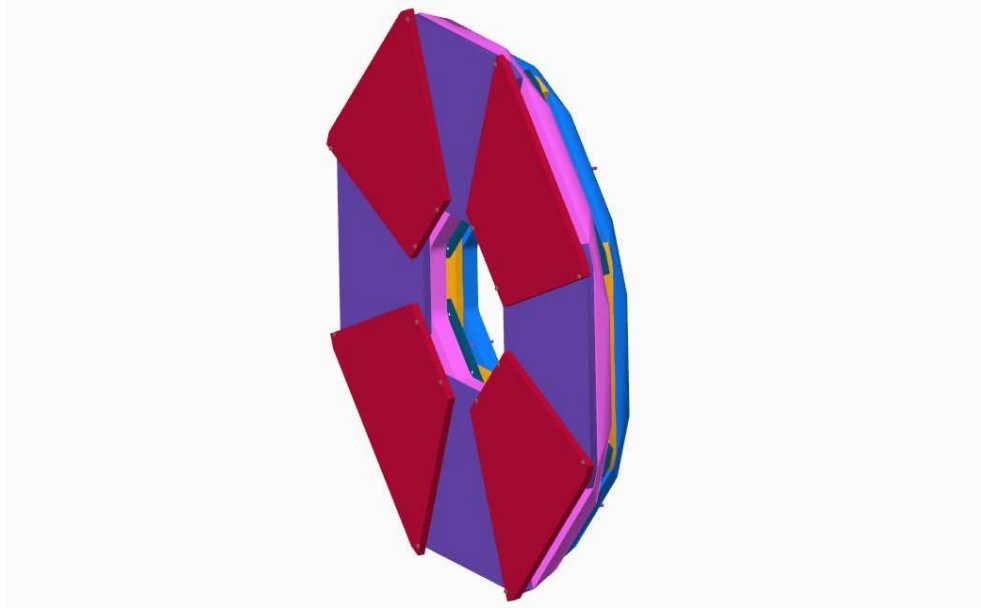
Figure 3.61: Separate view of the fully assembled RPC1.
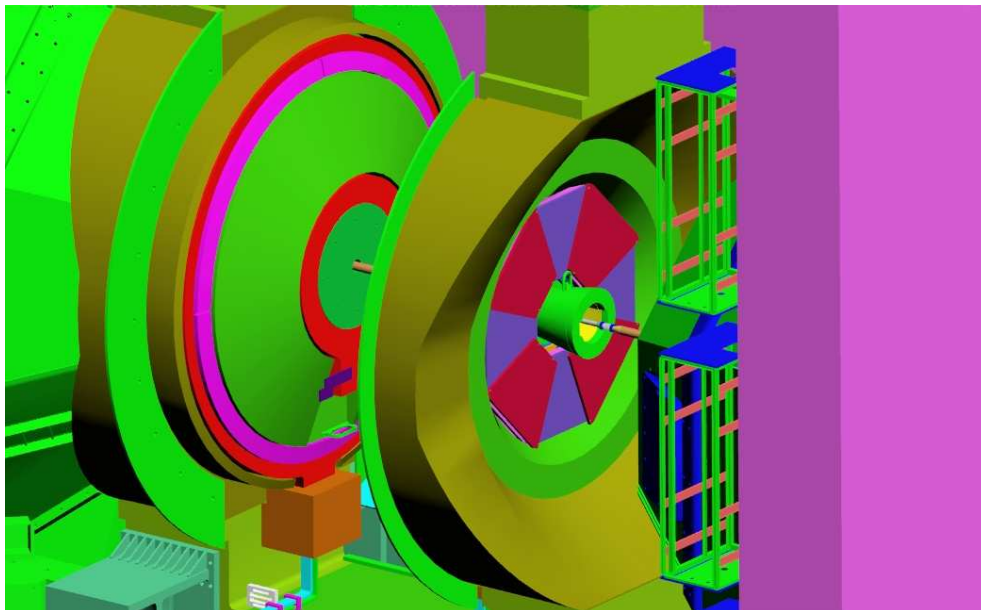


Figure 3.62: View of the completely installed RPC1.

**RPC2 installation**

The RPC2 detector will be placed between the muon magnet and the first steel plate of the MuID (muon wall) . The installation of RPC2 is different for north and south as the south muon magnet can be moved, leaving sufficient space to work in. For the south installation a length in $z$ of more than 1 m is available and manlifts can be used to access the muon wall support to put the RPC2S structure in place hanging down similar to the muon wall. The north magnet is fixed and the access to this area is more restricted. Only 30.2 cm in $z$ are available to install the detector (see Figure 3.63).

The RPC2N will be supported and assembled using a auto-locking mechanism between the different half octants. The lower half-octants can be slid into place on a rail at the bottom of the space. All modules will be lowered from above after they have been turned into the correct angle and moved into the correct $z$-position on the west side of the muon magnet. Lifted with the crane, the half-octants clear the muon magnet if the south muon magnet and the central magnet are both moved south (see Figure 3.69). The clearance of the main crane to the upper edge of the muon magnet is 45". Cable channels on top of the space to be used for the RPC2 have to be moved for the installation. The upper beams of the support structure have to extend to the outside area of the muon magnet, such that there is space to work (see Figure 3.64 for the support beam structure). They are just fixing the $z$-position of the upper parts of the detector, the weight will be supported by the support structure of the lower detector octants. The inner side of all half-octants will be fixed on the downstream side of the muon magnet donut (see Figure 3.68). The gas, HV, LV services as well as the readout system are routed to the outer side of the octants and into the lower IR region.

**RPC3 installation**

The RPC3 detectors are going to be placed between muon ID steel absorber 5 and the wall of the IR region. The distance in $z$ between the downstream edge of the absorber and the wall is 18.4 cm, however, in the south tunnel, gas lines to other detectors reduce this space even further (see Figure 3.72). Its installation will be performed through the beam tunnel. All detector half-octants will enter the beam tunnel over the access points north and south respectively. By a suitable rigging mechanism the half-octants are then turned from the horizontal position (see Figure 3.74) into a position parallel to the space for the detector (see Figure 3.75). The half-octants are then lowered into this space starting with the lower central pair. Since the lower octants cannot be reached on their outer edges they are placed into a holding rail on the bottom, thus automatically aligning them against each other. An additional support structure will pick up the sides of the other lower half-octants (see Figure 3.76). The support structure of all but the upper and lower pair of half-octants will contain beams reaching out of the inaccessible

Figure 3.63: Picture of the available space for the installation of RPC2N between the muon magnet(right) and the muon wall(left). The muon magnet donut is visible in the center of the picture.
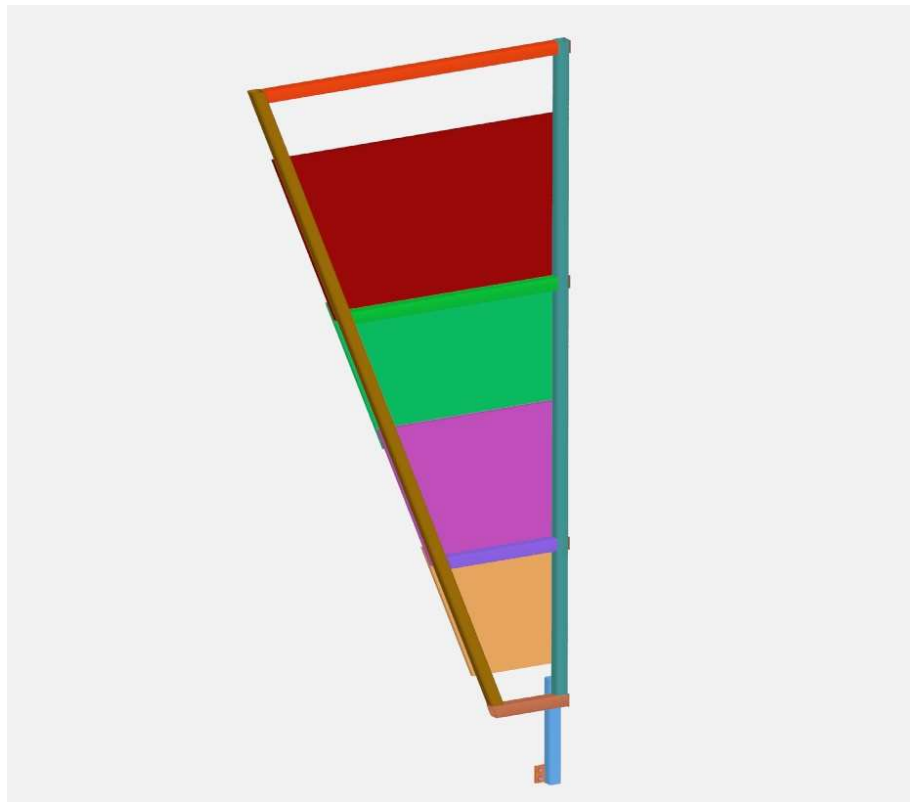
Figure 3.64: Downstream view of one half octant of RPC2N including its support structure.
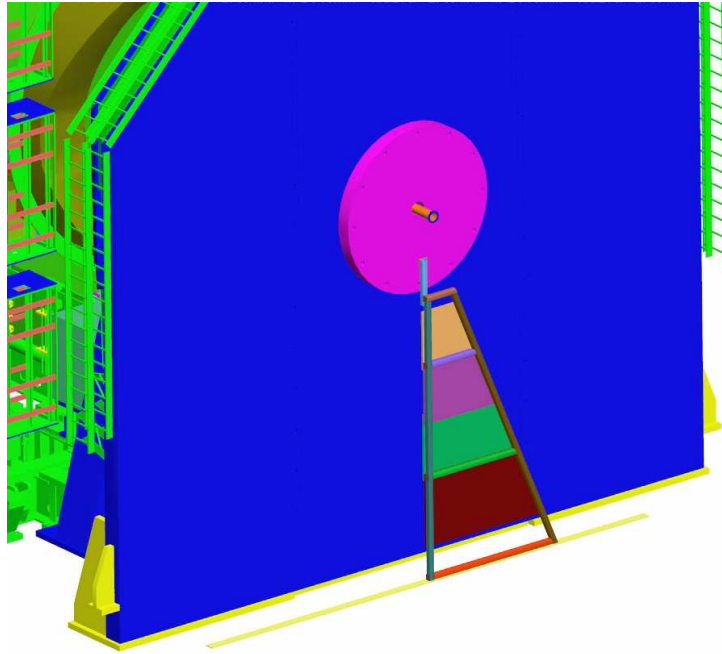
Figure 3.65: First half octant of RPC2N placed onto the alignment rail at the bottom of the hall.
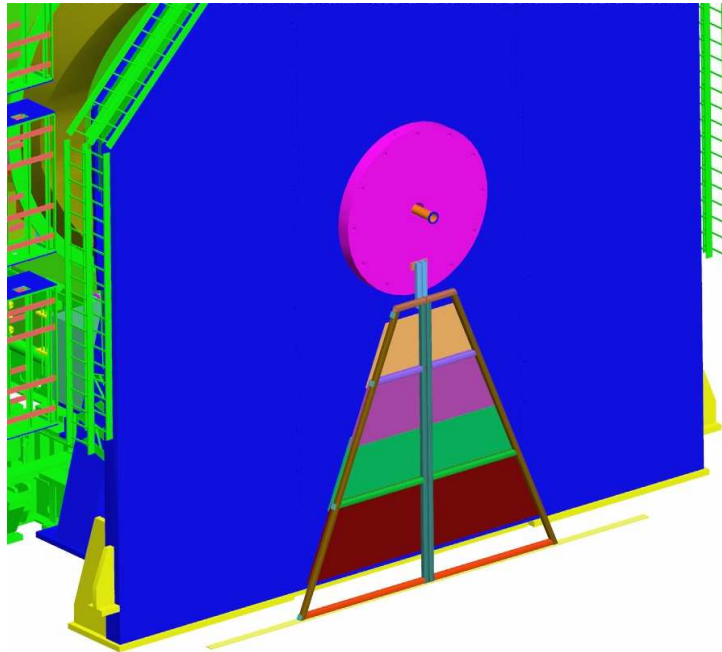


Figure 3.66: Second half octant of RPC2N placed onto the alignment rail at the bottom of the hall.
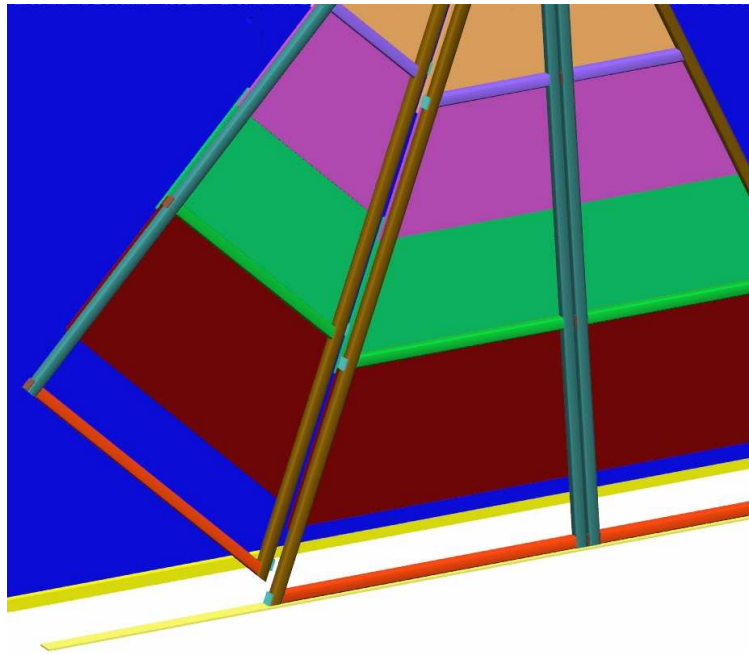
Figure 3.67: Closeup view of moving the third half octant of RPC2N vertically onto the locking mechanism on the second half octant.
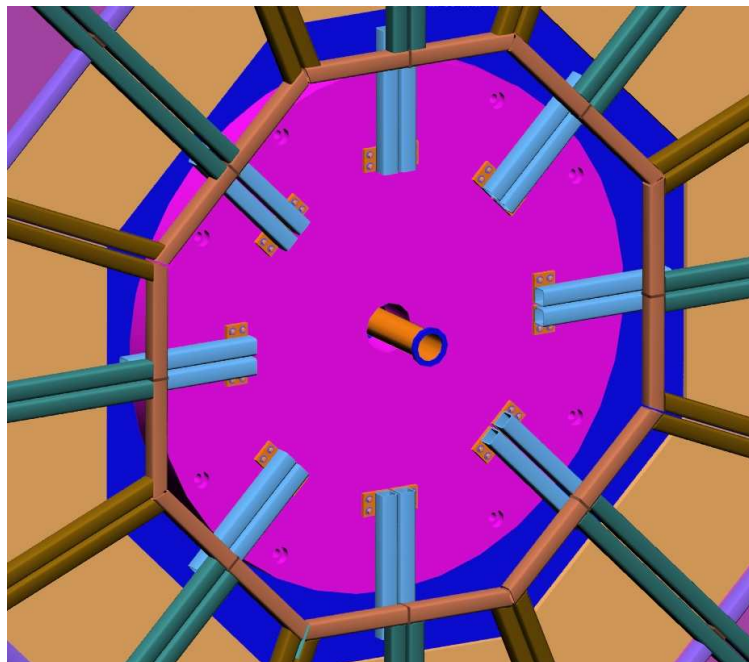


Figure 3.68: Drawing of the inner region of RPC2N and the support beams screwed to the muon magnet donut.
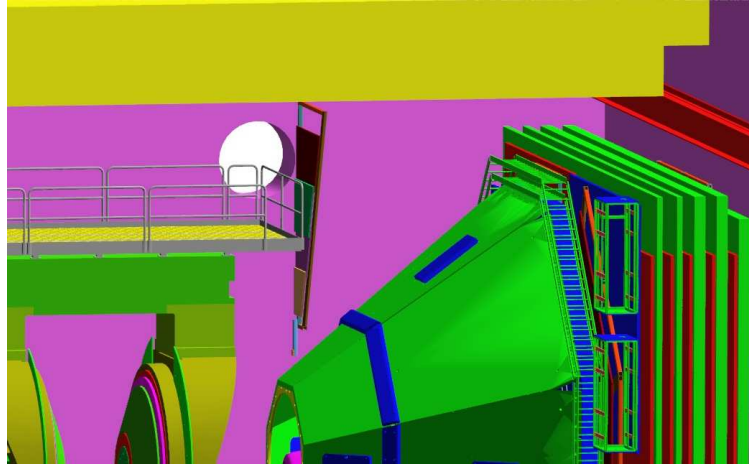
Figure 3.69: Drawing of one RPC2 half octant attached to the crane being moved from the east to the west side of the hall over the muon magnet.
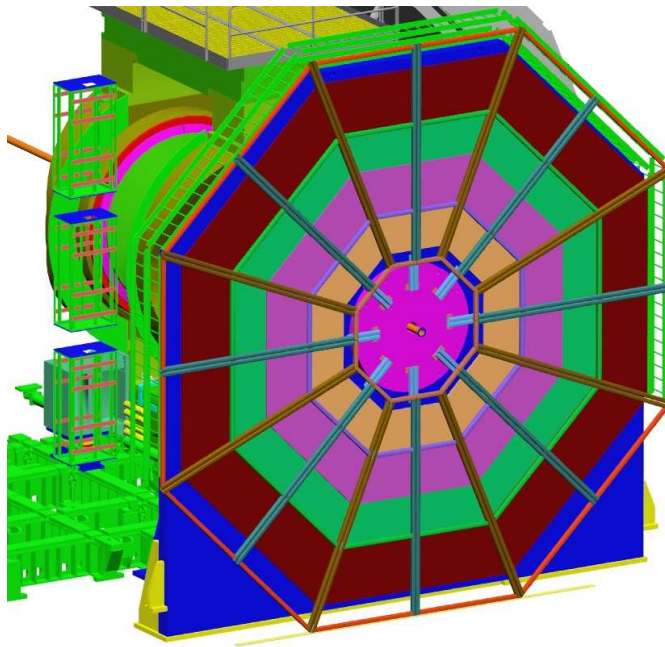


Figure 3.70: Downstream view of the fully installed RPC2N detector.
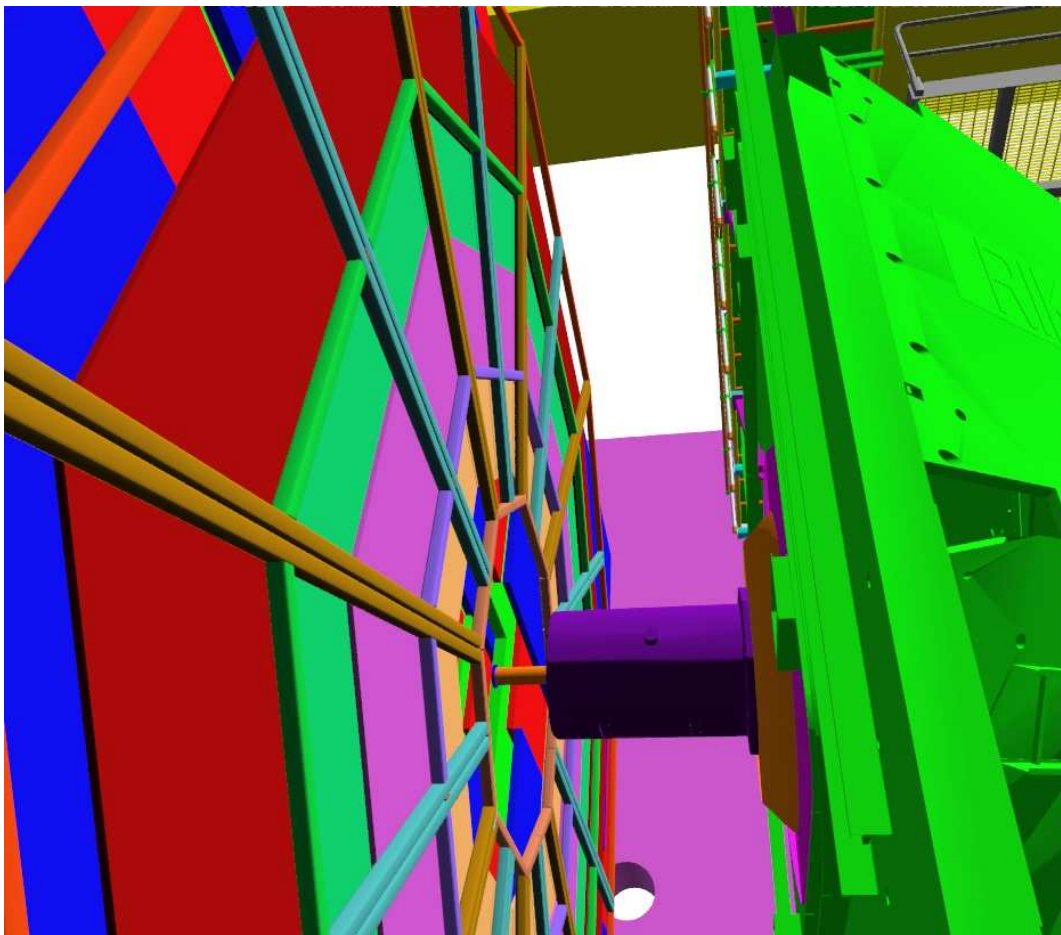
Figure 3.71: Upstream view of the fully installed RPC2S detector.
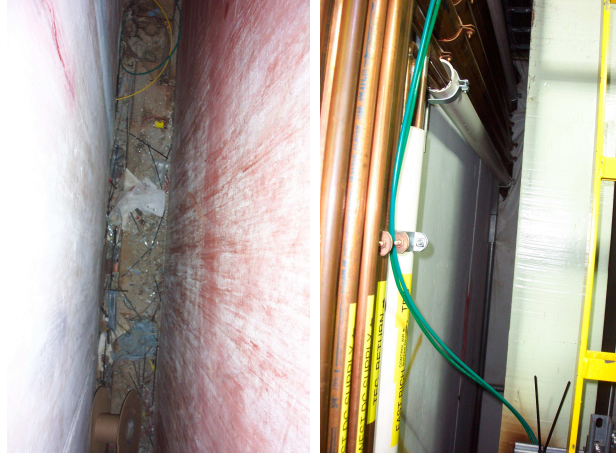
Figure 3.72: Left: Picture of the available space for the installation of RPC3N after the muon wall (right) before the cement block of the tunnel area. Right: Gas pipes in the southern tunnel area as seen from the IR region. The muon wall can be seen on the right, the concrete of the tunnel on the left.

area (see Figure 3.78). Via these beams the detector can be attached to the muon wall. Similar to RPC2N these upper support beams define the $z$-positions while the positioning in the transfer plane is provided through the auto-lock mechanism in reference to the bottom octant.

The services for gas, HV and LV are provided via the beam tunnel from the inner edge of the detector along the radial support beams.



Figure 3.73: Upstream view of one half octant of RPC3N including its support structure.
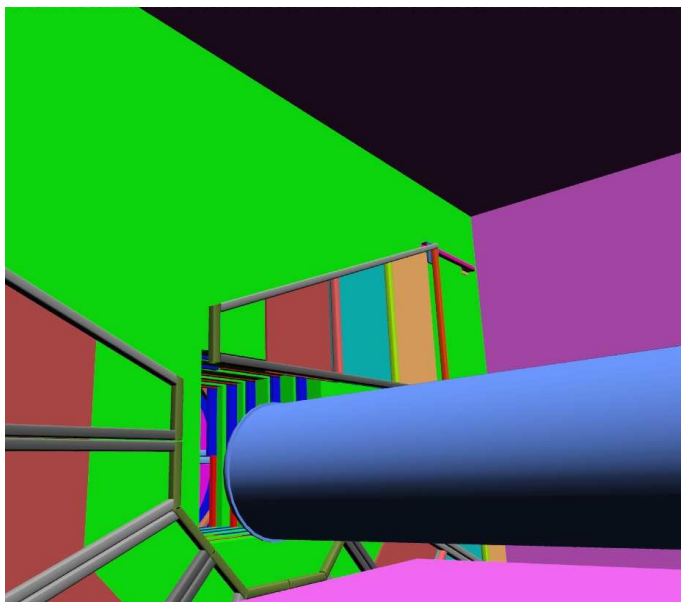
Figure 3.74: View of one half octant of RPC3 detector in place to be moved and lowered into its final position.
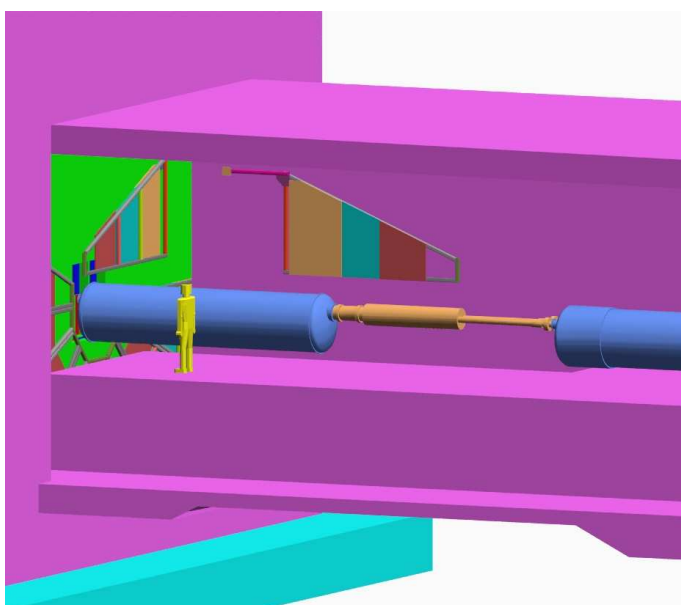


Figure 3.75: View of one half octant of RPC3 detector still in the tunnel which has to be turned and put in place to be moved and lowered into its final position.
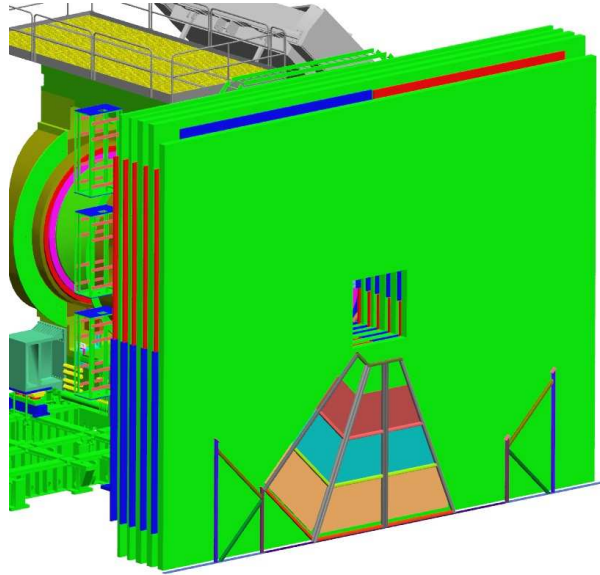
Figure 3.76: Downstream view of the first three half octants of RPC3N installed including the outer support structure.
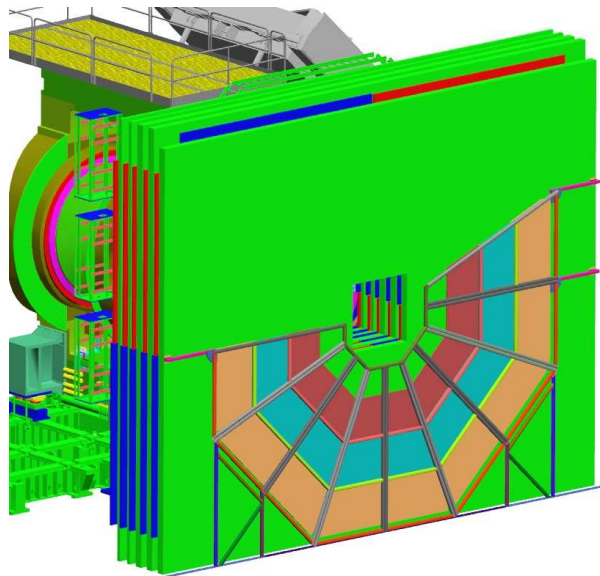


Figure 3.77: Downstream view of more than half of RPC3N installed including the outer support structure in the upper part attached to the Muon Absorber.
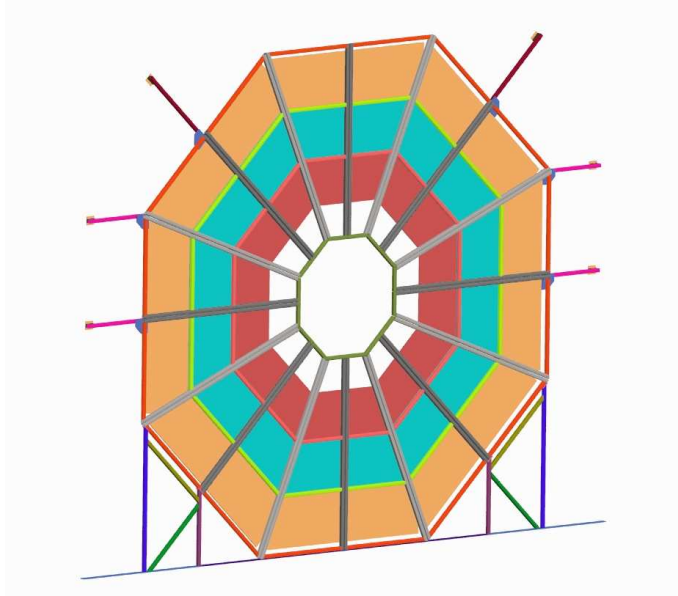
Figure 3.78: Downstream view of the fully installed RPC3N including all support structures.
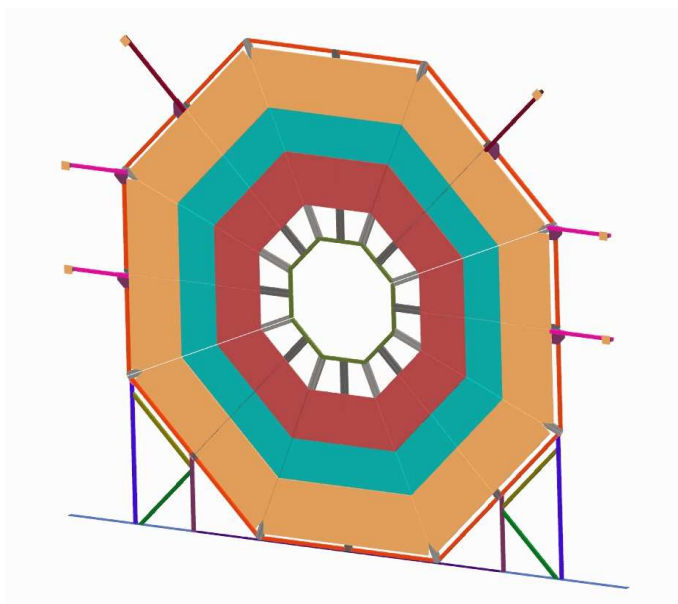


Figure 3.79: Upstream view of the fully installed RPC3N including all support structures.
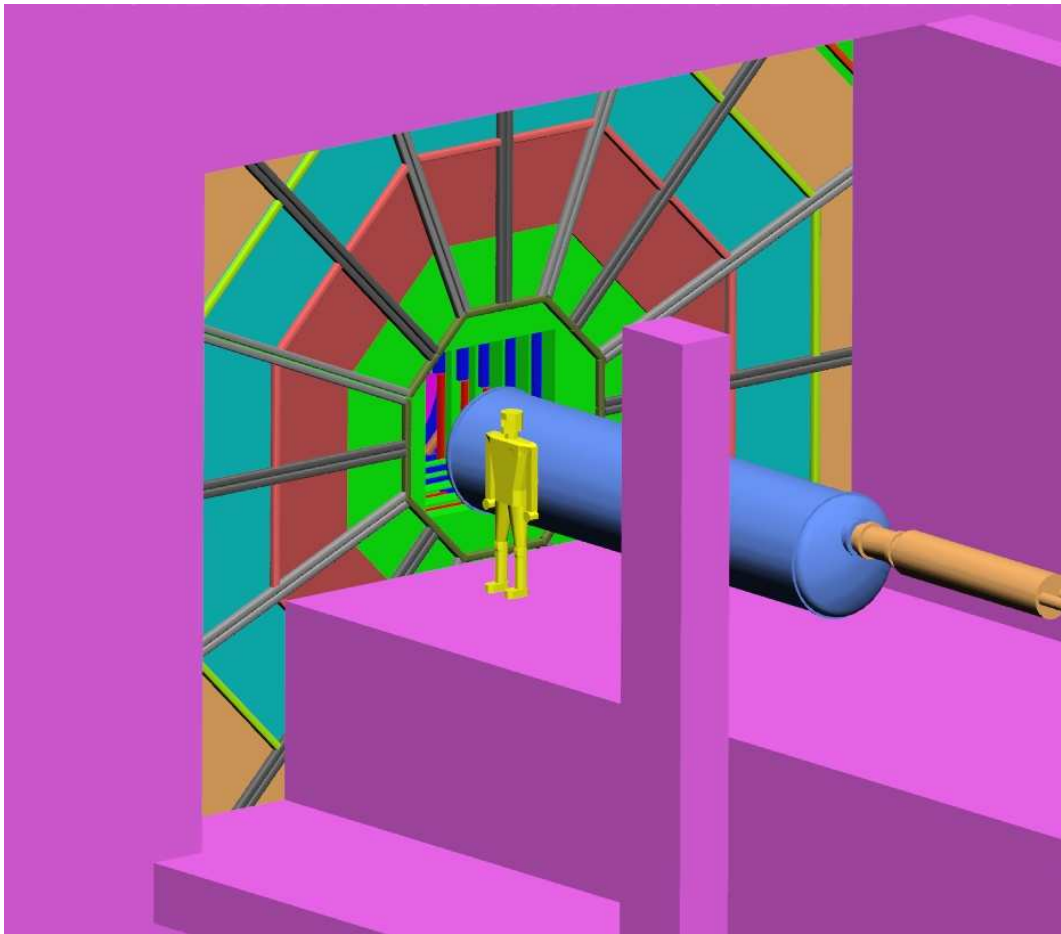
Figure 3.80: Downstream view of the installed RPC3 detector including the walls of the Tunnel.
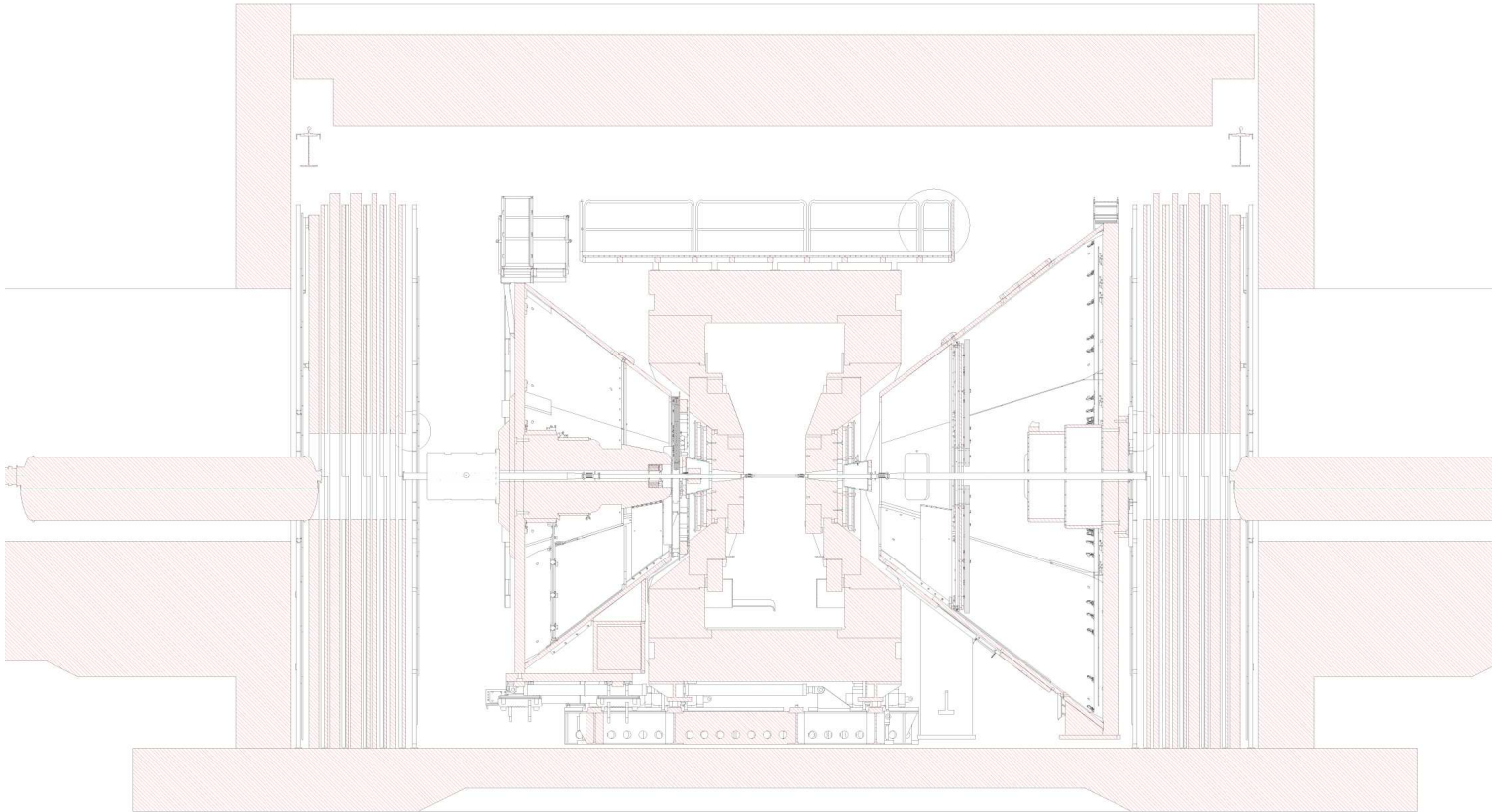
Figure 3.81: Section View of all RPCs installed.

### 3.6.2 RPC Gas and Safety Systems

The gas mixture for the RPC chamber will be R134a(95%)+ISO(4.5%)+SF$_6$(0.5%). The biggest concern is that R134a is very heavy (4.245 kg/m$^3$) and can produce a large pressure gradient in large size chambers like RPC2 and RPC3. The chamber can only hold up to 10-20 mbar before being damaged. Therefore the gas system must be able to protect the chamber from overpressure while satisfying requirements from other factors like gas operation rate. The factors like the gas purge rate, operation rate and operation pressure can be accommodated in the design by adjusting input pressure regulators and maintaining a desired vent line pressure with a PID controller (proportional-integral-derivative controller) and maintaining a stable pressure at the input of the compressor.

Here we discuss one possible design of the gas system. Figure 3.82 shows the global diagram of the system. R134a, ISO and SF$_6$ are mixed according to the proper ratio and put through the chamber. The gas compression system on the downstream of the chamber produces a proper negative pressure to suck the gas out for recycle. The oxygen and water vapor in the gas mixture are removed via the purifier and dryer. Then the gas is put through the analyzer to check the purity before being sent back into the chambers. The recycle procedure is mainly for economic reasons and possible safety concerns.

Figure 3.83 shows the finer details of the system. For illustration the diagram shown in the figure has only one input and output per sector. In reality, each detector module can have one input and one output to reduce the pressure gradient but this depends on the space available for installing the system. For convenience, the upstream pressure can be set to be the same for all gas channels. One pressure indicator (PI) on each channel is used to display the pressure and to adjust the pressure manually when necessary so that the internal pressure of each chamber can be set to the same value. Downstream of the chamber, an output flowmeter is used for controlling the output flow rate and therefore the pressure is paralleled with a bubbler to prevent overpressure in the chamber. The flowmeter will also be used to hold back the gas in the detector to prevent it from siphoning out. The hydrostatic pressure for the gas mixture is 0.301 mbar/meter. In the worst case when we have to have one gas input and output per sector, the maximum pressure gradient is about 1.5 mbar which is far below the 10 mbar threshold. In the case of the large pressure changes caused by, for example a hurricane, the air compression system shown in Fig.3.77 will automatically adjust the output flow rate to balance the pressure. The bubbler will also be able to prevent chamber overpressure when the compression system malfunctions.

Figure 3.84 shows one possible design on how the gas flows inside RPC1A and B. One of the two gaps of RPC1 is split from the middle to allow signal readout. The gas goes into the chamber from the top module of the split gap and exhausts from the diagonal side of the module. Then the gas flows into the top of the second gap and exhausts to the diagonal side the gap and continues to flow into
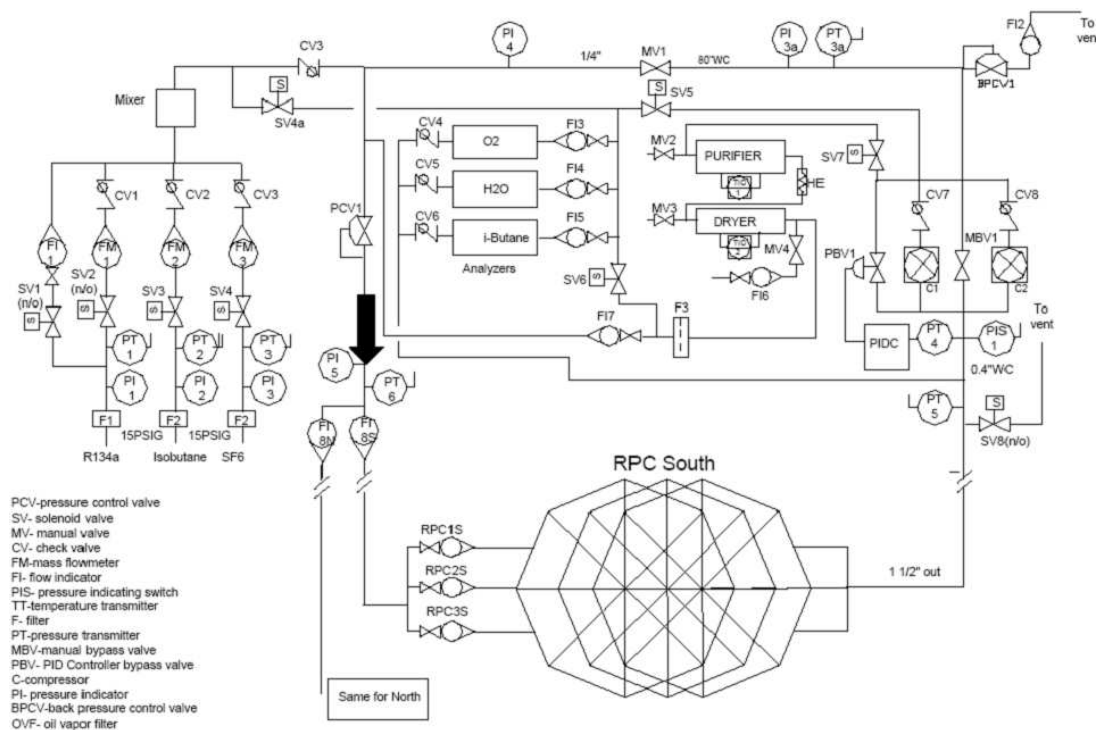
Figure 3.82: Global diagram of a possible muon trigger RPC chamber gas system design.

the upper side of the bottom module in the first gap and exhausts diagonally again.

Figure 3.85 shows the possible design for the gas flow inside RPC2 and RPC3. The gas goes into the module from the upper side of the first gap and exhausts diagonally from the first gap. The gas continues flowing into the upper side second gap and exhausts diagonally.

ISO is a flammable gas and can be safely handled by the existing PHENIX safety alarm system. R134a and $SF_6$ are denser than air and can displace air in lungs and result in asphyxiation if excessively inhaled. $SF_6$ is heavier and can deposit in the small confined space for a long time and lead to a asphyxiation hazard to people who enter it. To address all these concerns, we plan to install multiple $SF_6$ sensors in the IR and gas mixing house. The sensor is based on non-dispersive infrared technology and has reasonable sensitivity and low price. One good candidate is the 8-channel sensor from SENTEC company. The sensor is equipped with both sound and strobe alarm systems and can scan the 8 channels in serial in 15 minutes with a sensitivity of 10 ppm that is far below the $SF_6$ occupational limit. Since it's based on infrared technology, it can also serve as a R134a detector and can detect 300 ppm of R134a. This is well below the 8-hour
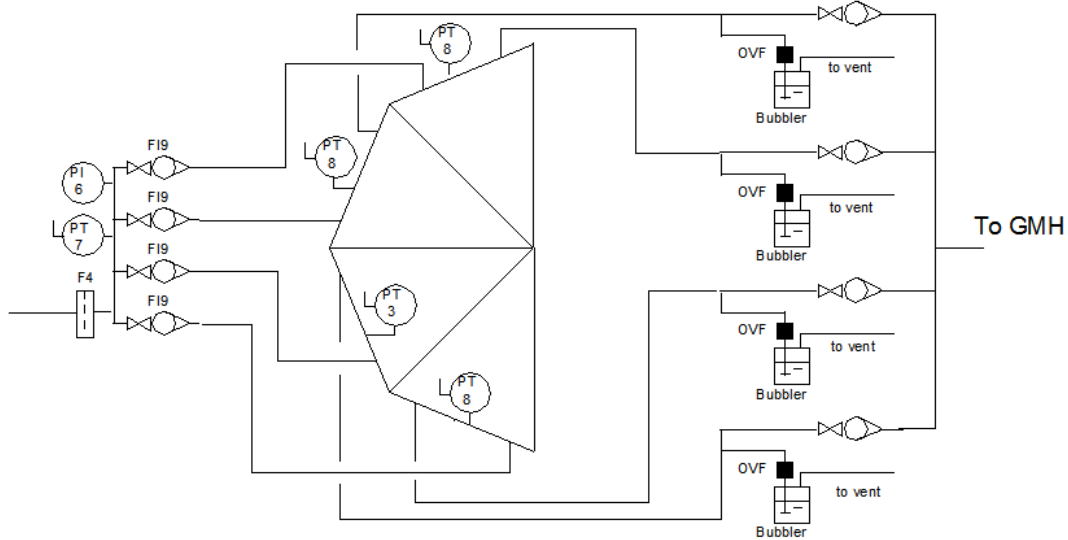
Figure 3.83: Finer details on the gas system design and illustration of how the pressure of individual channels is balanced.

overexposure limit of 1000 ppm. The detector has 3 alarm levels and 0-10 vdc or optional 4-20 mA analog output which enable it to be easily plugged into the PHENIX safety system. Each channel has a sampling distance of 250 ft. Therefore by employing a few of this kind of sensor, we can quickly detect gas leakage in the whole area of the IR and gas mixing house. The details of the sensor can be found in the attachment Figure 3.7.2 at the end of the chapter.

### 3.6.3 Muon Tracker FEE Mechanical Structure

New Front End Electronics (FEE) of the muon tracker are composed of an AD board and a TX board. Each AD board and TX board are enclosed by an individual chassis. The AD board chassis has a backplane which has two major purposes. Small raw analog signals from the cathode strip of the muon tracking chamber are fed into the backplane and then divided into the new FEE for trigger upgrade and the old FEE for the original readout system. The other purpose is supplying electrical power. Due to feeding the small analog signal, the AD board must be close to the old FEE system, so it will piggy back on the old FEE.

Three yellow boxes in Figure 3.86 are AD board chases for station2 which are mounted on the top of the old FEE chassis. The AD board chassis for station 3 is installed the same way on the old station 3 FEE. These chassis are located out of Muon Tracker fiducial volume.
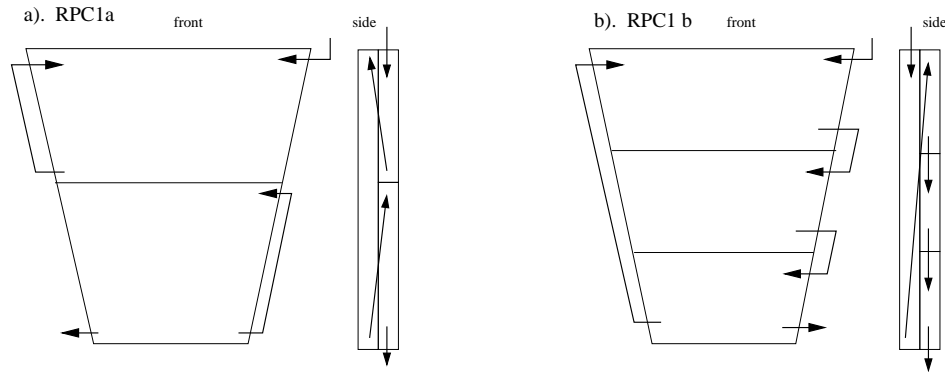
Figure 3.84: Gas flow pattern inside the chamber: a) for RPC1A and b) for RPC1B.
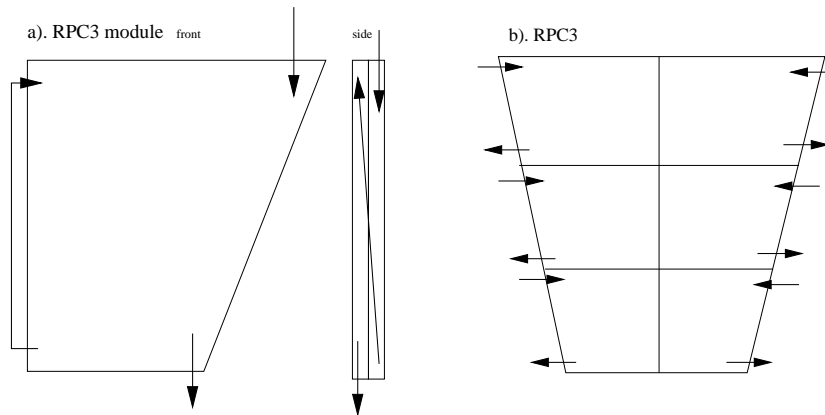


Figure 3.85: Gas flow pattern inside the chamber: a) for one RPC2 or 3 module and b) for RPC3.

The digital binary signals from the AD board are propagated to the TX board which is located on the space which is indicated by the white arrow in Figure 3.86.

Figure 3.86 shows the AD board and TX board locations for station 1 of the south arm. The AD board chassis is mounted on the old FEE chassis as well for station 2 and 3. The TX board chassis is mounted on the side of the muon magnet which is shown as a green box.

The north arm has a similar but a little larger magnet and chamber size.

Both types of chassis need electrical power and a cooling water supply/return to remove electronics heat. TX board needs an optical link for the beam clock, signal transmission, and arc-net for slow control. The arcnet is daisy chained to the AD board.

Figure 3.86: Location of station 2 new FEE. Yellow boxes are new FEEs which are piggy backed on the old FEE. The TX board is installed at the space indicated by the white arrow.
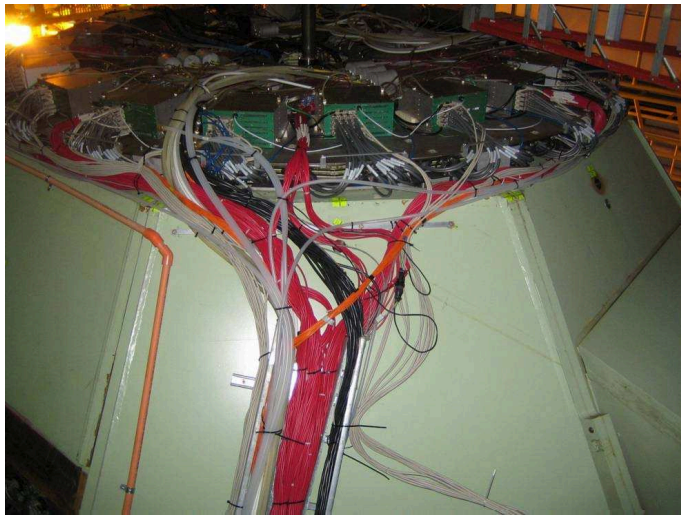


Figure 3.87: Photo of south station 1 with muon magnet. FEE location is indicated by the white arrow and TX board chassis are indicated by the green rectangular.

## 3.7 Quality Assurance

### 3.7.1 Resistive Plate Chamber Quality Assurance

**Introduction**

The PHENIX Forward Muon Trigger RPC production model will be similar to what CMS had. The bakelite sheets will be purchased from Italy and shipped to Korea where the gas cells will be produced by the group at Korea University. This group has been making RPC gas cells for CMS for the past three years and has agreed to produce similar gas cells for PHENIX. The chamber frame components will be made by the combined group (CIAE and KPU) in China. The final assembly will be done at BNL.

In order to assure the overall quality of the chambers, we have studied the QA process in CMS and will make sure that high quality testing is done for each stage of the chamber production. These tests mainly include:

- Bakelite inspection at the factory in Italy before shipping to Korea.

- Gas cell inspection in Korea before shipping to BNL.

- Gas cell inspection at BNL upon arrival (spacer, gas leakage, etc.)

- Main chamber certification tests (see details below).

The quality control of the RPC chamber is accomplished with a series of accurate measurements and tests intended to verify the correctness of the assembly and detector performance. The quality control procedure consists of the main certification tests and subsidiary control tests. The main tests regard leakage current versus high voltage curves, chamber efficiency and noise versus high voltage and front-end voltage threshold. The subsidiary control tests regard pulse test, gas volume leak test, front-end current absorption, and gas volume leakage current temporal drift.

**Quality Assurance in Korea**

For the quality control of the gas gaps, two kinds of tests will be performed in Korea before shipping them to BNL. The first test is checking the gas tightness and failures of spacer bonding for each gas gap. The second test consists in the measurement of the current values of the gas gaps at several high voltage settings. To search for gas leaks and failures of spacer bondings, an over-pressure of 20 hPa is slowly applied to each gap placed on the flat metric table. For a gas gap to be qualified, the loss of the applied pressure should be less than 0.2 hPa over a 15 minute period. In addition, no failure of a spacer bonding is required with the presence of 20 hPa over pressure. The gas gaps, showing significant gas leaks,

Table 3.15: Current limits at 8.5 and 9.4 kV for qualified CMS RE2/2 gas gaps.

|  | 8.5 kV | 9.4 kV |
|---|---|---|
| Small cut gaps | 2.0 $\mu$A | 3.0 $\mu$A |
| Large cut gaps | 3.0 $\mu$A | 5.0 $\mu$A |
| Full gaps | 5.0 $\mu$A | 8.0 $\mu$A |

can be fixed by dispensing epoxy on the leak positions. For the CMS forward RPCs, roughly 5% of the assembled gas gaps were rejected due to the failure of a spacer bonding or a misalignment of the block component for gas in/outlets, which causes serious gas leaks.

The gas mixture for the measurement of the chamber currents is 96.5% $C_2H_2F_4$ and 3.5% $i$-$C_4H_{10}$. An amount of the mixed gas, equivalent to roughly 15 times the detector volume, is circulated through the gas gaps before applying the high voltage. At the beginning of the test, the high voltage applied to the gas gaps is set to 2 kV to check if there exist any disconnection and/or electrical shortage. Then, the high voltage is raised up to 8.5 kV slowly over 5 hours. The high voltage is then kept at 8.5 kV, which is the beginning of the gas avalanche, for 12 hours to observe the behavior of the ohmic dark currents of the gas gaps. The high voltage is then increased with steps of 100 V from 8.5 to 9.4 kV. The expected high voltage value to obtain a 95% detection efficiency at 1013 hPa is 9.1 kV with the gas mixture of 96.5% $C_2H_2F_4$ and 3.5% $i$-$C_4H_{10}$. The high voltage for the gas gaps is kept at 9.4 kV for 36 hours to monitor the current behavior at the operation voltage. The acceptance criteria for dark currents depend on the size of the gas gap. One example of such criteria for the CMS RE2/2 RPCs is shown in Table 3.15. Figure 3.88 shows the facilities for the high voltage test and 22 RE2/2 full gas gaps for CMS, placed on multi-layer shelves.

**QA Plan at BNL**

The QA at BNL represents the very first full chamber characterization and allows extraction of statistical information useful to monitor the assembly line and give useful feedback for improvements. The RPC QA will be performed in the same area where the RPC will be assembled in order to minimize potential damage to the chambers from moving from place to place.

We have started to set up a RPC assembly and Q&A facility in the CAD department at BNL. The layout of the facility is shown in Figure 3.89. The combined CIAE and PKU group is currently setting up a RPC test stand where a prototype RPC assembly can be exercised before all the chamber components will be made in the factory. This test stand will then be shipped to BNL for full

Figure 3.88: Facilities for the high voltage test at Korea University. Three high voltage supplies, four 12-channel current measurement units, and a 6-channel gas supply system are shown on the left panel. The right panel shows 22 RE2/2 full gas gaps for CMS, placed on multi-layer shelves, for the test. After completing the high voltage test, a bar code is assigned to each gas gap for later tracking.

chamber assembly following the overall schedule of this project.

## 3.7.2  Muon Tracker FEE

All electronics for the Muon Tracker FEE upgrade are checked for proper operation and stability before installation and then installed at the specified location. After installation a test of the integrated system is performed.

### Quality Assurance Before Installation

All electronics for the muon tracker upgrade must be checked before installation on the test bench. Each board will be tested individually.

Configurations of each test bench are shown in Figures 3.90, 3.91, and 3.92.

The AD board in Figure 3.90 is fed an analog hit pattern by a pulse pattern generator which emulates the cathode strip of the muon tracker. Then they are converted to the binary digital signals as LVDS output and transmitted to a FIFO module which acts as the TX board. These input and output hit patterns are compared by the PC and the functionality and stability of the AD board is evaluated. The PC can control the threshold of the discriminator on the AD board. A beam clock emulator generates the beam clock.

Figure 3.91 shows the configuration of the TX board test bench. The pulse pattern generator, which acts as the AD board, feeds digital hit data and the TX
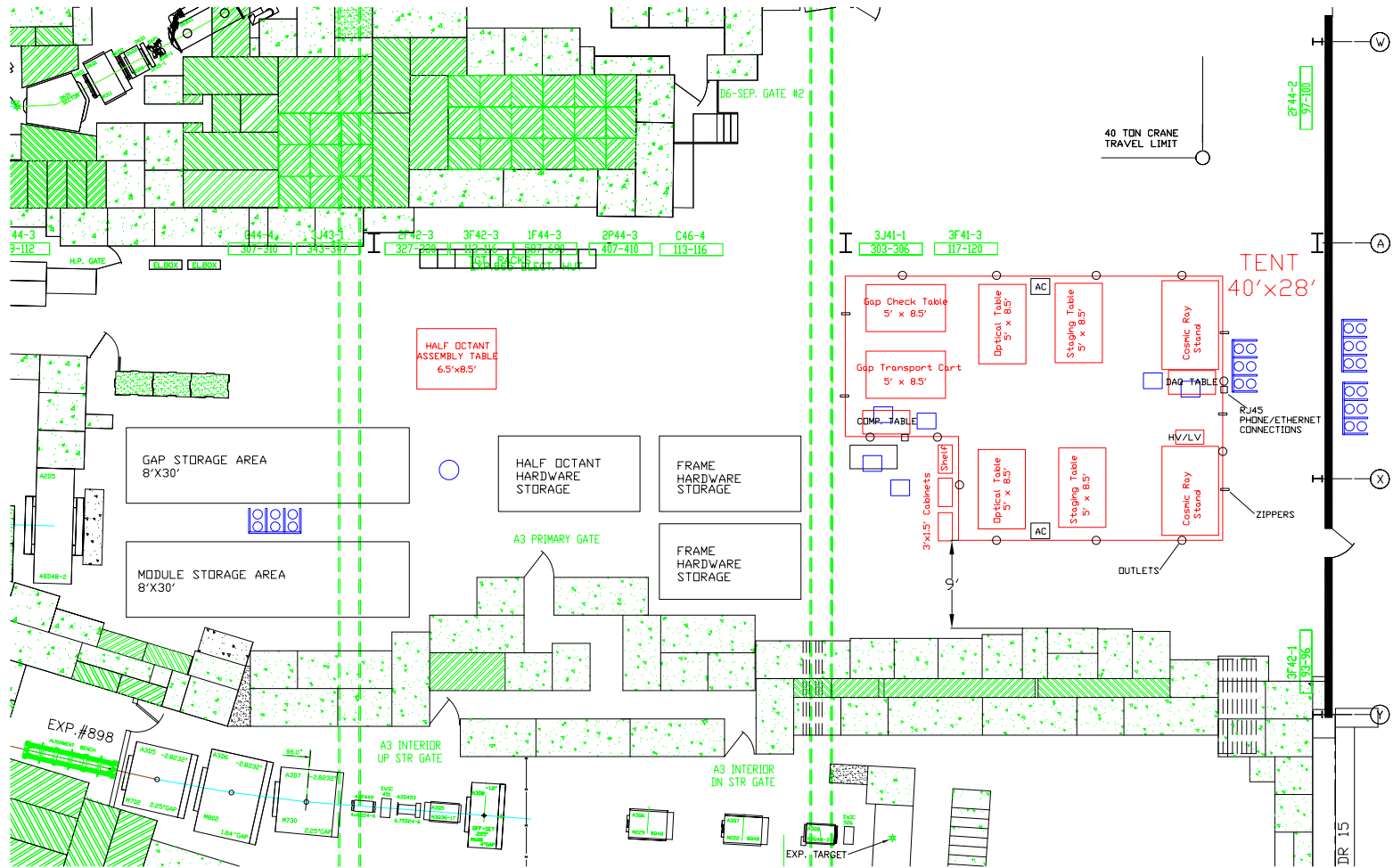
Figure 3.89: Area layout for RPC assembling and QA.
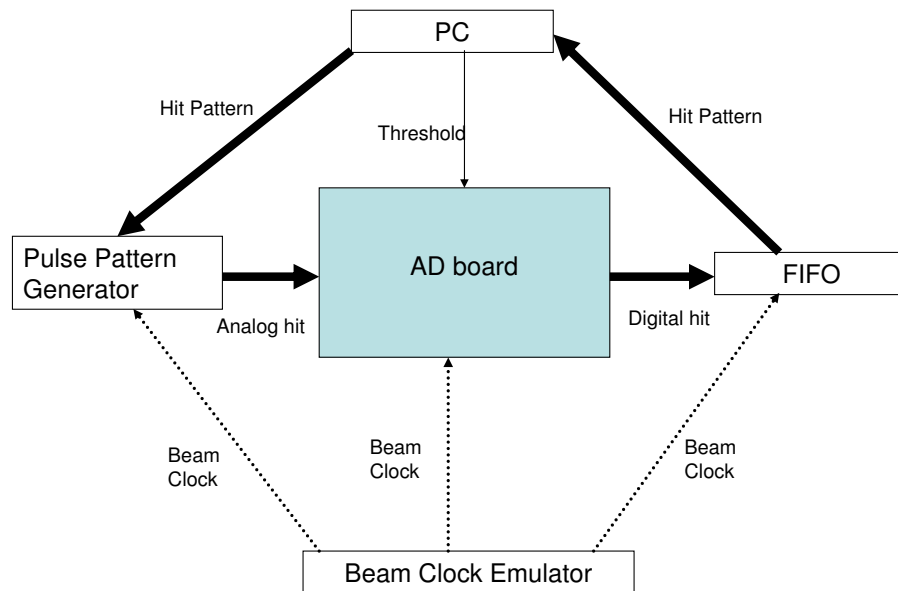
Figure 3.90: Test bench for AD board.

board converts this to serial and transmits it to ROCKET I/O. ROCKET I/O converts the information to parallel and the PC compares the input and output.

The merger board has two serial inputs and one serial output. All of them are connected to ROCKET I/O and the PC compares input and output patterns as in the other test bench.

**Installation**

The chassis of the AD board is mounted on the top of the old FEE chassis, and the TX board chassis is mounted on the muon magnet. The chassis are connected to DC power lines and cooling water supply/return lines. Each individual board has its own voltage regulator, so voltage drop along the power supply line is not so critical to determine the operation voltage. The ARCNET line is needed for slow control and downloads the FPGA program for the TX board and threshold values for the AD board.

In the case of a noisy AD board, an individual AD board can be switched off by remote control, because it is not easy to access to fix it during beam operation. The merger boards are installed in the rack room of the counting house side.
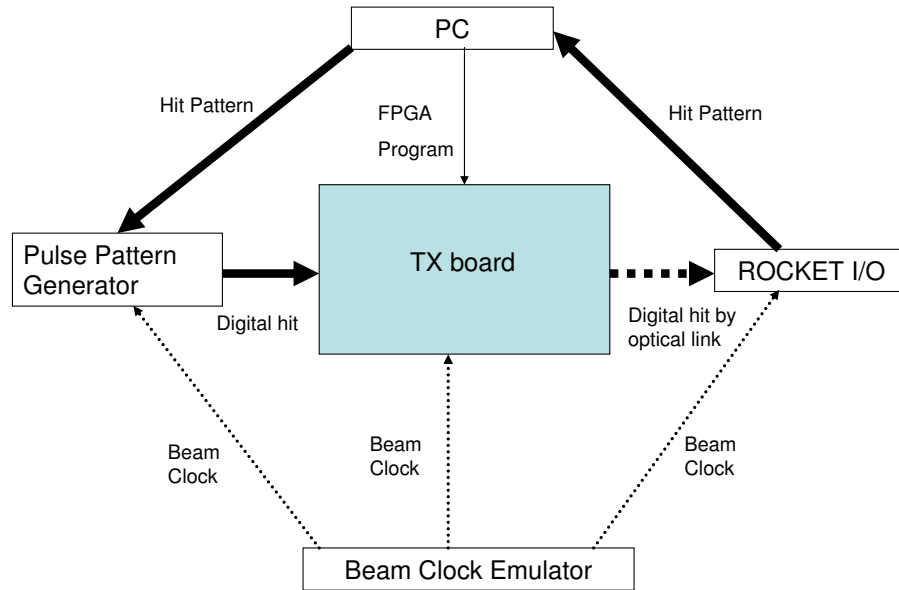
Figure 3.91: Test bench for TX board.
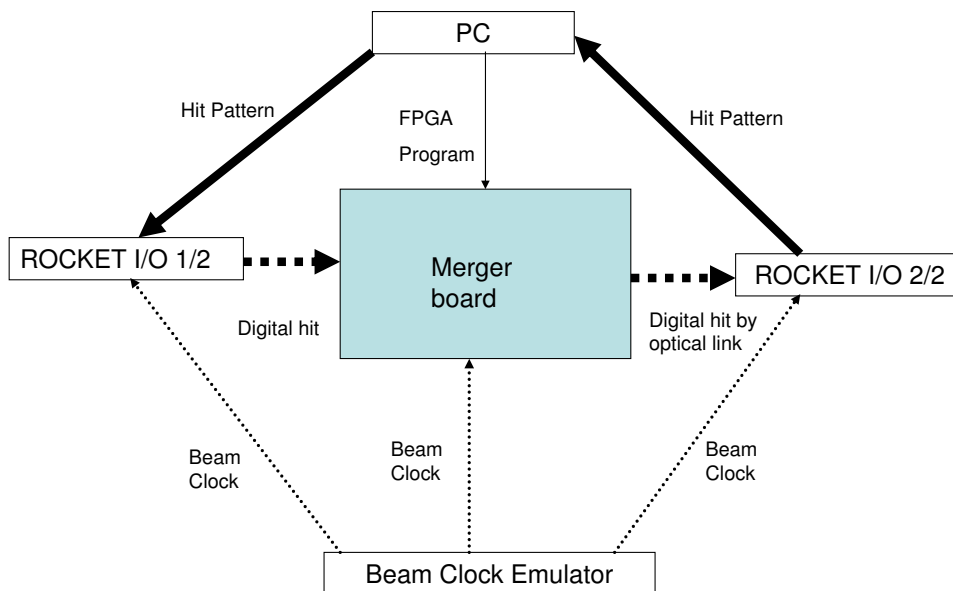


Figure 3.92: Test bench for merger board.

**SF6-MCD SULFUR HEXAFLUORIDE**
**Loss Prevention Monitors**

The Environmental System SF6 Multiple Channel Detection monitors are advanced "Early Warning" loss detection monitoring systems designed specifically for SF6-charged systems.

SenTech's SF6-MCD models are cost effective, self-contained active air-draw sampling systems offering highly reliable Infrared based performance with the flexibility to satisfy a wide range of continuous monitoring applications. SenTech's monitors utilize NDIR (Non-dispersive infrared) and pyroelectric (absorptive sensing) technology featuring multi-zone detection point capability from a single field-programmable self-contained metal enclosure featuring SenTech's unique built-in leak wait period that minimizes nuisance false alarms of halogen gases.

The SF6-MCD's multiple channel architecture combines Infrared detection of halogen based refrigerants/agents available in single, four, eight and sixteen zone models. Each zone is capable of monitoring and responding to SULFUR HEXAFLUORIDE at concentrations levels as low as ten parts per million (10ppm). In addition, the MCD's remote sensing capabilities for other gasses through up to four remote transmitters offers an unique configuration that allows the SF6-MCD to be set up as a combined gas monitor that senses SF6 and additional gasses by remote sensors including Carbon Monoxide, Carbon Dioxide, Hydrogen and Oxygen.

SenTech's SF6-MCD monitors provide compliance with ASHRAE Standard 15.

**SF6-MCD SULFUR HEXAFLUORIDE**
**Loss Prevention Monitors**

**FEATURES**

- Detects Sulfurhexafluoride and SF6 agents.
- Infrared sensor technology
- Active air draw sampling system
- Multiple zones (1,4,8,16, zones)
- Sampling distance of 250 ft (500 ft coverage)
- Multiple channel architecture allows multiple gas detection configurations
- Factory calibrated-/-auto-zero w/fresh air - No field calibration required
- Four line digital display w/ keypad for programming and operation
- Visual indication of alarm levels and system malfunction
- Three alarm levels (Four 5 amp contacts per relay)
- Separate programmable horn alarm relay
- 0-10 vdc analog output
- Setup function and Keypad access password protected

- Optional Nema 4 enclosure with keyed lock
- Optional 4-20 ma analog output
- Optional individual zone alarm output to indicate alarm zone
- Optional four channel analog input for multiple channel detection
- Optional serial data output (RS 485)
- Optional remote control interface
- ETL listed - conforms to UL STD 3101-1 and CAN/CSA No. 1010.1 (Pending)

**SF6-MCD MODELS**

- SF6-MCD1 (1 Zone, 3 Alarm levels)
- SF6-MCD4 (4 Zone, 3 Alarm levels)
- SF6-MCD8 (8 Zone, 3 Alarm levels)
- SF6-MCD16 (16 Zone, 3 Alarm levels)
- SF6-MCD Custom Configurations

**ACCESSORIES**

- Remote PPM indicator w/audible silent switch
- Remote transmitters: Oxygen & Toxic gases
- Strobe light, Horn, Combination strobe/horn
- Air-sampling pickup tubing

**SPECIFICATIONS**

**Sensitivity**
As low as 10 PPM

**Weight**
32 lbs, (14.4 Kgs)

**Dimensions**
W 16.5in x H 15in x D 6.75in
(42cm x 38.1cm x 17cm)

**Power Requirements**
120 Volt 60 Hz

**Range**
0 to 1000 PPM

**Alarm Trip Points**
Low Alarm  0 to 100% of Full Scale
Main Alarm 0 to 100% of Full Scale
High Alarm 0 to 100% of Full Scale

**Operating Environmental Range**
32° - 125° Fahrenheit
0° - 50° Celsius

**Alarm Outputs**
Indicator Light
Alarm Relays with 4 Form C contacts
(5 amps maximum)
RS 485 computer interface

**SenTech Corporation**
5745 Progress Rd.
Indianapolis, IN 46241
Tel: (888) 248-1988
Fax:(317) 248-2014
www.sentechcorp.com

Figure 3.93: Details of the SF$_6$ sensor.

# Chapter 4

# Monte Carlo Study of $W$ Physics with the PHENIX Muon Systems

## 4.1 Background Studies and Event Rates

### 4.1.1 Introduction

There is great interest in measuring the spin contribution of $u$, $\bar{u}$, $d$, $\bar{d}$ quarks in the proton via the production of $W$ bosons ($u + \bar{d} \rightarrow W^+$ and $d + \bar{u} \rightarrow W^-$). The rate for $W$ production in proton-proton collisions at 500 GeV is small and thus the measurement requires high luminosity running and a high signal to background ratio. In the PHENIX muon spectrometers the high transverse momentum ($p_T$) muons from $W$ decay are measured to tag the $W$ charge sign.

There are multiple possible sources of background for high $p_T$ muon candidates to the $W \rightarrow$ muon measurement. Here we list a few possible sources and then go into greater detail on what is believed to be the dominant source.

1. High $p_T$ muons from heavy flavor (D and B) semi-leptonic decays. However, earlier studies indicate the $p_T$ distribution even for beauty falls off and have contributions well below the $W \rightarrow$ muons at $p_T > 20$ GeV/$c$.

2. Some light hadrons (pions and kaons) will decay into muons before the front absorber and then penetrate the muon spectrometer as muons. These contributions are included in our simulation. However, the $p_T$ distribution for these light hadrons falls steeply and thus mostly contributes at low $p_T$.

3. Decay muons, which undergo a large scattering interaction in MuTr station 2 and thus have a mis-reconstructed high $p_T$. We find that this contribution is small, noting that station 2 is low material.

4. High $p_T$ light hadrons can punch through the absorber and into the MuID. These reconstruct near the correct $p_T$.

5. Light hadrons can punch through the absorber, and then decay into muons inside the MuTr tracking volume. The kink angle from the decay can lead to an incorrect determination of the reconstructed $p_T$, and thus low $p_T$ hadrons can create "fake" high $p_T$ background.

The simulations for this study, except the subset without hadronic interactions, include backgrounds 2-5. We find types 2 and 3 to have negligible contributions, so our discussion focuses on the main contributors, types 4 and 5. We report here on the estimated level of these backgrounds, taking into account the capability of the current detector to reject such backgrounds.

We find that fake high $p_T$ tracks, type 5, are the dominant source of background and lead to a predicted signal/background of ~0.3 with the current detector, including the RPC and MuTr FEE trigger upgrades proposed in this CDR. Due to the nature of the background, knowing the exact background level to better than 50% may be challenging and has not been worked out. A signal/background of ~5.0 is probably necessary to make this measurement. Thus, we feel the current detector is insufficient for the precision measurement we hope to achieve. In the last sections of this document we outline some possible detector upgrades and their likely impact on these backgrounds.

### 4.1.2 Physics Requirements

The desired measurement is of the parity-violating single-longitudinal spin asymmetry:

$$A_L^W = \frac{1}{P} \times \frac{N_-(W) - N_+(W)}{N_-(W) + N_+(W)} \tag{4.1}$$

The uncertainty in the case of no background is then

$$\sigma_{A_L^W} = \frac{1}{|P|} \frac{1}{\sqrt{N_+(W) + N_-(W)}} \tag{4.2}$$

Ignoring issues of the kinematic smearing caused by the detection of decay muons from $W$ bosons which are not at rest, the asymmetry must be corrected for the effects of background; this requires knowledge of the background fraction $r$ ($r = B/(S + B)_W$) and the asymmetry of this background $A_L^B$. To find the physics asymmetry $A_L^W$ from the measured asymmetry $A_L^M$, we can use the standard correction

$$A_L^W = \frac{A_L^M - r A_L^B}{1 - r} \tag{4.3}$$

which has an associated uncertainty of

$$\sigma_{A_L^W} = \frac{\sqrt{\sigma_{A_L^M}^2 + r^2 \sigma_{A_L^B}^2}}{1 - r} \tag{4.4}$$

This assumes that $r$ is well enough known that the uncertainty of separating signal from background does not contribute, i.e., one can accurately determine the background. From the discussion in the remainder of this document, the issue of knowing the background level is non-trivial and needs detailed study. Usually this is studied as a systematic error (e.g., varying the constraints that define the particle ID and sidebands of a mass peak. In the case of the $W$ decay lepton, however, there will not be a mass peak. Instead the best definition of the signal therefore will follow from a measurement of the $W$ and $Z$ cross sections and the comparison of the cross sections to theory.

The formula above shows that if $r$ is nearly 1, i.e., S/B is very small, then the uncertainty in the physics asymmetry blows up, independent of the values of the asymmetry of the background. If the background has a spin asymmetry, which is comparable or larger than the $W$ physics asymmetry, then it must be precisely known in order to not dominate the measured asymmetry. In general, the damage done by the background is not a simple function of S/B because of the additional effect of the background asymmetry $A_L^B$ relative to the $W$ asymmetry, but it is easy to calculate for particular choices.

As a simple example, lets assume that we have S/B = 0.1, 1, and 10, and the true $W$ asymmetry is 10%. Assuming 10,000 measured events (signal plus background) and $A_L^B = 0$. The results for the relative statistical uncertainty are shown below.

| S/B | $\sigma_{A^W}/A^W$ |
| --- | --- |
| 0.1 | 1.5 |
| 1 | 0.24 |
| 10 | 0.11 |

Again, this assumes that the separation between signal and background is well defined, and also that the asymmetry determined for pure background comes reliably from the background events in the total sample.

## 4.2   $W$ Production Modeling

In the spin planning document [89] the estimate for $W$ yields was using PYTHIA and RESBOS [90]. It estimates the cross sections for $W^+$ and $W^-$ from proton-proton reactions at 500 GeV as 1.3 nb and 0.4 nb respectively. For 800 pb$^{-1}$ of integrated RHIC luminosity, the document states that "PHENIX expects about 8000 $W^+$ and 8000 $W^-$ in the muon arms [for $p_T \geq 20$ GeV/$c$]." It notes that the roughly equal numbers are due to the different production levels being canceled by the different kinematic distribution of the $W$s.

For our studies in this document, we are using PYTHIA 6.205. For detail see AN506 [91].PYTHIA yields cross sections for $W^+$ and $W^-$ of 1.0 nb and 0.3 nb, respectively. Note that these are approximately 30% lower than the results quoted

Figure 4.1: $W \rightarrow$ muon $p_T$ distributions in the PHENIX muon pseudorapidity ($\eta$) range 1.2-2.2 (corresponding to theta angles of 12.6 and 33.5 degrees).
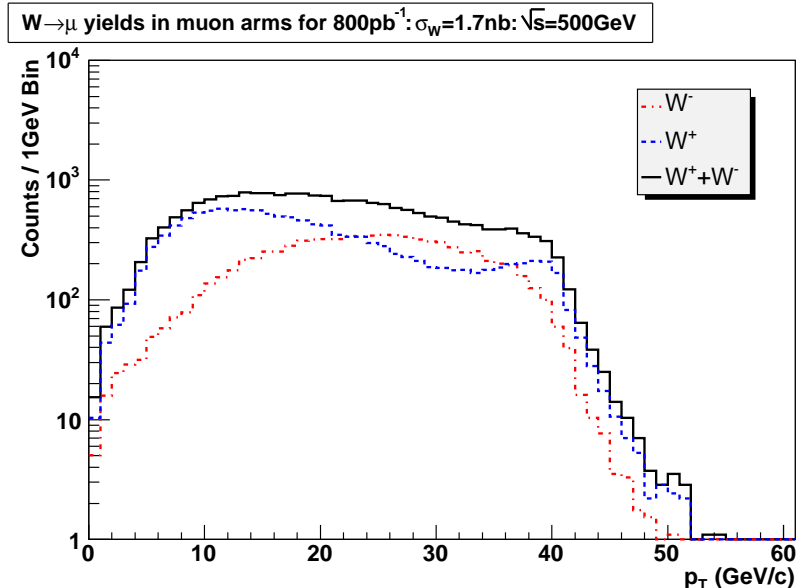
above from PYTHIA + RESBOS. For the numbers used in the rest of this Analysis Note we will scale up by 30% our PYTHIA cross section values to match the previous documented results.

If we integrate the $p_T$ distributions shown in Figure 4.1 for $p_T \geq 20$ GeV/$c$, we obtain 7306 $W^+$ and 7664 $W^-$ (combining the statistics from North and South arm). These results are very consistent with those quoted (8000 of each) in the document. For other kinematic distributions from this study, see AN506 [91].

## 4.2.1 Pion and Kaon Production Modeling

The sources of background we are modeling in this note (types 2-5) originate from the abundant production of pions and kaons in the proton-proton collisions. We need as input to our Monte Carlo simulations the pseudorapidity and $p_T$ invariant distributions of both signed pions and kaons in proton-proton reactions at 500 GeV pointed toward the muon spectrometers (pseudorapidity $\sim$1.2-2.2).

We are using the UA1 measured transverse momentum $p_T$ distribution of unidentified hadrons $[(h^+ + h^-)/2]$ in proton-antiproton collisions at 500 GeV at midrapidity, and their results are described in [93]. In Table 3 of [93], they fit the $p_T$ distributions to a power law. We also need to know the fractions of these unidentified hadrons which are pions and kaons of both signs. At the ISR there are measurements in proton-proton reactions at 53 GeV (and lower energies) of

pions, kaons and protons/antiprotons [94].

We roughly estimate $\pi^+$/total = 0.32, $\pi^-$/total = 0.32, $K^+$/total = 0.12, $K^-$/total = 0.12 and assume the ratios are independent of $p_T$ over the range 1-10 GeV/$c$. These estimates are only good at the ±30-40% level, which is adequate for this study. For backgrounds originating from hadrons at $p_T > 10$ GeV/$c$ we use PYTHIA (see Section 4.2.4).

Thus, if we utilize the UA1 spectra and the ratios for the different light hadrons detailed in AN506 [91], we obtain:

$$d\sigma[\pi] = 0.32 \times 5.13(barns/GeV^2)(1 + p_T/1.61)^{-10.64}p_Tdp_Tdy \qquad (4.5)$$

$$d\sigma[K] = 0.12 \times 5.13(barns/GeV^2)(1 + p_T/1.61)^{-10.64}p_Tdp_Tdy \qquad (4.6)$$

For now we will ignore any rapidity dependence, and thus assume that the particle production is flat from pseudorapidity 0 to 2.2. Note that we are concerned with pions and kaons at pseudorapidity 1.2-2.2. We have checked this rapidity dependence using PYTHIA, and we find it to be less than a factor of 2. These yield estimates are probably only accurate at the level of a factor of 2.

## 4.2.2 Background Simulation Results with the Existing Detectors

**Simulation details**

We have run the Monte Carlo simulation for single particles through GEANT based PISA + Detector Response + Reconstruction and output an evaluation Ntuple with reconstructed track and Monte Carlo truth information. We ran 10 million single particles for each of the following types and in each of the following $p_T$ bins ($\pi^+$, $\pi^-$, $K^+$, $K^-$ and $p_T$ 0-1, 1-2, 2-3, 3-4, 4-5, 5-6, 6-7, 7-8, 8-9, and 9-10 GeV/$c$). For each bin we throw the $p_T$ as flat within the range of the bin and the pseudorapidity is flat over the range $|\eta| = 1.4$-1.9. Thus, we have scaled the background up by a factor of 2 to account for the smaller $\eta$ range.

Some details of the Monte Carlo simulation are listed below. More are detailed in AN506 [91].

- $z$-vertex = 0.0 for all events

- We input MuTr and MuID efficiencies at 100%. We also input no dead areas in the detector.

- The MuTr common mode noise is turned on to give a more reasonable agreement between the Monte Carlo and real data. This gives a resolution on the order of 300 microns as opposed to the design goal of 100 microns.
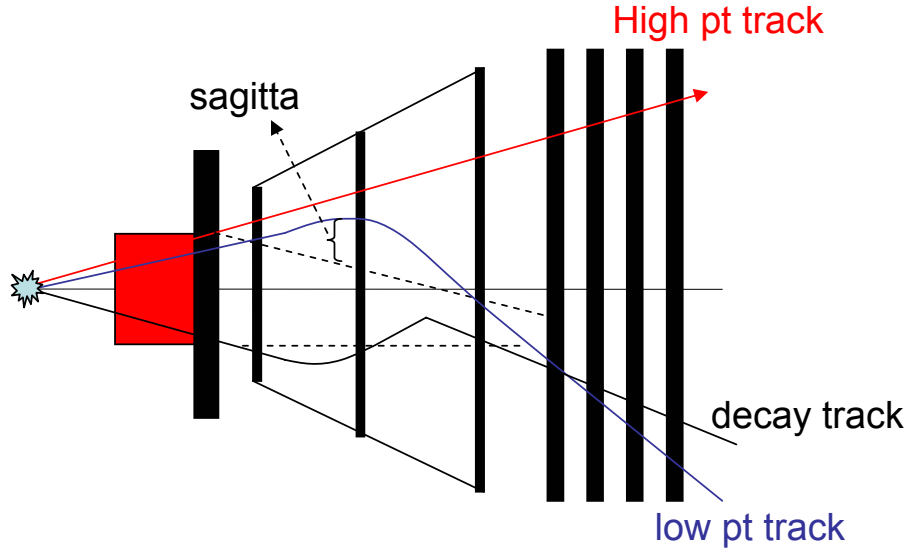
Figure 4.2: Diagram demonstrating how a decay of a low $p_T$ hadron can create a fake high $p_T$ track.

- No mis-alignments in the MuTr and/or MuID are applied. Thus we are assuming that none of the cut selections we might apply will be limited by the detector alignment.

**Fake high $p_T$ background**

A potentially significant background source has been identified where a low $p_T$ pion or kaon penetrates through the muon front absorber and then decays in the muon tracker (MuTr) volume. The kink in the decay can lead to a mis-measurement of the momentum and thus the incorrect identification as high $p_T$ as illustrated in Figure 4.2. Here we describe the main points of AN506 [91], a detailed study of this background.

In this section, we show results for the South Arm only. We consider a candidate to be reconstructed if the offline software finds a minimum requirement MuTr track and associated MuID road with at least one gap 4 hit (deep road). There are minimum hit requirements coded into the track and road finding algorithms and we utilize the default settings in CVS in pro.71.

First, we calculate the rate of reconstructed candidates as a function of reconstructed $p_T$ per single input particle to the Monte Carlo. We consider a minimum set of additional cuts, which are quite loose for real very high $p_T$ particles and motivated by well studied cut selections for the $J/\psi$ analysis [92]. We refer to this combination as "basic" cuts.

131
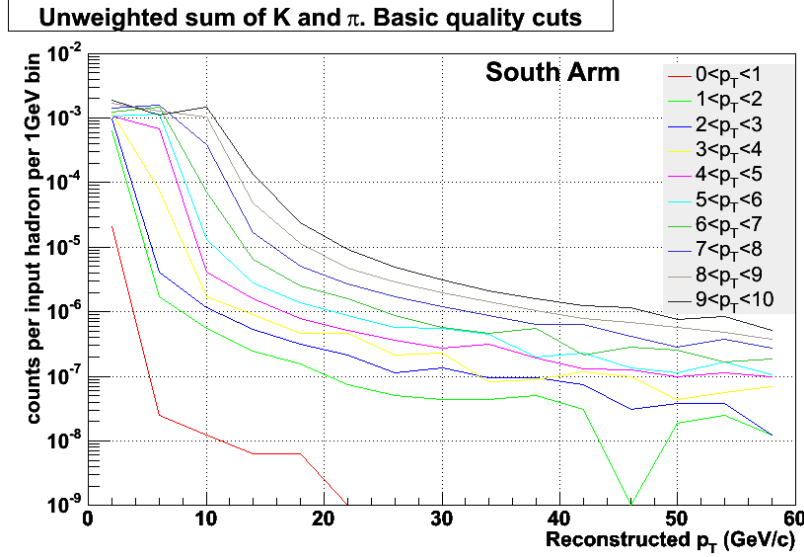
Figure 4.3: Rates per 1 GeV/$c$ $p_T$ bin per input hadron for combined pions and kaons after "basic" cuts. The species weighting is accounted for, but the production weighting is not.

1. DG0 < 20 cm [matching track and road spatial position between the MuTr track projected to the MuID gap 0 position]

2. DDG0 < 9 degrees [matching track and road angle of the MuTr track projected to the MuID gap 0 position]

3. MuTr track $\chi^2$/DOF < 30

4. MuID must have at least 8 of 10 possible hits

5. MuID road must be deep (at least one hit in gap 4 of the MuID)

In Figure 4.3, one can see that there is a peak in each distribution around the $p_T$ of the input hadron. This contribution is from hadrons with punch through (only dE/dx with no inelastic collisions) the nosecone absorber material and into the MuID. One can also see a distribution below this $p_T$ value. This contribution is from pions and kaons which shower or decay to muons before the front absorber. Thus, they typically have lower $p_T$ than the parent hadron. In addition there is a long tail of background candidates that extends to very high $p_T$. The source of this background is hadrons punching through to the MuTr and then decaying in the MuTr volume causing an incorrect momentum reconstruction. The high $p_T$ background is greater per input particle when the hadron has larger $p_T$. This is presumably because a smaller kink in the decay is easier to move the reconstruction toward a much higher $p_T$, see Figure 4.2.

**Weighted sum of K and $\pi$ with basic quality cuts**

**South Arm**
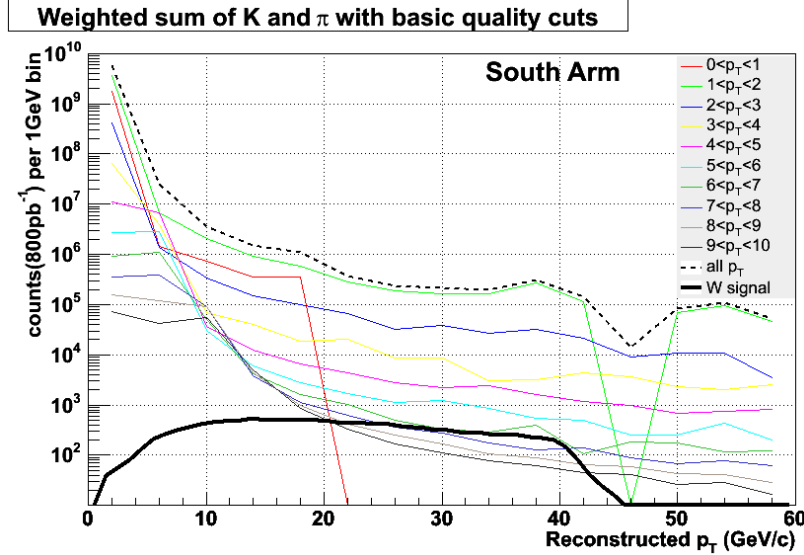
Figure 4.4: Count per 1 GeV/$c$ $p_T$ bin for 800 pb$^{-1}$ for combined production weighted pions and kaons after "basic" cuts. The estimate for $W \rightarrow \mu$ is also shown.

In order to determine the true background rate, we must weight the $p_T$ bins by the expected production rates as determined earlier in this note. After doing this, we combine the results of all particle species to determine the total background candidate rates as show in Figure 4.4.

We find that now the lowest $p_T$ (1-2 GeV/$c$) contributes the most to the background candidates since it has such a large production weight. Note that the $p_T$ 0-1 GeV/$c$ contributes only a small amount, but the statistics are a limitation since it gets the largest weight.

We compare this background level to the expected signal for the $W \rightarrow$ muons from our PYTHIA simulations. In the following, we assume 100% efficiency for $W \rightarrow$ muons with the range $|\eta| = 1.2$-$2.2$ and overlay the expected rate. This is shown in Figure 4.4 (note that this is both charge signs together). The background level is three orders of magnitude higher than the signal.

Note that the background distribution continues smoothly above $p_T > 40\,\text{GeV}/c$, but the $W \rightarrow$ muon signal does not. This means that this shoulder could serve as confirmation in real data of a good signal to background. However, we can also see the statistical limitations of our simulation sample size. In the $K^+$ 1-2 GeV/$c$ $p_T$ bin we ran 10M single particles and with the basic cuts there are only of order 100 candidates with $p_T > 10$ GeV/$c$. Thus, as we explore tighter cuts, we can only check additional rejections up to approximately a factor of 100. If we wanted to check rejection factors of $10^4$, we would need to run 100 times more statistics
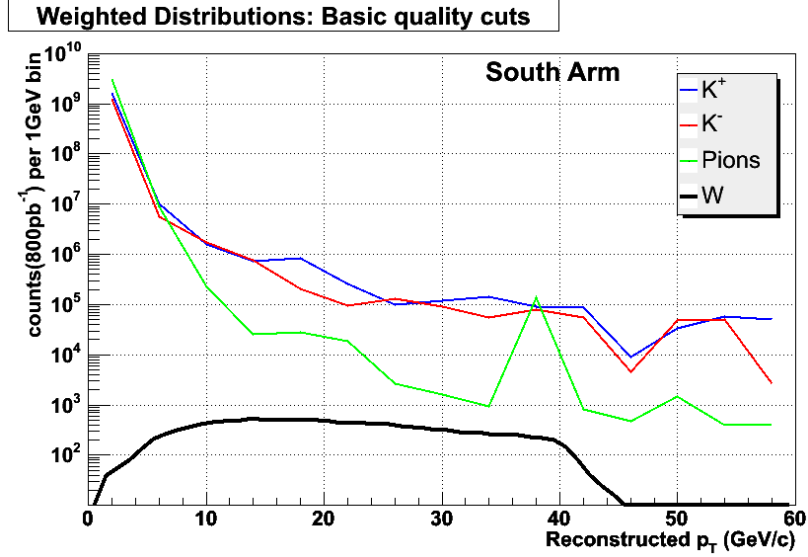
Figure 4.5: Breakdown of the background contributions by the originating light hadron type for 800 pb$^{-1}$ after "basic" cuts.

for the low $p_T$ kaon species.

In Figure 4.5 we plot the breakdown of the background contributions by the originating light hadron type. We plot the combined $\pi^+$ and $\pi^-$ contribution as "Pions" and then the different charge sign kaons separately. This background is larger for kaons than for pions due to the shorter lifetime ($c\tau$ kaon = 3.7 meters, $c\tau$ pion = 7.8 meters) and also the smaller Lorentz boost $\gamma$ for the kaon at the same $p_T$.

### Effect of absorbers on high $p_T$ background

As an addition to this analysis the effect of possible absorbers was tested. For this purpose 4 MC simulations with different detector geometries were created:

- original nosecone: This is the current PHENIX geometry with the current Cu nosecone.

- NCC: The current PHENIX geometry, but the nosecone replaced with Vasily's version of the nosecone calorimeter including the $W$ which will act also as absorber.

- NCC + 10 cm Fe absorber: Additionally to the NCC $W$ another absorber is added downstream of the central magnet in the lampshade region. This absorber covers the polar angles between 12 - 37 degrees and was assumed to be made out of iron.

134
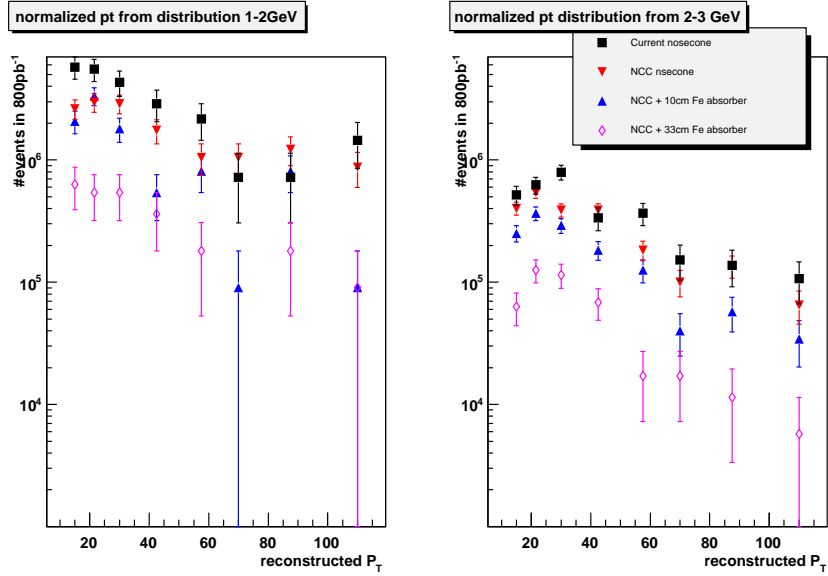
Figure 4.6: Transverse momentum distributions for 800 pb$^{-1}$ after "basic" cuts for generated $K^+$ in the $p_T$ ranges 1-2 and 2-3 for different detector and absorber geometries as described in the text.

- NCC + 33 cm Fe absorber: Instead of using 10 cm of Fe absorber the width was increased to 33 cm filling most of the available space before the muon magnets.

Since the contribution of $K^+$ at low transverse momenta are dominating the background only $K^+$ with transverse momenta between 1-2 and 2-3 GeV were created. The amount of statistics was between 11M events (for the original nosecone) up to 33M events (for the productions including absorbers). The momentum distributions rescaled for a 800 pb$^{-}$1 data sample can be seen in Figure 4.6. It can be clearly see that each additional level of absorbers reduces the amount of background significantly and reaches a reduction of about one magnitude with the NCC and the 33 cm of additional absorber installed.

The integrated reductions due to the additional absorbers are summarized in Table 4.1.

**Comparison of real data (200 GeV) and simulations**

We have looked at real PHENIX data from Run-4 proton-proton results as detailed in AN506 [91]. We plot the reconstructed $p_T$ distribution in the South Muon spectrometer per sampled interaction. For the plot we apply the "basic" set of cuts detailed in the previous section. Then to compare with the simulated

Table 4.1: Reduction factor of the fake high $p_T$ yields depending on the absorber geometry as discussed in the text.

| $1 < p_T < 2$ GeV | | | | |
|---|---|---|---|---|
| Simulation | Events (800 pb$^{-1}$) | % remaining | Events $p_T > 20$ GeV | Reduction Factor $p_T > 20$ GeV |
| Current nosecone | 26.915.205 | 100 | 19.225.146 | 1. |
| NCC | 17.040.471 | 63.3 | 13.370.215 | 0.695 |
| NCC + 10cm Fe | 10.273.438 | 38.2 | 7.119.312 | 0.370 |
| NCC + 33cm Fe | 2.703.536 | 10.0 | 1.892.475 | 0.098 |
| $2 < p_T < 3$ GeV | | | | |
| Simulation | Events (800 pb$^{-1}$) | % remaining | Events $p_T > 20$ GeV | Reduction Factor $p_T > 20$ GeV |
| Current nosecone | 3.444.264 | 100 | 2.697.499 | 1. |
| NCC | 2.648.829 | 76.9 | 2.100.185 | 0.779 |
| NCC + 10cm Fe | 1.520.200 | 44.1 | 1.120.147 | 0.415 |
| NCC + 33cm Fe | 491.493 | 14.3 | 400.052 | 0.148 |
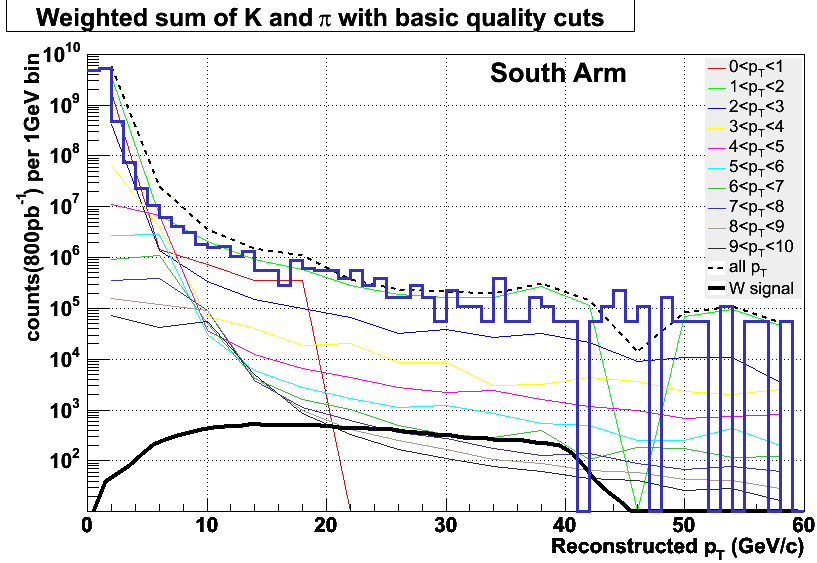
Figure 4.7: Data from proton-proton reactions at 200 GeV scaled to 800 pb$^{-1}$ (blue histogram) compared to simulated background from pions and kaons after "basic" cuts. The total simulated hadronic background is shown as the dashed black curve.

background levels, we want to convert the plot to be the number of counts per 1 GeV/$c$ $p_T$ bin from sampling an integrated luminosity of 800 pb$^{-1}$. One way to do this is calculate the number of inelastic interactions corresponding to 800 pb$^{-1}$. This is $(800 \times 10^{12}$ barns$^{-1}) \times (43 \times 10^{-3}$ barns$) = 3.4 \times 10^{13}$ interactions.

The resulting background distribution from real data (recall that at 200 GeV there is no expectation of a significant $W$ signal) is shown as the blue histogram in Figure 4.7. We can directly compare this background level to that from our simulations. Recall that the data is proton-proton reactions at 200 GeV and the simulations are modeled on proton-proton reactions at 500 GeV. We expect this to be a modest effect (less than a factor of 2) since the multiplicities at low $p_T$ scale logarithmically, and it is the low $p_T$ light hadrons that we believe dominate the background. Note that we have applied the identical "basic" cuts in both cases. Within a factor of two, there is agreement of the simulated and data observed high $p_T$ background level in the south muon arm.

Note that in the real data there are only ∼150 actual counts above reconstructed $p_T > 20$ GeV/$c$, and thus future investigations of background reduction will need larger data samples, as expected. We have not applied any of the tighter cuts on the real data at this time. In part this is due to the detector mis-alignment issues, which would not normally allow such tight DG0, DG4, DDG0 selections.

Table 4.2: Rejection factors over "basic" cuts for background with $p_T > 20$ GeV/$c$ from all properly weighted sources.

| Cut Selection | Background Rejection Factor |
|---|---|
| DG0 < 4.35 cm | 8 |
| DG4 < 4.8 cm | 24 |
| DDG0 < 2.0 degrees | 5 |
| MuTr chi2/DOF < 7.3 | 2 |
| MuID chi2/DOF < 1.34 | 1.1 |
| All above combined | 137 |

### 4.2.3 Tighter Cut Selections with Existing Detector

We also consider a tighter set of cuts motivated by the comparison of Monte Carlo simulation of high $p_T$ muons to select cut values which are 95% efficient for these muons. We use a Monte Carlo distribution from single muons with $p_T = 20$ GeV/$c$ and require a flat pseudorapidity distribution. We then apply these tight cuts to the full mix of Monte Carlo background. We summarize in Table 4.2 the rejections on the full mix of Monte Carlo background from each cut and the combined cuts.

Since the current background level with "basic" cuts is dominated for $p_T > 20$ GeV/$c$ by kaons in the input $p_T$ bin 1-2 GeV/$c$, we can really only check the background rejection up to a factor of $\sim$100. Any rejection greater than that will result in zero remaining counts and thus appear as an infinite rejection of background. Thus, we increased the statistics for the fake high $p_T$ background by turning off hadronic interactions in the simulations. This prevents us from studying other types of background, but increases the statistics by more than a factor of 50 for the same number of input hadrons for fake high $p_T$ tracks from decays in MuTr. We also note that these simulations use the full forward spectrometer pseudorapidity, $|\eta| = 1.2 - 2.2$.

There is an additional important cut using existing detectors which is not included in the above list. If the track is mis-constructed, just as it has a incorrect match at the MuID, it may also have a poor match to the $z$-vertex of the collision. Thus, we can do a straight line projection of the track back to the $z$-vertex plane of the collision as determined by the simulated BBC counter (i.e. a simulated $z$-vertex resolution of 2 cm). The background candidates should have a larger average transverse distance of closest approach (TDCA) due to multiple scattering (as they are light hadrons in the front absorber) and the poor MuTr track fit. A cut of TDCA < 2 cm is 95% efficient for the simulated high $p_T$ muons.

We have not explored significantly any special kinematic cuts. We note that though the background tracks are more concentrated at low angles, there is no

Table 4.3: Rejection factors over "basic" cuts for different $p_T$ bins broken down by cut variable for $p_T > 15$ GeV/$c$ background.

| | K+ | | | | K- | | | |
|---|---|---|---|---|---|---|---|---|
| pT GeV/c | 1-2 | 2-3 | 3-4 | 4-5 | 1-2 | 2-3 | 3-4 | 4-5 |
| DG0 < 4.35 cm | 9 | 4.9 | 3.5 | 2.7 | 8.6 | 5 | 3.6 | 2.7 |
| DG4 < 4.8 cm | 22 | 14 | 7.3 | 5.2 | 25 | 13.6 | 7.5 | 5.2 |
| DDG0 < 2.0 degrees | 3.8 | 2.5 | 1.9 | 1.6 | 4.1 | 2.4 | 1.9 | 1.7 |
| MuTR chi2 < 7.3 | 1.7 | 1.5 | 1.3 | 1.2 | 1.8 | 1.4 | 1.3 | 1.2 |
| TDCA < 2.0 cm | 17 | 8.4 | 4.5 | 2.9 | 18 | 8.1 | 4.6 | 3 |
| Combined | 508 | 128 | 43 | 18 | 1823 | 165 | 46 | 21 |

simple angle cut that provides significant rejection. This may be further explored.

The rejection factors for fake high $p_T$ tracks beyond the "basic" cuts are summarized in Tables 4.3 and 4.4. Table 4.3 shows the breakdown by cut variable for kaons, and Table 4.4 shows the total rejection factor for all combined cuts for each $p_T$ bin. Note that the cuts have a strong $p_T$ dependence, i.e. they are better at rejecting background with a low $p_T$ hadron source. This is perhaps not surprising since these light hadrons must have the largest kink in the decay to cause the mis-reconstruction to high $p_T$.

The "remaining counts" column of Table 4.4 shows the number of counts left after applying cuts. The "projected background counts" column shows the background counts estimated for 800 pb$^{-1}$ over 20-40 GeV/$c$ $p_T$ by applying the rejection factors to the earlier fully production weighted backgrounds like those in Figure 4.4. From this we see that the 5.3M background events after "basic" cuts drops to $\sim 25$k events after the tight cuts using the existing detector.

Considering the effect of the cuts in Table 4.3 on the signal (the combined cuts except for TDCA are 84% efficient for the 10 GeV/$c$ $p_T$ muons) we estimate a signal/background of $\sim$0.3 from fake high $p_T$ background. We feel that this is not sufficient for the precision measurement we hope to achieve.

## 4.2.4 Punch Through Background

Type 4 background is produced when high $p_T$ light hadrons punch through the nosecone absorber and into the MuID without suffering a hadronic interaction. These are reconstructed near the correct $p_T$; i.e. affected only by detector resolution. Some fraction dE/dx with no inelastic collisions through the entire forward spectrometer (MuTr+MuID). This small fraction of "true punch through" represents the truly irreducible punch through background for the current detector.

Table 4.4: Combined rejection factors for different $p_T$ bins for $p_T > 15$ GeV/$c$ background. The red rejection factors are from a power law extrapolation from lower $p_T$. The projected background is for 800pb $^{-1}$.

| pT GeV/c | K+ | | | K- | | | Pi+ | | |
|---|---|---|---|---|---|---|---|---|---|
| | rejection | remaining counts | projected background counts | rejection | remaining counts | projected background counts | rejection | remaining counts | projected background (Pi+ + Pi-) |
| 1-2 | 508 | 7 | 4412 | 1823 | 2 | 820 | >13 | 0 | ? |
| 2-3 | 128 | 30 | 3845 | 165 | 22 | 1340 | >8 | 0 | ? |
| 3-4 | 43 | 108 | 2222 | 46 | 103 | 1118 | 16 | 1 | ? |
| 4-5 | 18 | 286 | 1438 | 21 | 252 | 637 | 31 | 1 | ? |
| 5-6 | 11 | 505 | 843 | 11 | 500 | 416 | 6.3 | 7 | 1292 |
| 6-7 | 8 | 721 | 463 | 8.2 | 729 | 247 | 4.6 | 26 | 986 |
| 7-8 | 6 | 994 | 319 | 6.1 | 1006 | 214 | 2.9 | 61 | 1042 |
| 8-9 | 4.5 | 1363 | 247 | 4.9 | 1292 | 156 | 2.2 | 143 | 1019 |
| 9-10 | 3.3 | | 225 | 3.4 | | 157 | 1.7 | | 1015 |
| sum | | | 14015 | | | 5105 | | | 5354 |

In this section we will discuss the fraction of "true punch through" and "partial punch through" based on simulation and the ability of the current detector to reject punch through. This background was not present for $p_T > 20$ GeV/$c$ in the previously described simulations since input hadrons with $p_T > 10$ GeV/$c$ were not included.

In Figure 4.8 we show how DG4, a measure of road to track matching with projections to the back of the MuID similar to DG0, distributions vary depending on the gap where a shower occurs in the MuID. For 10 GeV/$c$ $p_T$ pions which dE/dx through the entire MuID, the DG4 distribution is the same as for 10 GeV/$c$ $p_T$ muons. The earlier a shower occurs, the broader the DG4 distribution becomes.

We vary the track-road matching cuts from a "loose" set of DG0 < 20 cm and DDG0 < 9.0 degrees to a "tight" set of DG0 < 4.3 cm, DG4 < 4.8 cm, and DDG0 < 2.0 degrees. We find that for 10 million 10 GeV/$c$ $p_T$ pions, 1k are "true punch through" and 56k are "partial punch through" for "loose" cuts. The "tight" cuts reduce the "partial punch through" to 9k while the "true punch through" is unchanged. For 10 million 20 GeV/$c$ $p_T$ pions, 1k are "true punch through", and the "partial punch through" is 71k and 9k with "loose" and "tight" cuts respectively. The fractions are similar (within 50%) for kaons.

We use these results to weight PYTHIA simulations of charged hadrons to obtain an estimate for the $p_T$ distribution of punch through background. Motivated by the above simulations, we assume 1% of hadrons with $10 < p_T < 40$ GeV/$c$ produce a deep road before quality cuts and 0.1% produce a deep road after "tight"
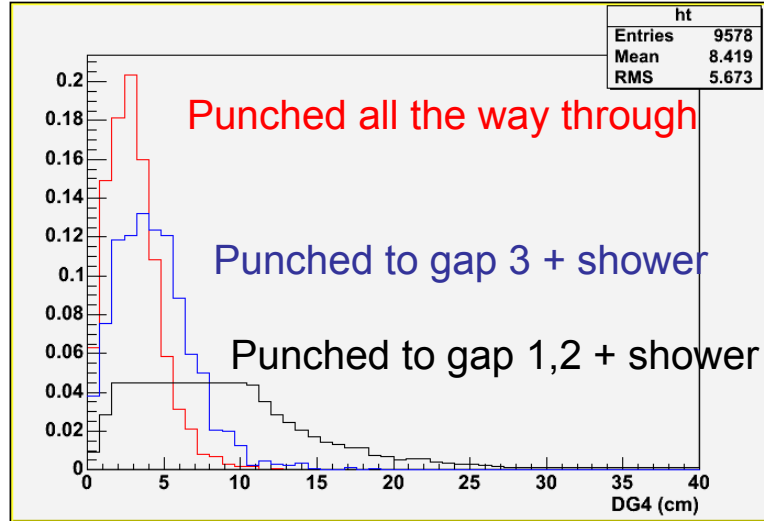
Figure 4.8: DG4 distributions of deep roads 10 GeV/$c$ $p_T$ pions for different penetration depths of the original hadron.
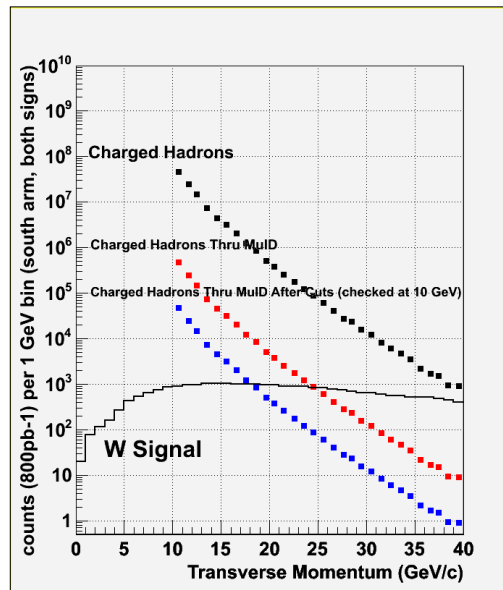


Figure 4.9: Punch through background for different cuts. The original yields into the muon arms from PYTHIA is shown in black. The red curve is a factor of 100 lower due to the absorber material. The addition of quality cuts, shown in blue, is estimated to add another factor of 10 rejection.
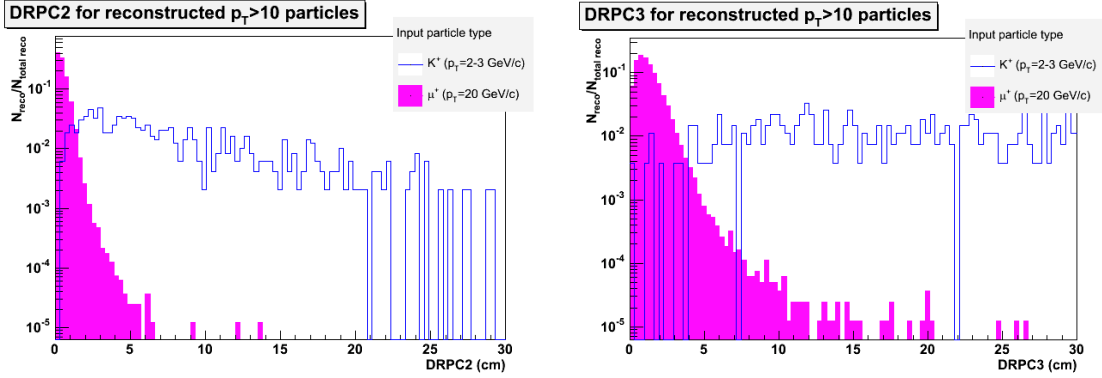
Figure 4.10: The DG0RPC and DG4RPC assuming RPCs with exact position resolution.

quality cuts. As shown in Figure 4.9 hadrons without cuts drop below the $W \rightarrow \mu$ signal for $p_T > 25$ GeV/$c$ and hadrons with cuts drop below the $W$ signal for $p_T > 19$ GeV/$c$. From these estimates, we conclude that the punch through background from penetrating hadrons can be reduced to a level which does not present a serious issue for the $W$ measurement with the current detector.

## 4.3 Background Simulation Results with Additional Detectors

There are different categories of additional detectors that might help further reduce the fake high $p_T$ background source.

### 4.3.1 The RPC Upgrade in this CDR

We have already found that projecting the MuTr track forward to the MuID and requiring a match is a powerful cut (DG0 and DG4). The ability to cut tighter on this match is limited by the resolution (tube size) of the MuID. One might consider a finer granularity detector (e.g. a modified design RPC) that could allow a tighter match and thus a greater rejection.

We have plotted in Figure 4.10 the projection of the MuTr track to the $z$ plane for the proposed RPC2 (in front of the MuID) and RPC3 (at the back gap of the MuID) and compared it with the position at the RPC assuming a PERFECT detector (exact position resolution). We label these variables as DG0RPC (using RPC2) and DG4RPC (using RPC3).

The above plots are assuming perfect resolution in the RPC's! Thus it gives an indication of the minimum RPC pad size that would be useful. Note that these
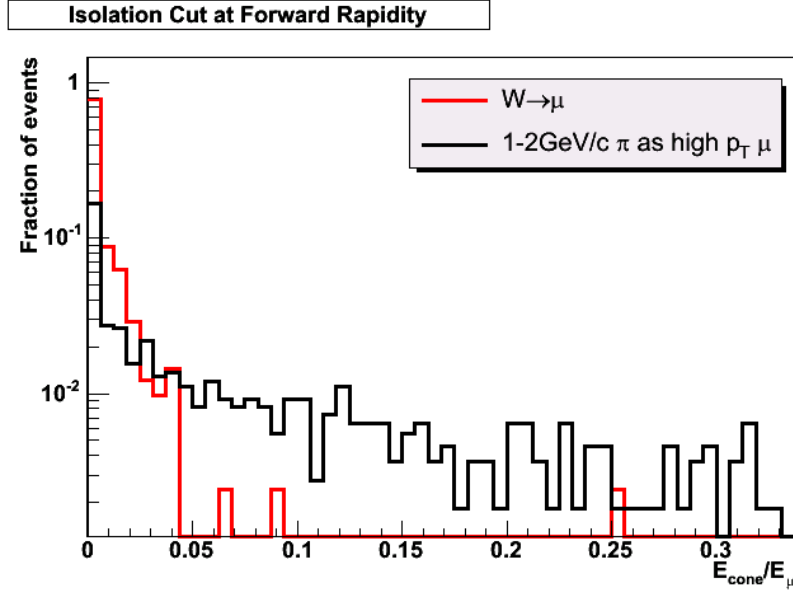
Figure 4.11: E(cone) / E(mu) distributions for $W \to \mu$ and background pions.

sizes are quite a bit smaller than we are considering. One can see that additional rejection might be gained by a cut of DG0RPC < 1.5 cm and DG4RPC < 4.0 cm. Presumably the primary contributor to the width of these distributions for high $p_T$ muons is the MuTr track vector resolution, and then projecting this over the distance to the RPC positions.

Just to give one idea though, on DG4RPC one might ideally like to cut at a circle radius of 4 cm. However, the nominal size of inner RPC3 strips is $\sim$ 6 cm $\times$ 40cm.

**Other proposed upgrades**

- The nosecone calorimeter (NCC) and the forward vertex detector (FVTX) can be used to Reject fake high $p_T$ tracks using an isolation cut. We have carried out a zeroth order study by examining PYTHIA $W$ events and constructing the ratio of E(cone) / E(mu) as plotted in Figure 4.11. The E(cone) is the energy of other particles (not including the muon) sometimes called the excess energy in a cone around the muon of size:

$$\Delta R = \sqrt{(\Delta\phi_{lab})^2 + (\Delta\eta_{lab})^2} \tag{4.7}$$

In this first look, a cone size of 0.4 is used, similarly to the method described in a CDF $W$ paper [95]. Then we run minimum bias PYTHIA events and

use a $p_T$ 1-2 GeV/$c$ pion as the trigger, but randomly assign it a high $p_T$ 15-35 GeV/$c$ (flat) to model the background problem of mis-reconstruction. The same ratio is then also plotted as a black histogram.

A cut could be placed on this ratio which keeps 96% of the $W$ signal, and has a rejection factor of 4 for the "modeled background." Further studies are needed. Note that this study assumes 100% coverage, and perfect hadronic and electromagnetic (all) energy resolution. A realistic model of the nosecone calorimeter and the forward vtx (for track numbers) is needed to see how this might degrade.

- The forward vertex detector [96] would provide a tracklet from four silicon layers. Position and angle matching similar to DG0 and DDG0 are likely to provide some additional rejection, and studies are underway to quantify the benefit.

**Other possible upgrades**

- One could add additional material in the front absorber to reduce the punch through of light hadrons into the MuTr where they can then decay. Two nuclear interaction lengths of material would reduce the background by a factor of $\sim$10. Adding this much material would likely have significant conflicts to overcome.

- If one had additional tracking constraints in the MuTr a fourth station for example, one might have better rejection of the kinked tracks. Other ideas in the area of improved tracking should be explored.

- Once the particles are in the MuTr or MuID, an ideal solution would be a threshold Cherenkov counter that can discriminate between the real high $p_T > 20$ GeV/$c$ muon and the low $p_T$ light hadron decaying to a low $p_T$ muon background. Just to include a few example numbers, if one wanted to reject hadrons with $p_T < 8$ GeV/$c$, one would need a detector with an index of refraction n = 1.0001.

  Early studies of the number of emitted photons / meter of material indicate that a substantial sized detector which might not even fit in the South arm between the magnetic backplate and the MuID would be needed.

  Recently it has been proposed to use a DIRC Cherenkov counter and first studies are underway.

Here we summarize this study of the feasibility of measuring muons from $W$ decay. Tagging muons from $W$ decay without a missing energy measurement (as is often done in high energy experiments) is challenging and one must consider various background sources particularly given the low signal rate from $W$ decay.

We have completed a first round of full Monte Carlo simulations and have identified different background sources. With the existing detector and the trigger upgrades, we find a signal to background $\sim 0.3$ for high $p_T$ "muons" in the $W$ range of interest. We believe this is insufficient for making precision spin measurements. With the introduction of additional absorber material, the signal to background is improved to $\sim 3$ (with further simulation studies underway). Thus, we are pursuing this option as the default.

In any such measurement, having additional rejection power is always beneficial and thus significant studies of how detectors coming online after the $W$ program has started are being conducted (including the Nosecone calorimeter and forward vertex detector). The additional absorber option has some significant drawbacks including worse momentum vectoring due to multiple scattering and future difficulty in matching MuTr tracks to FVTX tracks in heavy ions. Thus, additional rejection options are being pursued with the thought of eventually being able to remove the additional absorber and insert RPC 1A/B as well.

## 4.4    Tracking in $p + p$ Collisions at High $p_T$

The general tracking of the high energetic muons from $W$ decays will be performed with the already existing MuTr detector. The limited position resolution of the MuTr will have an effect on the momentum resolution of the reconstructed muons. For this purpose MC studies have been performed in 2003 using the libraries pro.59, with the 3D03 magnetic field map. For simplicity positive muons in the south arm were generated in 14, flat $p_T$ bins via the routine *cfm_multi*. The $p_T$ binning is $[1, 2, 3, 4, 5, 6, 7, 10, 20, 30, 50, 70, 100]$. The position resolutions for the MuTr were taken to be 150, 300 and 600 $\mu m$ and of Gaussian nature. The design position resolution for the MuTr was approximately 150 microns, but the current real data performance is somewhere between 300-500 microns depending on the plane. We hope to improve this resolution, but consider these different scenarios as a relevant range. We also note that the momentum resolution impacts not only the charge sign identification, but how well we constrain the x dependence of the quark polarizations. Further studies of how the momentum resolution impacts the physics program (other than charge mis-identification) are underway.

As an example the reconstructed momentum distributions for the highest and lowest $p_T$ bins using 150 $\mu m$ are displayed in Figure 4.12. Obviously these distributions are not Gaussian and thus the RMS value is not a good approximation of the momentum resolution. As a better estimate the momenta corresponding to 95.4/2%(2 sigma) or 68.3/2% (1 sigma) of the data below the average being contained in this interval where defined as $\sigma_-$ and similarly above the average of the distribution for $\sigma_+$. The average of $\sigma_+$ and $\sigma_-$ was then taken as the momentum resolution containing either 68.3% of the data or 95.4%. At high mo-
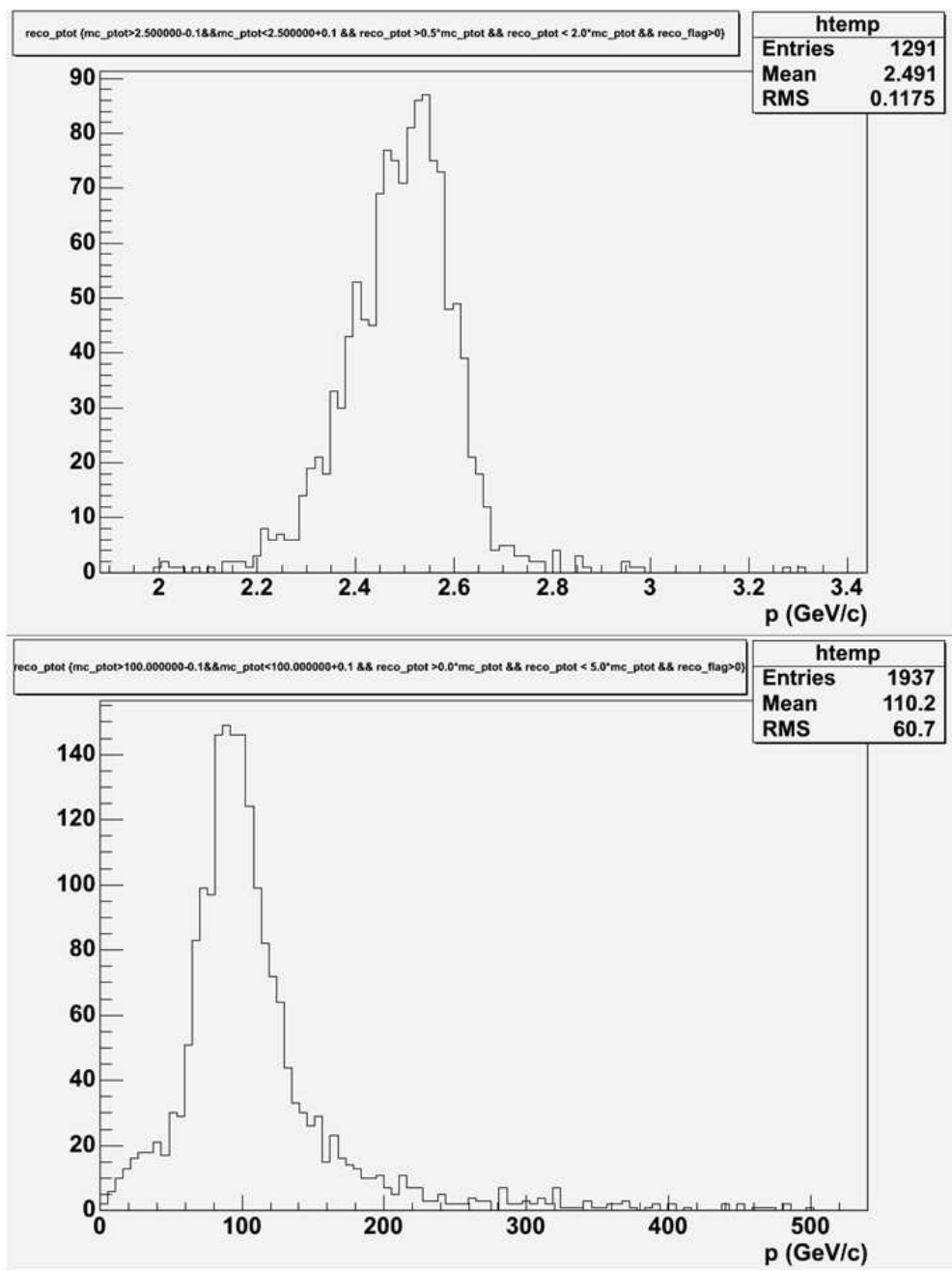
Figure 4.12: Momentum distributions for a real momentum of 2.5 GeV (top plot) and 100 GeV (bottom plot).
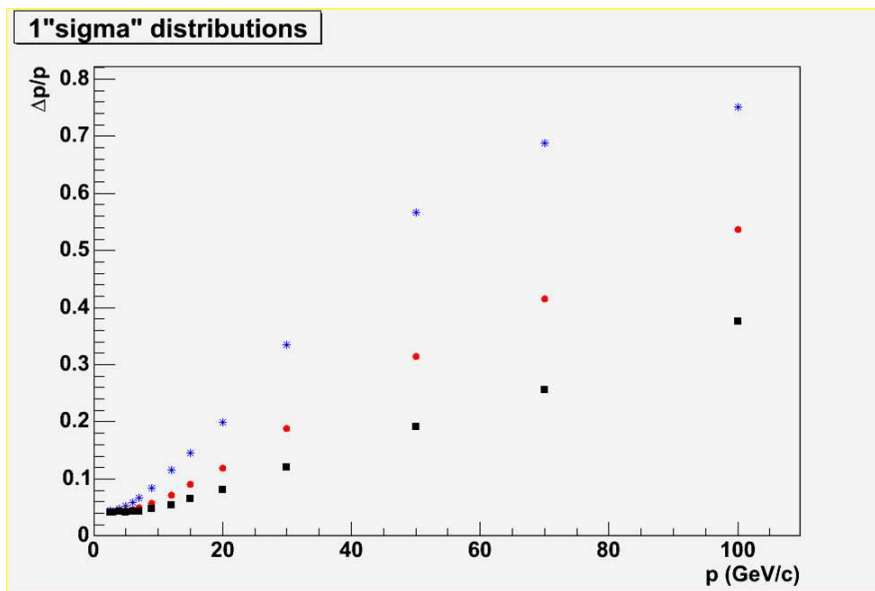
Figure 4.13: Momentum resolutions $\Delta p/p$ for MuTr position resolutions of 600 $\mu m$ (blue stars), 300 $\mu m$ (red circles) and 150 $\mu m$ (black squares) as a function of the generated momentum. The resolutions are based on the $1\sigma$ reconstructed momentum range.

menta the large tail to higher momenta dominates these resolutions as can be seen Figure 4.13. The resolutions are summarized in Table 4.5.

This tail to higher momenta can be explained by the very small angular deviation of such a track in the magnetic field. The finite resolution of the MuTr might even lead to a misidentification of the charge sign of the muon which could have severe implications on the extraction of the quark and sea quark (helicity) distributions. The fraction of misidentified muons reaches about 9% at highest momenta when applying a position resolution of 300 $\mu m$. The misidentification fractions are displayed in Figure 4.14. More thorough studies on the misidentification rate have to be performed, taking realistic MuTr position resolutions into account. In an $W$ analysis these misidentified fractions have to be corrected for.
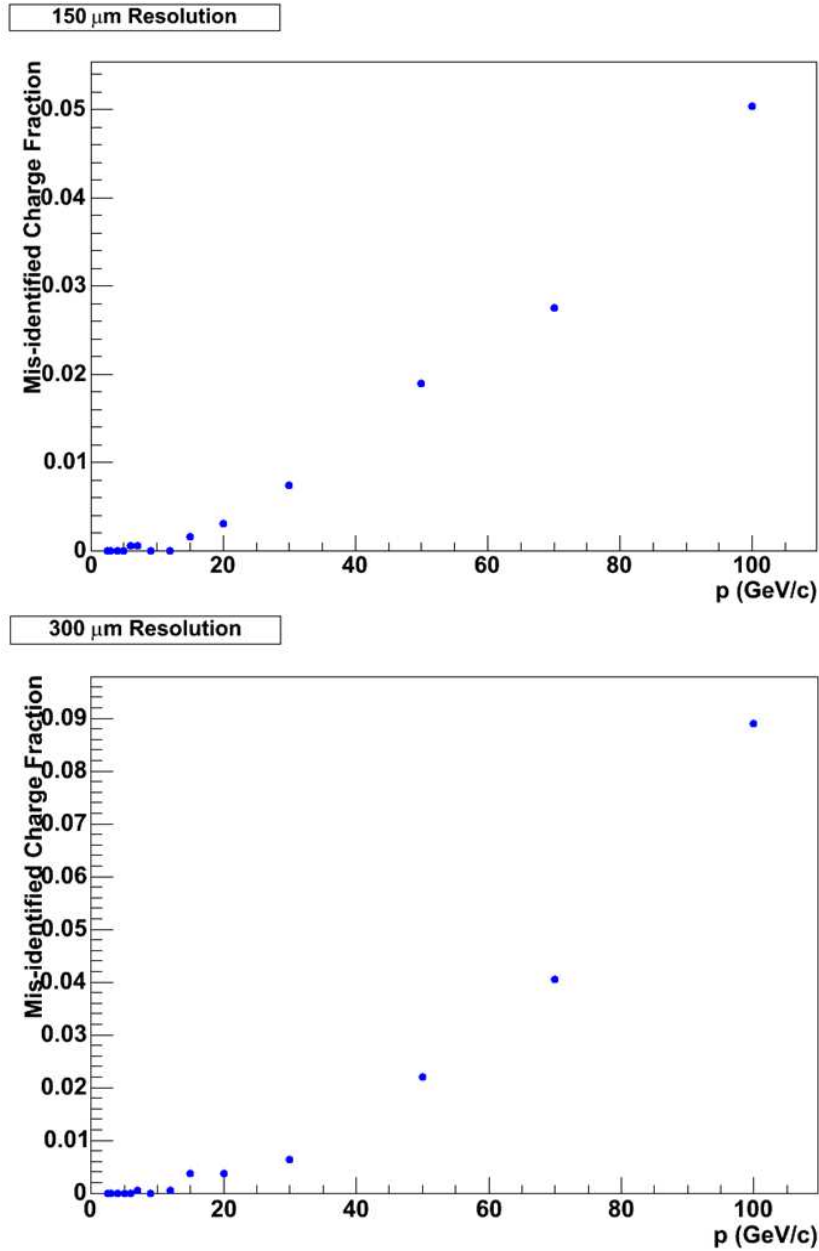
Figure 4.14: Fraction of events where the charge of the muon has been misidentified as a function of the generated momentum. Plots are for a MuTr position resolution of 150 $\mu m$ (top plot) and 300 $\mu m$ (bottom plot).

Table 4.5: Momentum resolutions for 300 $\mu m$ position resolution.

| P true | $1\sigma_-$ | $2\sigma_-$ | $1\sigma_+$ | $2\sigma_+$ | $\Delta p/p(1\sigma)$ | $\Delta p/p(2\sigma)$ |
|---|---|---|---|---|---|---|
| 2.5 | 0.11 | 0.26 | 0.1 | 0.21 | 0.042 | 0.094 |
| 3 | 0.13 | 0.3 | 0.12 | 0.27 | 0.042 | 0.095 |
| 4 | 0.19 | 0.47 | 0.16 | 0.43 | 0.044 | 0.113 |
| 5 | 0.24 | 0.59 | 0.21 | 0.68 | 0.045 | 0.127 |
| 6 | 0.3 | 0.83 | 0.26 | 0.95 | 0.047 | 0.148 |
| 7 | 0.38 | 1.01 | 0.32 | 1.29 | 0.05 | 0.164 |
| 9 | 0.49 | 1.39 | 0.53 | 2.18 | 0.057 | 0.198 |
| 12 | 0.85 | 2.67 | 0.85 | 4.07 | 0.071 | 0.281 |
| 15 | 1.3 | 3.98 | 1.41 | 7.47 | 0.090 | 0.382 |
| 20 | 72.16 | 6.18 | 2.58 | 11.35 | 0.119 | 0.438 |
| 30 | 4.48 | 13.05 | 6.8 | 40.17 | 0.188 | 0.887 |
| 50 | 12.21 | 25.89 | 19.2 | 129.87 | 0.314 | 1.558 |
| 70 | 20.98 | 44.83 | 37.21 | 173.09 | 0.416 | 1.557 |
| 100 | 38.55 | 73.07 | 68.86 | 229.58 | 0.537 | 1.513 |

# Chapter 5

# Project Management and Responsibilities

The organization and management of the proposed upgrade is embedded in the management structure of the PHENIX experiment which is part of the RHIC project at BNL. The organization must provide a clear interface to the existing PHENIX and RHIC management structure and clear roles and responsibilities within the PHENIX subsystem structure. We point out that significant parts of the project are supported by an NSF-MRI and also by the Japanese Society for the Promotion of Science (JSPS). The responsibilities will be formalized in memoranda of understanding (MOU's) between PHENIX and the participating institutions. In this section we outline our proposed management structure and delineate responsibilities within the project.

## 5.1  Project Background

This project is part of a detailed upgrade program to enhance the capabilities of the PHENIX detector over the next few years. The upgrade proposed here will allow us to advance our understanding of QCD by fully exploiting the unique spin physics possible with the RHIC polarized proton beams.

The beginning of the project can be traced back to 1994 when J. Moss at LANL and K. Imai at RIKEN proposed to build a second muon arm at PHENIX. One motivation for a second muon arm was to be able to carry out a $W$ physics program to determine the contribution of u and d quarks separately to the polarization of the proton and to minimize interference from $Z^0$ decays. The proposal was approved by RIKEN for $10,000,000 in April 1995 to build what eventually became the PHENIX south muon arm. The program was reviewed by BNL in May 1995 by a committee chaired by V. Hughes which resulted in the start of the PHENIX spin program in May 1995. In 1998 a taskforce led by S. Sorenson carried out studies to determine how to fit the muon arm into the available budget. In addition

the PHENIX north muon arm was built with AEE funds provided by the U.S. Department of Energy. The PHENIX south muon arm was completed and took the first data in PHENIX Run-2 in 2002.

A muon I.D. Local Level-1 Trigger was built in order to provide sufficient rejection for use with 100 GeV polarized beams used in the spin program. The rejection obtained will not be sufficient for the spin program with 250 GeV protons or the higher luminosities to be obtained with the RHIC-II upgrade. It was thus proposed to build triggers for the two PHENIX forward spectrometers with higher rejection power.

The program to upgrade the muon trigger evolved into two separate but highly dependent parts. One part is to build Resistive Plate Chambers (RPCs) to track muons through the muon tracker and muon I.D. and provide signals for the muon I.D. Local Level-1 Trigger. This part is primarily funded by an NSF-MRI grant. The other part is to divide signals from the muon tracker FEEs and use part of the signal to produce inputs to the muon I.D. Local Level-1 trigger. This part is primarily funded by a grant from the Japanese Society for Promotion of Science (JSPS).

The RPC project began in 2003 with the preparation of a letter of intent to PHENIX management entitled "Letter of Intent for a PHENIX Forward Spectrometer Upgrad". This letter of intent proposed both dedicated first level trigger detectors for the PHENIX muon arms (the subject of this CDR) and a pair of nosecone calorimeters. The letter of intent was submitted to PHENIX management during January 2004. The letter of intent was reviewed very positively in a joint meeting of the PHENIX detector council (DC) and executive council (EC) and as a result PHENIX project management encouraged us to develop a conceptual design report (CDR) for an upgraded muon trigger system. It was also pointed out that the upgrade of the first level muon trigger with momentum resolution is critical for the planned $W$ measurement in polarized proton collisions at 500 GeV.

As the next step in the trigger upgrade project a proposal entitled "Collaborative Research: Development of a Fast Muon Trigger to Study the Quark-Gluon Structure of the Proton" was submitted to the National Science Foundation Major Research Instrumentation (NSF-MRI) program on January 2005. This was a joint proposal from University of Illinois as the lead university, University of California at Riverside, Iowa State University and Abilene Christian University. The request to the NSF was for $2,000,000 and in addition the four above universities contributed a total of $250,000 in matching funds. The NSF-MRI was fully funded for a five-year period starting on September 1, 2005. The NSF-MRI funds provide resources to build a series of Resistive Plate Chambers (RPCs) to provide input for the fast muon triggers.

In parallel the group of N. Saito at KEK has been developing a system to extract signals from the Front End Electronics (FEEs) of the muon tracker stations

to use as additional input for the fast muon triggers. This project began in April 2004 with a grant of $150,000 for a two-year period. In addition D. Fields at the University of New Mexico built a muon tracker sector chamber to be used in Japan as a test facility for the muon tracker FEE project. In 2006 Prof. Saito was funded by the JSPS for a total of approximately $2,600,000 to build the above muon tracker FEE system. These funds are for a total of five Japanese Fiscal Years (JFYs), namely JFY 2006-10.

The muon trigger upgrade involves the input of signals to the fast muon trigger from both the RPC detectors funded by the NSF-MRI and the upgraded muon tracker FEEs funded by JSPS. Although the funds come from different sources, both projects are included in this CDR since they will work together to optimize the performance of the upgraded muon trigger for the highest proton-proton collision rates foreseen at RHIC.

## 5.2 Management Plan for the Fast Muon Trigger

### 5.2.1 PHENIX Management Structure

The fast muon trigger upgrade project is part of the PHENIX project and is therefore integrated into the PHENIX management structure as described by the PHENIX bylaws. The PHENIX detector council (DC) will advise PHENIX management on the design, construction and integration of the muon trigger into the PHENIX detector. The DC is co-chaired by the operations manager (Ed O'Brien) and upgrades manager (Axel Drees). The muon trigger subsystem manager is Matthias Grosse Perdekamp.

### 5.2.2 PHENIX Subsystem Leadership

The fast muon trigger upgrade project is logically divided into two parts, namely the RPC detector upgrade and the muon tracker FEE upgrade. This is convenient since the RPC detector is funded by a NSF-MRI grant and the muon tracker FEE upgrade is funded by a grant from JSPS. Matthias Grosse Perdekamp of UIUC is the Project Manager for the RPC portion of the project funded by the NSF-MRI grant. The Project Manager for the muon tracker FEE upgrade part of the project funded by JSPS is Naohito Saito of KEK. The overall director for the whole project is Dr. Grosse Perdekamp. He will report to PHENIX Project Management and represent this project. His deputy starting July 1, 2007 is Prof. John Hill from Iowa State University. Prof. Hill has the responsibility to monitor project cost and schedule and for project activities in general in the absence of the project manager. For the first two years of the project this function was carried
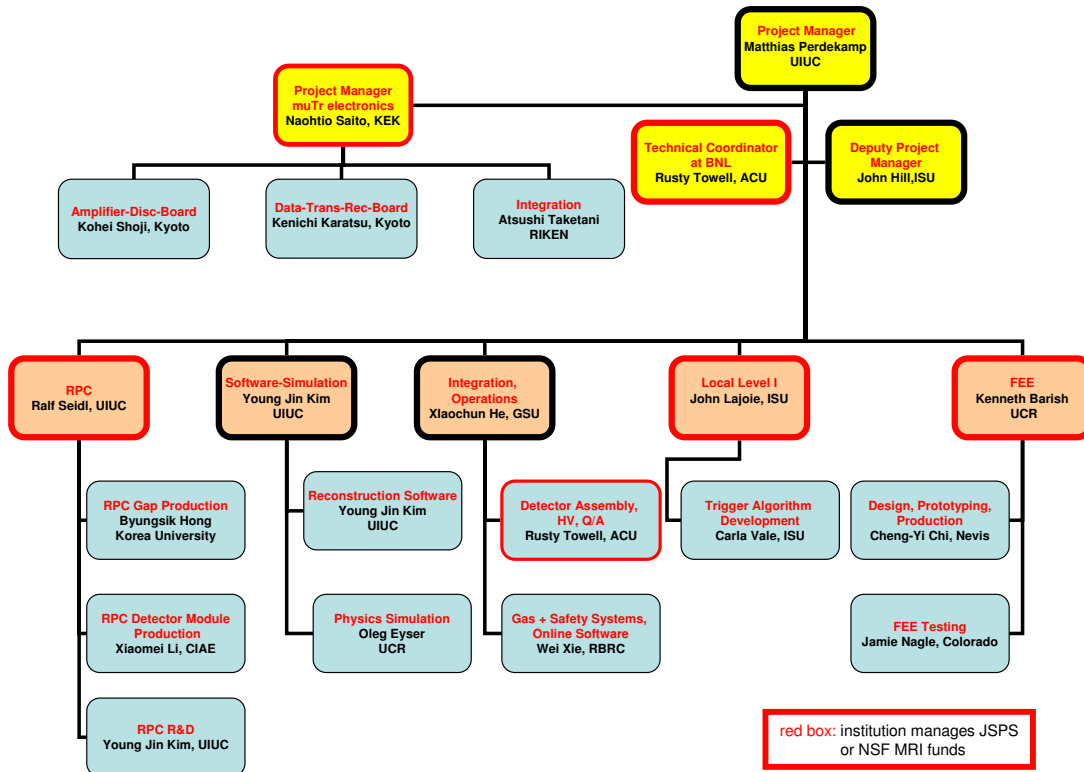
Figure 5.1: Management chart for the fast muon trigger project.

out by Prof. Edward Kinney of the University of Colorado. A management block diagram for the entire fast muon trigger upgrade project is given below in Figure 5.1.

## 5.3 Personnel for Tasks

The following tables document tasks for the trigger upgrade project and personnel available.

Table 5.1: Senior collaboration members working on R&D for the RPC subtask.

| Task | People | Status and Job |
|---|---|---|
| RPC Manager | M. Perdekamp (UIUC) | Faculty |
| RPC R&D | X. He (GSU) | Faculty |
| | M. Perdekamp (UIUC) | Faculty |
| | J. Nagle (Colo) | Faculty |
| | E. Kinney (Colo) | Faculty |
| | B. Fadem (Muhl) | Faculty |
| | R. Towell (ACU) | Faculty |
| | D. Isenhower (ACU) | Faculty |
| | S. Williamson (UIUC) | Faculty |
| | J. Ying (GSU) | Post Doc |
| | A. Glenn (Colo) | Post Doc |
| | R. Seidl (UIUC) | Post Doc |
| | K. Oleg Eyser (UCR) | Post Doc |
| | C. Butler (GSU) | Scientist |
| | J. Blackburn (UIUC) | Technician |
| | E. Thorsland (UIUC) | Technician |

Table 5.2: Student collaboration members working on R&D for the RPC subtask.

| Task | People | Status and Job |
|---|---|---|
| | K. Kiriluk (Colo) | Grad Student |
| | J. Koster (UIUC) | Grad Student |
| | B. Meredith (UIUC) | Grad Student |
| | R. Yang (UIUC) | Grad Student |
| | S. Wadhams (UIUC) | Grad Student |
| | A. Burnap, N. Mucia (UIUC) | Student |
| | T. Natoli (UIUC) | Student |
| | C. Oakley (GSU) | Student |
| | J. Adams, A. Caringi (Muhl) | Student |
| | J. Ide, P. Lichtenwalner (Muhl) | Student |
| | A. Basye, D. Jumper (ACU) | Student |
| | N. Sparks, C. Watts (ACU) | Student |
| | J. Wood, R. Wright (ACU) | Student |

Table 5.3: Collaboration members working on construction FEE and assembly for the RPC subtask.

| Task | People | Status and Job |
|---|---|---|
| RPC Construction | B. Hong (Korea) | Faculty |
| | K. Lee (Korea) | Faculty |
| | S. Park (Korea) | Faculty |
| | K. Sim (Korea) | Faculty |
| | Y. Mao (Peking) | Faculty |
| | S. Zhou (Peking) | Faculty |
| | X. Li (CIAE) | Scientist |
| | S. Hu (CIAE) | Scientist |
| | Y. Meng (CIAE) | Engineer |
| | K. Lee (Korea) | Grad Student |
| | B. Kim (Korea) | Grad Student |
| | R. Han (Peking) | Grad Student |
| RPC FEE | K. Barish (UCR) | Faculty |
| | J. Nagle (Colo) | Faculty |
| | C.Y. Chi (Nevis) | Scientist |
| | W. Sippach (Nevis) | Engineer |
| RPC Assembly & QA | R. Towell (ACU) | Faculty |
| | M. Perdekamp (UIUC) | Faculty |
| | B. Fadem (Muhl) | Faculty |
| | D. Isenhower (ACU) | Faculty |
| | B. Hong (Korea) | Faculty |
| | K. Sim (Korea) | Faculty |
| | Y. J. Kim (UIUC) | Post Doc |
| | J. Ying (GSU) | Post Doc |
| | R. Seidl (UIUC) | Post Doc |
| | C. Butler (GSU) | Scientist |
| | J. Blackburn (UIUC) | Technician |
| | D. Northacker (UIUC) | Technician |
| | E. Thorsland (UIUC) | Technician |
| | K. Lee (Korea) | Grad Student |
| | B. Kim (Korea) | Grad Student |
| | B. Meredith (UIUC) | Grad Student |
| | R. Yang (UIUC) | Grad Student |
| | A. Burnap (UIUC) | Student |
| | J. Adams, A. Caringi (Muhl) | Student |
| | J. Ide, P. Lichtenwalner (Muhl) | Student |
| | A. Basye, D. Jumper (ACU) | Student |
| | N. Sparks, C. Watts (ACU) | Student |
| | J. Wood, R. Wright (ACU) | Student |

Table 5.4: Collaboration members working on the muon tracker FEE subtask.

| Task | People | Status and Job |
|---|---|---|
| Muon Tracker FEE | N. Saito (KEK) | Manager & Faculty |
| Amplifier-Discriminator | T. Murakauri (Kyoto) | Faculty |
| | K. Imai (Kyoto) | Faculty |
| | K. Shoji (Kyoto) | Grad Student |
| | K. Aoki (Kyoto) | Grad Student |
| | A. Sato (Kyoto) | Grad Student |
| | K. Senzaka (Kyoto) | Grad Student |
| Transmitter-Receiver | A. Taketani (RIKEN) | Scientist |
| | K. Karatsu (Kyoto) | Student |
| Assembly & QA | T. Murakami (Kyoto) | Faculty |
| | K. Tanida (Kyoto) | Faculty |
| | J. Murata (Rikkyo) | Faculty |
| | K. Kurita (Rikkyo) | Faculty |
| | A. Taketani (RIKEN) | Scientist |
| | Y. Fukao (RIKEN) | Post Doc |
| | K. Shoji (Kyoto) | Grad Student |
| | K. Karatsu (Kyoto) | Grad Student |
| | S. Dairaku (Kyoto) | Grad Student |

Table 5.5: Collaboration members working on the level-1 trigger subtask.

| Task | People | Status and Job |
|---|---|---|
| LVL-1 Trigger | J. Lajoie (ISU) | Manager & Faculty |
| | J. Hill (ISU) | Faculty |
| | G. Sleege (ISU) | Engineer |
| | T. Kempel (ISU) | Grad Student |

Table 5.6: Collaboration members working on the simulation subtask.

| Simulations | J. Nagle (Colo) | Faculty |
|---|---|---|
| | J. Lajoie (ISU) | Faculty |
| | E. Kinney (Colo) | Faculty |
| | B. Fadem (Muhl) | Faculty |
| | R. Towell (ACU) | Faculty |
| | A. Glenn (Colo) | Post Doc |
| | Y. J. Kim (UIUC) | Post Doc |
| | T. Kempel (ISU) | Grad Student |

## 5.4 Institutional Involvement

Abilene Christian University

Abilene Christian University (ACU) in collaboration with the University of Illinois at Urbana-Champaign (UIUC), the University of California at Riverside (UCR), and Iowa State University (ISU) was awarded a National Science Foundation's Major Research Instrumentation grant to upgrade the muon triggering system of PHENIX. The ACU particle physics research group is responsible for the high voltage system, quality assurance of the front-end electronics, and assembly of RPC modules into detector stations at BNL. Additionally we are helping on the RPC design team. This group is composed of 3 professors (Dr. Donald Isenhower, Dr. Michael Sadler, and Dr. Rusty Towell) and a large team of undergraduate students. During the summer of 2006 Dr. Isenhower, Dr.Towell and 6 students (Austin Basye, Daniel Jumper, Nathan Sparks, Cole Watts, John Wood, and Ryan Wright) worked at UIUC and BNL on this project. At UIUC the group helped set up a RPC test stand and at BNL worked on design and integration tasks.

Brookhaven National Laboratory, Physics Department

The PHENIX Group from the Physics Department provides infrastructure and technical support through the Systems Engineering and Integration (SE&I) group for the entire PHENIX experiment. The group provides a staff of mechanical and electrical engineers and experienced technicians intimately familiar with the detector. The group closely works with the Collider-Accelerator Department (CAD). The PHENIX BNL group designed much of the infrastructure of the PHENIX detector and carried out installation of all of the present subsystem detectors. This group will be closely involved with the design of the infrastructure and support for the various upgrades for the PHENIX forward spectrometers.

The BNL PHENIX group has primary responsibility for the Electronics Facil-

ities and Infrastructure (EF&I), Online Computing Systems (ONCS) and Offline Computing. The BNL group will participate in the electronic integration and readout of the forward detector upgrades into the PHENIX data acquisition system. We will closely collaborate with Dr. John Haggerty who leads the PHENIX online effort overall and Don Lynch who is the PHENIX chief engineer.

University of California at Riverside

The UCR prime responsibility will be associated with the RPC electronics. The group will be responsible for managing the mass production of the front end electronics. Other contributions have included contributions to the detector design, simulations and the evaluation of CMS front end electronics. In the future the group expects to contribute to the monitoring and analysis software. The group includes faculty members Ken Barish and Richard Seto, 1 FTE of a postdoctoral researcher and 1 FTE graduate student.

CIAE and Peking University

The CIAE group contributes to the mechanical design for the RPC detector modules and parts and carries major responsibility for the production of all mechanical components for the detector modules. Finally the group will lead the assembly and QA of the detector modules at BNL for the PHENIX muon trigger upgrade. Faculty from CIAE include Xiaomei Li (CIAE contact person, QA and Assembly manager, 0.5 FTE), Shuhua Zhou (0.2 FTE), Shouyang Hu (0.5 FTE), one engineer and two graduate students (1.5 FTE), and two technicians (0.5 FTE).

University of Colorado

The Colorado group has been active in the upgrade project since the development of the MRI proposal; a sub-contract has provided instrumentation and materials in addition to $70,000 from the University of Colorado to renovate the test facility used to evaluate RPC prototypes. Limited operating costs are provided by the existing DOE grants of Nagle and Kinney, the two faculty in the group. Colorado will continue to test and evaluate prototype detectors as well as on-chamber tests of FEE prototypes provided by Columbia (Nevis) and the University of California, Riverside. In addition, the group will continue to develop the overall physics program of the upgrade.

Columbia University

The Nevis Laboratory of Columbia University will develop the front-end electronics (FEE) for the PHENIX muon trigger resistive plate counters (RPC's). The principal investigator for the subcontract at Nevis is Professor William Zajc. Technical leadership responsibility will be carried by Dr. Cheng-Yi Chi. Nevis

engineers have custom-designed and build the front-end electronics for two major detector systems in PHENIX. Cost estimates for the trigger project have been provided by Dr. Chi based on previous experience at Nevis with PHENIX FEEs. The prototype electronics will be used for RPC R&D and test efforts at UIUC, Colorado, GSU and BNL.

Georgia State University

The Georgia State University (GSU) group consists of three people who are actively working on RPC R&D. Prof. Xiaochun He is the group leader. Dr. Jun Ying (a post-doc) is an expert on RPC chamber construction and testing who has worked on the CMS/LHC RPC project at Beijing University before joining the GSU group. Ms. Carola Butler is a staff member in the Department of Physics & Astronomy at GSU who plays an engineering role in building the RPCs and the associated supporting components. It is anticipated that a graduate student, Christopher Oakley, will join the project in the future. The main tasks for the GSU group are two fold. One is an intense RPC R&D effort at GSU with the goal to gain detailed expertise in operating RPC chambers in the PHENIX experiment. The second responsibility is to lead the RPC assembly and QA at BNL working together with the groups from ACU, UIUC, CIAE and RBRC.

University of Illinois at Urbana/Champaign

UIUC has the responsibility for the overall project management of the PHENIX muon trigger upgrade. Illinois is further responsible for the management and co-ordination of the R&D, design, production, installation and operation of the RPC detector hardware in PHENIX. In these tasks UIUC will closely collaborate with the groups from ACU, CIAE, University of Colorado, GSU, Korea University, Muhlenberg, PKU and RBRC and coordinate the efforts among these institutions.UIUC will carry out R&D in Urbana with the goal to determine the position resolution and rate capabilities of the RPC detectors.

The UIUC group administers the NSF MRI funds transferred to Illinois. Specifically, it initiates and manages subcontracts for the electronics development to Columbia University, the gas system construction to RBRC, the mechanical engineering to Bartoszek engineering, the RPC gap production to Korea University and for the detector module construction to CIAE.

Participating faculty from UIUC include Matthias Grosse Perdekamp (0.5 FTE, project manager), Jen-Chieh Peng (0.2 FTE from 2008) and Naomi Makins (0.3 FTE from 2009). Research faculty includes Ralf Seidl (0.5 FTE, PRC detector hardware manager) and Steve Williamson (0.1 FTE). Recently Dr. Young Jin Kim joined the UIUC group from GSI, Darmstadt. He comes with first hand RPC experience gained at GSI and during his thesis work at Korea University. In addition there will be another postdoctoral researcher (0.5 FTE) starting in Fall 2007. UIUC aims to contribute 3 graduate students (two at 0.7 FTE and

the third with 0.2 FTE). Two technicians in the group, John Blackburn and Eric Thorsland will be available 0.2 FTE. With David Northacker UIUC has hired a new staff person from FNAL with extensive experience on the CMS muon tracking chamber assembly factories. He will work full time on the RPC project and will be available for extended stays at BNL. UIUC undergraduate students will actively participate in the assembly and QA at BNL. We estimate that on average during R&D and construction UIUC undergraduate students will contribute 1 FTE to the muon trigger project.

Iowa State University

Iowa State University (ISU) was one of a group of four universities that submitted a proposal to the National Science Foundation's Major Research Instrumentation program to upgrade the muon trigger system for the PHENIX forward spectrometers. The proposal was funded for five years starting in September 2005. The ISU experimental nuclear physics group has the responsibility for building the Level-1 Trigger system for this upgrade project. This system will use input from both the RPCs and the modified muon tracker FEEs to obtain the desired rejection needed to study events from rare $W$ decays. The trigger design effort is led by Prof.John Lajoie. The group has the contractual responsibility to maintain and upgrade the PHENIX Level-1 Trigger and designed the trigger electronics upgrade for the PHENIX muon spectrometers. The trigger design team also includes our electronics engineer Gary Sleege. The group is assisted by ISU graduate students Todd Kempel and Feng Wei. Prof. John Hill was the editor for the initial Letter of Intent for a PHENIX Forward Spectrometer Upgrade the successful NSF-MRI proposal and is editor for this CDR. He is also in charge of managing the finances for the NSF-MRI and will become deputy manager to Prof. Grosse Perdekamp starting on July 1, 2007.

KEK

The director for the muon tracker FEE part of the project is Naohito Saito who is the P.I. on a five year grant from the JSPS for $2,000,000 to develop the inputs from the muon tracker FEEs for the fast muon trigger. As P.I. he will be in charge of all spending for the muon tracker FEE portion of the project. The KEK group will hire a full time postdoctoral researcher for the project. Responsibilities include overall management, development of on-line and off-line software and the oversight of installation and operation at BNL.

Korea University

The nuclear physics group of Korea University is responsible for the production of all gas gaps for the muon trigger RPCs in the PHENIX upgrade program. The Korea University group has worked on the development and the production of the

forward muon trigger RPCs for the CMS collaboration at LHC/CERN since 1997. The CMS forward muon trigger RPCs, covering the pseudorapidity from 0.9 to 2.1 were designed for high rate at about 1 kHz/$cm^2$, which should be sufficient for PHENIX. The Korea University group has designed and built various tools for the mass production of muon trigger RPCs, such as the electrode coating silk screening tool, the large area PET film coating machine, the gas gap assembly facilities, and the oil coating unit, etc. These facilities and expertise will be utilized for the PHENIX gas gap production. The RPC gas gap production for PHENIX will be led by Prof. Byungsik Hong, and three other faculty members, Profs. Kyong Sei Lee, Sung Keun Park, and Kwang-Souk Sim, will actively participate in this effort. All participating faculty members are close collaborators for the forward RPC production for CMS from the very beginning. Kyong Sei Lee is the research professor dedicated to the RPC development, and he will take care of all technical aspects for the gas gap production. Prof. Sung Keun Park is the director of the Korea Detector Laboratory, where all production facilities reside. Prof. Park will manage the operation of the gas gap production facilities for PHENIX, and his contribution to the project is essential for the successful completion of the RPC gas gap production. Prof. Kwang- Souk Sim will supervise the RPC gas gap production at Korea University with Prof. Byungsik Hong. There also will be two graduate students from Korea University.

Kyoto University

Major contributors to the muon tracker FEE upgrade project are the faculty and students of Kyoto University. Prof. Imai is a Full Professor and was co-spokesperson for the muon arm project. Prof. Murakani supervises the day-to-day activities of the graduate students involved in hardware development. Prof. Tanida is the day-to-day supervisor for graduate students involved in simulations. He was co-convenor of the PHENIX spin physics working group.

Mr. Shoji is the graduate student in charge of building and testing the amplifier-discriminator board. He is assisted by Mr. Senzaka, a new student. Mr. Karatsu is the graduate student in charge of building and testing the transmitter-receiver board. Mr. Aoki is a student close to his Ph.D. who had the idea for the FEE trigger and tested it's performance using PISA. Mr. Sato also is a graduate student involved in simulations of the trigger performance. Mr. Dairaku is a new graduate student who just joined the project. Most of these students will be available to help in the testing and installation of the muon tracker FEE system at BNL.

Los Alamos National Laboratory

The Los Alamos group is one of the groups in PHENIX who has great knowledge and experience with designing, installing and using the muon tracker FEE. This experience will be a vital resource for us as the muon FEE upgrade proceeds.

In particular Drs. Mike Leitch and Melynda Brooks of LANL will be available as consultants as the project progresses.

Muhlenberg College

The group at Muhlenberg College consists of Professor Brett Fadem and presently 4 undergraduate students. In the summer 2006 the group has contributed to the RPC R&D effort at UIUC. In the future the group will work on the assembly and quality assurance for the RPC detector modules in the assembly factory at BNL. In addition the group will contribute to the effort to improve the detector simulations as needed for future $W$-physics with the PHENIX muon arms.

University of New Mexico

Prof. Doug Fields has constructed one sector of a muon tracking chamber to be used as a test stand for the muon tracker FEE boards now being constructed and tested at Kyoto University.

Riken-BNL Research Center (RBRC)

RBRC is responsible for the development and construction of RPC gas systems and all safety systems and responsible for development of timing and calibration procedures for the RPC system. The contribution in the past includes leading the initial simulation effort for the trigger conceptual design being used as one of the key inputs for the NSF-MRI proposal; Leading the background test in run4 $p + p$ collisions and participating in the PKU RPC proto-type test in run5 $p + p$ collisions; Coordinating with PHENIX engineers and technicians to build the mini-gas system that is being used for RPC electronics R&D at Nevis lab. The group members include Dr. Gerry Bunce and Dr. Wei Xie.

RIKEN Institute

Dr. Taketani is a senior staff member at RIKEN and is closely involved with the design and testing of the transmitter-receiver board. He works closely with the Kyoto University students involved in board production and testing. He will also supervise the installation and Q.A. of the FEE system at BNL. Dr. Fukao is a RIKEN post doc who will devote most of his effort to the muon tracker FEE project. He will be involved in R&D and electronics quality assurance in Japan. During the installation stage at BNL he will be at BNL and serve as link between BNL and physicists in Japan.

Rikkyo University

Profs. Kurita and Murata are Professors at Rikkyo. Prof. Kurita managed the muon I.D. factory at BNL and will help at BNL with the installation of the muon

tracker FEE system. Prof. Murata was instrumental in designing the optical alignment system for the PHENIX muon tracker. He will be involved at BNL in the mechanical installation phase of the muon tracker FEE system.

# Chapter 6

# Budget and Schedule

## 6.1 Total Estimated Cost

In the following we present a first estimate of the total project cost. We expect to carry out a detailed analysis of the project costs in combination with the currently ongoing development of a detailed Work Breakdown Structure. It is planned to present the WBS and cost analysis in a technical design report for review to the PHENIX collaboration in December 2007.

(I) Resistive Plate Chamber System:

1) High Voltage: $92074

| 2 SY 1527 Mainframe | $14112 | $28224 |
|---|---|---|
| 10 A1526 HV modules | $5761 | $57610 |
| 120 CME connectors | $22 | $2640 |
| 1200 m HV cable | $3/m | $3600 |
| Labor | UIUC | 0 |

2) Gas System: $50000

3) LL1 electronics: $299080

| Engineering | | $95200 |
|---|---|---|
| Contingency | | $21000 |
| Parts, boards | | $133700 |
| Contingency | | $28000 |
| Prototype production | | $21180 |

4) FEE development: $312000

| Engineering, Amp/Disc board | | $90000 |
|---|---|---|
| Readout + Trigger Board | | $150000 |
| Contingency | | $72000 |

5) FEE production cost: $360300

| Amplifier-Discriminator-Board | | |
|---|---|---|
| Parts, boards, assembly | $7.2/ch. | $115200 |
| Contingency | 20% | $ 23040 |
| Readout+trigger board | | |
| Parts, boards, assembly | $10.2/ch. | $172800 |
| Contingency | | $34560 |
| Test stand | | $14700 |

6) RPC detector module construction: $664203

| 20 RPC1A gaps | $600 | $12000 |
|---|---|---|
| 20 RPC1B gaps | $700 | $14000 |
| 135 RPC2 gaps | $800 | $108000 |
| 116 RPC3 gaps | $800 | $92800 |
| Contingency | 30% | $68040 |
| Detector boxes | | $218882 |
| Contingency | 20% | $65665 |
| Support BNL visitors | | $84816 |

7) RPC design and integration: $357000

| Engineering | | $90000 |
|---|---|---|
| Materials | | $200000 |
| ACU students | | $67000 |
| Labor | BNL, CIAE, UIUC | 0 |

The total cost for the RPC project amounts to $2134657. Available funds include the NSF MRI of $1984797 and matching funds from ISU, $50000 and UIUC, $100000. During the installation phase, UC Riverside also contributes a postdoctoral fellow for a period of 2 years. CIAE provides a mechanical engineer to be stationed at BNL for 6 months during the second half of 2007. RBRC provided an institutional contribution of approximately $30000 to purchase equipment and the University of Colorado provided an institutional contribution of $70000.

(II) Muon tracker trigger electronics: A cost analysis is not available yet. The total project cost is estimated to funding, $2600000, available from the JSPS.

## 6.2   Schedule

A detailed schedule is under development for the technical design report. At the present time there are still significant uncertainties connected to the preliminary schedule given below. They arise from (a) the decision between custom developed RPC amplifier-discriminator boards for the PHENIX RPCs or the existing CMS chips and/or boards, (b) the availability of the Italian CMS bakelite vendor, (c) the CMS schedule for the use of the RPC gap production line at Korea University (d) the availability of engineering resources for the mechanical design. At the present time, we expect that the schedule will follow the timeline given in the table below.

| | |
|---|---|
| Mar-15-07 | RPC prototype A available |
| May-15-07 | Start setup of RPC factory at BNL |
| July-01-07 | RPC prototype B available |
| July-07 | Review MuTr-trigger-board performance |
| Aug-07 | Installation of MuTr-trigger-board in 1 octant |
| | each in north muon arm station 1 and 2 |
| Sep-07 | Complete RPC Prototype C using BNL factory |
| Oct-07 | Complete engineering design for RPC detector-module and integration |
| Nov-07 | Review of LL1 trigger processor design |
| Dec-07 | Final review of RPC mechanical design and RPC front end electronics |
| Dec-07 | Review MuTr-trigger board octant test performance |
| | + final review of MuTr-trigger board |
| Dec-07 | Complete technical design report and review |
| Feb-08 | Complete RPC Prototype C in BNL factory |
| Feb-Jul-08 | Production (LL1, MuTr-trigger board, RPC FEE, |
| | RPC detector modules for RPC 3 north + south) |
| | for first installation step in summer 08 |
| Jul-Aug-08 | Installation of MuTr-trigger-boards in north muon arm stations 1 and 2 |
| | Install RPC3 north |
| | Install north LL1 |
| | Install Cu shielding for 1 north octant |
| Jun-Oct-09 | Installation of MuTr-trigger-boards in south muon arm stations 1 and 2 |
| | Install RPC3 south |
| | Install RPC2 south and north |
| | Install LL1 north |
| | Install Cu shielding for all octants south and north |
| | Install NCC tungsten |
| Nov-10 | Decision on final muon trigger configuration |
| Summer-11 | Remove Shielding |
| | Install RPC1AB north and south |
| | Install MuTr-trigger-boards in stations 3 |

# Bibliography

[1] Adare, A. *et al.*,
http://www.npl.uiuc.edu/phenix/muon-trigger/cdr/review-feb-2007.pdf .

[2] Bradamante, F., Nucl. Phys. A622 (1997) 50c-65c.

[3] Adeva, B. *et al.*, Phys. Lett. B420 (1998) 180-190.

[4] Stratmann, M. and Vogelsang, W., Phys. Rev. D64 (2001) 114007.

[5] Daleo, A. and Sassot, R., Nucl. Phys. B673 (2003) 357-384.

[6] Sissakian, A. N., Shevchenko, O. Yu. and Ivanov, O. N., Phys. Rev. D70 (2004) 074032.

[7] Grosse-Perdekamp, M., Talk given at the XII International Workshop on Deep Inelastic Scattering (DIS2004),
http://www.saske.sk/dis04/talks/F/perdekamp.ppt .

[8] Bunce, G., Saito, N., Soffer, J. and Vogelsang, W., Ann. Rev. Nucl. Part. Sci. 50 (2000) 525-575.

[9] Hirai, M., Kumano, S. and Saito, N., Phys. Rev. D74 (2006) 014015.

[10] Sjostrand, T. *et al.*, Comput. Phys. Commun. 135 (2001) 238-259.

[11] Adloff, C. *et al.*, Eur. Phys. J. C19 (2001) 289-311.

[12] Lai, H. L. *et al.*, Eur. Phys. J. C12 (1999) 375-392.

[13] Martin, A. D., Roberts, R. G., Stirling, W. J. and Thorne, R. S., Eur. Phys. J. C39 (2005) 155-161.

[14] Gluck, M., Reya, E., Stratmann, M. and Vogelsang, W., Phys. Rev. D53 (1996) 4775-4786.

[15] Goto, Y. *et al.*, Phys. Rev. D69 (2004) 054021.

[16] Laenen, E., Sterman, G. and Vogelsang, W., Phys. Rev. Lett. 84 (2000) 4296-4299.

[17] Laenen, E., Sterman, G. and Vogelsang, W., Phys. Rev. D63 (2001) 114018.

[18] Ashman, J. *et al.*, Nucl. Phys. B328 (1989) 1-35.

[19] Baum, G. *et al.*, Phys. Rev. Lett. 51 (1983) 1261-1265.

[20] Bunce, G. *et al.*, Phys. Rev. Lett. 36 (1976) 1113-1116.

[21] Adams, D. L. *et al.*, Phys. Lett. B265 (1991) 462-466.

[22] Adams, J. *et al.*, Phys. Rev. Lett. 92 (2004) 171801.

[23] Bland, L. C., hep-ex/0602012.

[24] Sivers, D., Phys. Rev. D41 (1990) 83.

[25] Collins, J. C., Nucl. Phys. B396 (1993) 161.

[26] Ralston, J. P. and Soper, D. E., Nucl. Phys. B152 (1979) 109.

[27] Qiu, J. and Sterman, G., Phys. Rev. D59 (1998) 014004.

[28] Airapetian, A. *et al.*, Phys. Rev. Lett. 84 (2000) 4047-4051.

[29] Airapetian, A. *et al.*, Phys. Rev. Lett. 94 (2005) 012002.

[30] Boer, D. and Vogelsang, W., Phys. Rev. D69 (2004) 094025.

[31] Seidl, R. *et al.*, The Belle Collabotation, Phys. Rev. Lett. 96 (2006) 232002.

[32] HERMES Collaboration, hep-ex/0512019.

[33] Collins, J. C., Heppelmann, S. F. and Ladinsky, G. A., Nucl. Phys. B420 (1994) 565.

[34] Mulders, P. J. and Tangerman, R. D., Nucl. Phys. B461 (1996) 197-237.

[35] Bacchetta, A., Bomhof, C. J., Mulders, P. J. and Pijlman, F., Phys. Rev. D72 (2005) 034030.

[36] Anselmino, M. *et al.*, Phys. Rev. D73 (2006) 014020.

[37] Airapetian, A. *et al.*, Phys. Rev. D71 (2005) 012003.

[38] Bourrely, C. and Soffer, J., Phys. Lett. B314 (1993) 132-138.

[39] Doncheski, M. A., Halzen, F., Kim, C. S. and Stong, M. L., Phys. Rev. D49 (1994) 3261-3269.

[40] Nadolsky, P. M. and Yuan, C. -P., Nucl. Phys. B666 (2003) 35.

[41] Matsui, T. and Satz, H., Phys. Lett. B178 (1986) 416.

[42] Morrin, R. *et al.*, PoS LAT2005 (2006) 176.

[43] Abreu, M. C. *et al.*, Phys. Lett. B410 (1997) 337.

[44] Alessandro, B. *et al.*, Eur. Phys. J. C39 (2005) 335.

[45] Adare, A., nucl-ex/0611020.

[46] Thews, R. L., Eur. Phys. J. C43 (2005) 97.

[47] Thews, R. L. and Mangano, M. L., Phys. Rev. C73 (2006) 014904.

[48] Yan, L., Zhuang, P. and Xu, N., Phys. Rev. Lett. 97 (2006) 232301.

[49] Glenn, A. .M., Quark Matter 2006 Proceedings.

[50] Adare, A. [PHENIX Collaboration], nucl-ex/0611018.

[51] Liu, H., Rajagopal K. and Wiedemann, U. A., hep-ph/0607062 and private communication.

[52] Friedman, J. I. and Kendall, H. W., Annu. Rev. Nucl. Sci. 22 (1972) 203.

[53] Abromowicz, H. *et al.*, Z. Phys. C15 (1982) 19.

[54] Conrad, J. M., Shaevitz, M. H. and Bolton, T., Rev. Mod. Phys. 70 (1998) 1341.

[55] Gottfried, K., Phys. Rev. Lett. 18 (1967) 1174.

[56] Bloom, E. D. *et al.*, Proc. 15th Int. Conf. on High Energy Phys., Kiev, USSR (1970).

[57] Bloom, E. D., Proc. 6th Int. Sym. on Electron and Photon Interactions at High Energies, edited by Rollnik, H. and Pfeil W. (North-Hollan, Amsterdam, 1974) 227.

[58] Aubert, J. J. *et al.*, Nucl. Phys. B293 (1987) 740.

[59] Arneodo, M. *et al.*, Phys. Rev. D50 (1994) R1.

[60] Baldit, A. *et al.*, Phys. Lett. B342 (1995) 339.

[61] Towell, R. S. *et al.*, Phys. Rev. D64 (2001) 052002.

[62] Ackerstaff, K. *et al.*, Phys. Rev. Lett. 81 (1998) 5519.

[63] Kumano, S., Phys. Rep. 303 (1998) 5519.

[64] Speth, J. and Thomas, A. W., Adv. Nucl. Phys. 24 (1998) 83.

[65] Garvey, G. T. and Peng, J. C., Prog. Part. Nucl. Phys. 47 (2001) 203.

[66] Barger, V. D. and Phillips, R. J. N., Collider Physics (Addison - Wesley Publishing Company, 1987).

[67] Alitti, J. *et al.*, Phys. Lett. B276 (1992) 365.

[68] Abe, F. *et al.*, Phys. Rev. D44 (1991) 29; Badgett, W. F., Fermilab Preprint, FERMILAB-Conf-94/258-E (1994).

[69] Abe, F. *et al.*, Phys. Rev. Lett. 68 (1992) 1458; Alitti, J. *et al.*, Phys. Lett. B276 (1992) 365.

[70] Peng, J. C. and Jansen, D. M., Phys. Lett. B354 (1995) 460.

[71] Acosta, D. *et al.*, Phys. Rev. D71 (2005) 051104.

[72] The Science and Experimental Equipment for the 12 GeV Upgrade of CE-BAF, Thomas Jefferson National Accelerator Facility, 2005.

[73] Close, F. E., Phys. Lett. B43 (1973) 422.

[74] Carlitz, R., Phys. Lett. B58 (1975) 345.

[75] Farrar, G. R. and Jackson, D. R., Phys. Rev. Lett. 35 (1975) 1416.

[76] Melnitchouk, W. and Peng, J. C., Phys. Lett. B400 (1997) 220.

[77] Whitlow, L. *et al.*, Phys. Lett. B282 (1992) 475.

[78] Lai, H. L. *et al.*, Phys. Rev. D51 (1995) 4763.

[79] Santonico, R. and Cardarelli, R., Nucl. Instr. and Meth. 187 (1981) 377-380.

[80] Belle, Barbar, and LHC experiments.

[81] Ying, J. *at al.*, Nucl. Instr. and Meth. A459 (2001) 513-522.

[82] Abbrescia, M. *et al.*, Nucl. Instr. and Meth. A431 (1999) 413; Nucl. Instr. and Meth. A398 (1997) 173.

[83] Park, S. *et al.*, Nucl. Instr. and Meth. A550 (2005) 551-558.

[84] Aftab, Z. *et al.*, Nucl. Phys. B158(Proc. Suppl.) (2006) 16-20.

[85] Hong, B. *et al.*, J. Korean Phys. Soc. 48(2006) 515-529.

[86] Abbrescia, M. *et al.*, Nucl. Instr. and Meth. A456 (200) 143.

[87] Sjostrand, T. *et. al*, Comp. Phys. Comm. 135 (2001) 238.

[88] Wang, X. N. and Gyulassy, M., Phys. Rev. D44 (1991) 3501; Phys. Rev. D45 (1992) 844; Comp. Phys. Comm. 43(1987) 387.

[89] Aidala, C. *et al.*, http://www.bnl.gov/henp/docs/spinplan0205.pdf (2005).

[90] Balazs, C. and Yuan, C. P., Phys. Rev. D56 (1997) 5558.

[91] Adare, A. *et al.*, https://www.phenix.bnl.gov/phenix/WWW/p/info/an/506/ (2006).

[92] Adare, A. *et al.*, https://www.phenix.bnl.gov/phenix/WWW/p/info/an/408/ (2006).

[93] Albajar, C. *et al.* Nucl. Phys. B335 (1990) 261.

[94] Alper, B. *et al.*, Nucl. Phys. B100 (1975) 237.

[95] Acosta, D. *et al.*, Phys. Rev. D73 (2006) 052002.

[96] Pak, R. *et al.*, http://www.phenix.bnl.gov/phenix/WWW/docs/upgrades/fvtx/PHENIX_FVTX_march2006 .